MEASUREMENTS OF ENERGY AND MOMENTUM IN THE MESOSPHERE

D. J. Murphy, B.Sc.(Hons), M.Sc.

A thesis for the degree of Doctor of Philosophy

DEPARTMENT OF PHYSICS AND MATHEMATICAL PHYSICS

UNIVERSITY OF ADELAIDE

awarded 20.12.90

September 1990

...and the only thing worth doing for the race is to increase its stock of ideas. Then, if you make available a larger stock, the people are at liberty to help themselves from out of it. By this process the means of improvement is offered, to be accepted or rejected freely, and there is a faint hope of progress in the course of the millennia. Such is the business of the philosopher, to open new ideas. It is not his business to impose them on people.

The Book of Merlyn
T.H. White

This thesis contains no material which has been accepted for the award of any other degree or diploma in any university and, to the best of my knowledge and belief, contains no material previously published or written by another person, except where due reference is made in the text of the thesis. I consent to the thesis being made available for photocopying and loan if applicable upon acceptance of the degree.

Damian Murphy

Abstract

In this thesis, aspects of radar methods currently used to obtain important parameters of energy and momentum transport in the mesosphere are examined. Methods that enable the extraction of the rate of dissipation of energy through turbulence, from radar echoes, are presented. It is suggested that one of these methods, which utilises the width of the Doppler spectrum to obtain the energy dissipation rate, is susceptible to contamination by high-frequency gravity waves motions. This hypothesis is tested through some case studies carried out on high time resolution data obtained using a VHF radar at Poker Flat, Alaska. It is found that the effect of high-frequency gravity waves can be important in data obtained with sampling times of the order of a minute. This data set utilised sampling times of around ten seconds and it was shown that this was of short enough duration to avoid the effects of high-frequency gravity waves. Values of the turbulence energy dissipation rate are then calculated and their variation as a function of time are also discussed.

Much of the remainder of the work in this thesis involves the methods of analysis of data obtained using the Buckland Park HF radar near Adelaide. Two problems associated with previous measurements of the vertical flux of horizontal momentum are considered. The first involves the effective pointing angle of the radar beams that are used. This angle is important in calculations of momentum flux using the dual beam method proposed by Vincent and Reid. The effective pointing angle usually differs from that expected from the antenna phasing and can vary as a function of height and time. A method of calculating the effective pointing angle from the spatial correlation function of the echoes on the ground is developed and tested. Some modelling of the effect of time variations of pointing angle on momentum flux measurements was carried out and is presented.

The second problem associated with momentum flux measurements using the Buckland Park HF radar involves the presence of outliers in the velocity data. Suitable methods of outlier rejection for different period bands were developed. It was then possible to analyse 12 momentum flux data sets taken on a campaign basis over one year from March 1985 to February 1986. The results of this analysis are presented.

Seasonal variations of the vertical flux of zonal and meridional momentum are considered. It is found that $\overline{u'w'}$ and $\overline{v'w'}$ vary as a function of season and that this effect is most clearly exhibited in the short period (8 min – 1 hr) data. The relative magnitudes of the momentum fluxes in various period bands are considered and it is found that, although $\overline{u'w'}$ is generally largest for the short period band data, this is not the case for $\overline{v'w'}$. It is also found that the magnitude of $\overline{v'w'}$ is often of similar amplitude to that of $\overline{u'w'}$.

The implications of the $\overline{u'w'}$ and $\overline{v'w'}$ data in the balancing of the mesospheric momentum budget are discussed briefly. Calculations of the mean-flow acceleration due to the divergence of the momentum flux are carried out and the results are compared to the Coriolis accelerations present at the corresponding times.

Acknowledgements

The work presented in this thesis spans three houses, three continents, at least one sheep station and a large number of lunchtimes. I would like to thank everyone who has helped me along the way, either by putting up with my anti-social PhD-student habits or by telling me, for the hundredth time, how to spell parallel. I'd like to do that but I'll probably forget a few people so sorry about that but here goes.

Doing a PhD involves a certain amount of guidance. Thanks go to Bob Vincent, my supervisor, for his support and forbearance, to Dave Fritts for giving me the opportunity to live and work in Alaska and for his help while I was there and to Wayne Hocking for his help with the turbulence part of the project. I'd also like to thank Dr. Basil Briggs who was always happy to help me when I wandered, ill prepared and confused, into his office, who read many of the chapters and taught me quite a few things about grammar that would have escaped me otherwise and whose example I wish I could follow. Thanks also to Iain Reid for his friendship, both in Germany and in Adelaide and for the advice he gave me in numerous conversations about my work and social realism.

Experimental work requires a significant amount of technical support and this was no exception. Thanks go to Bob Hurn and Alex Didenko for helping out at Buckland Park and to Shane Dillon for the diagram of BP and for telling me to hurry up all the time. Brian Fuller, to whom significant parts of Buckland Park owe their existence, shouldn't be forgotten either.

Lyn Birchby and Dallas Kirby have to take alot of orders in their capacity as data assistants and yet they smile on. Their help with things too numerous to mention (which include darning the sleeve of my favorite jumper and some good advice on washing machines) cannot be undervalued. Thanks very much for that.

And to my colleagues (Drazen, Steve, Trevor, Laurie, Brenton, Dave, Kong and the one whose name I can't remember): research groups get considerable variety from the parade of students that pass through them (at varying rates) and I'd like to say thanks to them. I'd also like to say thanks to the staff of the Mawson Institute for Antarctic Research (my current employers) for the freedom they have given me in letting me finish

my PhD. It's weeks since I did anything worthwhile for them and I am sure that they are having to do more to prepare for my (rapidly approaching) trip south. Many thanks to them.

To my Mum and my sister, who are probably still wondering what it is that I do, my love and thanks. To the Thompsons, who wonder why I haven't finished yet but give me the occasional feed anyway, thanks for the chocolates.

To the kids: thanks for making me feel young and to the courage you show me. If, on the day I die I realise that I have *lived* my life, it will be in your honour.

Finally, to my friends. To Jane and Richard at Lilydale, to Lew who has always been around, to Duncan who listened to my hassles and was there when I got back from OS. To the exceptional Bennett girls and to Wal, to Chalks and S.J. and Wos, to J for letting me win at squash, and to Fizz for being Fizz (and for the tassie trips). And to the others referred to above (Murphy 1990). Whatever the future may bring, the part you have played in my life has been very important to me and I thank you for it.

> *The years have turned the rusted key, and time is on the jog,*
> *Yet spend another night with me around the boree log.*

John O'Brien

Contents

Chapter 1

Introduction

In this thesis, some aspects of energy and momentum in the mesosphere are considered. Much of the emphasis is on the experimental and data handling techniques used to obtain quantitative information on these properties, but some interpretation of the measurements that are made is also presented. The interpretation, and that of others who consider the data presented here, seeks to build on the knowledge of this region of the atmosphere; however, this cannot occur without suitable foundation. The aim of this chapter is to lay that foundation for the rest of the thesis. General aspects of the atmosphere that pertain to this study are presented here. Further reviews and discussions of more particular topics are presented at the appropriate times later in the thesis.

1.1 Atmospheric structure

The structure of the atmosphere can be considered in a number of ways, depending on the property of interest. For example, if the electrical properties of the atmosphere are to be investigated, then knowledge of the density of free electrons as a function of height (say) would be useful. Because the data considered here were obtained through the use of atmospheric radars which rely on the presence of free electrons for reflection or scatter, some aspects of ionospheric physics will be considered briefly.

The ionosphere, i.e. that part of the atmosphere where the constituent gases have been ionised, thereby liberating electrons, is divided into three main parts. These are called the D-, E- and F- (made up of F1- and F2) regions and are depicted in figure 1.1 where the number of electrons per unit volume is plotted as a function of height. The range of heights that are considered in this thesis covers the upper part of the D-region and the lower part of the E-region. The processes that lead to ionisation in these regions will be considered briefly.

Figure 1.1 typifies the situation during daylight. At night, the electron density becomes much smaller suggesting that it is solar radiation that is ionising the atmospheric gases. Nicolet suggested in 1945 (see Brasseur and Solomon, 1984) that, in the D-region, the gas being ionised was nitric oxide and the process involved photoionisation by Lyman$-\alpha$ (121.6 nm) radiation. A later theoretical study by Nicolet and Aiken (1960) suggested that, as well as the NO^+ (whose molecular mass is 30), O_2^+ (mass 32) would be present. This was verified with rocket-borne mass-spectrometric measurements carried out by Narcisi and Bailey (1965) whose results are presented in figure 1.2. It can be seen that some other species with molecular masses of 19 and 37 are present in significant concentrations. These are due to the cluster ions H_3O^+ and $H_5O_2^+$. Cluster ions with larger orders of hydration (n in $H^+(H_2O)_n$) also exist; however, their abundance and orders of hydration depend on water vapour content and temperature and are spatially and temporally variable as a result. Experiments seeking heavy negative ions in this region find few below 80 km at night and 70 km during the day. Because the atmosphere is electrically neutral, the free electron concentration can be attributed to the positive ions discussed above. In the lower E-region, extreme ultraviolet radiation (Lyman$-\beta$ 102.6 nm) and soft X-rays play a more important role in producing the ions O_2^+ and NO^+.

An alternative system for classifying altitude regions of the atmosphere is one that has temperature as its basis. Temperature turns out to be a useful parameter for this work because atmospheric dynamics forms the main field of interest in this thesis and, as will be seen shortly, the dynamics of the atmosphere is closely tied to its temperature structure (and vice versa). This distribution is presented in figure 1.3 from Brasseur

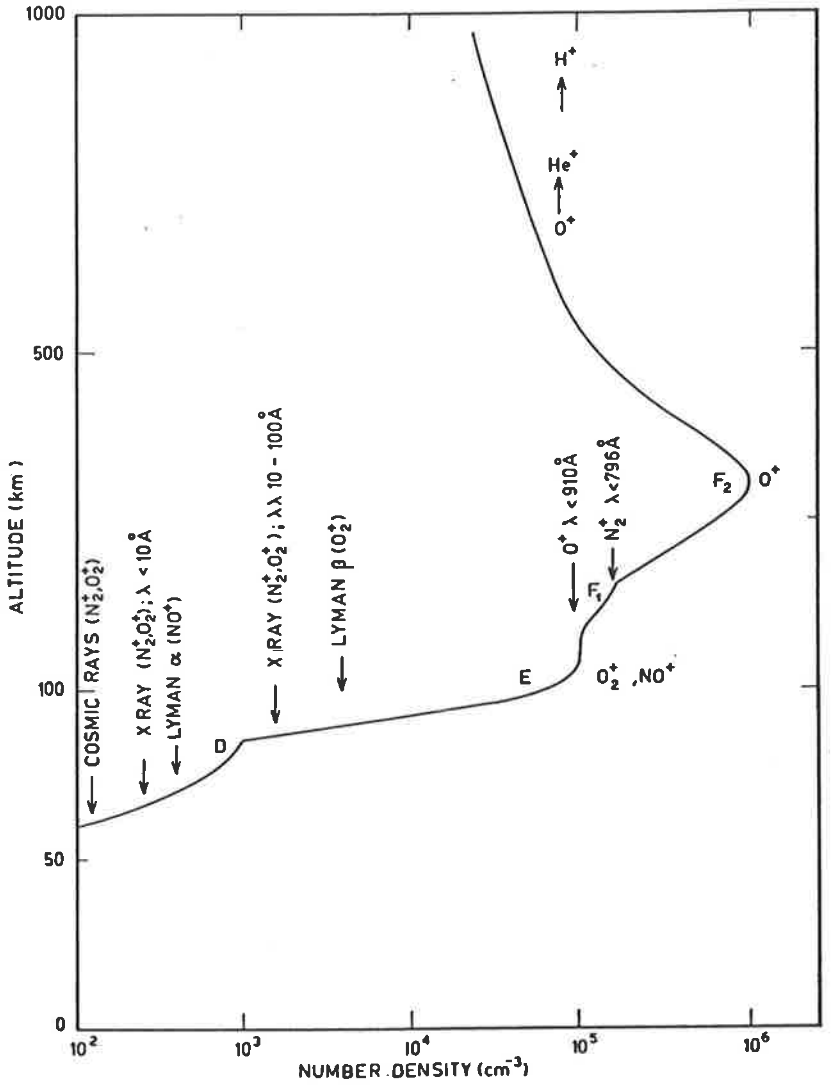

Figure 1.1: A typical daytime electron density profile of the ionosphere indicating principal ions at the various layers. (Banks and Kockarts, 1973)

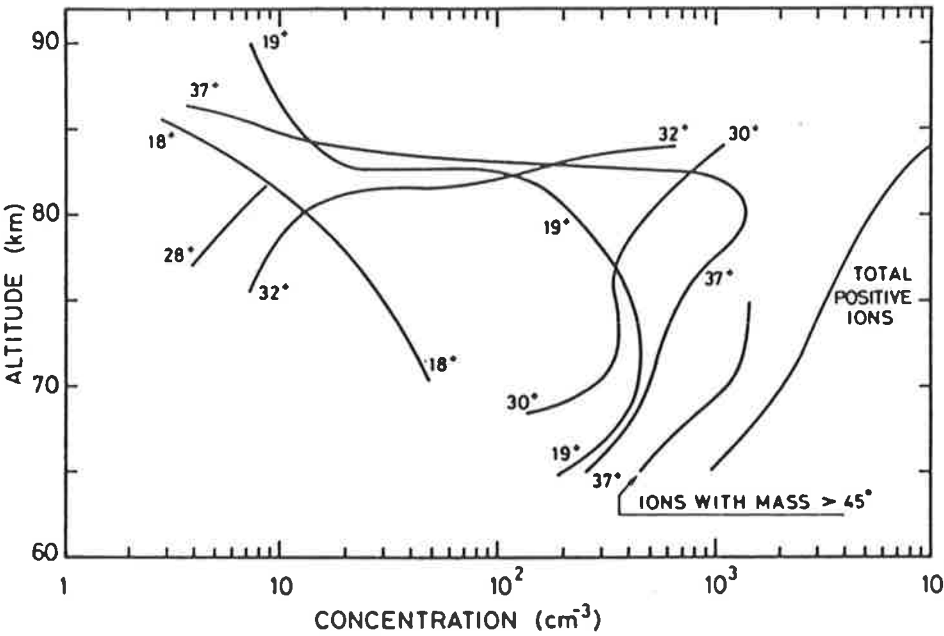

Figure 1.2: Mass spectrometric observations of positive ions in the region 65 to 90 km. Molecular masses are indicated on the diagram. (Narcisi and Bailey, 1965)

and Solomon (1984) where it can be seen that the temperature alternately decreases and increases as a function of height. The lowest region, where a decrease in temperature with height is evident is called the "troposphere". The temperature distribution in this region is due to heating of CO_2, H_2O and other "greenhouse gases" by infrared radiation. This radiation, incident from below, results from the heating of the earth's surface due to solar insolation and reradiation at infrared wavelengths. If the troposphere did not contain these gases, the temperature there would be 20–30 K less than it is. This temperature enhancement is called the "greenhouse effect". The decrease in temperature through the troposphere ceases at a height of approximately 10–15 km. The temperature remains essentially constant throughout the next region which is known as the "tropopause".

The "stratosphere" takes in the height range 20–50 km. It is characterised by increasing temperatures from the low of around 220 K at the tropopause to around 270 K where the temperature becomes constant again in the "stratopause". A second region of decreasing temperature, known as the "mesosphere" then follows. The upper parts of the mesosphere and the region above it where the temperature once again becomes constant, (the "mesopause") are the coldest parts of the terrestrial atmosphere with temperatures that can fall below 180 K. From there, at around 85 km, temperature

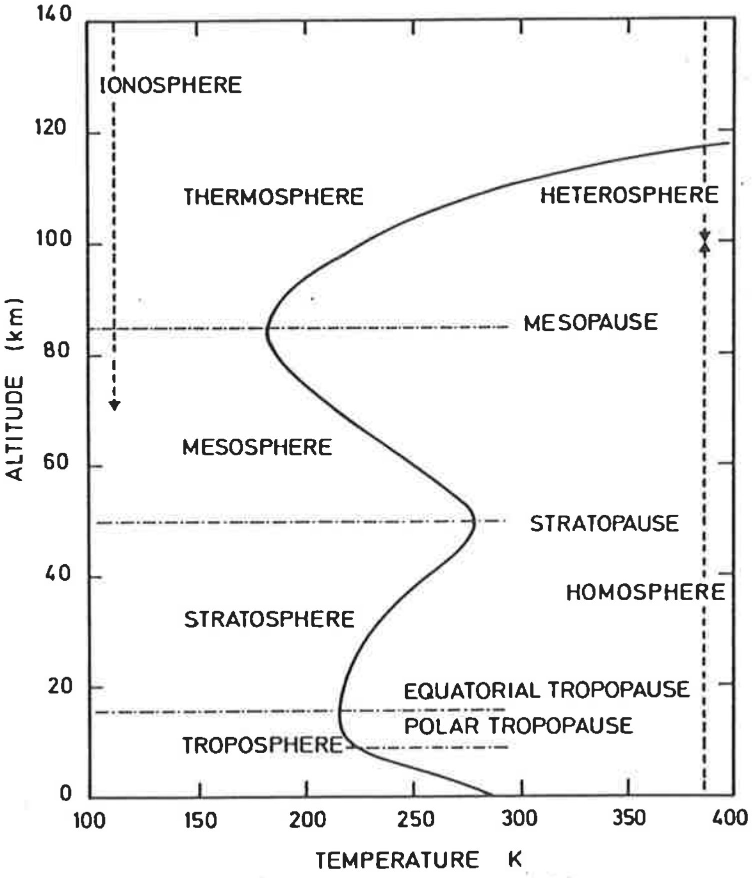

Figure 1.3: The temperature structure of the atmosphere

once again increases and continues to do so throughout the uppermost region of the atmosphere, the "thermosphere".

The increase in temperature that is evident in the stratosphere (figure 1.3) must be associated with a source of heating in that region. Figure 1.4 depicts the rate of heating in K/day at the solstice (London 1980) due to absorption by O_3, O_2, NO_2 and CO_2. It can be seen that the stratopause corresponds in height to a peak in the heating rate. A similar but slightly different profile is presented in Kiehl and Solomon (1986). The differences between the two profiles are mainly due to the differences in the ozone distributions used in the two papers, but both profiles have peaks in heating at the stratopause. Of the first three chemicals given above, it is ozone that is the most important contributor to heating in the region 20–60 km (Kiehl and Solomon 1986) but O_2 makes an important contribution to heating in the upper mesosphere (see figure 1.4).

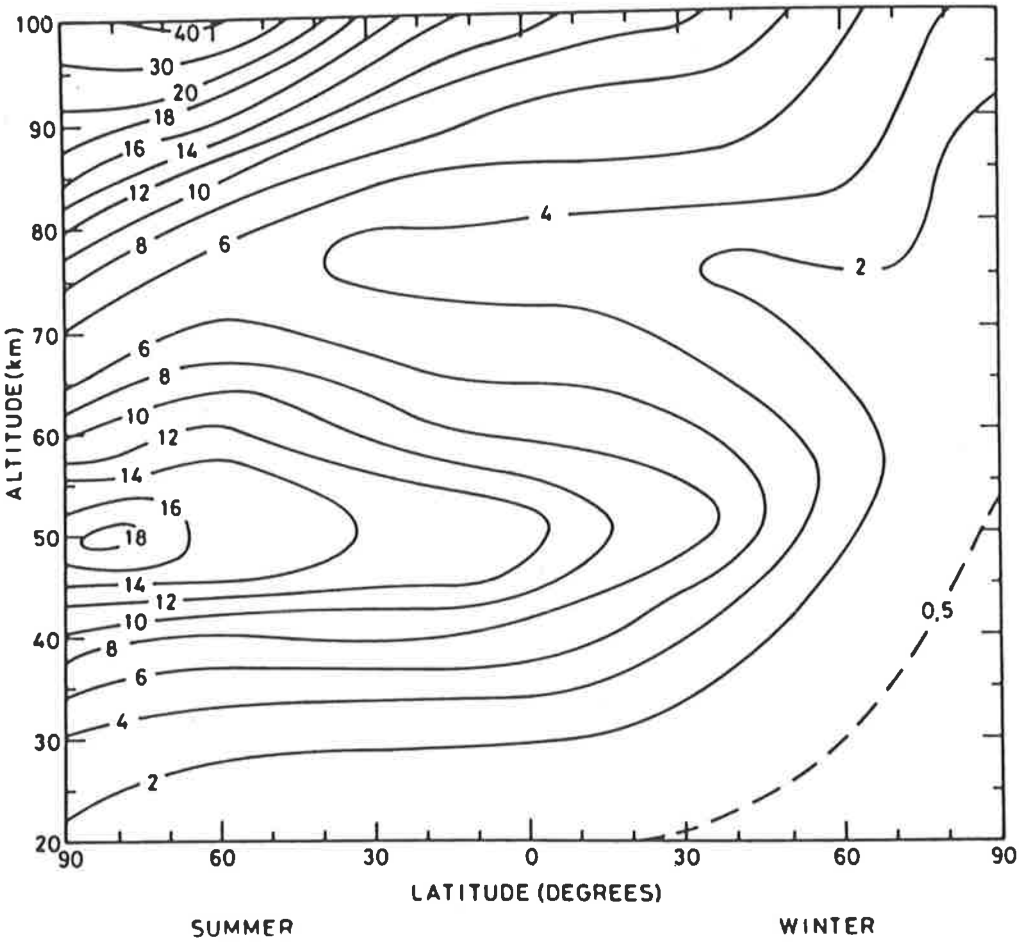

Figure 1.4: Heating rate in K/day due to solar absorption by O_3, O_2, NO_2 and CO_2 (London 1980)

1.2 The mesospheric momentum budget

If the arguments applied to ozone in the stratosphere were applied to heating by O_2 in the mesosphere then one would expect this to be a warm region as well but, as stated previously, this is not the case. Early measurements of temperature in this region were made using rocket-grenade techniques (Ference *et al.* 1956) at Fort Churchill in Canada (55°N, 94°W) by Stroud *et al.* (1960). Not only did these authors find a cold summer mesosphere, but they also found that the winter mesosphere was approximately 40K warmer than the same region in summer. This cannot be explained using the radiative equilibrium arguments that were applied in the stratosphere, making it is necessary to consider some non-radiative processes to account for the observations. Haurwitz (1961) suggested that these processes are dynamical. It was proposed that vertical motions near the poles, and the associated cooling (heating) due to the adiabatic expansion (compression) of the air parcels as they rose (fell) over the summer (winter) pole, would explain the observations.

A number of models have been used to test whether vertical motions in the polar regions do adequately reconcile theory and observations. The observational data set that is often used for comparison is that due to Murgatroyd (1969) and it is presented in figure 1.5. Representing the condition at the solstice, information on both the summer and the winter hemispheres is present. This can be compared to model results like the ones presented by Geller (1983), reproduced in figure 1.6. The model assumes that the atmosphere is in radiative equilibrium, where the heating due to absorption of solar radiation and the cooling through infra-red reradiation are in balance in the local environment, and no dynamical effects are included. In the temperature cross-sections, it can be seen that the summer-winter temperature inversion above 70 km that is obvious in the observations is not evident in the model temperature field.

It is also possible to use the meridional cross-section of temperature to calculate the meridional cross-section of the zonal wind using the thermal-wind equation (which assumes geostrophic balance). The results of this calculation are given in the lower

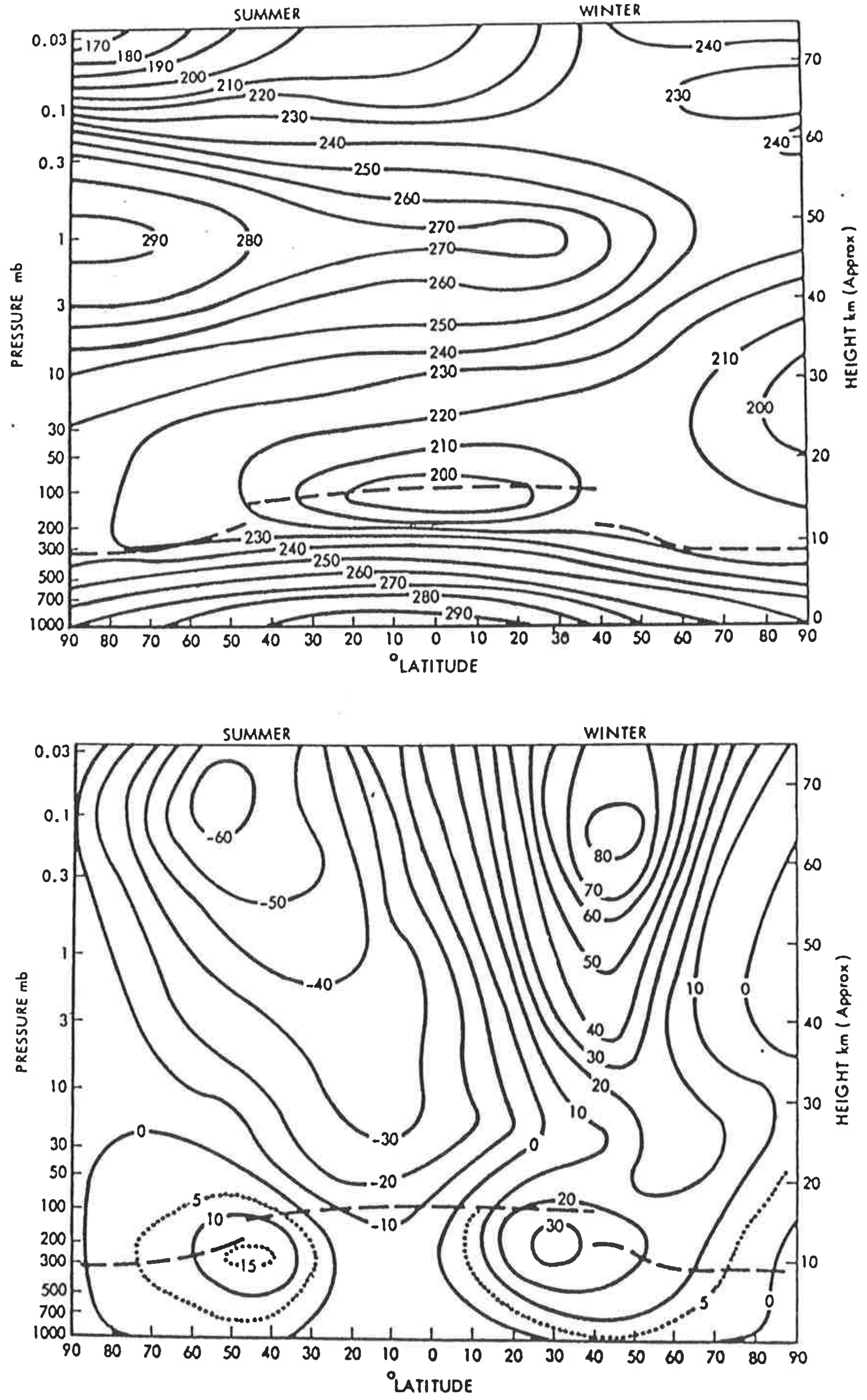

Figure 1.5: Observed meridional cross-sections of temperature (°K, upper panel) and zonal wind (ms^{-1}, lower panel) for the solstice. (After Murgatroyd 1969.)

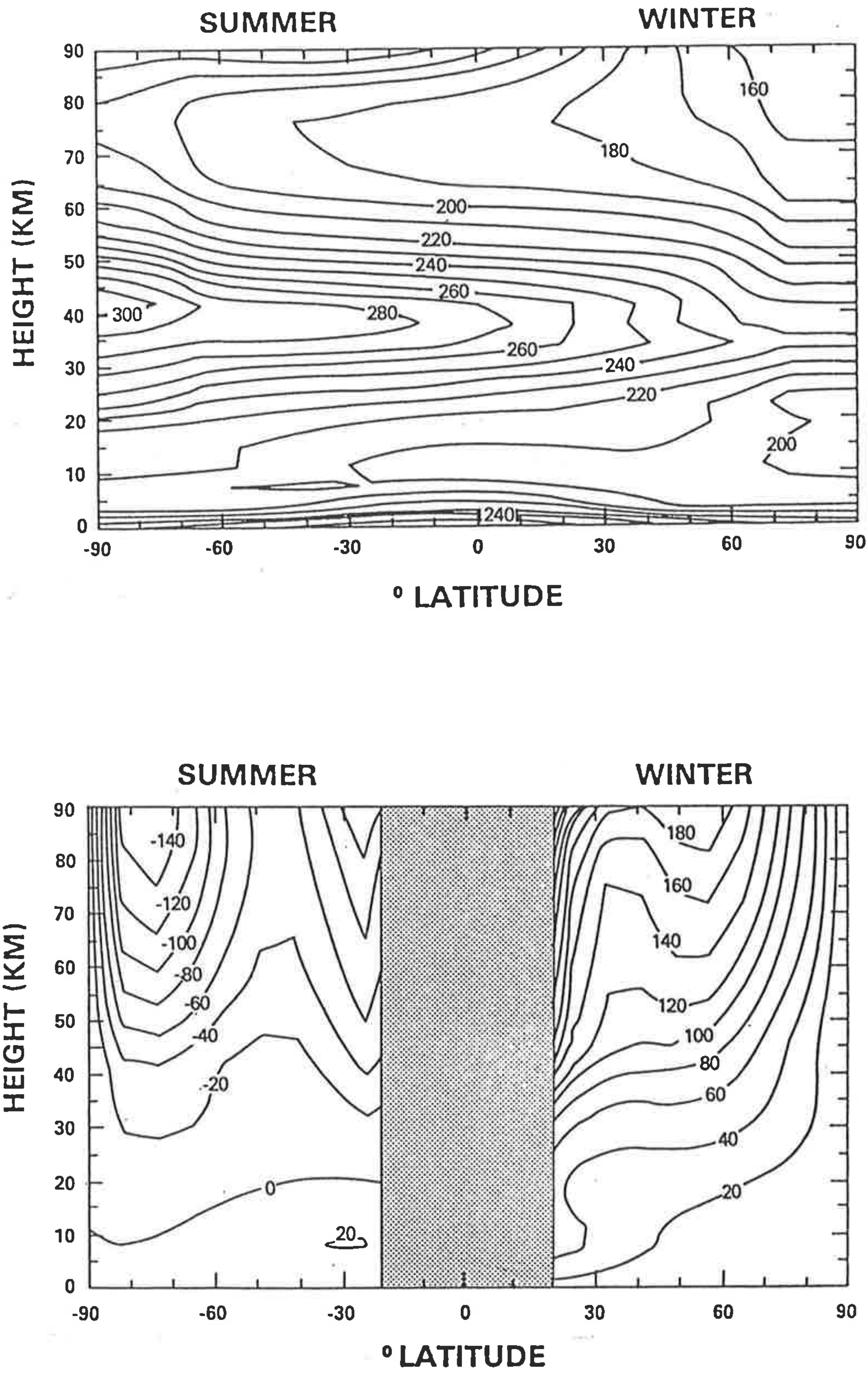

Figure 1.6: Model radiative equilibrium temperatures and geostrophic winds from Geller (1983)

part of figure 1.6. The grey band in the centre of this panel denotes the region where the geostrophic approximation is not applicable. Although there are some similarities between these model winds and the observed winds of figure 1.5, the two cross-sections are quite different in many respects and it could not be said that the assumptions used to formulate the model are extensively applicable throughout the middle atmosphere. But then, these models do not yet contain the dynamical effects that were proposed by Haurwitz (1961).

In order to include dynamical effects and still have a model that can be realistically applied to the atmosphere, it is necessary to maintain momentum balance in the model. The zonal velocities in figure 1.6 result from that requirement to balance momentum. The flow from the warm summer pole (near the stratopause) to the cool winter pole is turned into a zonal flow by the Coriolis force acting due to the earth's rotation. An alternative interpretation of this notes that a flow toward or away from the pole involves a change in the total angular momentum of the atmosphere. The total angular momentum of the earth and its atmosphere must be conserved and, as the average rate of rotation of the earth is observed to be very close to constant, then the total angular momentum of the atmosphere must also be conserved. Thus parcels of air that move in a manner that would change the angular momentum are acted on by a force (or pseudo force) that maintains the momentum balance. But herein lies a dilemma. The dynamical effect that has been proposed to explain the temperature structure of the mesosphere involves vertical motions over the poles. By continuity, these in turn involve a meridional flow but by the arguments just presented, any meridional flow must be turned into a zonal flow to maintain an angular momentum balance. Therefore, in the absence of other sources of momentum, meridional flows and this solution to the question of the atmospheric temperature structure, cannot exist. Observational evidence of a meridional flow *does* exists though, an example of which is given in figure 1.7 after Nastrom *et al.* (1982). (Note that the level at which these wind measurements have been made is above the temperature minimum.) Thus, it seems that the model needs another source of momentum.

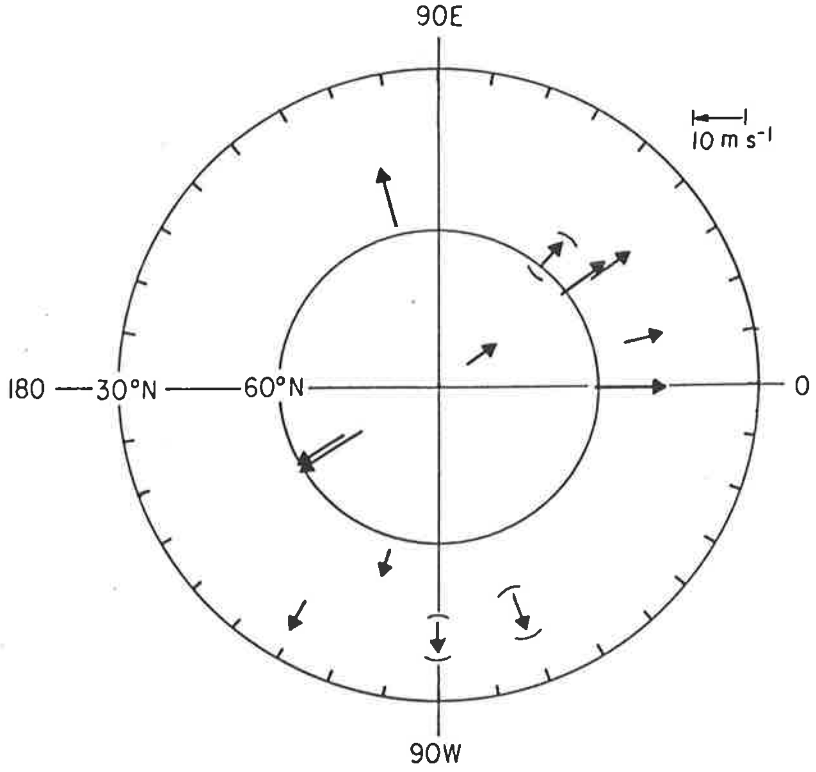

Figure 1.7: Averaged meridional wind components at 90 km in June in the Northern hemisphere (after Nastrom *et al.* 1982)

Haurwitz (1961) realised the need for another momentum source and suggested that friction due to eddy viscosity be considered. This friction would decelerate the mean flow thereby altering its momentum. Some calculations by Haurwitz showed a qualitative agreement with observations in a broad sense. This concept was incorporated into a model by Leovy (1964) through a term known as Rayleigh friction. This term acted to decelerate the mean flow in proportion to the mean-zonal wind with the constant of proportionality known as the Rayleigh drag coefficient. The Rayleigh drag concept is a simple one but it has no physical basis and therefore provides few clues as to what may supply the momentum needed in the mesosphere. It can, however, be used to investigate the qualitative nature of the momentum source (or sink) that is required to reconcile theory and observations. Leovy's success in this regard was limited by the fact that he only used Rayleigh drag profiles that were constant with height and only a fair agreement could be obtained.

It was some time before a height varying Rayleigh drag profile was used in a model.

Considerable improvements to the models (and to the computers used to make the calculations) were made in the time before the models of Cunnold *et al.* (1975) and Schoeberl and Strobel (1978) were developed. Cunnold *et al.* derived their drag value from eddy flux arguments, whereas Schoeberl and Strobel (1978) used a drag profile that drove the meridional winds in the mesosphere but did not damp out the quasi-biennial oscillation at lower levels. Improvements to the treatment of heating and differing drag profiles were used in the models of Holton and Wehrbein (1980), Wehrbein and Leovy (1982) and Apruzese, Schoeberl and Strobel (1982) yielding better agreement between theory and observations. But Rayleigh drag was still a convenient parameterisation that had no physical basis. It showed how the mesospheric momentum budget could be balanced but gave no clue as to what was the momentum source. The answer to the question of a source was proposed by Houghton (1978) who considered the role that various types of waves could take in balancing the mesospheric momentum budget. He concluded that gravity waves were the most likely mechanism for supplying the momentum that was sought.

1.3 Atmospheric gravity waves

Early height profiles of wind in the mesosphere showed distinctly wavelike features as can be seen in figure 1.8 from Liller and Whipple (1954). A theory to explain these features in terms of internal-gravity waves (or "buoyancy" waves) was presented by Hines (1960) which, despite some scepticism in the beginning (Hines 1989), has become widely accepted and used. The high-frequency limit on these waves is called the Brunt-Väisälä frequency. If a parcel of air is displaced vertically, it will have a density that differs from its surroundings due to the vertical gradient of atmospheric density. It therefore experiences a force that, in certain circumstances, will act toward the parcels original position. The result is that the parcel of air oscillates about a mean position with a frequency N, the Brunt-Väisälä frequency, given by

$$N^2(z) = \frac{g}{\overline{T}}\left[\frac{\partial \overline{T}}{\partial z} + \frac{g}{C_p}\right] = \frac{g}{\overline{\theta}}\frac{\partial \overline{\theta}}{\partial z}. \tag{1.1}$$

Here, z is the vertical coordinate of a Cartesian system, g is the acceleration due to gravity, C_p is the specific heat at constant pressure and $\overline{T}$ and $\overline{\theta}$ are the mean temperature and the mean potential temperature respectively. (e.g. Fritts (1984). This description of gravity waves follows that of Fritts (1984), but a variety of other treatments are available. See e.g. Hines (1960), Gossard and Hooke (1975) and Andrews *et al.* (1987)). A lower limit on the frequency of these waves is set by the rotation of the earth. Known as the inertial frequency, f, this quantity is a function of latitude and is given by $f = 2\Omega \sin\phi$ where Ω is the rotation rate of the earth and ϕ is the latitude. (This parameter, f, is also called the Coriolis parameter and is equal to the vertical component of the earth's rotation vector.) If we restrict our attention to oscillations whose frequency, ω, satisfies $f \ll \omega \ll N$ then it is also possible to assume that all motions are in the $x - z$ plane (x being a horizontal coordinate of a Cartesian system,) and that the mean velocity $\overline{u}(z)$ is in the x-direction. The passage of a wave causes variations in numerous quantities such as velocity, pressure, temperature and density. If we assume that these can be represented by a mean and a perturbation about that mean such that

$$\psi(x,z,t) = \overline{\psi}(z) + \psi'(x,z,t), \tag{1.2}$$

where,

$$\overline{\psi}(z) = \frac{1}{\lambda_x}\int_0^{\lambda_x} \psi dx, \tag{1.3}$$

ψ being any one of the above quantities and λ_x being the horizontal scale of the variation, then it is possible to linearize the equations of x and z momentum, the adiabatic energy equation and the continuity equation. If it is assumed that solutions are of the form

$$\psi'(x,z,t) = \psi'(z)e^{z/2H}e^{ik(x-ct)} \tag{1.4}$$

where $k(= 2\pi/\lambda_h)$ and $m(= 2\pi/\lambda_v)$ are the horizontal and vertical wavenumbers, and λ_h and λ_v are the horizontal and vertical wavelengths of the perturbation, H is the local atmospheric scale height ($H = R\overline{T}/g$, R being the gas constant for dry air), then linearizing and combining the above equations yields

$$w'_{zz} + \left[\frac{N^2}{(\overline{u}-c)^2} - \frac{\overline{u}_{zz}}{(\overline{u}-c)} - k^2 - \frac{\overline{u}_z}{(\overline{u}-c)H} - \frac{1}{4H^2}\right] w' = 0 \tag{1.5}$$

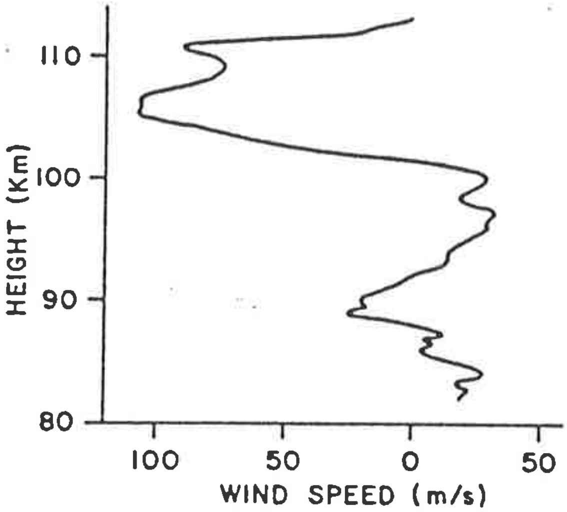

Figure 1.8: A height profile of wind velocity from Liller and Whipple (1954)

where c is the horizontal phase velocity of the wave motion, w' is the vertical component of the perturbation velocity vector $(u', 0, w')$ and the subscripts denote differentiation. This equation, known as the Taylor-Goldstein equation, can be simplified under the conditions described above and the assumptions that N^2 is constant, $\overline{u}_{zz}$ is small and that H is large, to

$$w'_{zz} + [N^2/(\overline{u} - c)^2]w' = 0 \tag{1.6}$$

For slowly varying m, this equation can be solved, using WKBJ methods (see Andrews *et al.* (1987), p215) to give

$$w'(x, z, t) = Am^{-1/2}e^{z/2H}e^{i(kx+mz-kct)}. \tag{1.7}$$

This equation describes the vertical velocity as a function of space and time. One important feature is the presence of an $e^{z/2H}$ dependence. The vertical velocity amplitude grows with height to conserve energy in an environment where density is decreasing. This wave growth is what makes gravity waves a significant part of dynamics at high altitudes.

Given the nature of the vertical perturbation velocity, it is possible to relate other perturbations to w. The equations involved are called the "Polarisation Relations". These include

$$u' = -\frac{m}{k}w' \tag{1.8}$$

which relates the horizontal perturbation velocity to the vertical component. It can be seen that the horizontal and the vertical velocities are in anti-phase. Another polarization relation relates potential temperature fluctuations to w', viz

$$\theta' = -\frac{\overline{\theta}_z}{ik(\overline{u}-c)}w' \tag{1.9}$$

So far, nothing has been said about the way gravity waves change as a function of frequency, ω. This is described through the dispersion relation, which, for the assumptions above is

$$\omega^2 = \frac{k^2N^2}{k^2+m^2}. \tag{1.10}$$

It is possible to calculate the phase and group velocity of a wave (packet) using this relation by noting that, in this formulation, where motion is restricted to the $x-z$ plane, the phase velocity, $c_p = (\omega/k, 0, \omega/m)$ and that the group velocity $c_g = (\partial\omega/\partial k, 0, \partial\omega/\partial m)$. Applying these results to the dispersion relation yields $c_p = (N/m, 0, kN/m^2)$ and $c_g = (N/m, 0, -kN/m^2)$. These expressions represent what to many is the most surprising property of gravity waves. It can be seen that the z-component of the phase and group velocities have opposite signs. Thus a wave whose energy is propagating upwards appears to be moving downwards through the action of the surfaces of constant phase.

If waves with frequencies closer to the inertial frequency f are considered, then it is necessary to include terms involving the Coriolis force in the basic momentum equation. The result of this is that motions are no longer constrained to the plane of propagation (previously defined as the $x-z$ plane). A phase difference between the y and x components of velocity v' and u' respectively shown by the i in the polarisation relation

$$v' = ifu'/\omega \tag{1.11}$$

means that the velocity vector traces out an ellipse in a horizontal plane as a function of time. (Note that the vertical velocity remains in antiphase with u'.)

The above equations demonstrate that, given a disturbance in a density stratified atmosphere, a wave solution to the equations of motion, energy conservation and continuity exists with frequencies like those of periodic structures observed in the atmosphere.

Other characteristics such as tilted phase-fronts in velocity vs height data (e.g. Balsley *et al.* 1983) consistent with the gravity-wave solution have also been observed routinely. Therefore, gravity waves must be prime candidates for the mechanism that was sought to transport momentum to the mesosphere. Possible sources of these gravity waves will be considered next. It is worth noting that some philosophical discussion on the subject of waves and their momentum has taken place (see e.g. McIntyre 1981). It is now generally accepted that, although a wave can act to transport momentum, the wave itself contains no momentum. Instead, the wave redistributes the momentum that resides in the medium as the wave passes through a region but, in the case of non-dissipating waves, that region is left in its initial state once the wave has passed. Thus phrases such as “waves giving up their momentum”, although in common usage, are not strictly true: the momentum is not in the waves to give up.

The high density of the atmosphere in the troposphere (relative to the mesosphere) and its increased absorption of solar energy make it a region of the atmosphere that is energy dense. This makes it the most likely source of gravity waves that are seen to be propagating energy upwards in the mesosphere. Studies identifying the exact characteristics of the gravity-wave source distribution and the physical processes that produce vertically-propagating gravity waves are few. Some examples have been presented though, including Lu *et al.* (1984) where gravity waves were associated with thunderstorm activity. This study highlights one of the problems in this work. Because the VHF radar that was used to obtain the vertical velocities that were considered in Lu *et al.* (1984) was situated some distance from the thunderstorms being investigated, it was possible to detect horizontally propagating gravity waves but difficult to detect vertically propagating ones. Statistical studies such as those of Clarke and Morone (1981) and Bowhill and Gnanalingam (1986) were able to overcome this problem of limited horizontal range and correlate mesospheric gravity waves with tropospheric sources. Airglow observations by Taylor and Hapgood (1988) were successful in associating a thunderstorm with short-period gravity waves in the mesosphere as well. Gavrilov and Shved (1982), suggested that fronts, cyclones, jet streams and airflow over mountains were also important sources of gravity waves.

The distribution of gravity waves in the mesosphere would be the same as that at the gravity-wave source if the medium through which they propagated did not alter the waves. There are, however, two important ways in which propagation of a gravity wave can be affected. These will now be considered.

The formulation of gravity wave theory presented above assumes that the atmosphere is stratified. Density decreases exponentially with height and $\overline{u}$ is also allowed to vary in the vertical. It is not surprising, then, that a parameter that describes the vertical structure of a gravity wave, the vertical wavenumber $m(= 2\pi/\lambda_v)$, is important in considerations of gravity-wave propagation. The two cases where gravity-wave propagation is affected, namely turning levels and critical levels, are characterised by m^2 going negative and m^2 tending to infinity respectively. Before considering these cases, it is useful to note that, using $\omega = k(\overline{u} - c)$, the dispersion equation (eq. 1.10) can be rearranged to give

$$m^2 = \frac{N^2}{(\overline{u} - c)^2} - k^2. \tag{1.12}$$

For a turning level to occur, m^2 must become negative. Inspection of equation 1.12 shows that this can be caused by N^2 becoming small or by $(\overline{u} - c)$ becoming large. The first of these possibilities can come about through variations in temperature as a function of height, the second through changes in the mean wind with height. As a gravity wave approaches a turning layer, the phase fronts become more and more vertical until, at the turning layer, the parcel motions, which are parallel to the phase fronts, are vertical. This means that their frequency of oscillation must be equal to the local Brunt-Väisälä frequency and that m is equal to zero. Further decreases in m result in an overturning of the wave, which propagates on in the same horizontal direction but in the opposite direction in the vertical. A noteworthy aspect of this reflection process is that it does not dissipate energy. Thus, if another turning level is present below the source, a waveguide can be formed and the wave energy can be "ducted" such that it travels great distances horizontally from the source. This is in fact the mode of propagation that was suggested by Lu *et al.* (1984) in their study.

Inspection of equation 1.12 shows that for m^2 to tend to infinity, $(\overline{u} - c)^2$ must tend to zero or $\overline{u} \rightarrow c$. The phase speed of a wave is (generally) an invariant property so it must be variations in $\overline{u}$ with height that bring about critical level interactions. The phase fronts become more horizontal, as do the parcel motions, as critical layers are approached. The increase in m and the corresponding decrease in λ_v also implies that the phase fronts become closer together. This "compression" of the wave packet leads to the dissipation of the energy it contains.

A laboratory study of both of these interactions has been carried out by Koop (1981), the results of which elegantly illustrate the above situations. The density stratification in a water tank is enhanced using a salt solution and sheared horizontal flows can be set up. Finally, a piston at the end of a rod that is immersed in the tank can be oscillated at frequencies near the local Brunt-Väisälä frequency to produce gravity waves. Photographic results of a particular experiment where a sheared flow is present are presented in figure 1.9a and a schematic representation of that photo is given in figure 1.9b. The rod that is used to excite the gravity waves can be seen in the centre of the photo. The measured velocity profile has been superimposed onto the right hand side of the photograph. The flow in this case is from right to left so that $\overline{u}$ is negative. The waves, characterised by the lighter regions of the photo can seen emanating from the piston. Those on the right hand side of the rod have phase speeds $c > 0$, where those on the left have phase speeds $c < 0$. The result is that waves on the right encounter a turning level and those on the left reach a critical level and are dissipated. The orientation of the phase fronts as a critical or turning level is approached are presented in figure 1.9b.

The above cases prevent a gravity wave from propagating any further in the vertical. There are, of course, cases where the gravity wave is deviated by variations in vertical wavenumber that do not reach the limits that characterise turning and critical levels. These cases are analogous to refraction effects in optics.

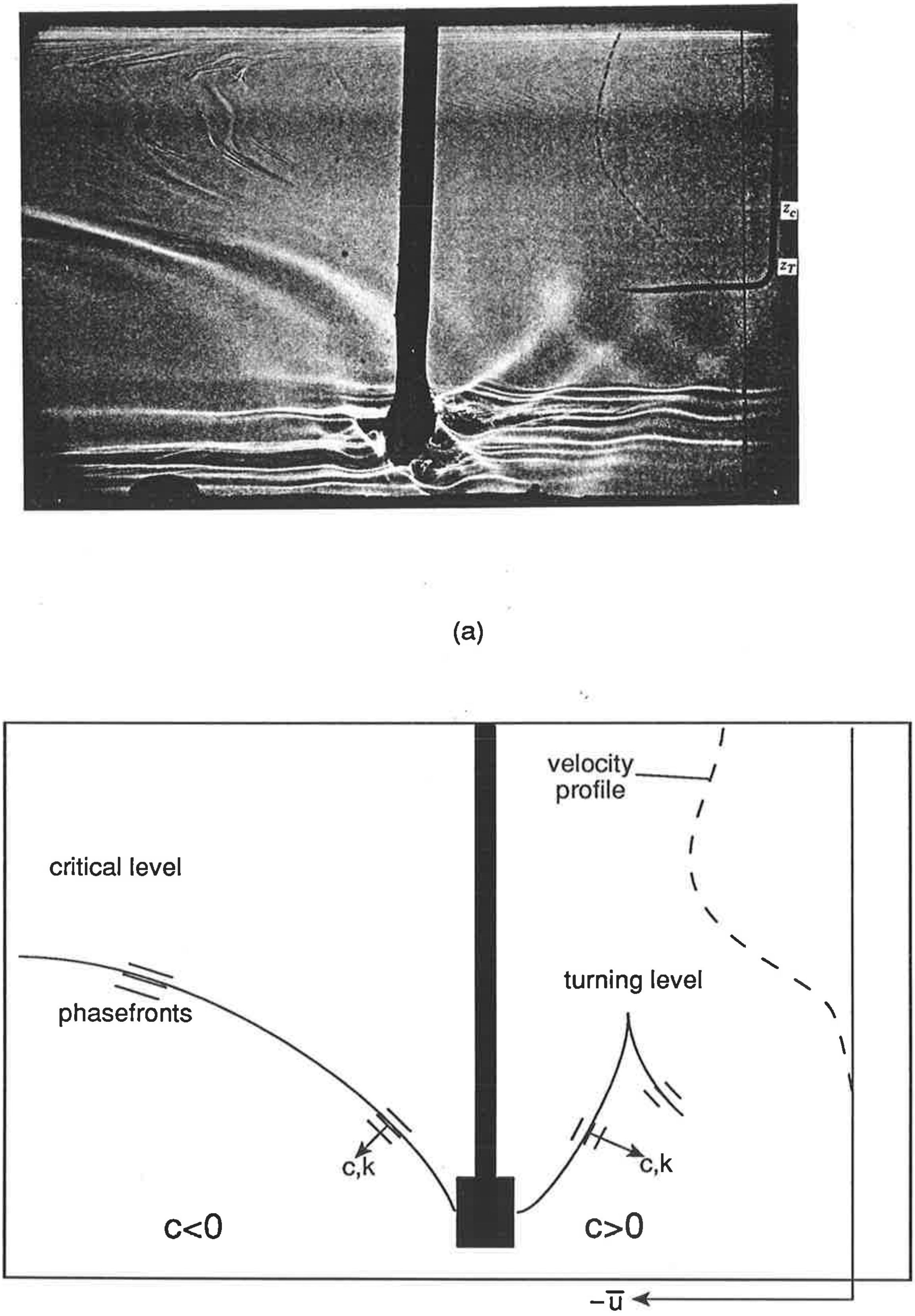

(a)

(b)

Figure 1.9: Turning and critical levels in a sheared flow (after Koop 1981)

1.4 Momentum deposition by gravity waves

Thus far, sources of momentum, a mode of momentum transport (gravity waves) and effects that could act to filter that mode of transport have been presented. The way in which this momentum is deposited into the mean flow is now considered. Although the concept of gravity waves causing eddy diffusion and thereby depositing energy and momentum into the mean flow was discussed by Hodges (1967, 1969) and Hines (1970, 1972), it was the work of Lindzen (1981) that brought about a renascence in work on the subject of gravity wave breakdown and it is that work which will now be discussed.

The discussion of gravity waves that was presented above began with the consideration of the restoring force that was experienced by a parcel of air displaced vertically upward in a density stratified fluid. Of interest now is the potential temperature of that parcel of air. This vertical displacement will not change the potential temperature of the air parcel, but the potential temperature of the environment may change with height. Thus, the potential temperature of the parcel may differ from that of the environment (θ_e). If θ_e increases with height, an air parcel that is displaced upward will experience a force toward its original position. If θ_e decreases with height, however, a parcel displaced upward will continue to do so giving rise to an unstable situation. This form of instability is known as a static or convective instability and is characterised by $\theta_z < 0$, or in terms of temperature, by $T_z < -g/c_p$ where T is the local temperature and the z subscript denotes differentiation with respect to height. If the potential temperature polarisation relation presented previously is differentiated with height, one obtains

$$\theta'_z = \frac{-\overline{\theta}_z m w'}{(\overline{u}-c)k} = \frac{u'\overline{\theta}_z}{(\overline{u}-c)}. \tag{1.13}$$

The condition for instability mentioned above, when applied to a height varying mean potential temperature with a superimposed perturbation, is $(\overline{\theta}+\theta')_z < 0$ which reduces to $u' > c - \overline{u}$. Thus if the ground-based (Eulerian) velocity $\overline{u}+u'$ exceeds the phase velocity of the wave, the wave is convectively unstable. The works of Hodges (1967,1969) and Lindzen (1981) have as their basic premise the idea that once a wave reaches saturation amplitudes defined by the conditions for stability described above, it will produce just enough turbulence to maintain that wave amplitude which just satisfies the static stability criterion. It is implicitly assumed that the characteristics of the wave and its propagation are unaffected. Assuming that the effects of turbulent diffusion are immediate and complete, the saturation conditions become (Fritts 1984)

$$\theta'_z \geq -\overline{\theta}_z \tag{1.14}$$

which for monochromatic wave motions, is equivalent to

$$|u'| \leq |c - \overline{u}| \tag{1.15}$$

A possible scenario for gravity wave breaking and momentum deposition is presented by Andrews *et al.* (1987). As a gravity wave propagates upward, its amplitude increases to compensate for the decreasing density. Material surfaces such as those depicted in figure 1.10 become more distorted. For short period waves, material surfaces are analogous to "isentropes" or surfaces of constant potential temperature. Thus when the wave grows to a state similar to that in figure 1.10c, convective instabilities cause turbulence and a convergence of horizontal momentum at the appropriate phase of the wave. Although this picture illustrates wave breaking, it is a rather simple one, and complications such as the presence of a gravity-wave spectrum rather than just one monochromatic wave should be borne in mind when the real atmosphere is being considered.

It should be noted that the critical level interaction described in the previous section, where $(\overline{u} - c)$ tends to zero, will be convectively unstable before this limit is reached. Thus, variations in $\overline{u}$ can bring about convective instabilities as can the wave growth, and the associated increase in u', as described in this section.

The convective instability discussed above is important for gravity waves of shorter periods. For gravity waves of frequency closer to the inertial frequency, it has been shown that waves become dynamically unstable before they become convectively unstable (Dunkerton 1984, Fritts and Rastogi 1985). Dynamical instabilities occur as a result of the presence of a vertical shear of horizontal velocity. An important parameter in

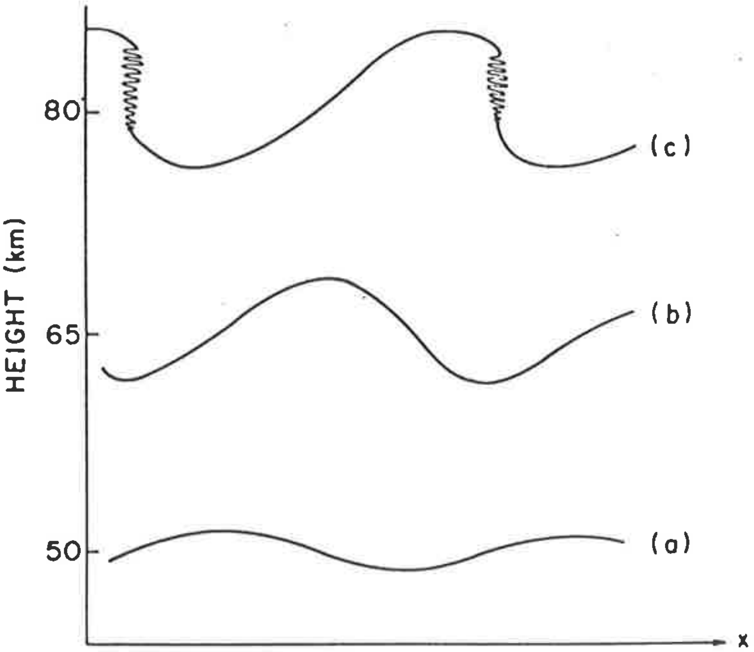

Figure 1.10: Schematic diagram illustrating the breaking of a vertically propagating gravity wave. The curves denote material surfaces. (Andrews *et al.* 1987)

considering these instabilities is the (gradient) Richardson number, Ri given by

$$Ri = \left(\frac{g}{\overline{\theta}}\frac{\partial\theta}{\partial z}\right) / \left(\frac{\partial\overline{u}}{\partial z}\right)^2, \tag{1.16}$$

Qualitatively, the Richardson number represents the ratio of the work required to interchange vertically adjacent air parcels against the acceleration of gravity to the kinetic energy available to do the work (e.g. Gossard and Hooke, 1975). The threshold where a fluid becomes dynamically unstable is given by $Ri = 1/4$. Figure 1.11 presents the ratio $u'/(\overline{u} - c)$ as a function of frequency (normalised to the inertial frequency) that corresponds to $Ri = 1/4$. Convective instability will occur when $u'/(\overline{u} - c) = 1$ with this quantity being less than unity when the wave is stable. Thus it can be seen that at longer frequencies, dynamic instability will occur before the condition for convective instability is reached (Fritts and Rastogi 1985).

One final mode of energy exchange results from nonlinear interactions of waves. Falling into two main groups, i.e resonant and non-resonant interactions, these interactions are reviewed by Muller *et al.*(1986) in an oceanic context and are discussed by Yeh and Liu (1981) and Dunkerton (1989) in an atmospheric context.

The conditions for convective instability described above can be combined with the

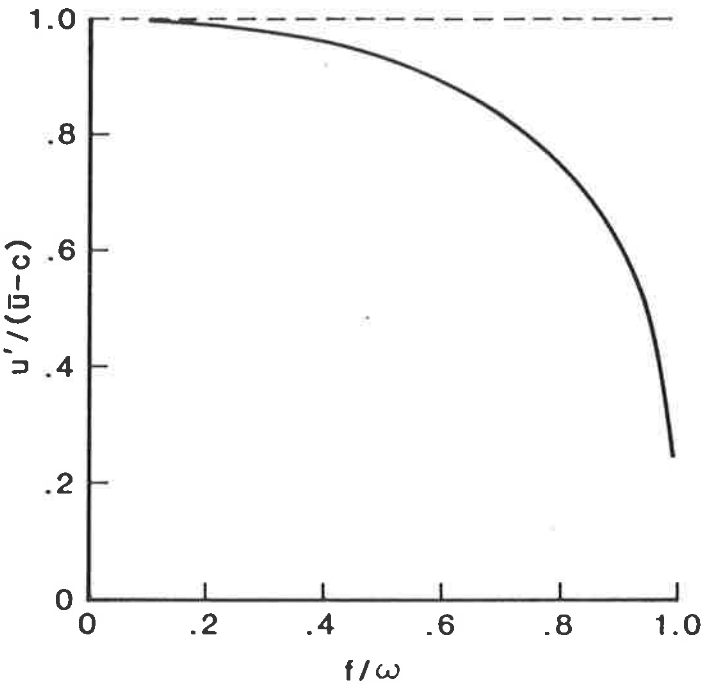

Figure 1.11: Normalised wave amplitude as a function of f/ω from Fritts and Rastogi (1985)

polarisation relations for gravity waves to infer the mean-flow acceleration due to a monochromatic gravity wave of period ω that satisfies $f \ll \omega \ll N$ (Lindzen 1981). The mean flow acceleration is given by

$$\overline{u}_t = -(\rho_0 \overline{u'w'})_z / \rho_0. \tag{1.17}$$

This quantity is zero for conservative wave motions but will become non-zero for breaking waves (Eliassen and Palm, 1960; Andrews and McIntyre 1978). If it is assumed that the waves attain saturation amplitudes at a height z_s, then above z_s, $|u'_s| = |c - \overline{u}|$. For linear theory, w' can be obtained using

$$w'_s = -\frac{k}{m} u'_s = \frac{k}{N} (\overline{u} - c)^2. \tag{1.18}$$

The momentum flux of this gravity wave above the saturation level is then

$$\rho_0 \overline{u'_s w'_s} = -\frac{\rho_0}{2} \frac{k}{N} (\overline{u} - c)^3 \tag{1.19}$$

Differentiating this with respect to height and dividing by ρ_0 then gives the mean flow acceleration;

$$\overline{u}_t = \frac{-k(\overline{u} - c)^2}{2N} \left[\frac{(\overline{u} - c)}{H} - 3\overline{u}_z \right]. \tag{1.20}$$

The acceleration, u_t due to a monochromatic saturating gravity wave acts toward the phase speed of the wave c. It also has the potential to vary in an environment where the horizontal velocity $\overline{u}$ is sheared with height.

1.5 The mesospheric momentum budget revisited

In section 1.2, the need for a process whereby the mean flow in the mesosphere was decelerated to balance the momentum budget and account for the presence of meridional and vertical flows was highlighted. It has been shown that convergence of gravity-wave momentum flux can contribute to the momentum budget and some simple parameterisations of the momentum flux and mean-flow acceleration due to a monochromatic gravity wave have been presented. The momentum budget of the mesosphere is considered again in the light of this information.

As was noted above, the action of gravity wave breaking draws the mean flow toward the phase speed of the wave. This could imply an acceleration in some circumstances but in general a deceleration occurs in the mesosphere due to stratospheric filtering of the gravity-wave phase-speed distribution. The mechanism for this was proposed by Lindzen (1981) and is represented in figure 1.12. A gravity-wave phase-speed distribution centred on zero is assumed at the top of the troposphere. In summer, as the waves propagate upward, westward winds in the stratosphere bring about critical level interactions that remove negative (and some small positive) phase speeds from the distribution (figure 1.12a). Thus, on reaching the mesosphere where the gravity waves break, the phase-speed distribution has a mean value of opposite sign to the mean wind. Therefore, gravity-wave breaking will cause an acceleration (because the mean flow is negative in this case) of the flow. This effect is manifest in the increase in velocities above the breaking level denoted by z_{break}. A similar situation, where the mean flow is decelerated toward zero, can be seen in figure 1.12b. The winter stratospheric flow acts to filter out the gravity-wave phase speeds that could accelerate the flow and a deceleration results.

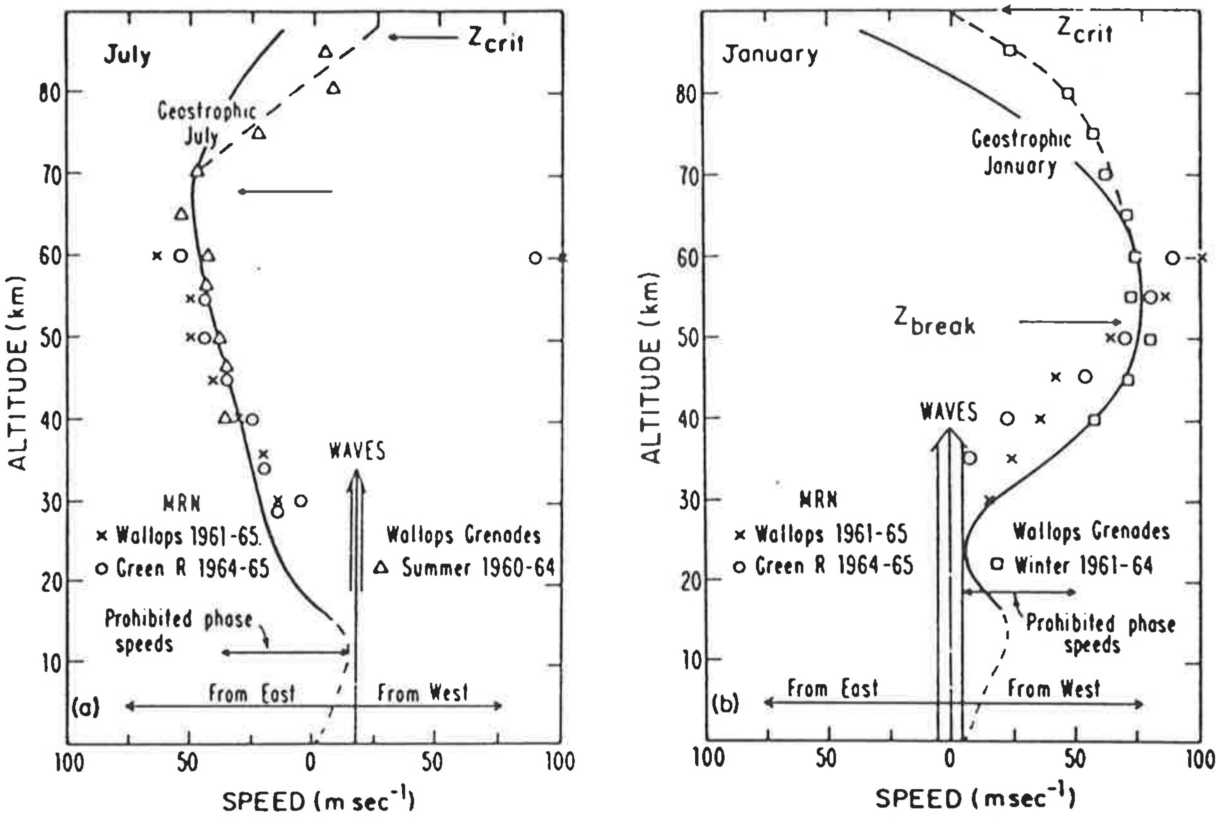

Figure 1.12: Filtering of the gravity-wave phase-speed distribution as it passes through the summer (a) and winter (b) stratosphere

Figure 1.12 supports the theories presented above but includes some idealisation. It is also limited in the spatial and temporal range it represents. An extensive data set of parameters such as $\overline{u'w'}$ would be of considerable use in testing these ideas and it is to this end that much of this thesis is dedicated. Another test involves the inclusion of gravity-wave drag into the models that attempted to balance the mesospheric momentum budget in the first place. Holton (1982) developed a parameterisation for gravity-wave drag and diffusion and included this into a simple β-plane model. It was necessary to assume a form for the gravity-wave phase-speed distribution at the base of the model and this took the form of waves with c =-20, 0 and 20 ms^{-1}. These ideas were then applied to a spherical-geometry primitive-equation model in Holton (1982). A more sophisticated phase-speed distribution based on the work of Matsuno (1982) was then incorporated into Holton's β-plane model in Holton and Zhu (1984). This included a collection of phase speeds as well as a variety of directions of propagation.

An alternative approach to this was used by Rind *et al.* (1988a,b). It involved a formulation developed by Lindzen (1984) which used parameters such as the wind velocity, density and Brunt-Väisälä frequency in conjunction with convection, topography and shear to produce gravity waves. These were then allowed to propagate vertically, saturate and deposit momentum. Realistic mean wind and temperature fields resulted when the model was run but some aspects of the model were found to be deficient. In Rind *et al.* (1988b), variable phenomena such as stratospheric warmings are successfully reproduced; however the problems associated with modelling sub-grid scale phenomena were proposed as a limitation to the model.

A study of the importance of these sub-grid scale phenomena was presented by Hayashi *et al.* (1989). In this paper, the results of two models with differing spatial resolutions were compared and the gravity-wave momentum fluxes were found to be quite different. The reason for this was that the low-resolution model could not adequately describe gravity waves of small horizontal scale. The high resolution model could cope with these waves better and their effect on the global circulation was detected. This does not, however, ensure that *all* of the short-period waves are being simulated correctly, because the high- resolution model still does not agree with observations. As stated in Hayashi *et al.*, the latitudinal maximum of the zonal westward flow in the (summer) southern hemisphere occurs nearly 20° south of that observed by Barnett and Corney (1985).

1.6 Energy deposition

Thus far, the deposition of momentum into the mean flow by gravity waves has been discussed. It was noted earlier that the momentum of a gravity wave actually resides in the mean flow (McIntyre 1981). Near the leading edge of a (non-dissipating) wave packet, the momentum that resides in the mean flow is redistributed. The mean flow is then returned to its original state after the passage of the wave. If the wave breaks and isotropic turbulence is produced, then the mean flow cannot be returned to its original state. Turbulence, which involves irreversible processes, uses momentum and so makes it unavailable for redistribution as the wave leaves the region.

Turbulence can be considered in a number of ways. One approach involves a spectrum of eddies of various scales. Large scale eddies are produced and these produce smaller ones giving a spectrum of eddy sizes. At the smallest scales, viscosity causes a net heating of the atmosphere. The energy that is dissipated by these eddies is the subject of chapter 3 and the theoretical background for these measurements is set in chapter 2. A less physical treatment but one that involves a useful parameterisation of turbulence was initiated by Ludwig Prandtl. Known as "K-theory", it uses an analogy to molecular diffusion. Turbulent eddies are capable of diffusing momentum and heat through a medium. The rate at which this occurs is described by the eddy diffusion coefficient, K. In particular, the eddy diffusion coefficient for heat is K_n and the eddy diffusion coefficient for momentum is K_M.

Lindzen (1981) calculated the eddy diffusion coefficient for a breaking gravity wave, but assumed that this coefficient was the same for heat *and* momentum. This was equivalent to assuming that the Prandtl number, $Pr = K_M/K_n$ (the ratio of the eddy

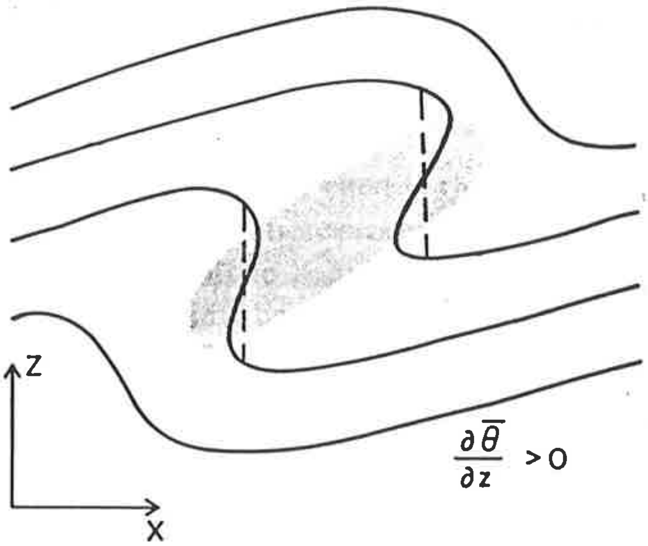

Figure 1.13: Schematic diagram of the occurrence of turbulence due to an unstable gravity wave (after Fritts and Dunkerton, 1985)

diffusion coefficients for momentum and heat), was unity. It was suggested by Chao and Schoeberl (1984) that localisation of the turbulence should lead to Prandtl numbers greater than one. The concepts of static stability presented previously suggest a non-uniform turbulence field like that presented in figure 1.13. In this figure, from Fritts and Dunkerton (1985), the region of the potential temperature field of a breaking gravity wave that is convectively unstable (i.e. where $(\overline{\theta} + \theta')_z < 0$ using the notation defined previously) is shaded. It is near this region that turbulence will occur. Prandtl numbers greater than one imply that momentum is diffused more effectively than heat. Some other theoretical calculations on the effect of localisation on diffusion have been carried out. These are reviewed briefly by Fritts (1989) and the reader is referred to this paper and the references therein for further information.

1.7 Other atmospheric waves

The internal gravity waves that have been discussed so far represent only one solution to the set of momentum, heat and continuity equations. Other solutions exist, where different heat or momentum sources are included, and some of these will now be discussed.

The heating of the atmosphere due to insolation during the daylight hours of each day has the effect of forcing an oscillation with a 24 hr period known as the diurnal tide. The non-sinusoidal nature of this forcing, however, also acts to produce a 12 hr (semi-diurnal) oscillation as well. The "classical" theory of tides, as presented by Chapman and Lindzen (1970), attempts to predict the amplitude and phase (time of maximum wind) of the (eastward and northward) velocity components as a function of latitude and season. In general, this theory has been quite successful although recent improvements have made the agreement between theory and observations even better (see e.g. the special issue of *Journal of Atmospheric and Terrestrial Physics*, **51**, 7/8, 1989). An important aspect of tides in this thesis, however, is their contribution to the momentum budget of the mesosphere. Their effect on the background flow and the resulting filtering of gravity waves (Walterscheid 1981, Fritts and Vincent 1987) does bring about an indirect effect on momentum deposition. The effect of breakdown of the tides themselves was considered by Miyahara and Wu (1989) who concluded that, below 120km, the momentum deposition due to the diurnal tide may be significant, but that the magnitude of the deposition is dependent on the vertical eddy diffusion profile. This profile was assumed *ad hoc* in their model.

Another important class of atmospheric waves are the planetary waves (Charney and Drazin 1961). These waves are essentially due to the variation of the Coriolis parameter with latitude and have periods of the order of days. Although they are thought to make some contribution to the momentum budget of the mesosphere, they are only evident at mesospheric heights during the winter. The summer wind profile in the stratosphere acts to prohibit their propagation into the middle atmosphere. Therefore, they can only be one part of the momentum balance in the mesosphere and not the whole story.

Chapter 2

Atmospheric Turbulence

Motions of many forms exist in the atmosphere. They range from waves with scales of thousands of kilometres down to eddies a few metres across. It is these eddies and their intrinsic dynamics that are of interest in this and the following chapter. A background for this discussion will be set here; however this chapter is meant only as a brief review. For further information, the reader is referred to the reviews by Hocking (1985,1989) and to classic turbulence texts such as Tatarski (1961), and Batchelor (1953).

2.1 About Turbulence

Because turbulence is not well understood, it is difficult to give a precise definition of what it is. A more instructive approach is to note some of the characteristics of turbulence. It is a fluid motion that is random in nature. The velocity at any point within the turbulence can vary in magnitude and direction and yet turbulence is a zero mean motion. Turbulence enhances transfer of heat, momentum and mass and, through viscosity, causes dissipation of energy. It is this last characteristic that makes turbulence important in the mesosphere. Energy from the energy-dense lower atmosphere is transported to the mesosphere by gravity waves. These waves grow with altitude until, at mesospheric heights, they become unstable and break, creating large eddies. Lewis Richardson, inspired by a verse by Jonathan Swift, described the process that then occurs, stating: "We realize thus that: big whirls have little whirls that feed on their velocity, and little whirls have lesser whirls and so on to viscosity" L. F. Richardson (1922, p66) The energy cascades from larger to smaller scales until the eddies being created are so small that viscosity damps them out, heating the atmosphere.

The scales of the turbulence are split into various ranges according to the character of the turbulence in that range. These are summarised in figure 2.1 (after Blix 1988). $E(k)dk$ is the kinetic energy contained between k and $k + dk$, k is a measure of the scale of the turbulence (the number of waves per unit length in the Fourier analysis). [It should be noted that various forms of spectra exist. (Tatarski, 1961) In this case $E(k)$, being an energy spectrum, has contributions from all three components of velocity. Spectra of a single velocity component are also useful as will be seen later.] As the name suggests, viscous effects dominate in the viscous range. The large shears associated with these small scale-eddies bring about this dominance. The inertial range contains eddies that are larger but are not affected by buoyancy. The range of scales where buoyancy effects become important is called the buoyancy range. Here, the stratification of the atmosphere is thought to make the eddies elongated and anisotropic (Bolgiano 1959, Lumley 1964, Sidi and Dalaudier 1989). The inertial range is the most intensively investigated of all the turbulence ranges. It is a region of the turbulence spectrum where energy is neither being produced (by large scale shears or convection) or dissipated (by viscosity). Energy is essentially passing through from the larger to the smaller scales. Thus it is not surprising that the form of the energy spectrum in this subrange is independent of viscosity. The spectrum has the form (sometimes called the Kolmogorov-Obukhov law)

$$E(k) = \alpha\, \varepsilon^{\frac{2}{3}} k^{-\frac{5}{3}} \tag{2.1}$$

(e.g. Tennekes and Lumley 1972) with $\alpha \approx 1.5$. ε is the rate at which turbulent energy is being converted to heat.

The region of the atmosphere of prime interest in this thesis is the mesosphere. It is a region that is difficult to probe directly because of its remoteness. Occasional rocket experiments allow some *in-situ* measurements but these data are limited spatially and temporally. Radars can be used to fill this data gap, and it is the methods applicable

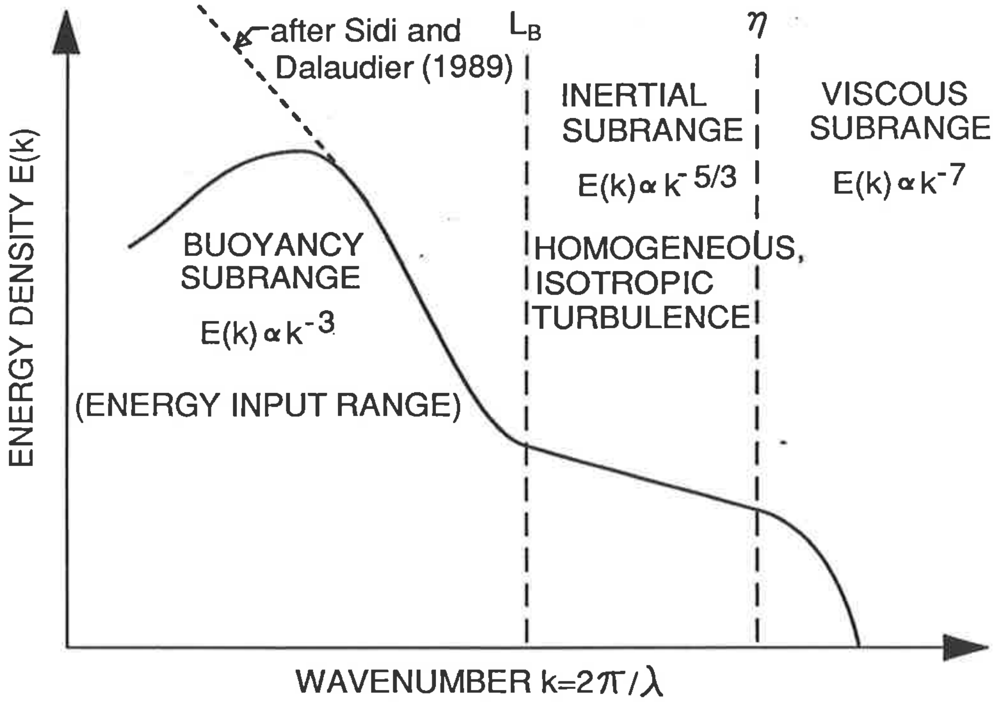

Figure 2.1: The turbulence energy spectrum (after Blix, 1988). Note that the spectrum is not thought to fall off at small k in the upper atmosphere (Sidi and Dalaudier 1989).

to their use that will now be discussed.

Two distinct methods exist for obtaining turbulence information using radars. One involves using the width of the Doppler spectrum of the returned signals, whereas the other relates returned power to the strength of the turbulence. Both of these are considered now.

2.2 The Spectral-Width Method

A radar operating at a frequency f_0 will receive enhanced backscatter when the scattering structure in the line of sight is of scale $\lambda/2$, where $\lambda(= c/f_0)$ is the radar wavelength and c is the speed of light in a vacuum. These structures could be turbulent eddies of that size that are formed during the energy cascade process from larger to smaller scales. This enhanced backscatter then makes these "Bragg-scale" structures act as tracers for the turbulence field. These small eddies are carried around by larger ones and so their overall motions are affected by scales from $\lambda/2$ to some upper limit. This

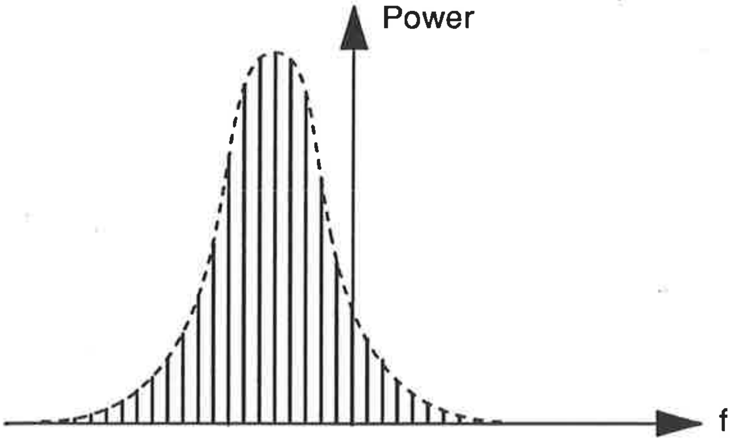

Figure 2.2: A Doppler spectrum.

limit can be due to the size of the radar sampling volume or the fact that eddies beyond a particular size do not exist. Information on the turbulence that lies between these limits is returned to the radar.

If the scattering structure is moving, then the component of its velocity radial to the radar will make the returned radio-wave frequency different to that transmitted. In Doppler radar systems this shift can be detected and then converted to a radial velocity. Obviously, if many scatterers of differing velocities are contributing to the backscattered signal, a range of frequency shifts will be detected giving a broadened frequency spectrum and hence a spectrum of velocities. In the absence of other effects, this spectrum would be expected to look something like that depicted in figure 2.2.

If the velocity due to one eddy is considered in isolation, a connection can be made between turbulence and the radar backscatter. The variations in the vertical component (say) of velocity due to this single eddy of wavenumber k ($k = 2\pi/l$, l being the scale of the eddy) will have a variance $\overline{v_k^2}$. The energy in the turbulence field at that scale is also related to $\overline{v_k^2}$. The fact that a multitude of eddies with scales ranging upward from $\lambda/2$ (as discussed previously) contribute to the width of the velocity spectrum of the scatterers (or Doppler spectrum) means that this spectral width can be equated to the energies summed over a range of scales. These concepts led to the expression (Hocking

1983a, 1989)

$$F\overline{v^2} = \int_{-k_\lambda}^{-k_B} \Theta_{11}(k)dk + \int_{k_B}^{k_\lambda} \Theta_{11}(k)dk \qquad (2.2)$$

Here $\Theta_{11}(k)$ is the longitudinal one-dimensional spectrum function, which represents the energy in one component of velocity, at a scale of wavenumber k, k_λ is the Bragg scale wavenumber, $k_B = 2\pi/L_B$ where k_B is the wavenumber and L_B the scale at which the turbulence begins to be affected by buoyancy and no longer satisfies the expression used for $E(k)$, and F is the fraction of the spectral width $\overline{v^2}$ that comes from inertial range turbulence. Note that the spectra $E(k)$ and $\Theta_{11}(k)$ are different. In the earlier literature, some confusion about the differences between the various kinds of spectra existed (Ottersten 1969).

In the inertial range,

$$\Theta_{11}(k) = 0.1244\, C_v^2\, \varepsilon^{2/3}|k|^{-5/3} \qquad (2.3)$$

where ε is the energy dissipation rate and C_v^2 is found by experiment to be close to 2.0 (e.g. Caughey *et. al.* 1978). From this, Hocking (1983a) derived the expression

$$\varepsilon = \frac{\varepsilon_* L_B}{[L_B^{2/3} - (\frac{\lambda}{2})^{\frac{2}{3}}]^{\frac{3}{2}}} \qquad (2.4)$$

where

$$\varepsilon_* = 2\pi[\frac{F}{0.3732\, C_v^2}]^{\frac{3}{2}} \frac{(\overline{v^2})^{\frac{3}{2}}}{L_B} \qquad (2.5)$$

If λ is much smaller than L_B and F is taken as 0.5, this reduces to

$$\varepsilon = \frac{3.45(\overline{v^2})^{\frac{3}{2}}}{L_B}. \qquad (2.6)$$

Weinstock (1978b) has related the buoyancy scale L_B to the Brunt-Väisälä frequency $\omega_b = 2\pi f_b$ and the energy dissipation rate through

$$L_B = \frac{2\pi}{0.62}\, \varepsilon^{\frac{1}{2}} \omega_b^{-\frac{3}{2}} \qquad (2.7)$$

which gives

$$\varepsilon = 3.1\overline{v^2} f_b \qquad (2.8)$$

It is this relation that is used to relate the width of the Doppler spectrum to the energy dissipation rate. A slightly different approach used by Frisch and Clifford (1974) should be noted; however it is the above equation that is used in this thesis.

In this treatment, vertical velocities were used. Any component could have been utilised in principle but some practical considerations suggest that data from a vertical-beam radar should be preferred. These practical considerations and their effect will now be discussed, however, for a full treatment the reader is referred to Hocking (1983a,1989).

Although turbulence itself is a zero-mean motion, it is usually "embedded" in a mean flow. In the case of a vertical beam, a vertical velocity will merely shift the spectrum leaving the spectral width unaffected. A horizontal velocity, however, may broaden the spectrum if the radar beam is of finite width. A radar beam of half-power half-width $\theta_{1/2}$ will see echoes from angles out to $\theta_{1/2}$ from the vertical and beyond, even though the backscattered power of their signal is reduced. A purely horizontal wind blowing across the beam will have no vertical component but it will have a component of velocity at an angle (say) $\theta_{1/2}$ from the vertical and echoes approaching the radar from this direction will be Doppler shifted by the horizontal wind. Thus turbulence contributions of the spectrum will be shifted in frequency resulting in a smearing out of the Doppler spectrum. This effect, known as beam broadening, is illustrated in figure 2.3 (after Hocking, 1983a).

The expression (Hocking 1989)

$$f_{0.5B} = \frac{2}{\lambda}(1.0)|\underline{V_{hor}}|\theta_{1/2} \tag{2.9}$$

relates the spectral half-power half-width due to beam broadening $f_{0.5B}$ to the radar wavelength λ, the magnitude of the horizontal velocity vector $|\underline{V_{hor}}|$ and the two-way beam half-power half-width (in radians) $\theta_{1/2}$.

The Doppler spectrum of the received echoes will be a convolution of the turbulence spectrum with the spectrum due to beam broadening. It is important to note that the beam-broadening contribution can and often does dominate the spectrum. Therefore it is vital that its contribution be calculated and removed from the measured value of

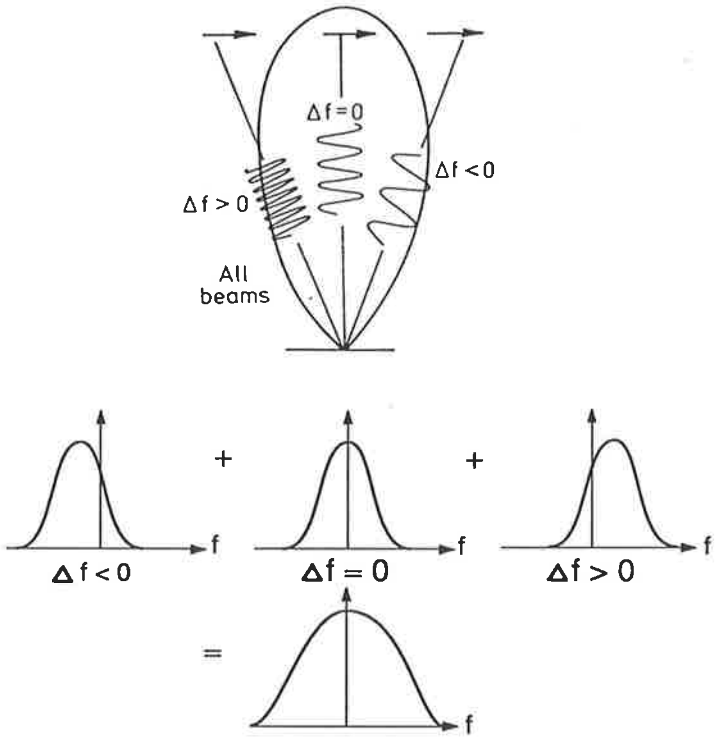

Figure 2.3: Beam broadening in a vertical beam.

width using

$$f_{0.5turb}^2 = f_{0.5exp}^2 - f_{0.5B}^2 \tag{2.10}$$

where $f_{0.5turb}$ is the spectral half-power half-width due to turbulence, $f_{0.5exp}$ the experimentally measured spectral half-power half-width and $f_{0.5B}$ is the spectral half-power half-width due to beam broadening. The velocity variance can then be calculated using the relation

$$\overline{v^2} = f_{0.5turb}^2/(2\ln 2) \tag{2.11}$$

and used to obtain the energy dissipation rate.

Another form of spectral modification, termed shear broadening/narrowing, exists but it is not considered important for vertical beams. The presence of a vertical shear of horizontal velocities over the radar sampling volume can spread or narrow the Doppler spectrum, an effect that is worsened by the increased range of heights contributing to the Doppler spectrum when tilted beams are used. It is for this reason the use of vertical-beam data is preferred for the spectral-width method.

2.3 The total power method of turbulence measurement.

The random nature of turbulence makes it difficult to describe individual particle motions so statistical approaches are used. One such method of description forms the basis of turbulence measurements using the total power returned to a radar from a defined scattering volume, and this will now be described.

The structure function of the scalar ξ is defined as

$$D_\xi(\underline{r}) = < |\xi(\underline{x}) - \xi(\underline{x} + \underline{r})|^2 > \tag{2.12}$$

where $D_\xi(\underline{r})$ is the structure function, $\underline{x}$ a position vector, $\underline{r}$ a displacement vector (from $\underline{x}$) and the angle brackets denote an average over space and time. ξ is some property that varies through the turbulent area (such as temperature) but whose statistical properties do not depend on position. Properties of this kind are called "passive tracers", and although *potential* temperature is a passive tracer, temperature is not. A vertical movement of an air parcel will cause expansion and (assuming that it is adiabatic) a change in temperature. The statistical properties of *this* parcel of air will differ from those around it. Thus care must be taken in choosing ξ appropriately.

For isotropic homogeneous turbulence in the inertial range, it can be shown (e.g. Tatarski 1961) that

$$D_\xi(\underline{r}) = C_\xi^2 |\underline{r}|^{\frac{2}{3}} \tag{2.13}$$

where C_ξ^2, the structure constant, depends on the intensity of the turbulence.

Turbulence fluctuations can also be considered as being composed of a combination of Fourier scales. If each scale is represented by a wavenumber $\underline{k} = (k_x, k_y, k_z)$, then the spectrum of fluctuations can be shown (again Tatarski 1961) to be

$$\phi_\xi(k_x, k_y, k_z) = 0.033\, C_\xi^2 |\underline{k}|^{-\frac{11}{3}} \tag{2.14}$$

for inertial-range turbulence. This equation uses a normalisation such that

$$\int\int\int_{-\infty}^{\infty} \phi_\xi(\underline{k}) d\underline{k} = < \xi^2 > .$$

In this thesis we are interested in obtaining turbulence parameters using radars which observe weak coherent backscatter. Such backscatter depends on variations in refractive index. Refractive index, however, is not a passive tracer. Thus potential refractive index is chosen as our tracer. Hocking (1985) after Booker (1956), Ottersten (1969) showed that for a radar operating at a radio wavelength λ, the backscatter cross-section σ was related to C_n^2, the potential refractive index structure constant, by

$$\sigma = 0.00655\,\pi^{\frac{4}{3}} C_n^2 \lambda^{-\frac{1}{3}} \tag{2.15}$$

The received power P_R of a radar system will also depend on σ. Hocking (1985,1989) showed that

$$P_R = \frac{P_T e_R e_t G A_R}{4\pi z^4} \frac{V}{\ln 2} \sigma \tag{2.16}$$

where P_T is the transmitted power, e_R,e_T the efficiencies of the receiving and transmitting systems respectively, G the gain of the transmitting array, A_R the effective area of the receiving array, z the range and V the volume of the sampling region defined by the pulse length and the two-way polar diagram. Combining these equations for the case of a monostatic radar (which uses the same antenna for transmission and reception) gives

$$C_n^2 \approx \frac{66\, P_R\, z^2 \lambda^{\frac{1}{3}}}{P_T A_R e_T^2 \Delta z} \tag{2.17}$$

where Δz is the pulse length.

An equation due to Tatarski (1961) relates C_n^2 to energy dissipation rate (ε) making measurement of this important parameter possible:

$$C_n^2 = a^2 K_n M_n \varepsilon^{-\frac{1}{3}} \tag{2.18}$$

where $a^2 \approx 2.8$, K_n is the turbulent diffusion coefficient for heat, and M_n is the gradient of the potential refractive index with height. Given that

$$K_M = c_2 \varepsilon / \omega_B^2 \tag{2.19}$$

(e.g. Weinstock 1978a,b Lilly *et. al.* 1974) where K_M is the turbulent diffusion coefficient for momentum, ω_B the Brunt-Väisälä frequency and c_2 a constant usually taken as 0.8, an equation for ε can be obtained:

$$\varepsilon = [\frac{C_n^2 \omega_B^2}{a^2 \alpha' c_2 M_n^2}]^{\frac{3}{2}}. \tag{2.20}$$

$(\alpha')^{-1}$ is equal to the Prandtl number, $P_r(= K_M/K_n)$.

This formulation assumes that the entire sampling volume V is filled with turbulence. If this is not true (as is often the case) a factor F_t must be introduced to account for this assumption. Let C_n^2 due to turbulence be $C_n^2(turb)$ and that measured by the radar be $C_n^2(radar)$. Then

$$C_n^2(turb) = \frac{C_n^2(radar)}{F_t}, \tag{2.21}$$

where F_t is the fraction of the radar volume which is filled with turbulence at any one time. The energy dissipation rate within the turbulent patch can then be calculated if F_t is known or if a value of F_t is assumed.

2.4 Some possible effects of gravity waves on turbulence measurements.

The widths of the Doppler spectra due to returned radar signals are subject to contaminations of various forms. In section 2.2 the effect on spectral width of horizontal mean velocities and beams of finite width, and of vertical shears of horizontal velocity in the mean flow, were discussed. In the first of these, there is no variation of the mean velocity over the sampling volume. In the second, however, there is a variation due to the presence of a vertical shear of horizontal velocity. Both these effects have two things in common. They involve *horizontal* velocity and they do not involve variations in time.

The question arises: is it possible that *vertical* velocities affect the spectral width? Considering a vertical beam, two possible cases of variation in the mean exist. They are variation in the vertical velocity with height and variation of vertical velocity with time. These two cases will now be examined for the particular case of a quasi-monochromatic gravity wave propagating through the radar sampling volume. It should be remembered that monochromatic waves may not be the norm, but any time or any height variation of vertical velocity could bring about similar results.

2.4.1 Variation of vertical velocity with height due to gravity waves.

High frequency gravity waves propagate vertically and have parcel motions that contain a significant vertical component. Therefore, it is conceivable that the bulk motion at the top of the sampling region could differ from that at the bottom by an amount that could cause contamination in the spectral-width measurements. If the spectrum due to turbulence (alone) at the top of the sampling region was shifted in relation to that at the bottom, then when the two are summed to compute the average spectrum (either by design or as a result of limitations of the radar's resolution,) a spectral width not representative of the turbulence activity would result. For this to occur, a gravity wave with a vertical wavelength λ_z less than or comparable to $2h$, where h is the vertical resolution of the radar, and a vertical velocity amplitude greater than or of the order of the spectral width (expressed in ms^{-1}) would be required. This width then becomes more dependent on the vertical velocity variations due to the gravity wave than those due to turbulence. As shown in figure 2.4, the effect that this wave would have would depend on the position of the sampling volume, or alternatively, the time as the gravity wave propagates through a sampling volume of fixed position. If the spectral widths obtained at a series of instances in time were examined, a peak in spectral width would occur twice per cycle (when the sampling volume contains the regions where the vertical velocity changes rapidly with height). This would produce a wavelike variation of the spectral width with a frequency twice that of the gravity wave.

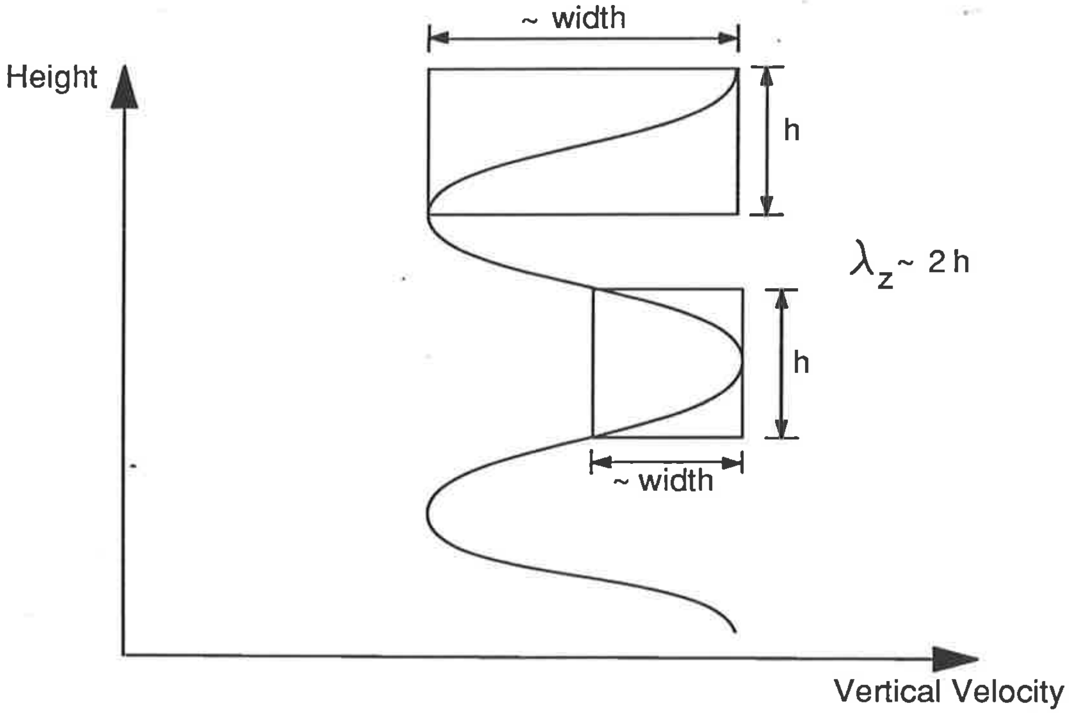

Figure 2.4: The effect of variations of vertical velocity with height, due to a quasi-monochromatic gravity wave, on the Doppler spectral width.

2.4.2 Variation of the vertical velocity with time due to gravity waves.

In the case where the gravity wave that is propagating through the sampling volume is one with vertical wavelength $\lambda_z \gg h$, effects within the sampling volume at one time can be ignored. However, the wave could be causing a net bulk motion through this volume and, if the time taken to sample is comparable to the wave period, variations of the mean will effect the spectral-width measurement. This is illustrated in figure 2.5a. Each line represents the velocity of one tracer in the turbulent field within the sampling volume. The spread of the lines is then an indication of the spectral width. It can be seen that, if a sampling time of T_1 is used, a good estimate of the spectral width due to turbulence will result. However if the sampling time of T_2 is used, then the movement of the mean will contaminate the spectral width estimate. As the sampling time is increased from T_1, the effect of the variation of the mean increases until the wave variance makes a significant contribution. The way in which this occurs depends on the phase of the wave at the beginning of the sampling interval. Figure 2.5a) represents a worst case example where figure 2.5b) illustrates some other possibilities.

2.5 Summary

In this chapter, two methods of ascertaining the energy dissipation rate using radars have been outlined. The methods are distinct in that they use different information to obtain the energy dissipation rate. The problems associated with the implementation of each method also differ. Some possible causes of contamination of energy dissipation rate values obtained using the spectral-width method are discussed. The importance of these forms of contamination in interpreting real data forms the subject of the next chapter.

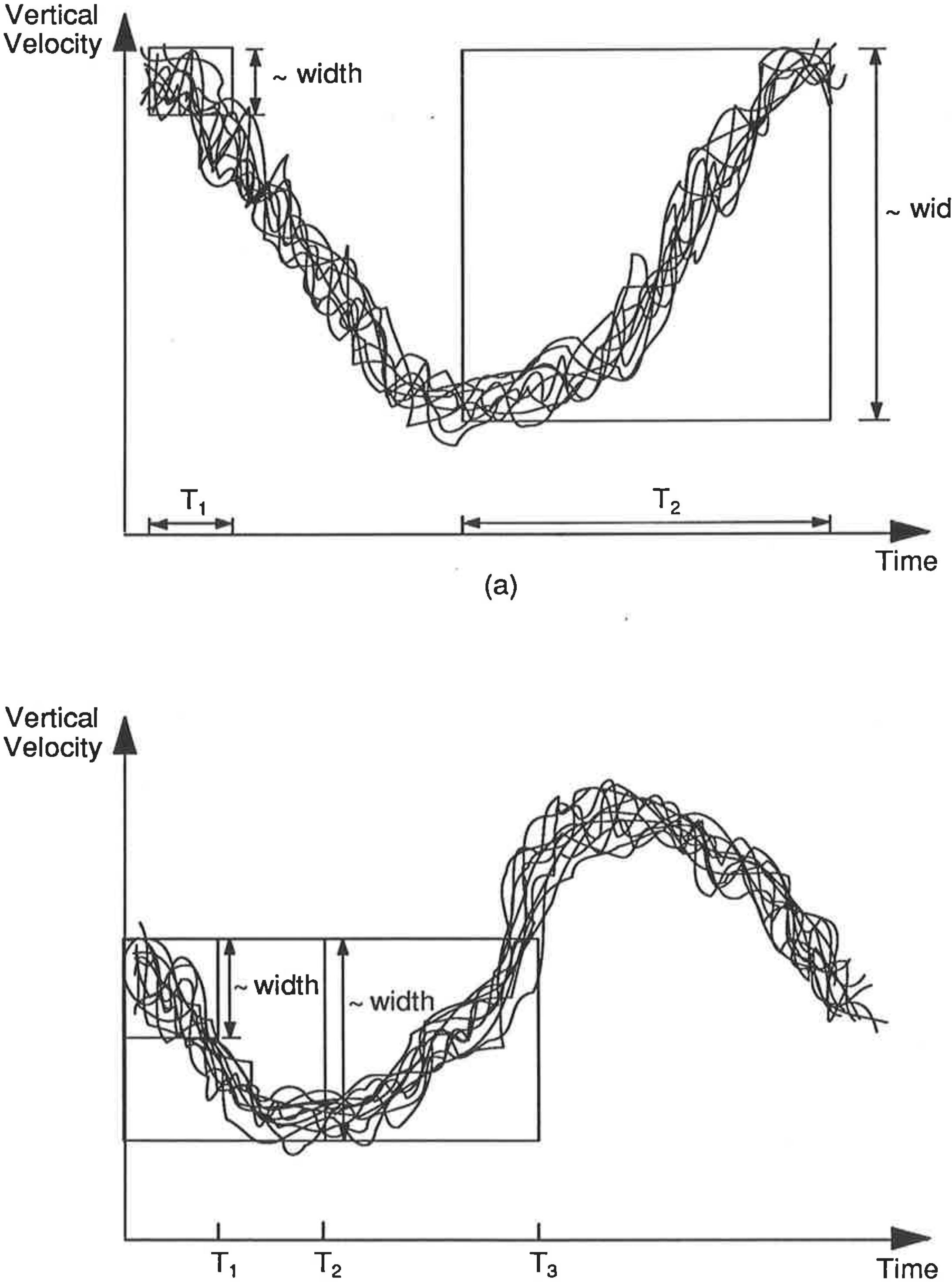

(a)

(b)

Figure 2.5: The effect of variations of vertical velocity with time, due to a quasi-monochromatic gravity wave, on the Doppler spectral width.

Chapter 3

Measurements of turbulence parameters in the mesosphere over Alaska during August 1986.

As a result of a discussion between Dr David Fritts and Dr Wayne Hocking, a decision was made to run an experiment, using the Poker Flat radar in Alaska, to study the effect, if any, of gravity waves on measurements of the spectral width and the energy dissipation rates that are obtained from them. This chapter describes the analysis of the data from this experiment.

3.1 The Poker Flat Experiment

3.1.1 Brief Description of the Poker Flat MST Radar

The Poker Flat MST radar was granted initial funding by the (American) National Science Foundation in September 1978. It was designed to allow continuous monitoring of the atmosphere up to approximately 100km, a task that was carried out successfully until April 1985. The radar was then reconfigured to allow both oblique beams to be steered and the philosophy of obtaining continuous data was relaxed.

The data presented in this chapter were collected on August the 1st. (day 213) of

Poker Flat MST Radar		
Location	65° 7′ 58″N 147° 21′ 30″W (near Fairbanks, Alaska)	
Frequency	49.920 MHz	
Antenna Area	4×10^4 m^2 for oblique and vertical beams	
Two Way Beamwidth	1.1° Full width half maximum	
For day 213, 1986		
Height range	75.0 km – 94.8 km	
Height resolution	300m (using Pulse coding)	
Acquire time	10 s	
Antenna Directions	both beams vertical	
	OR	
	beam 1	azimuth 64° clockwise from geographic north
		elevation 83°
	beam 2	azimuth 334° clockwise from geographic north
		elevation 83°

Table 3.1: The radar configuration used at Poker Flat on Day 213, 1986.

1986 between 7:50 and 14:50 (approximately). A summary of the radar configuration used is given in table 3.1. The data consist of 64 point Doppler spectra. Each spectrum was computed from the complex receiver signal levels obtained from each beam and sampled at the appropriate ranges. A 10 s series of these complex signal levels was transformed into the 64 point spectrum giving one spectrum for each height in each beam, every 10 s. A short dwell time of one or two seconds was then required to write the data to tape and to switch the beam between the two configurations described in table 3.1. It should be noted that, as a result of this beam switching, spectra for a particular beam and range were 11 s apart rather than the 1 s due to the dwell alone.

The frequency used corresponds to a wavelength of around 6m and thus a Bragg scale of 3m. This means that echoes will be due to turbulent structures of 3m scale,

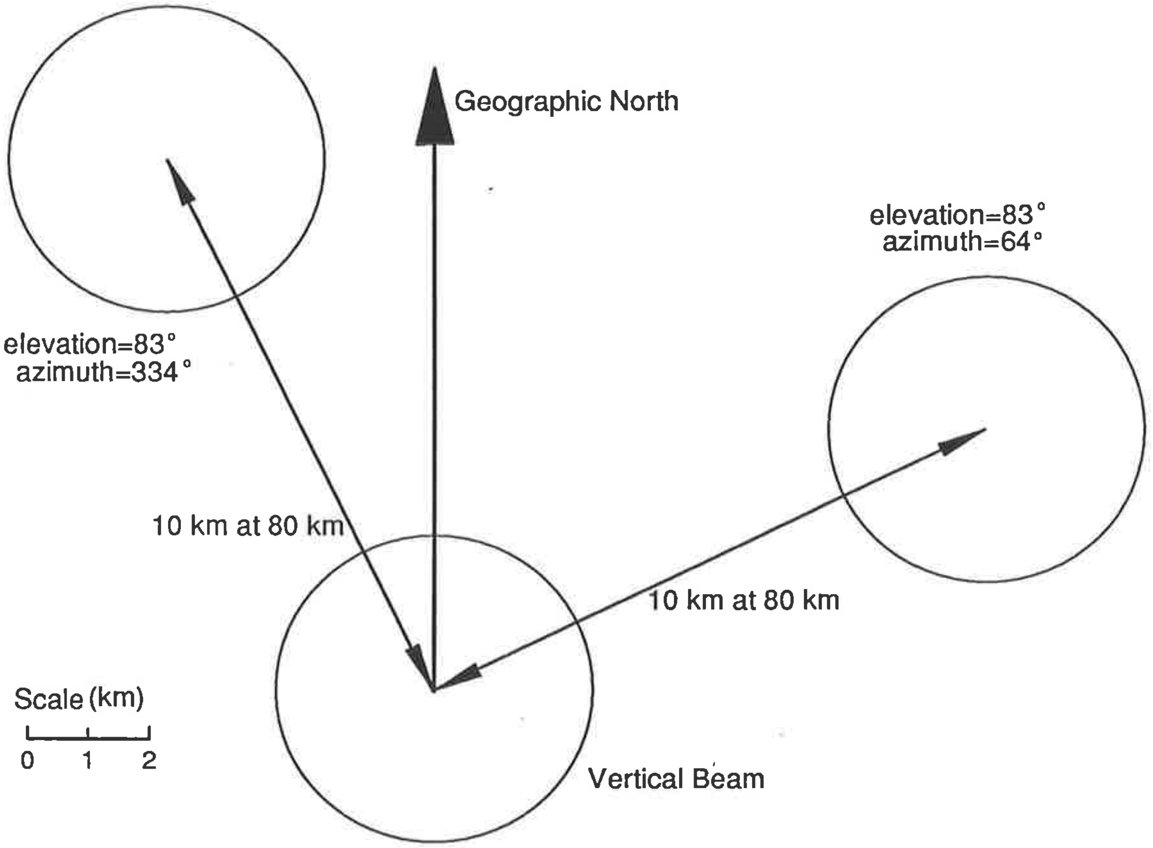

Figure 3.1: The positions of the sampling volumes at 80 km on day 213, 1986

which in the mesosphere, are thought to be in the viscous range (Hocking 1985) . It is felt that there will be enough of these structures to describe the larger scale turbulent motions despite their shorter lifetimes.

As the radar system is monostatic, the sampling volumes for the vertical beams and those for the oblique beams were not colocated. The separation between the sampling volumes at 80 km is illustrated in figure 3.1.

For the rest of this chapter, it will be assumed that the reader is familiar with the MST radar technique and the Poker Flat MST radar will not be discussed any further. However further information on the MST radar technique can be obtained from Röttger (1984) and information on the Poker Flat radar can be found in Balsley *et. al.* (1980).

3.1.2 Technique for obtaining spectral parameters

Having obtained a power spectrum of the echoes returned from the mesosphere, we must now evaluate the spectral parameters that are of interest to us. These include the mean frequency offset, which gives a measure of the velocity radial to the beam, and the width of the spectrum which is associated with turbulence. A measure of the signal-to-noise ratio can also be of interest.

A review of methods that can be used to obtain estimates of spectral parameters was compiled by Zrnić (1979) . This article, whose emphasis was on weather radars, formed the basis of Woodman (1985) which discussed spectral moment estimation in MST systems. Numerous methods are presented in these papers, however, as the data used in this study were in the form of spectra, only some of the methods are applicable here. These include calculating the zeroth (power), first (mean) and second (variance) moments of the spectrum, as well as fitting a Gaussian function to the spectrum. These methods were compared and the errors in the power,mean and width in each, for various values of signal-to-noise ratio (SNR), were calculated by Yamamoto *et. al.* (1988). They found that for signal-to-noise ratios approaching infinity, fitting a parabola to the logarithm of the power spectrum gave the best result but suggested further work be done before this method should be used at lower SNR. Under conditions of lower SNR they suggest that a Gaussian fit is best. Although other works on the errors associated with the various methods of obtaining spectral parameters exist, these usually do not consider the spectral width and are thus not discussed here. The presence of noise in the spectrum makes the problem of obtaining an estimate of the spectral width more difficult than just computing the standard deviation of the spectrum. A noise spectrum that is white over the finite range being considered would be expected. If this noise is not accounted for, it too will contribute to the spectral width giving a larger value than would result if no noise was present. Similarly, the mean will be biased toward the mean of the noise, zero, causing it to be erroneous also. Furthermore, the mean and standard deviation, even when correct, do not describe the shape of the noise-free spectrum.

A method utilising the best fit of a Gaussian function plus a constant to the spectrum was used because of these factors. Given that this fit was of suitable quality, this ensured that the spectra being considered conformed to the expected Gaussian form and, by appropriate choice of the function, allowed the noise,which should be the same throughout the spectrum, to be accounted for. An estimate of the signal-to-noise ratio could also be obtained but this estimate was not used in this work.

The form of the function used was as follows..

$$y = A_3 + A_4 e^{-(\frac{f-A_1}{A_2})^2} \tag{3.1}$$

It can be seen that by choosing a suitable set of the parameters A_i, any Gaussian function on a DC offset can be formed. The DC offset is described by A_3, the parameter to which y tends when f is a long way from A_1, the mean value. A_2 is the width parameter and A_4 is the maximum value the Gaussian attains relative to the DC offset. A_2 is related to the standard deviation of a Gaussian function by the expression $\sigma = A_2/\sqrt{2}$.

The task is then to find the set of A parameters that best describe the spectrum. The parameter χ'^2 is used to characterise how well the function y fits the spectrum and is calculated by summing the square of the quantity $y - P_R(f)$, where $P_R(f)$ is the radar power spectrum. Thus

$$\chi'^2 = \frac{1}{k} \sum_f (y - P_R(f))^2 \tag{3.2}$$

where k is a normalising factor related to the area under the spectrum. Thus, when $\chi'^2 < \chi'^2_{thresh}$, a threshold value of χ'^2, we can say that the fit of y to the spectrum $P_R(f)$ is a good one and the A parameters can be used to describe the spectrum. The value of (χ'^2_{thresh} which will depend on k) is chosen by inspecting spectra and the fits made to them. (Note that χ'^2 is not simply related to the χ^2 parameter of statistics.)

The quantity χ'^2 will vary with each of the A parameters giving us a multitude of χ'^2 values. The one we desire is the global minimum of these values and this minimum is found using the grid search routine GRIDLS from Bevington(1969). A first guess set of A parameters is obtained from the first and second moments of the spectrum, the maximum value and an average of values near the edges of the spectrum (where noise would be expected to dominate). Starting from this "first guess", GRIDLS repeatedly searches for χ'^2 minima by varying each A parameter until a minimum is found. It then repeats the process starting from *this* minimum until no change in the resultant χ'^2 occurs. This set of A parameters is then chosen as those best describing the spectrum. It is possible that they represent a local minimum and not a global one but the resulting χ'^2 value would not be acceptably small causing the fit to be rejected. It is important, however, to make the first guess of the A parameters as good as possible so that the starting point is close to the global minimum. This makes the possibility of settling on a local minimum less likely and decreases the computer time needed, improving the efficiency of the analysis. For the same reason, the 64 point spectrum stored on tape is averaged in pairs to form a 32 point spectrum, halving the number of calculations to be made in χ'^2 for no significant loss in fit quality.

The turbulence theory described in chapter 2 treats Gaussian spectra, and this method of spectral fitting is matched to these. However in practise, non-Gaussian components of the spectrum exist (Hocking 1983b). In particular, specular spikes that are not thought to be associated with turbulence exist as can be seen in figure 3.2. It is felt that in this analysis these are best ignored, and the following method is used to remove their effect.

The specular spikes have amplitudes typically much greater than that of the background Gaussian profile. Thus the first thing to do is to find the maximum value in the spectrum. If "one" spike is to be rejected, the Gaussian fit can be carried out on the spectrum ignoring this maximum point. Similarly, if "two" spikes are to be rejected, the maximum and second maximum values are ignored and so on. A number of levels of spike rejection can then be tried and the one that yields the best χ'^2 value is chosen as the one representing the Gaussian spectrum. In this analysis, up to 5 points are removed from the 64 point spectrum. It should be noted that this may not remove 5 spikes as two or more points that are adjacent to each other forming one spike, may be removed.

The method suggested by Yamamoto *et al* (1988) where a parabolic fit to the logarithm of the power spectrum is made is less sensitive to the effects of spikes. Its

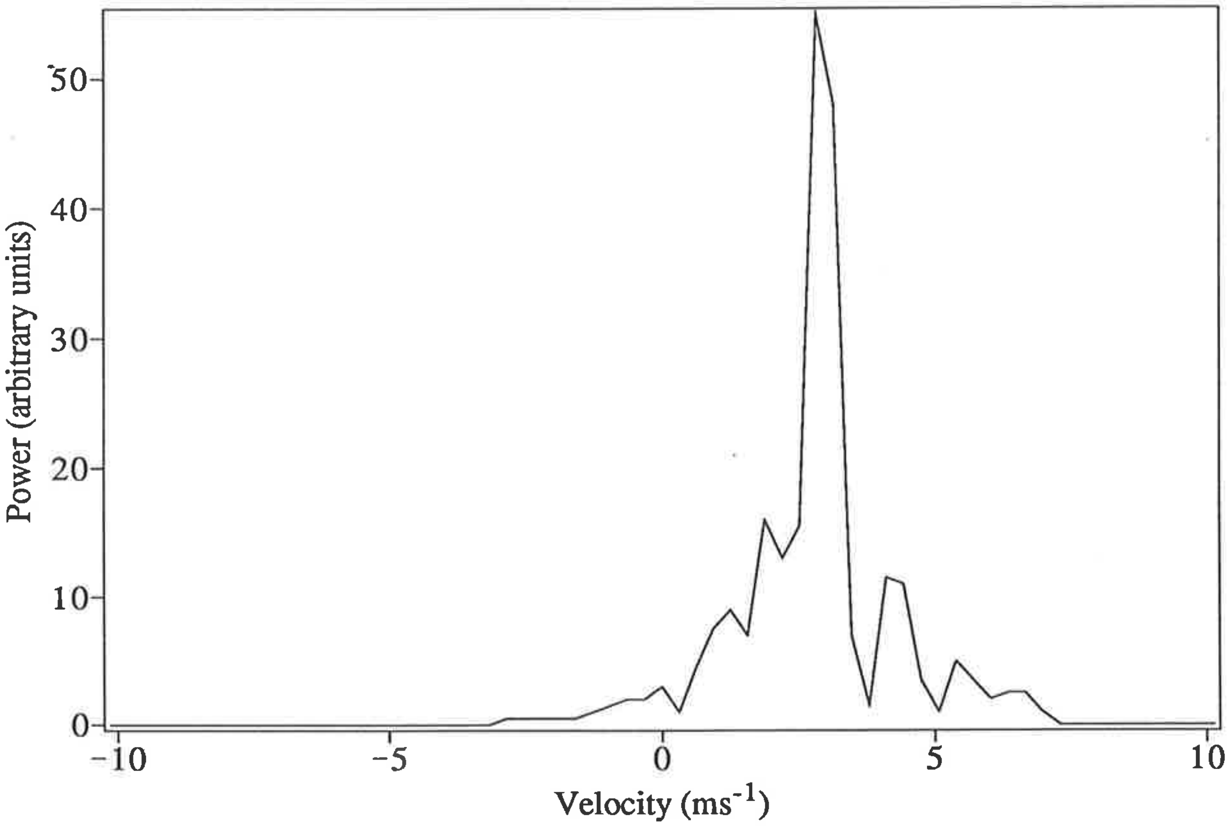

Figure 3.2: A typical spectrum from the Poker Flat radar.

application to situations where the signal-to-noise ratio is low, however, is still to be considered.

The Gaussian fitting method is not used in the routine operation of the Poker Flat system. Instead a subroutine called PROFILE calculates velocities, widths and signal-to-noise ratios. This routine uses the method of Hildebrand and Sekhon (1974) to calculate the noise present in the spectrum and uses these noise figures to avoid their effects on the mean and standard deviation. Plots comparing the velocities and widths obtained using the two methods, i.e. a Gaussian fit to a spike rejected spectrum or the use of PROFILE on a non-spike rejected spectrum are given in figures 3.3 and 3.4. The points in these figures correspond to cases where the data from *both* analysis methods are acceptable, i.e. the signal-to-noise ratio from PROFILE is greater than zero and the $\chi'^2 < 0.6$. It can be seen that there is a good agreement between the velocities obtained using the spectral fitting and the PROFILE methods. The different symbols indicate the various numbers of spikes that were "removed" and it can be seen that no significant bias in the velocity as a function of the spike rejection was present.

The widths obtained using the two methods are also in agreement although it is not as good as for the velocities. Spike rejection will cause the width of the spectrum to be increased because a strong narrow component has been removed. Therefore one would expect high levels of spike rejection to be associated with spectra where the spectral fitting width is broader, and low levels where the fit is narrower. The fact that few squares and circles occur below the $y = x$ line in figure 3.4 and that few crosses and diamonds occur above this line suggest that this is occurring. This is not a problem, in fact it probably means that the spike rejection is acting as it should.

Reinspection of the velocity plots of figure 3.3 with this in mind still does not suggest a bias. Thus the spikes do not seem to systematically affect the velocity estimates.

If the cases where no spikes are rejected are considered in isolation, it can be seen that in the 14:00 to 14:20 data, the width using Gaussian fitting is usually less than that from PROFILE. A possible cause of this may be that PROFILE is not adequately accounting for the noise in the spectrum. If this is the case, it is of no consequence in

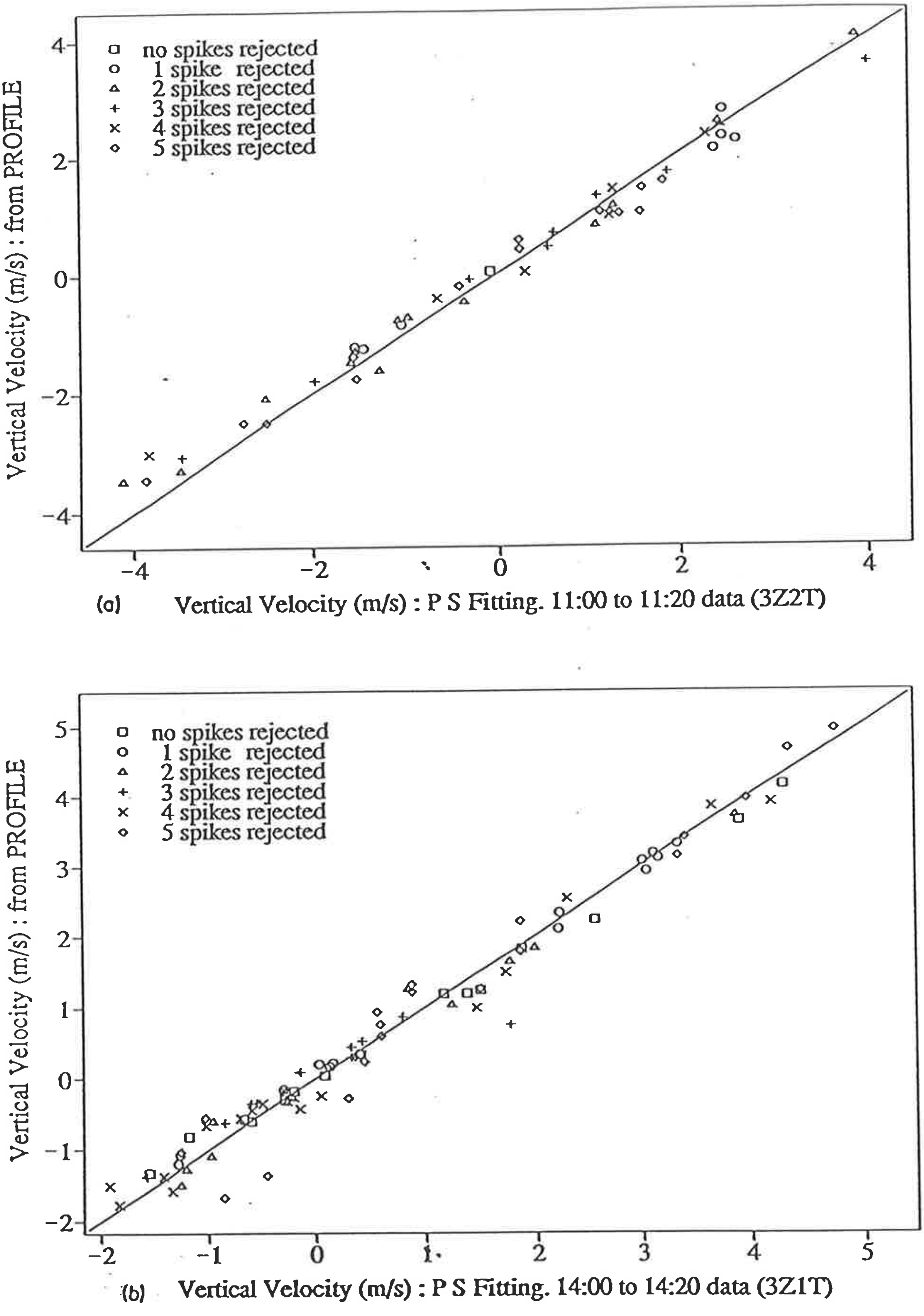

Figure 3.3: Comparisons of velocities obtained using the spectral fitting and the PROFILE methods, a) for 11:00–11:20 data and b) for 14:00–14:20 data.

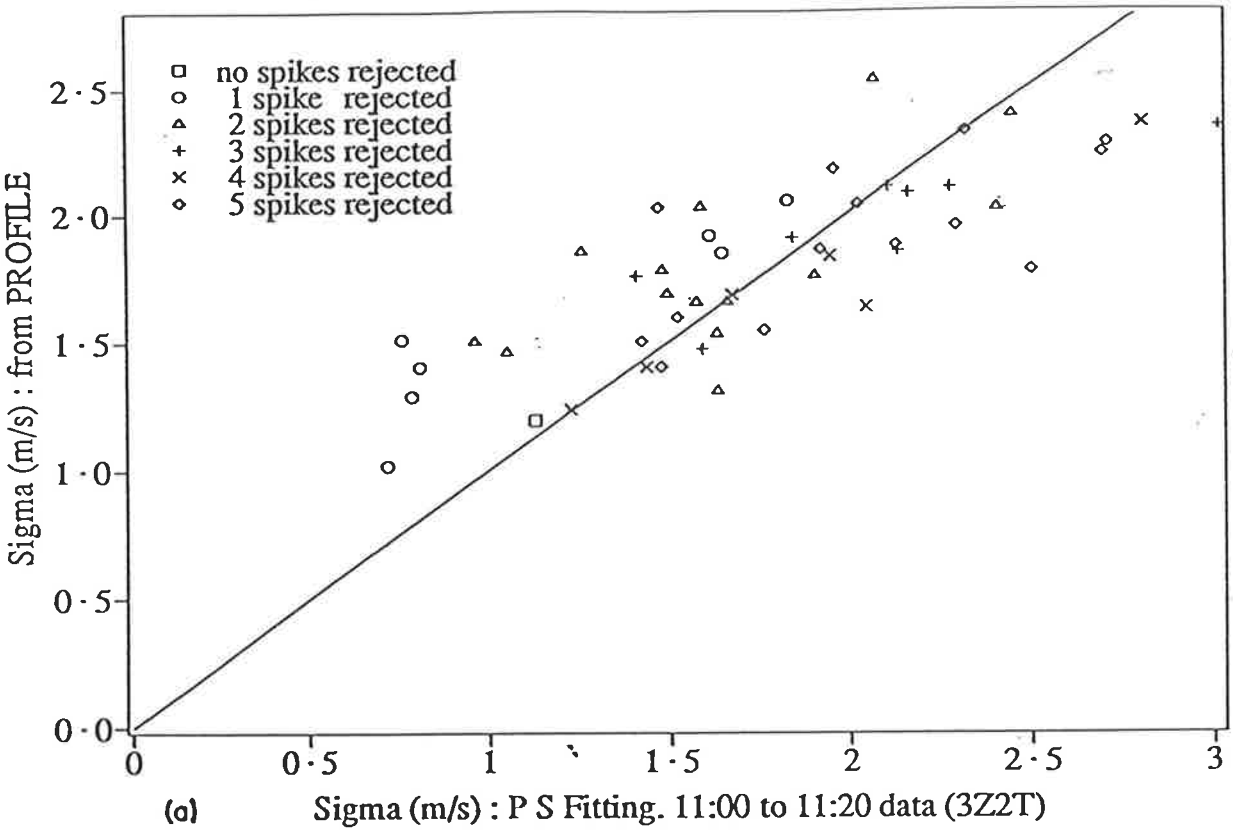

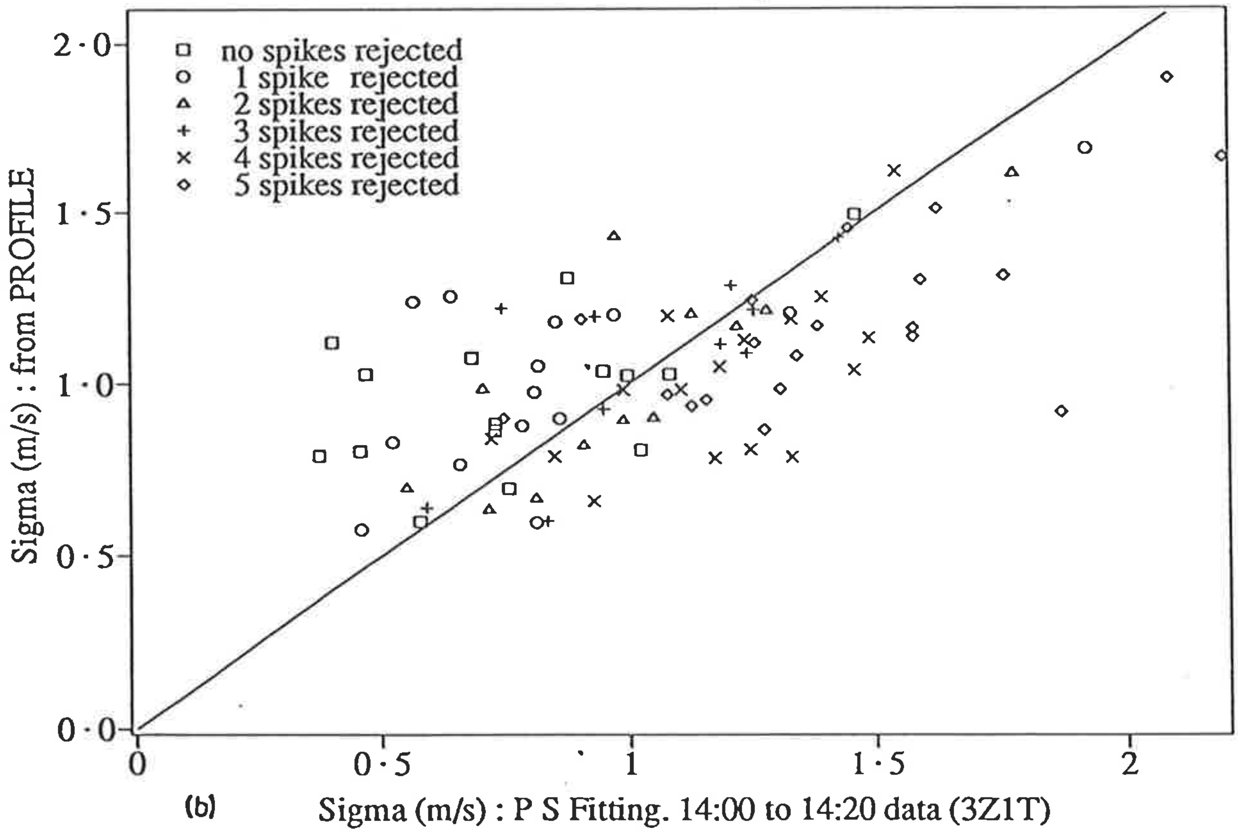

Figure 3.4: Comparisons of widths of the Doppler spectra (standard deviations) obtained using the spectral fitting and the PROFILE methods, a) for 11:00–11:20 data and b) for 14:00–14:20 data.

this study as the PROFILE widths are not used.

3.1.3 Assessing gravity wave contamination.

The prime objective of this experiment was to investigate the notion that short period fluctuations in wind velocities are contaminating radar estimates of turbulent energy dissipation rates (ε). As discussed previously, these contaminations are due to variations in the mean over the sample (in space or time) which contribute to the width of the resultant spectrum and thus ε. These contributions could obviously be minimised by choosing a suitably small sample but this is not always possible. In order to build up a spectrum of velocities, returned signals must be sampled for an appropriate length of time. Thus a minimum sampling time exists. It depends on parameters such as radar frequency and the nature of the turbulent structures being investigated and can be a significant fraction of the period of the gravity wave. In considering this latter point, it must be remembered that, even though the Brunt-Vaisala period in the mesosphere is of the order of 5 min, oscillations with ground-based periods less than this are possible due to Doppler shifting by the mean wind (Fritts and VanZandt 1987).

Because of the advantages in minimising the sampling time, the first stage of this part of the analysis involves choosing that minimum time. For these data, this can be $(2n-1)T_{sample}$, where n is any positive integer and T_{sample} is the time taken to acquire a spectrum, in this case 10-11 s. (The $2n-1$ factor is due to the switching of the beam configuration described earlier.) A lower limit of T_{sample} exists and comes about through the need for the sample to contain the minimum amount of data required for a reliable spectrum. Hocking (1983b) showed that if this is not the case, spectra that seem realistic but are in fact entirely spurious can result and suggested that 80-100 times $\tau_{1/2}$, the half-width of the autocorrelation function, be used. May (1988) suggests that 50 times the half-width could be enough.

Height accumulations, where spectra over successive heights for the same time are summed frequency bin by frequency bin are available also and should be considered in a similar way. One spectrum represents echoes from a height interval of approximately

300m, which is actually too small for the turbulence measurements envisaged here. It is thought that the outer scale of turbulence, L_B is of the order of 1km (e.g. Hocking 1983b), that is, turbulent eddies exist up to about 1km in scale. Therefore, a sample taken over a 300m height range will only contain echoes from part of a large scale eddy and will not fully describe it. If we are to measure turbulence parameters due to the whole range of scales, then more than one height sample will be necessary. In this case, a minimum of 3 height intervals are summed so that spectra contain information on these large scale eddies.

These arguments suggest a "basic unit" data block of 3 adjacent height samples accumulated for one time, denoted 3Z1T. There is however one more consideration. The distribution of the spectral widths obtained for these units showed that some spectra were quite narrow. Inspection of these spectra showed that their structure was dominated by the presence of specular spikes. Although the cause of these spikes is unclear, it is felt that they bias the turbulence parameter estimates and should be removed (Hocking 1983b). However at this stage of analysis, numerous levels of spike rejection have been used and the narrow cases yield the best (least) chisquare value. This suggests that not much exists in the spectrum other than the spike (and noise) and this is borne out by inspection of these spectra. In some cases, a Gaussian-like profile can be fitted to the rest of the spectrum but its extremely small amplitude makes it insignificant.

To overcome the problems of these narrow spectra, one can either ignore the cases where they occur and suffer the decrease in the data acceptance rate or move to 3Z2T where two successive time samples as well as 3 heights are accumulated, in the hope that the non-specular parts of the spectrum will become more significant. This latter method has the disadvantage that the spectra could also contain some or more gravity wave contamination. If the gravity wave present is of a long period, this may be an acceptable step so one must make this decision with this in mind.

In this experiment, we have the ability to simulate a number of sampling times. Having made a decision on the size and duration of the "base unit", it is possible to expand the sampling time to see the effect, if any, of gravity waves on the spectral widths. For example, if we consider a time and height block of 3Z10T (3 adjacent height samples and 10 time samples) and compare the spectral width obtained from this accumulation to those of the (say) 5×3Z2T base units that make up the set, it is possible to ascertain whether variations in velocity are contaminating the spectral width estimate of the larger set.

To do this, one must note that the width obtained from the Gaussian fit to a spectrum is independent of the position of the mean. Therefore by averaging the widths of the (here) 5 base units in some way, one gets an estimate of the spectral width value with longer term (> 10 s) velocity effects removed. This can then be compared to the spectral width from the larger set which will still be contaminated by these velocity effects. The averaging of the spectral widths of the base unit spectra must be done with some care if one is to maintain the analogy to echoes returning from the mesosphere. Not only is the spectral width independent of the position of the mean (velocity) but it is also independent of the amplitude of the Gaussian. A broad spectrum of low power will not contribute much to the accumulated spectrum and thus must be given a lower weighting in the averaging process that we use.

This averaging is done by considering the final spectrum, $S(f)$ as being the sum of a series of n component spectra $S_i(f)$ with properties as described in Table 3.2.

	Distribution	Mean	Variance	Area
Final Spectrum	$S(f)$	$\overline{f_S}$	σ_s^2	$\mathcal{A} = 1$
Component spectra	$S_i(f)$	$\overline{f_i}$	σ_i^2	$\mathcal{A}_i$

Table 3.2:

The areas $\mathcal{A}_i$ are the areas underneath each spectrum. When it is assumed that the area under the final spectrum, ($\mathcal{A}$) is equal to one, we obtain the following equations for the mean and variance of the final distribution (derived in appendix B):

Given $S(f) = \sum_{i=1}^{n} S_i(f)$ and $\sum_{i=1}^{n} \mathcal{A}_i = 1$,

$$\overline{f_S} = \sum_{i=1}^{n} \mathcal{A}_i \overline{f_i} \tag{3.3}$$

$$\sigma_s^2 = \sum_{i=1}^{n} \mathcal{A}_i \sigma_i^2 + \frac{1}{2} \sum_{i=1}^{n} \sum_{j \neq i=1}^{n} \mathcal{A}_i \mathcal{A}_j (\overline{f_i} - \overline{f_j})^2 \tag{3.4}$$

It is equation 3.4 that is of interest to us. It can be seen that the final variance has contributions due to the component variances *and* due to variations in the means of the component spectra. Note that this is a general result and can be used for any functions that satisfy the criteria above. The mean and variance of, and the area under, a Gaussian can all be obtained from the parameters produced by the Gaussian fitting routine described previously. In this way, noise can be accounted for but most importantly, by computing the variance without the second term in equation 3.4, effects of the variations in the mean are removed.

We can now devise a method of quantifying the effect of velocity variations on estimates of spectral width. In the example where 3Z10T data with a base unit of 3Z2T are considered, the spectral width from five 3Z2T component spectra could be calculated using equation 3.4 without the second term and compared to the width obtained over the whole 3Z10T accumulation. The former represents the average width over the interval with longer term velocity effects removed and the latter the width from a long time sample with potential for contamination.

For reasons that will become clear shortly, the ratio

$$Y_i = \frac{< \sigma_e^2(\tau_i) >}{< \overline{\sigma_e^2(\tau_0)} >} \quad i = 1, 2, \ldots \tag{3.5}$$

is used to measure the contamination, where $\sigma_e^2(\tau_i)$ is the variance of a spectrum accumulated over a time τ_i, and $\overline{\sigma_e^2(\tau_0)}$ is that quantity for the base units (each of duration τ_0) that make up the final spectrum, obtained using equation 3.4 without the second term. The angle brackets denote an average over all the cases that occur in the whole (typically 20 min) data set. Obviously if no contamination due to velocity effects is present in the spectral widths, both terms in Y_i will be the same and a value of one will result for all values of τ_i. If contamination *is* present however, non-unity values of Y_i will result for some values of i.

In the cases where the "base unit" chosen is suitably small, it is conceivable that the first ratio Y_1 will be close to one. One can then take this study of the contamination effect beyond showing it exists. The spectral width is not due to gravity wave effects alone. Turbulent spectral widths and contaminations discussed by Hocking (1985) are present as well. In the absence of gravity waves, Hocking states that the experimental half-power half-width f_e obtained using the methods of section 3.1.2 obeys

$$f_e^2 = f_{BN}^2 + f_T^2 \tag{3.6}$$

where f_{BN} is a component of the spectral width due to the broadening and narrowing effects of shears and the mean wind, and f_T is the width of the turbulent component of the spectrum. This equation actually describes the width of a Gaussian (f_e) obtained from the convolution of two other Gaussians of widths f_{BN} and f_T. This idea can be extended, with some approximations, to obtain some information on the magnitude of velocity effects on spectral widths by including a gravity wave width component. One would expect the following relation:

$$f_e^2(\tau_i) = f_{GW}^2(\tau_i, \phi) + f_{BN}^2 + f_T^2 \tag{3.7}$$

where $f_{GW}^2(\tau_i, \phi)$ is the component of the spectral width due to the gravity wave contamination in a sample of time τ_i taken when the phase of the wave is ϕ. This can only be an approximation however, because the profile of $f_{GW}^2(\tau_i, \phi)$ is not expected to be Gaussian. In fact it will be a segment of the gravity wave spectrum as shown in figure 3.5 (Details of how these spectra are produced are given in appendix A). It can be seen that, in the case of a half-cycle of the gravity wave being included in the sample τ_i, a spectrum that is anything but Gaussian will result. Two points, however, make the approximation that segments of this spectrum are Gaussian less of a problem. The first is that sampling times in this analysis are *generally* less than half the wave period and will not include the whole spectrum. Secondly and more importantly, the spectra from which $f_e^2(\tau_i)$ are obtained have had a Gaussian fitted to them and are therefore Gaussian to within the value of χ'^2_{thresh} that was used. If these spectra, which result from the convolution of turbulence, broadening/narrowing and gravity-wave effects, were being greatly affected by the shape of the gravity-wave component, they would not have Gaussian end products and would be rejected. This is not to say that eq 3.7 is *exact*, it

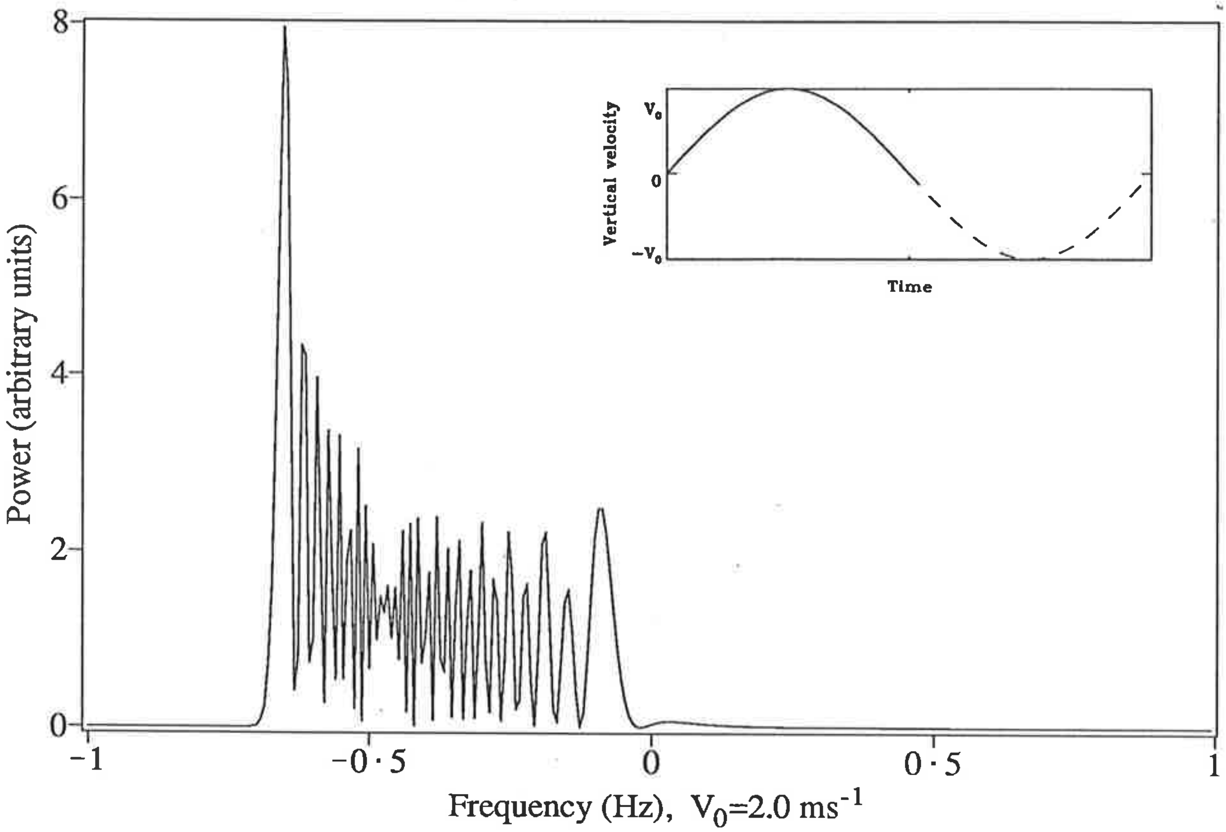

Figure 3.5: A segment of the Doppler spectrum due to a gravity wave only (see appendix). The solid line in the inset shows which part of the gravity wave cycle was sampled.

is just not as bad as first thought, and may be used to make a quantitative estimate of the gravity wave effect.

To obtain this estimate, we first average $f_e^2(\tau_i)$ over all the τ_i samples in the data set to get $< f_e^2(\tau_i) >$. If enough samples exist to average over all possible phases in the gravity wave, we can say

$$< f_e^2(\tau_i) > = < f_{GW}^2(\tau_i) > + < f_{BNT}^2 > \tag{3.8}$$

or, as everything is assumed Gaussian

$$< \sigma_e^2(\tau_i) > = < \sigma_{GW}^2(\tau_i) > + < \sigma_{BNT}^2 > \tag{3.9}$$

where $< f_{BNT}^2 > = 2\ln 2 < \sigma_{BNT}^2 >$ is the average of the broadening/narrowing and turbulence-width contributions combined and $< f_{GW}^2(\tau_i) > = 2\ln 2 < \sigma_{GW}^2(\tau_i) >$ is the width of the gravity wave segments averaged over all phases. This means that..

$$Y_i = \frac{< \sigma_{GW}^2(\tau_i) > + < \sigma_{BNT}^2 >}{< \sigma_{GW}^2(\tau_0) > + < \sigma_{BNT}^2 >} \tag{3.10}$$

where τ_0 is the duration of the base unit. If a case exists where $Y_1 \approx 1$, then $< \sigma_{GW}^2(\tau_1) >$ and $< \sigma_{GW}^2(\tau_0) >$ must be negligible compared to $< \sigma_{BNT}^2 >$ as the latter of the pair must be of a different magnitude to the former. This means that Y_1 can be used to estimate $< \sigma_{BNT}^2 >$ and that for the other i values,

$$Y_i \approx \frac{< \sigma_{GW}^2(\tau_i) > + < \sigma_{BNT}^2 >}{< \sigma_{BNT}^2 >} \tag{3.11}$$

Some algebraic manipulation then yields

$$(Y_i - 1) < \sigma_{BNT}^2 > \approx < \sigma_{GW}^2(\tau_i) > \quad \forall i \neq 1. \tag{3.12}$$

Thus if equation 3.9 is true,we can use our Y_i ratios and $< \sigma_{BNT}^2 >$ to estimate the value of the spectral width component that is affected by the sampling time, $< \sigma_{GW}^2(\tau_i) >$.

An expression for the variance, averaged over phase, of the velocity fluctuations due to a gravity wave has been derived by Hocking(1988) using the probability density function (in the appendix):

$$< \sigma_{GW}^2(\tau_i) > = \frac{V_0^2}{2} F \tag{3.13}$$

Table 3.3: Characteristics of the data segments

Time interval	Heights	Base Unit	Comments
11:00 – 11:20	84.6 – 86.1 km 2@3Z	(3Z2T)	385 s oscillation in w of amplitude 2.25 ± 0.25 ms^{-1}
14:00 – 14:20	84.0 – 85.5 km 2@3Z	(3Z1T)	300 s oscillation in w of amplitude 2.5 ± 0.5 ms^{-1}
13:00 – 13:20	84.3 – 84.9 km 1@3Z	(3Z1T)	little variation in w
9:00 – 9:20	84.9 – 86.4 km 2@3Z	(3Z2T)	Long period fluctuation in w
8:30 – 8:50	86.1 – 86.7 km 1@3Z	(3Z2T)	A ramp in w

where

$$F = 1 - \frac{1}{2\pi^2}\frac{T^2}{\tau}\{1 - cos(\frac{2\pi\tau}{T})\} \tag{3.14}$$

T being the period of the gravity wave , V_0 its amplitude and τ the sampling time. It is shown in appendix A that this equation can be applied to the power spectrum. It can then be compared to $(Y_i - 1) < \sigma^2_{BNT} >$ in order to judge its ability to estimate the contamination due to gravity waves.

3.2 Results

The analysis described previously was carried out on the data on a case study basis. These cases which include oscillations in vertical velocity w of various periods were chosen from the velocity vs height and time plots given in figure 3.6 and were subjected to further analysis. Although this figure consists largely of noise, some areas containing coherent velocity variations can be seen. The segments of the data set and some of their characteristics are summarized in Table 3.3.

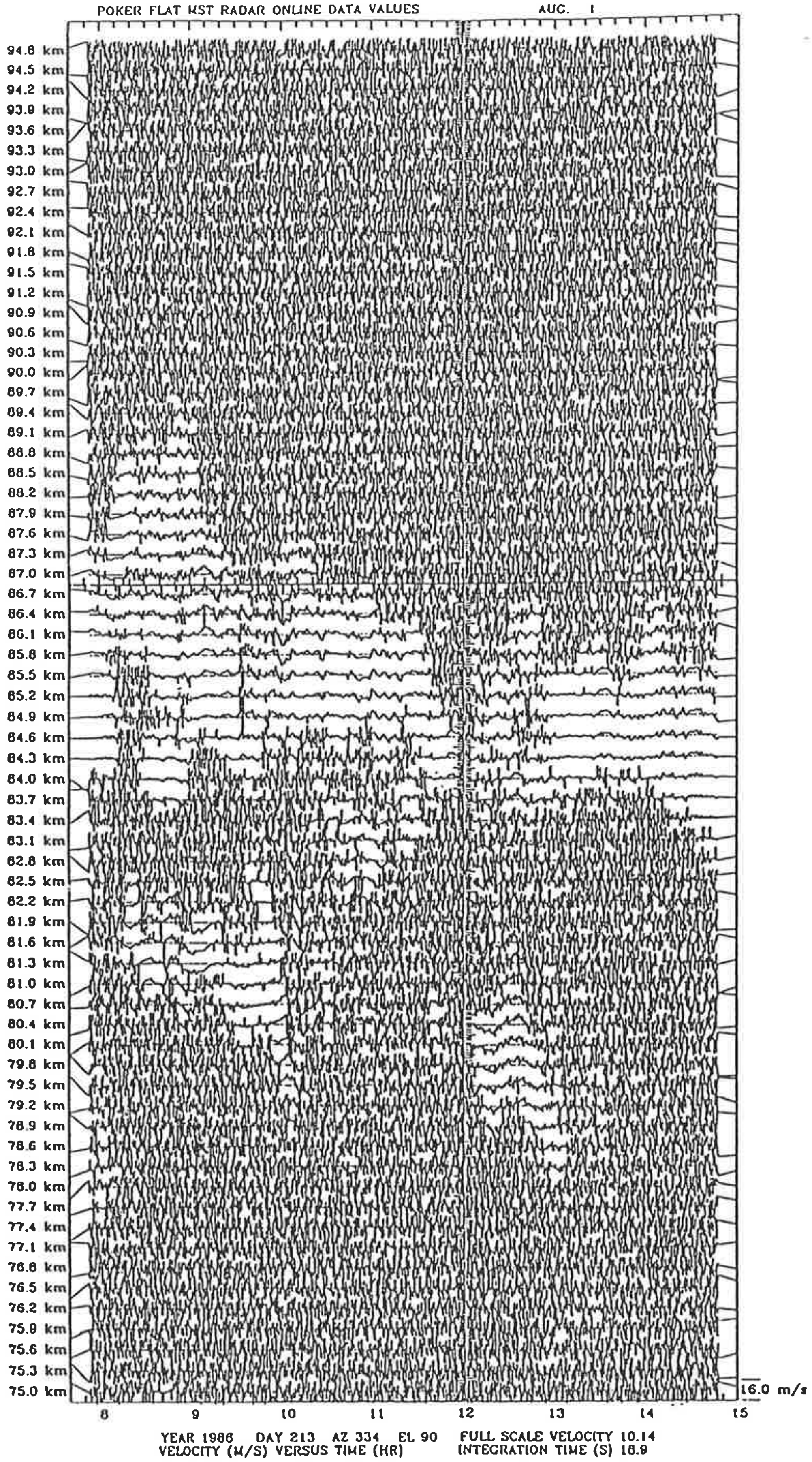

Figure 3.6: Plot of the velocities for the whole data set.

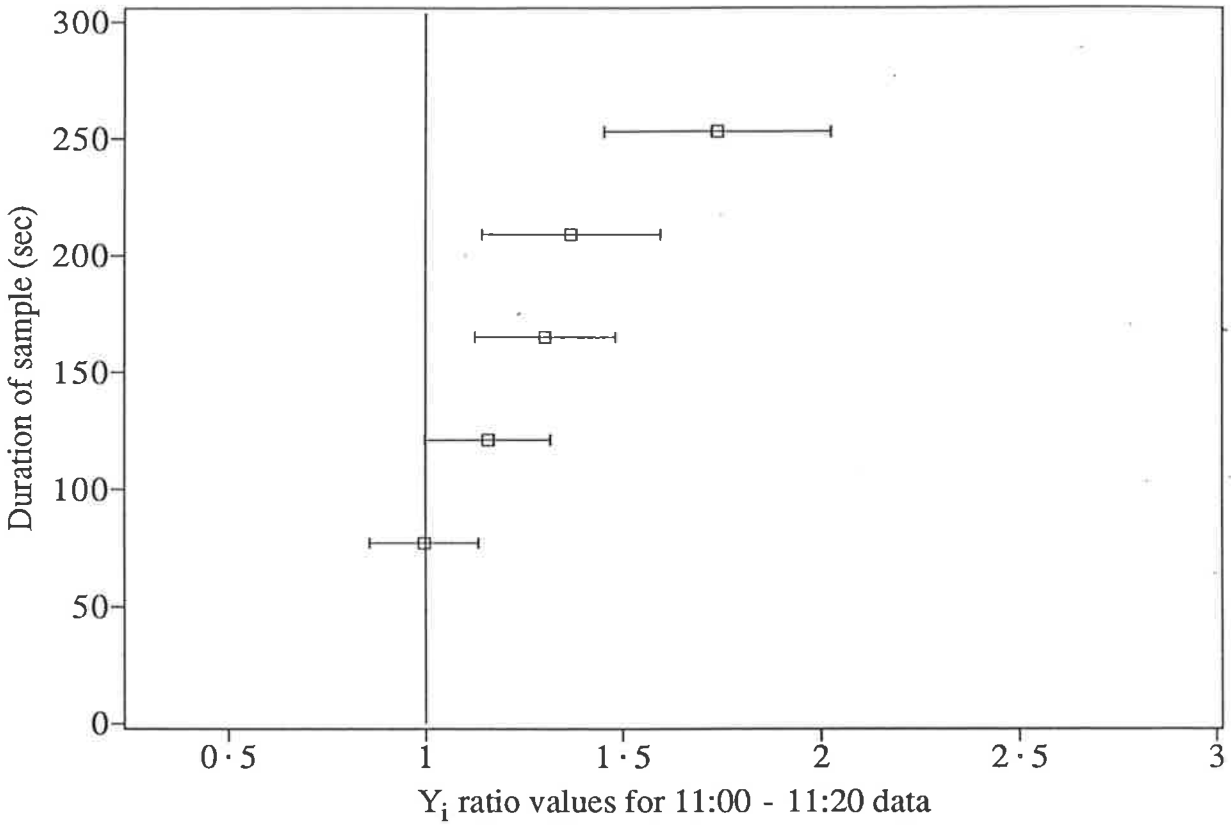

Figure 3.7: The Y_i values for the 11:00–11:20 data.

3.2.1 Gravity wave contamination.

The 11:00 – 11:20, 84.6 – 86.1 km data.

In this case the base unit, chosen using the criteria of section 3.1.3 was 3Z2T, i.e. 3 height samples and 2 time samples were accumulated to give the "minimum" spectrum that was analysed. These were then compared with multiples of the base unit to give the Y_i values shown in figure 3.7. The error bars are calculated using the one-standard-deviation errors in the mean of the numerator and denominator in equation 3.5, both of which involve an average through the data set.

The vertical axis in figure 3.7 represents the time over which the sample is accumulated. It can be seen that as this increases, Y_i, which is a measure of the contamination due to velocity variations, moves away from unity. The first *significant* non-unity Y_i value occurs at a sampling time of 165 s although the 121 s sample only just includes unity.

The amount of contamination is dependent on the period and the amplitude of the

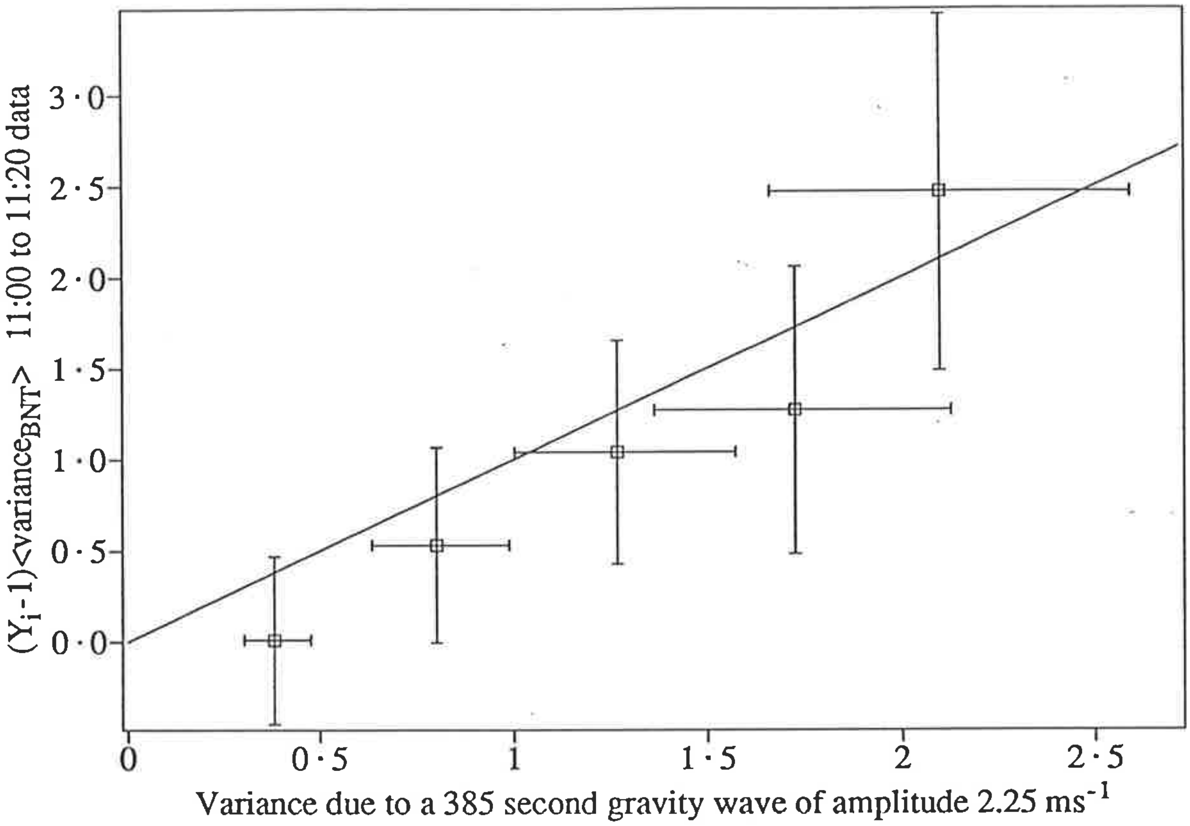

Figure 3.8: Comparison of predicted and measured spectral width contamination for the 11:00–11:20 data.

gravity-wave oscillation as expressed in equation 3.13. The ability of this equation to predict the contamination is assessed in figure 3.8. In this figure, the horizontal axis represents the predicted variance, averaged through the data set, of a gravity wave only (using equation 3.13). The central values are calculated using a period of 385 s and an amplitude of V_0= 2.25ms^{-1} and the error bars use V_0=2.0 ms^{-1} and 2.5 ms^{-1} respectively. On the vertical axis, the variance due to components that are independent of sampling time (i.e. the non "GW" terms) are plotted. The error bars denote one-standard-deviation uncertainties in the mean derived from the average over the data segment.

It can be seen from figure 3.8 that a good agreement between the experimentally derived widths and those predicted by equation 3.13 exists. The fact that the period of the oscillation varies through the data segment (i.e it is not "monochromatic") and is not *exactly* 385 s, and that V_0 also varies will act to degrade the quality of the predicted widths. Despite this though, equation 3.13 predicts the width of the gravity

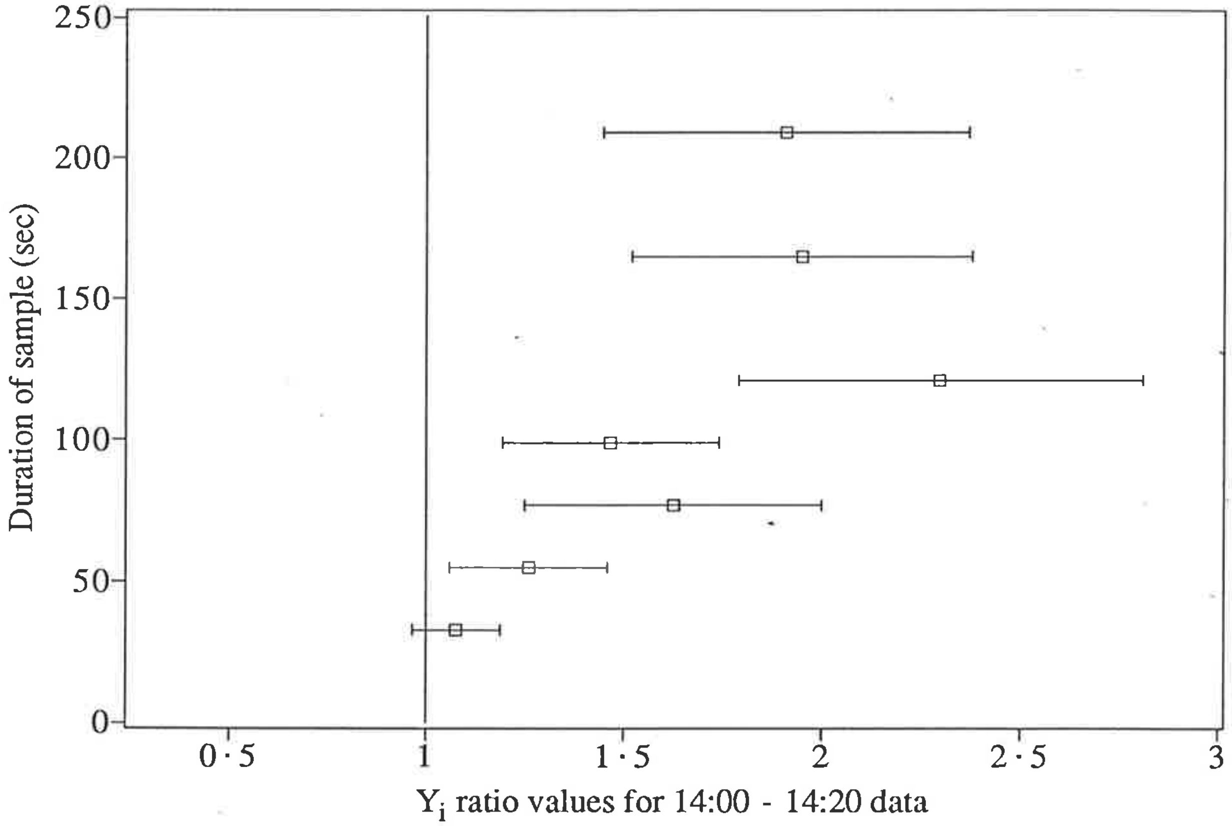

Figure 3.9: The Y_i values for the 14:00–14:20 data.

wave component quite well.

The 14:00 – 14:20, 84.0 – 85.5 km data.

The base unit for this segment was 3Z1T and the Y_i ratios for the 14:00–14:20 data segment are given in figure 3.9. The second data point, corresponding to a sampling time of 55 s, is non-unity to within the one-standard-deviation error in the mean. The Y_i values seem to level off between 2.0 and 2.2 for samples larger than 120 s. This may imply that *all* the gravity-wave contamination has been included in these spectra; however the number of individual Y_i values contributing to these points is small making the statistics unreliable.

Figure 3.10 shows the comparison between predicted and experimentally determined widths. The predicted values use a V_0 of 2.5 ms^{-1}, and a period of 297 s (equivalent to 14 samples) with the error bars corresponding to V_0=2.0 and 3.0 ms^{-1}. The vertical error bars correspond to the one-standard-deviation errors in the mean. There is good agreement between the predicted and experimental values for the smaller samples. The larger ones are probably being affected by the small number of samples. This will mean

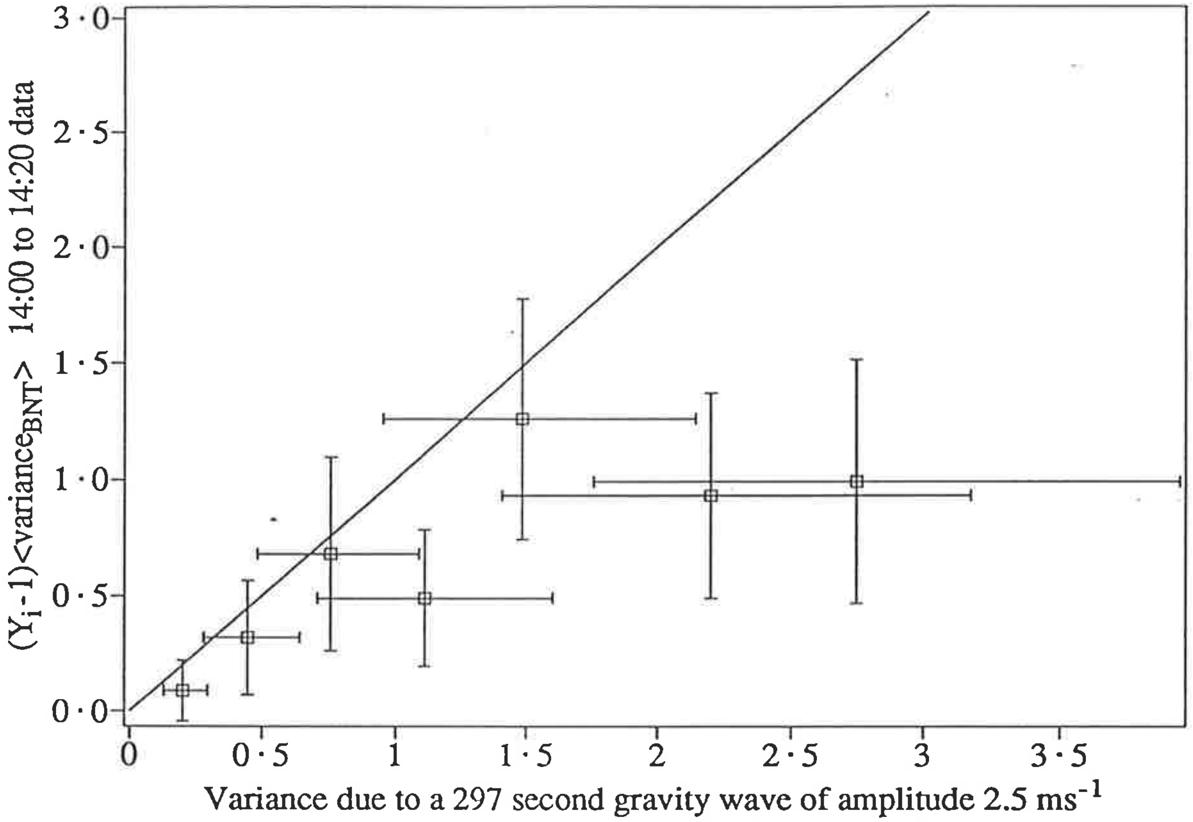

Figure 3.10: Comparison of predicted and measured spectral width contamination for the 14:00–14:20 data.

that averaging over the data set will not capture a variety of phases making the result incompatible with the theoretical prediction where all possible phases are averaged. This lack of data is due partly to the limited number of separate large samples that can be taken from a finite data segment but may also reflect a predominance of non-Gaussian spectra. This would be expected for larger samples, and numerous spectra were rejected on the basis on a poor χ'^2 at these long sampling times.

13:00 – 13:20, 84.3 – 84.9 km data.

The base unit on this occasion was 3Z1T; however the height range over which the data were available was less than for the previous two cases making it impossible to split it into two 3Z height regimes. The result is that fewer points are available and the error bars on the Y_i graphs given in figure 3.11 are correspondingly larger. It can be seen however that none of the Y_i values are significantly different to 1.0, a result which is not surprising as the variations in the data are of small magnitude (0.5 – 1.0 ms^{-1}). Thus, even though a 3Z1T base unit was chosen, a longer duration sampling time would

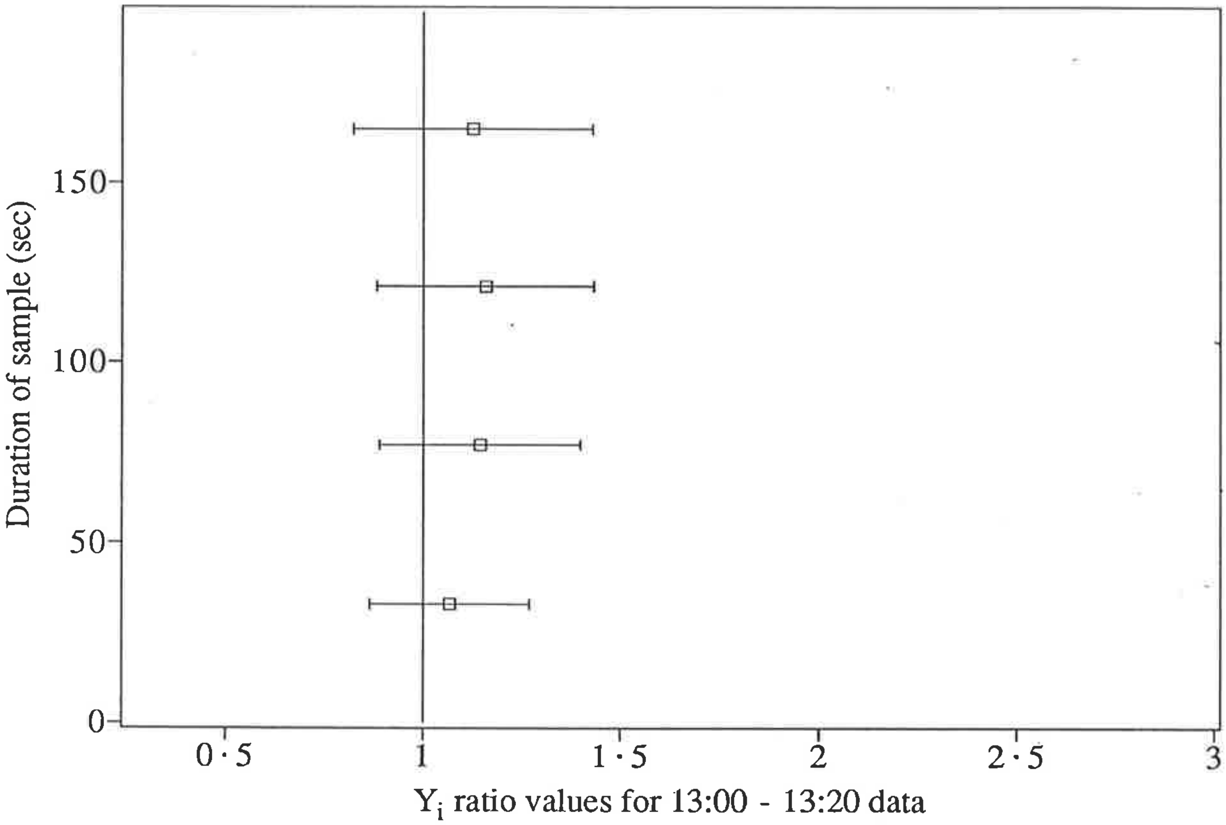

Figure 3.11: The Y_i values for the 13:00–13:20 data.

give results unaffected by gravity waves.

As no regular oscillation was present, a comparison of measured with predicted contamination could not be carried out.

9:00 – 9:20, 84.9 – 86.4 km data.

A base unit of 3Z2T was chosen for the data set. Figure 3.12 shows the Y_i values for this data set. The vertical velocity changed from -2 to +2 ms^{-1} approximately during the 20 min of the data set. If any oscillation is present it is of period much larger than the data set. None of the Y_i values are significantly non-unity and no comparison was possible with predicted broadening due to gravity waves.

8:30 – 8:50, 86.1 – 86.7 km data.

For this data set, a base unit of 3Z2T was needed. The vertical velocity fluctuated slightly around a linear decrease but no clear oscillation was present. The Y_i values are given in figure 3.13. None of those displayed are significantly different to 1.0. The large error bars are due to fewer points being available in this smaller height range.

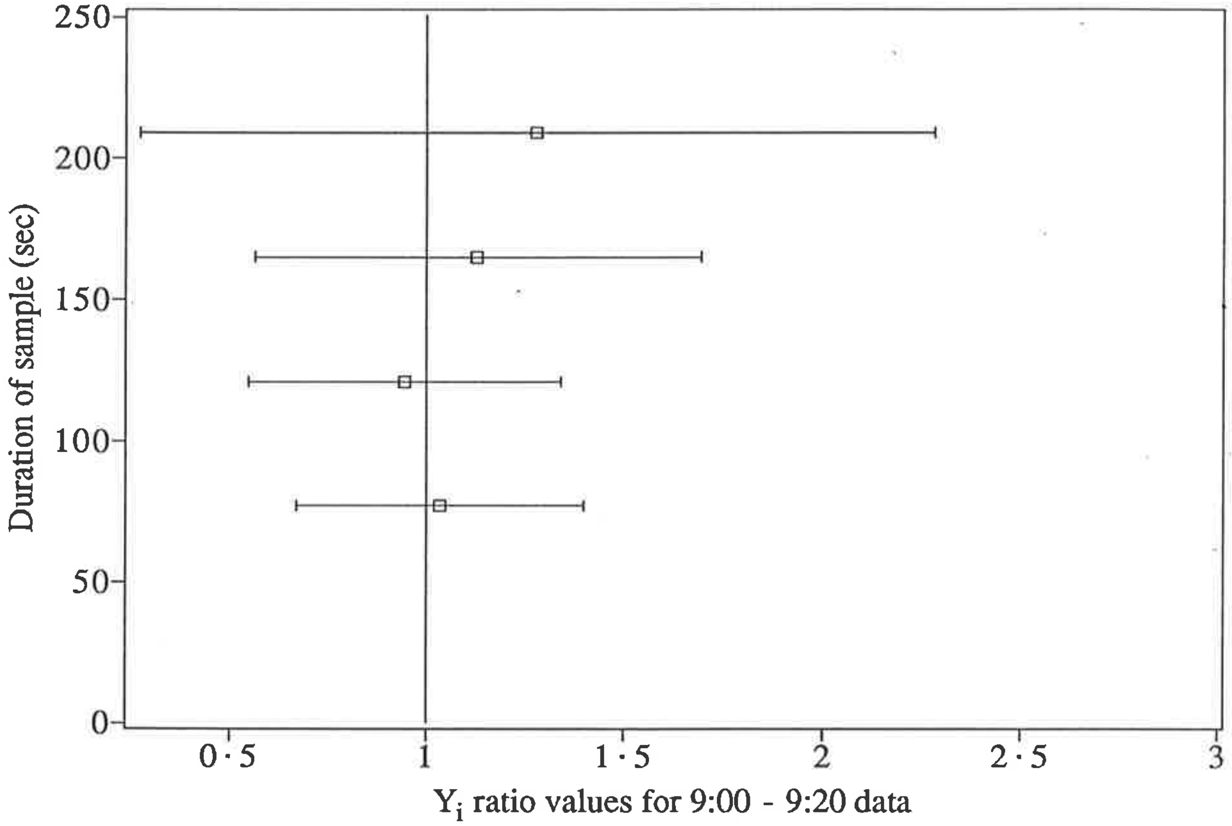

Figure 3.12: The Y_i values for the 9:00–9:20 data.

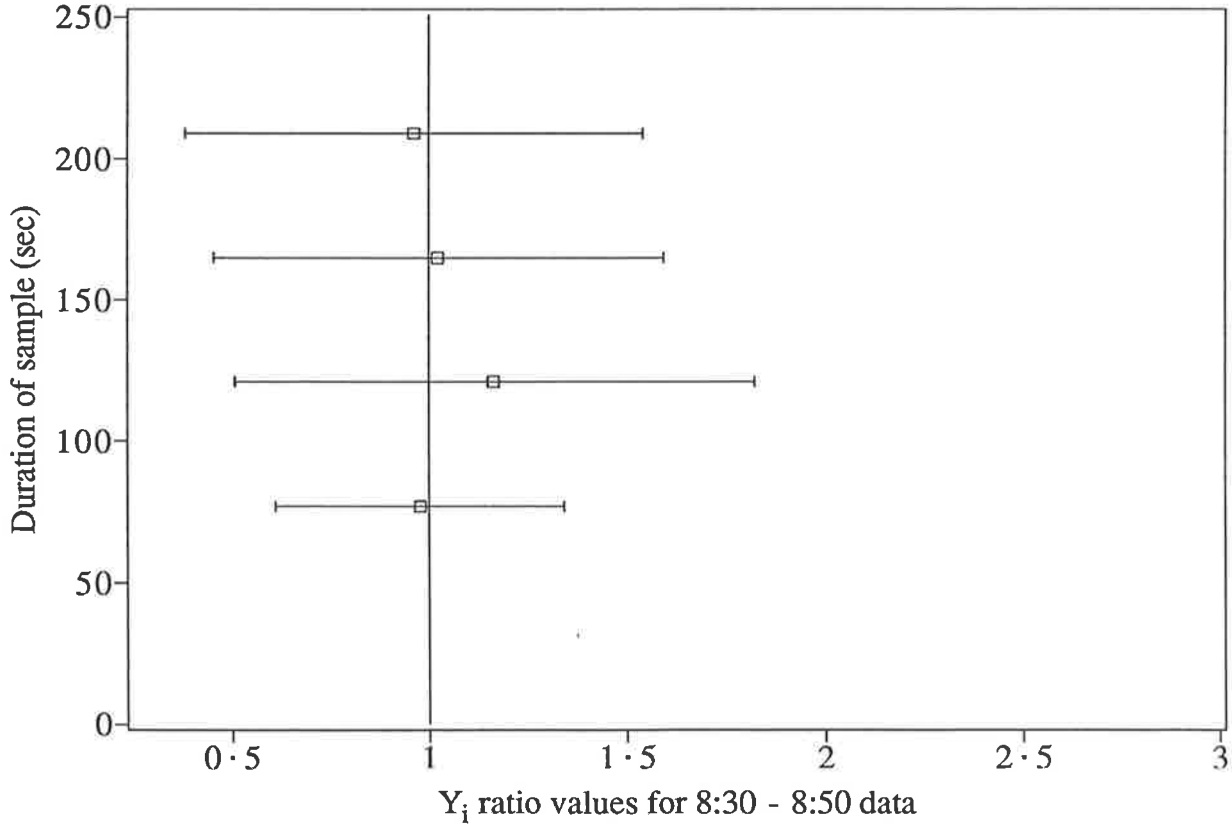

Figure 3.13: The Y_i values for the 8:30 – 8:50 data.

3.2.2 Energy dissipation rates from the vertical beam data.

The vertical beams can be used to obtain measurements of the turbulent energy dissipation rates. As discussed in chapter 2 and in Hocking(1989), this involves calculating the width of the spectrum of one of the beams, correcting for contamination effects, and converting this width to ε, the turbulent energy dissipation rate. For this experiment, the two beams are pointed vertically at the same time so that the spectra from each can be averaged to improve the signal-to-noise ratio. The width of this must then be corrected for non-turbulent contributions.

In the previous section, it was shown that gravity wave contamination can be avoided in this experiment by choosing a suitable base unit spectrum. The analysis here is confined to that spectrum, which must then be corrected for other forms of broadening and narrowing. Hocking (1983b) suggests that beam broadening is the most important for vertical beams, that is, shear broadening can probably be ignored. The use of an approximately 1 km height sample adds credence to this as the shear that would be required to produce an effect would need to be even greater than that for the 2-3 km height samples used by Hocking at MF. Thus beam broadening is the main contaminant. An equation to quantify this is given in Hocking (1985) and when applied here the result is:

$$f_{0.5BN}(Hz) = 0.0032 \times V \tag{3.15}$$

This uses a two way beam half-power half-width of 0.55° and a wavelength of 6m. The V here is the magnitude of the horizontal wind velocity vector in ms^{-1}.

As the sampling regions for the vertical and off-vertical beams were not colocated, an assumption must be made in order to proceed with this analysis. As shown in figure 3.1 the sampling regions for the off-vertical beams are approximately 10 km away from zenith at 80 km, thus we do not have a measure of the horizontal velocity in the region where the spectrum whose width we measure is sampled. To overcome this, it is assumed that the wind field in the region of the 3 sampling volumes is non-divergent. That is, the horizontal velocity measured at one of the oblique beams is the same as that at the other two beams and the vertical velocity measured at the vertical beam is the same as that at the oblique beams. This yields the following expression for radial velocity V_{rad}

$$\begin{aligned} V_{rad} &= u \sin\theta + w \cos\theta \\ &= u \times 0.122 + w \times 0.993 \end{aligned} \tag{3.16}$$

for $\theta = 7°$, where θ is the angle of each beam from the zenith, u is the horizontal wind component in the plane containing the vertical and oblique beams and w is the vertical velocity. This can be rearranged to give an expression for u viz:

$$u = \frac{V_{rad} - w \times 0.993}{0.122} \tag{3.17}$$

Although horizontal velocities are generally larger than vertical ones, it is variations of w between the beams that will cause the greatest concern. As equation 3.17 shows, an error in w will cause a significant error in u and, of the three wind components, it is w that is most likely to vary. The horizontal winds will most likely be due to longer period waves which have horizontal wavelengths much greater than the size of the beam separation, making small scale variations unlikely. Conversely, the vertical velocities are due to high-frequency waves which have shorter horizontal wavelengths and are more likely to vary from one beam to another. However, of all the possible assumptions that can be made, the non-divergent one is the best in spite of the above complications.

Using equation 3.17, the components of the horizontal wind can be calculated. The radial velocities come from a Gaussian fit to a 3Z1T base unit spectrum. Even though in some cases the widths from 3Z1T are unreliable, the velocities are acceptable and can then be averaged if necessary to obtain a suitable velocity sample. The averaging becomes necessary because the vertical and off-vertical beam measurements are not only separated in space but in time also. Thus to get a horizontal velocity for a particular vertical beam sample, some manipulation of off-vertical beam radial velocity data must be carried out. If the vertical beam samples are 3Z1T, then the oblique beam sample before and after are used to give the radial velocity. If 3Z2T is the vertical beam base unit, then the 3Z1T sample taken between the two time samples is utilised to obtain the radial velocity. With these radial velocities, the horizontal wind vector is calculated and the magnitude of this vector, V is then used in equation 3.15.

The first step in the energy dissipation rate analysis is to ensure that the spectra do contain information on turbulence and are not made up entirely of contamination effects. This is done by plotting the measured spectral half-power half-width against the spectral half-power half-width that would result from beam broadening/narrowing alone. If all the data lie on or close to the line of slope 1 passing through (0,0), then no turbulence information is available. If this is not the case, and the spectral widths are *not* all due to contamination effects, the measured spectral width can be calculated via equation 3.6.

Graphs showing the above processing are now presented. The "Total horizontal velocity" is the magnitude of the horizontal velocity vector calculated from the three beams. The half-width, $f_{0.5BN}$, is the width due to instrumental effects like beam broadening/narrowing and must be removed from the measured width; $f_{0.5turb}$ is the result of that correction. The signal-to-noise ratio (S/N) in dB produced by the PROFILE routine for the vertical beam data are presented along with the vertical velocity (in ms^{-1}) for comparison.

The average and median values of corrected half width for each data set are summarised at the end of this section. As the method of converting these half widths to energy dissipation rates requires some qualification, this has been left to the next (Discussion) section.

11:00 – 11:20, 84.6 – 86.1 km data.

The scatter plots in figures 3.14 and 3.15 show that in general only a small component of the measured spectral width can be attributed to beam broadening. Thus turbulence information can be obtained. This information is summarised in figures 3.16 and 3.17. It can be seen that a clear oscillation in w, the vertical velocity, is present. There is a suggestion that spectral width attains a maximum as w is increasing however little can be inferred from the two cases here. A correlation between corrected spectral width and the signal-to-noise ratio is not obvious.

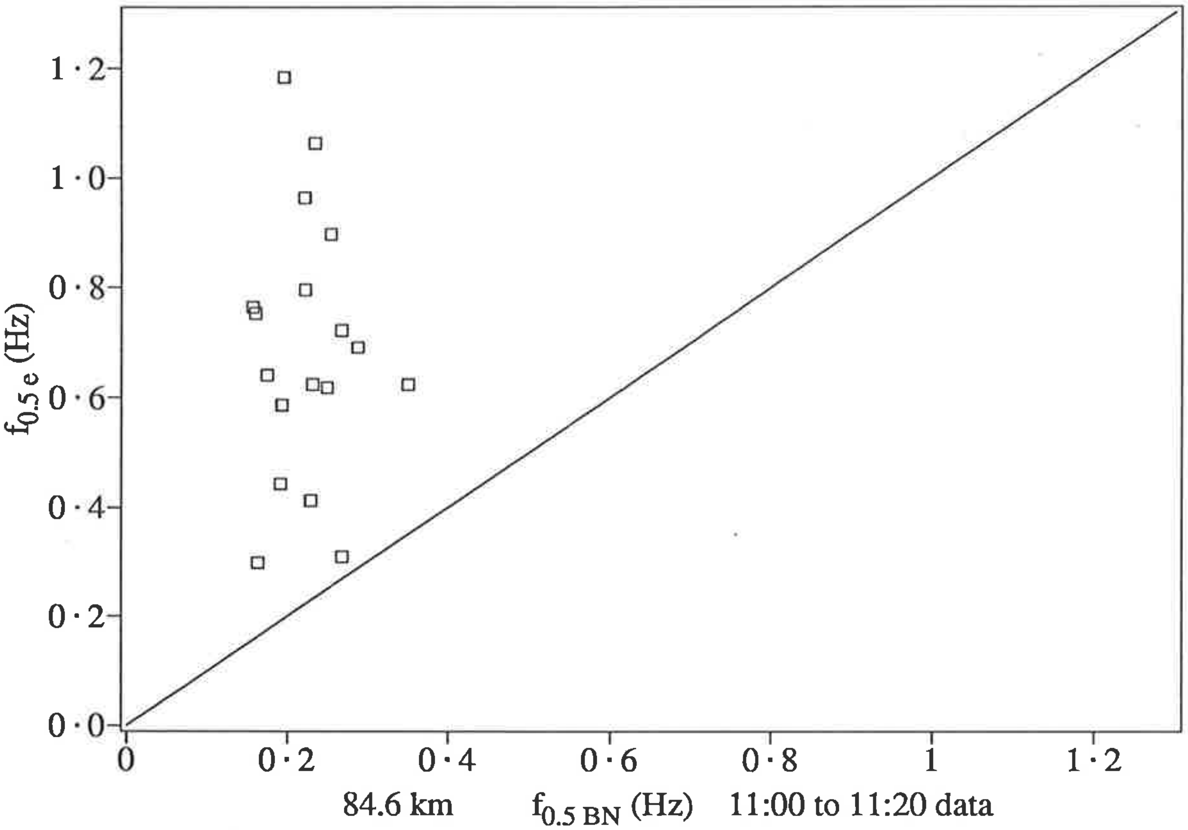

Figure 3.14: Scatter plot of measured spectral half-power half-width ($f_{0.5e}$) versus calculated half-power half-width due to beam broadening/narrowing ($f_{0.5BN}$), both in Hz for 11:00 to 11:20, baseheight 84.6 km data.

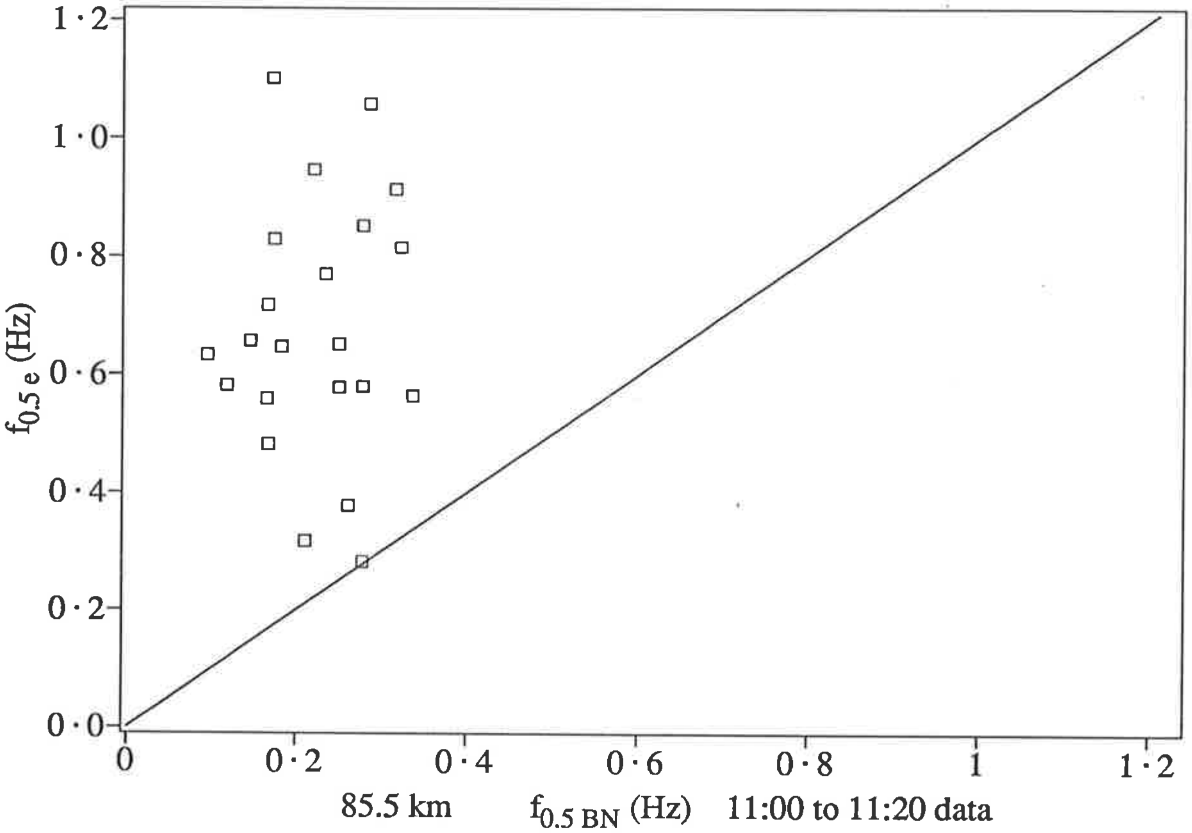

Figure 3.15: Scatter plot of measured spectral half-power half-width ($f_{0.5e}$) versus calculated half-power half-width due to beam broadening/narrowing ($f_{0.5BN}$), both in Hz for 11:00 to 11:20, baseheight 85.5 km data.

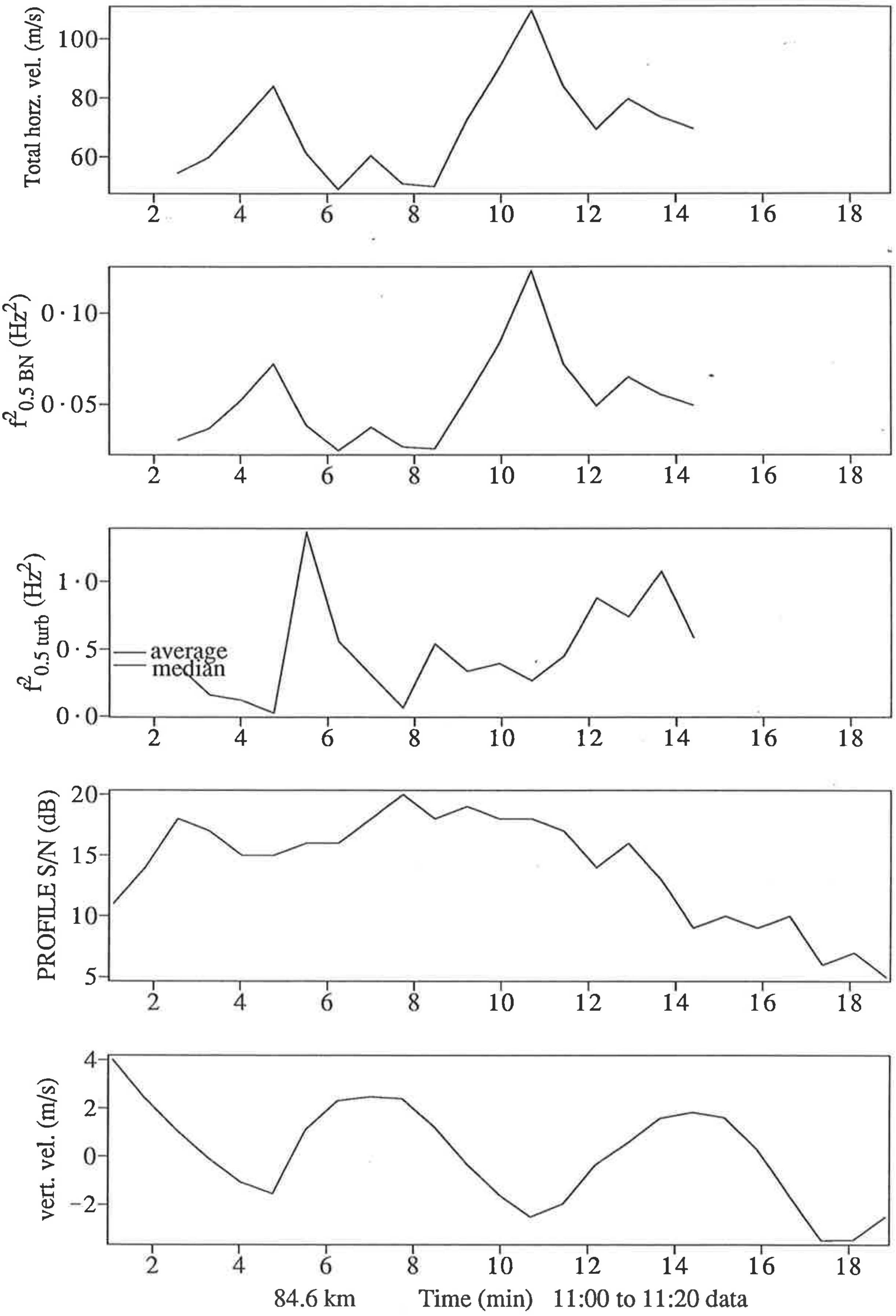

Figure 3.16: Spectral half-power half-widths and associated information for the 11:00 to 11:20, baseheight 84.6 km data. See text for details.

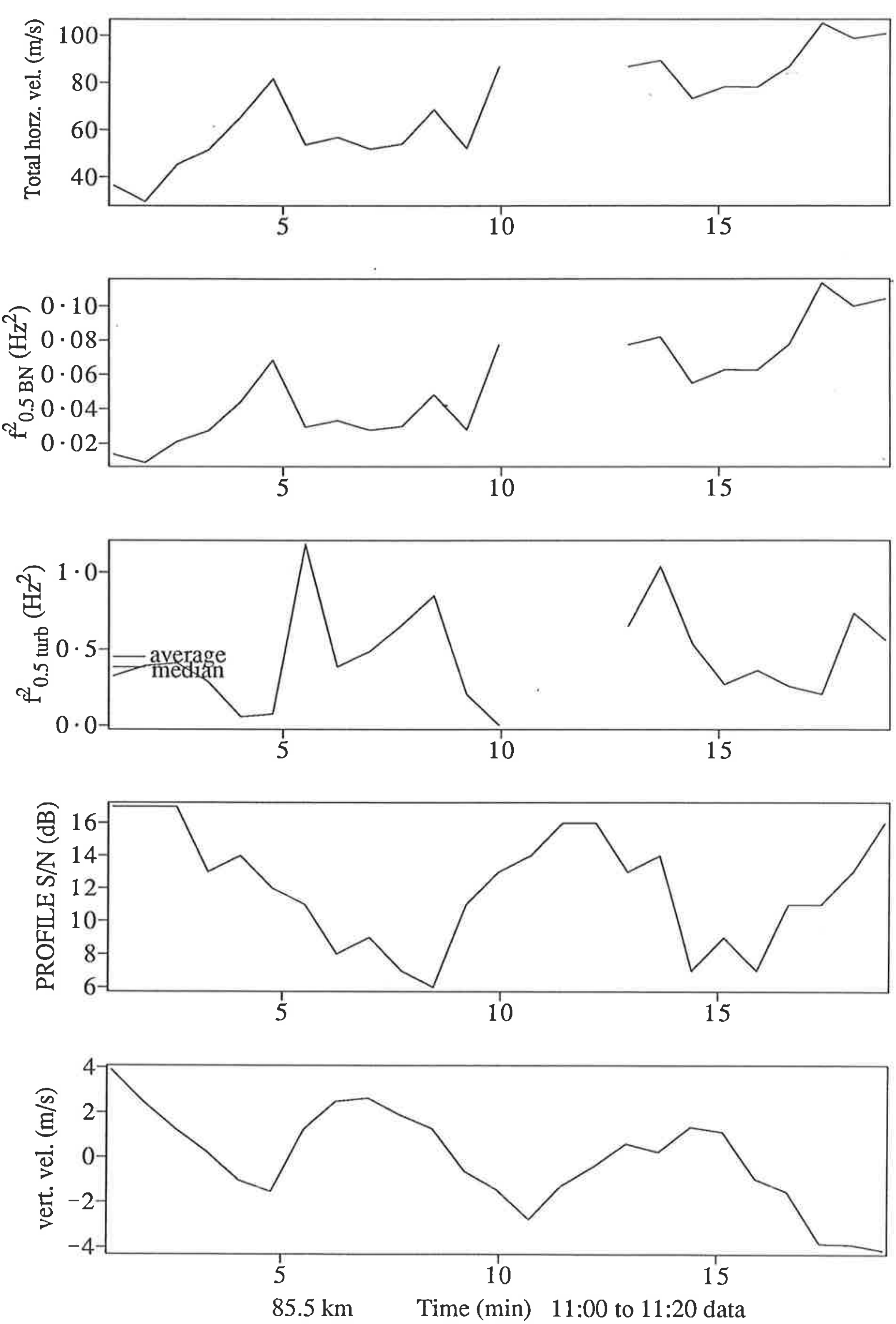

Figure 3.17: Spectral half-power half-widths and associated information for the 11:00 to 11:20, baseheight 85.5 km data. See text for details.

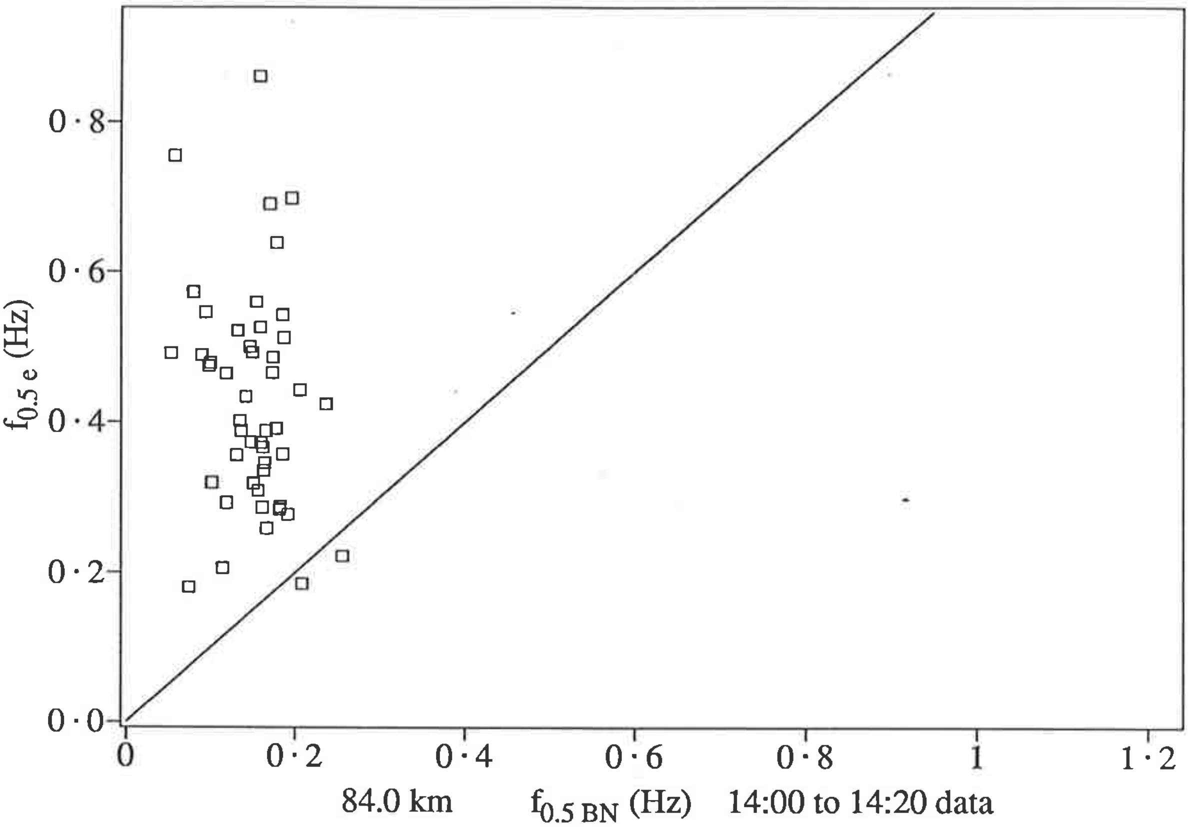

Figure 3.18: Scatter plot of measured spectral half-power half-width ($f_{0.5e}$) versus calculated half-power half-width due to beam broadening/narrowing ($f_{0.5BN}$), both in Hz for 14:00 to 14:20, baseheight 84.0 km data.

14:00 – 14:20, 84.0 – 85.5 km data.

The scatter plots in figures 3.18 and 3.19 allow further analysis by ruling out significant contamination. The oscillation in vertical velocity is less monochromatic than the previous case as shown in figures 3.20 and 3.21. The upper data range is a little intermittent due to the absence of spectra in *both* the vertical and off-vertical beams at various times. In either case, correlation between signal-to-noise ratio and corrected half-width is not obvious.

13:00 – 13:20, 84.3 – 84.9 km data.

Once again, figure 3.22 shows that turbulent effects dominate the spectra. The vertical velocity oscillates around a mean value by 0.5–1.0 ms^{-1} in an irregular fashion (figure 3.23). There is a slight suggestion that high signal-to-noise ratio is associated with narrow spectra.

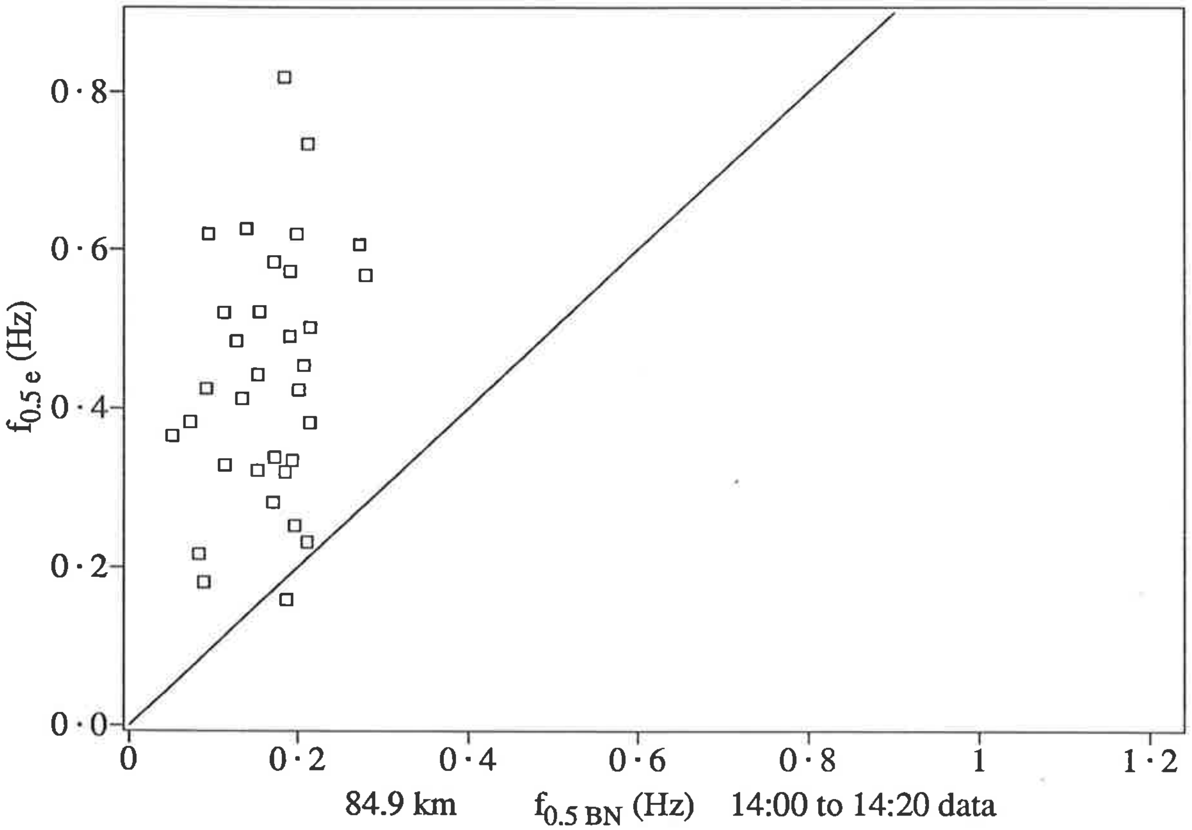

Figure 3.19: Scatter plot of measured spectral half-power half-width ($f_{0.5e}$) versus calculated half-power half-width due to beam broadening/narrowing ($f_{0.5BN}$), both in Hz for 14:00 to 14:20, baseheight 84.9 km data.

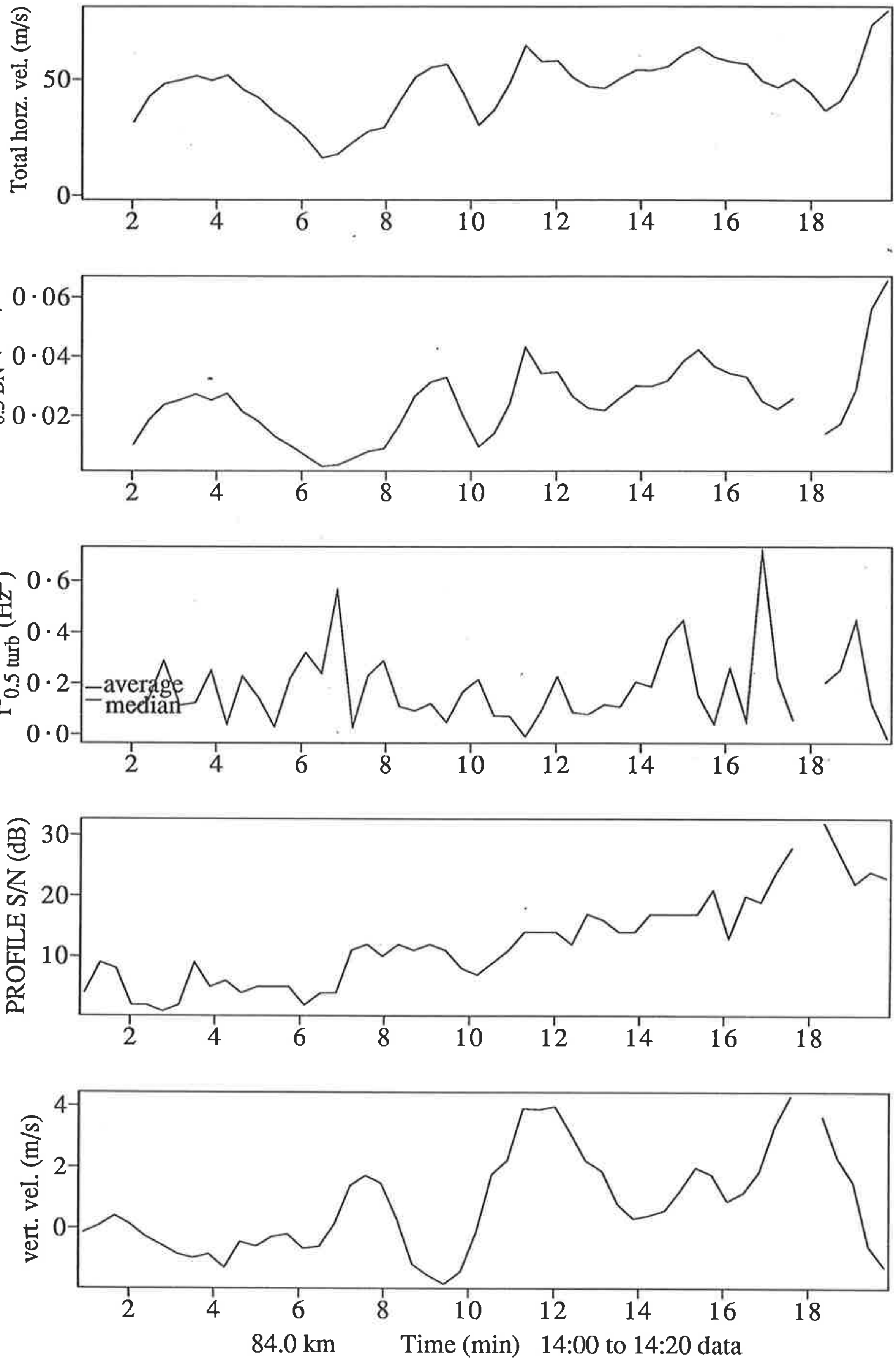

Figure 3.20: Spectral half-power half-widths and associated information for the 14:00 to 14:20, baseheight 84.0 km data. See text for details.

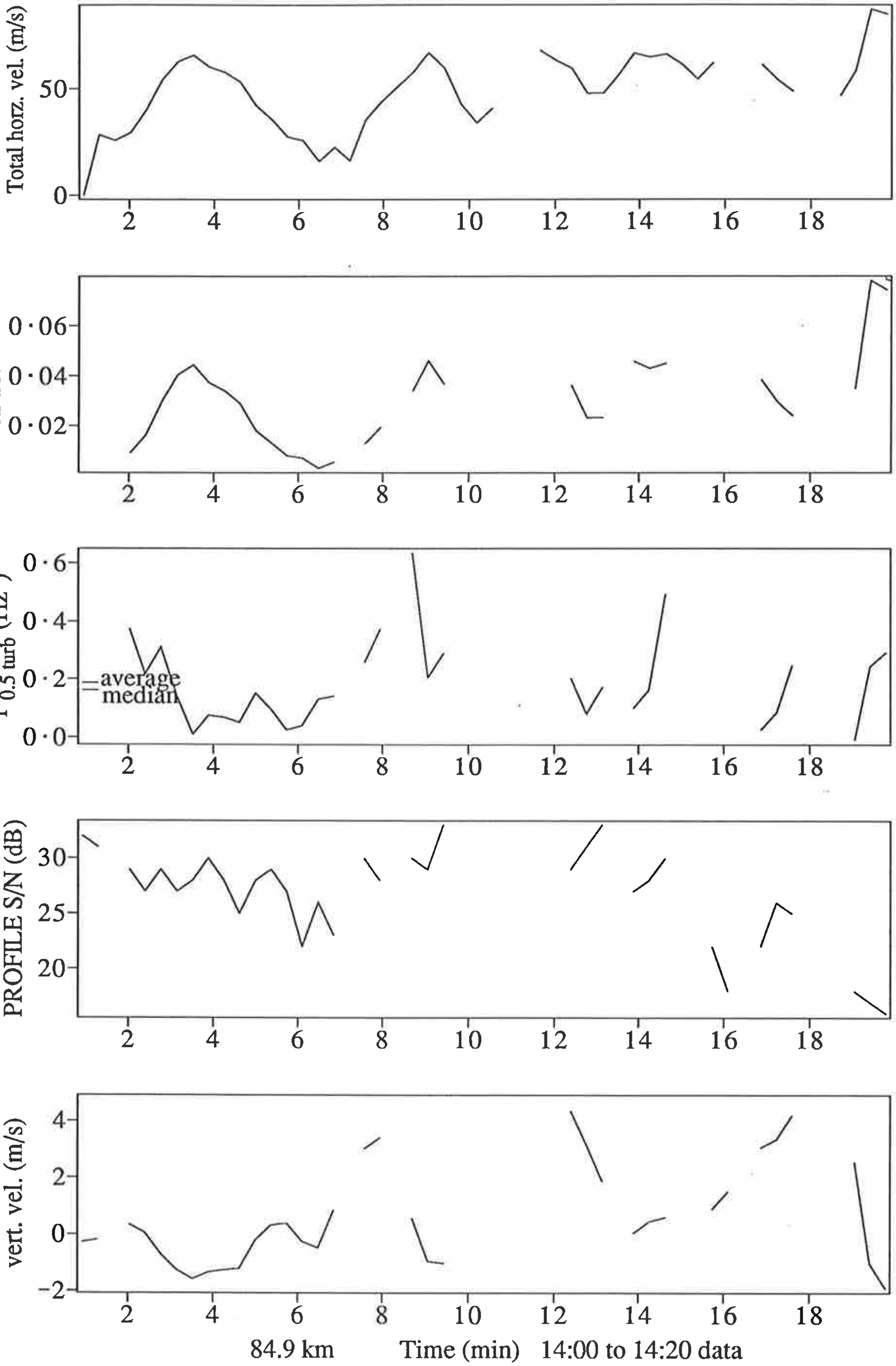

Figure 3.21: Spectral half-power half-widths and associated information for the 14:00 to 14:20, baseheight 84.9 km data. See text for details.

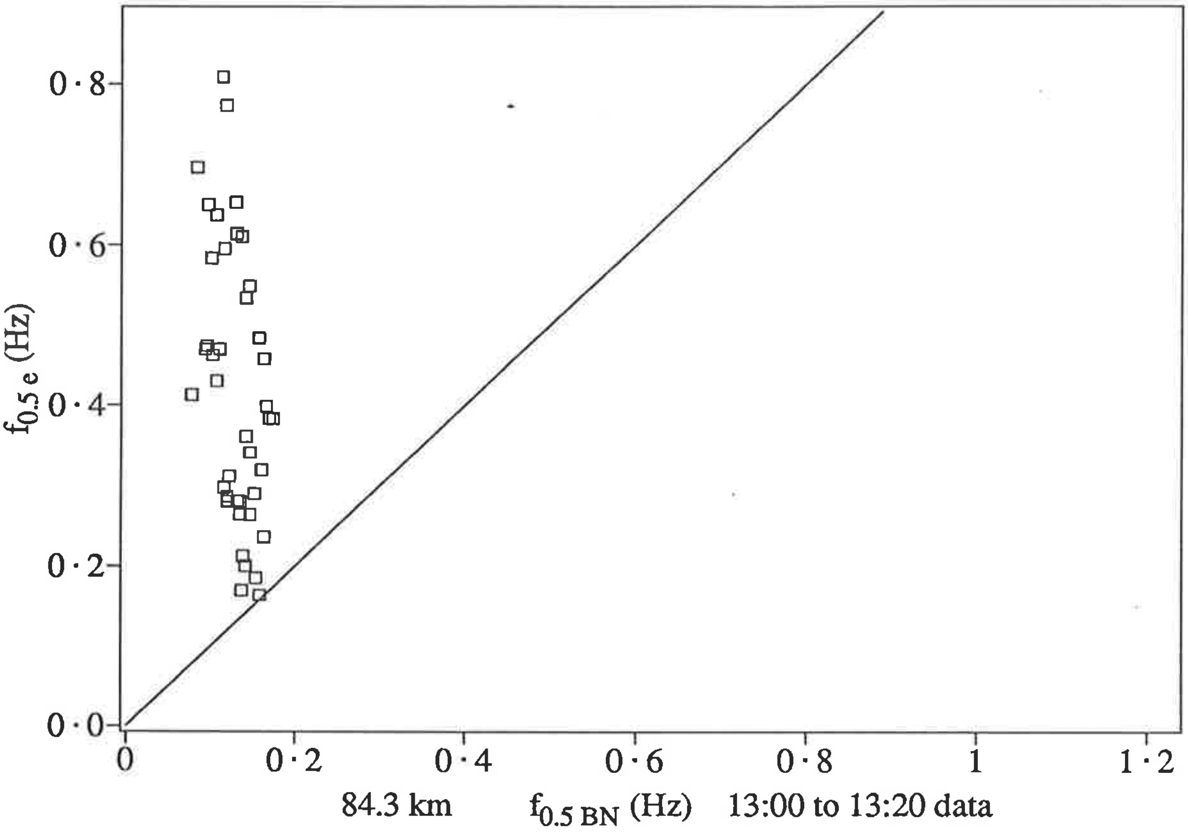

Figure 3.22: Scatter plot of measured spectral half-power half-width ($f_{0.5e}$) versus calculated half-power half-width due to beam broadening/narrowing ($f_{0.5BN}$), both in Hz for 13:00 to 13:20, baseheight 84.3 km data.

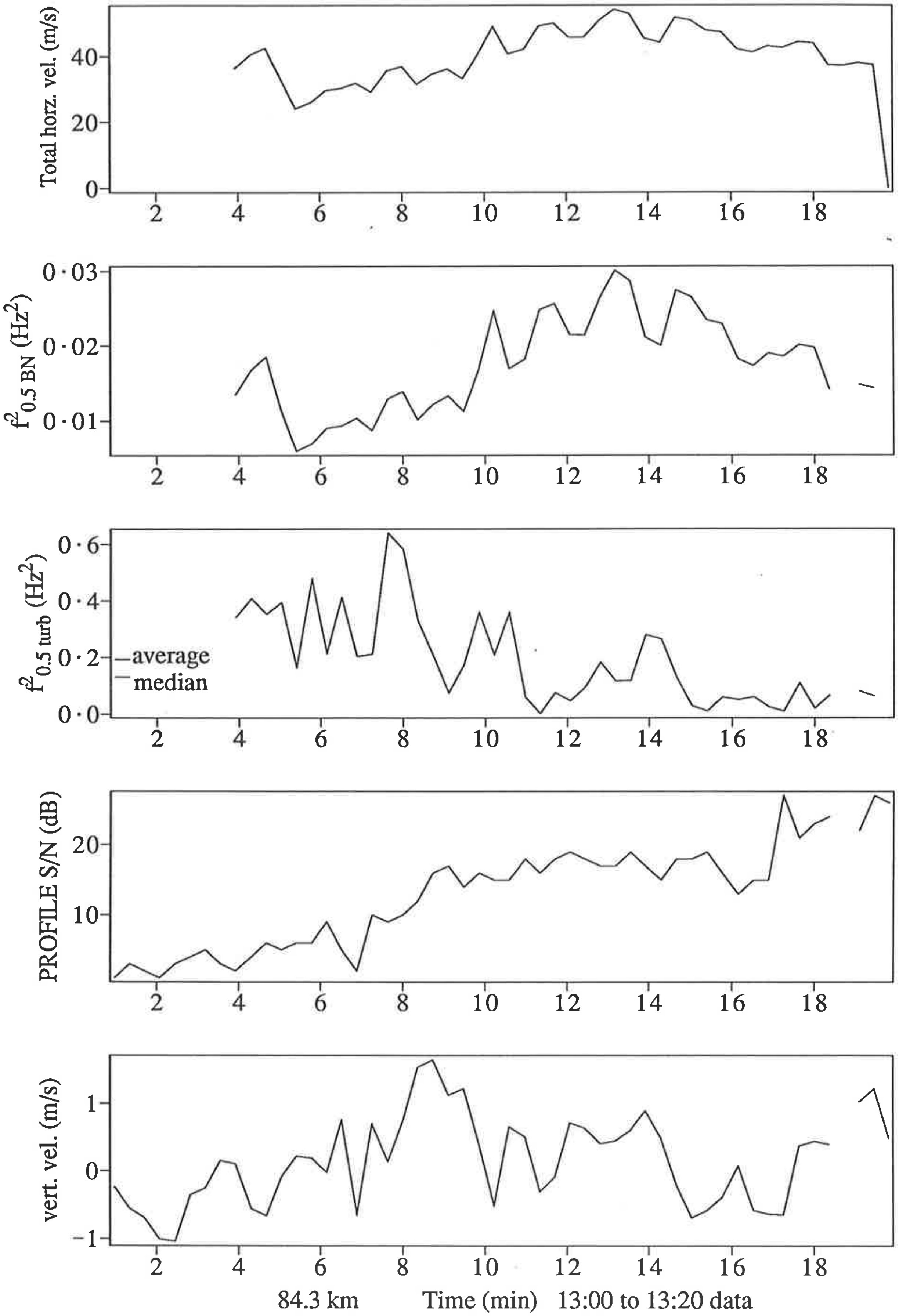

Figure 3.23: Spectral half-power half-widths and associated information for the 13:00 to 13:20, baseheight 84.3 km data. See text for details.

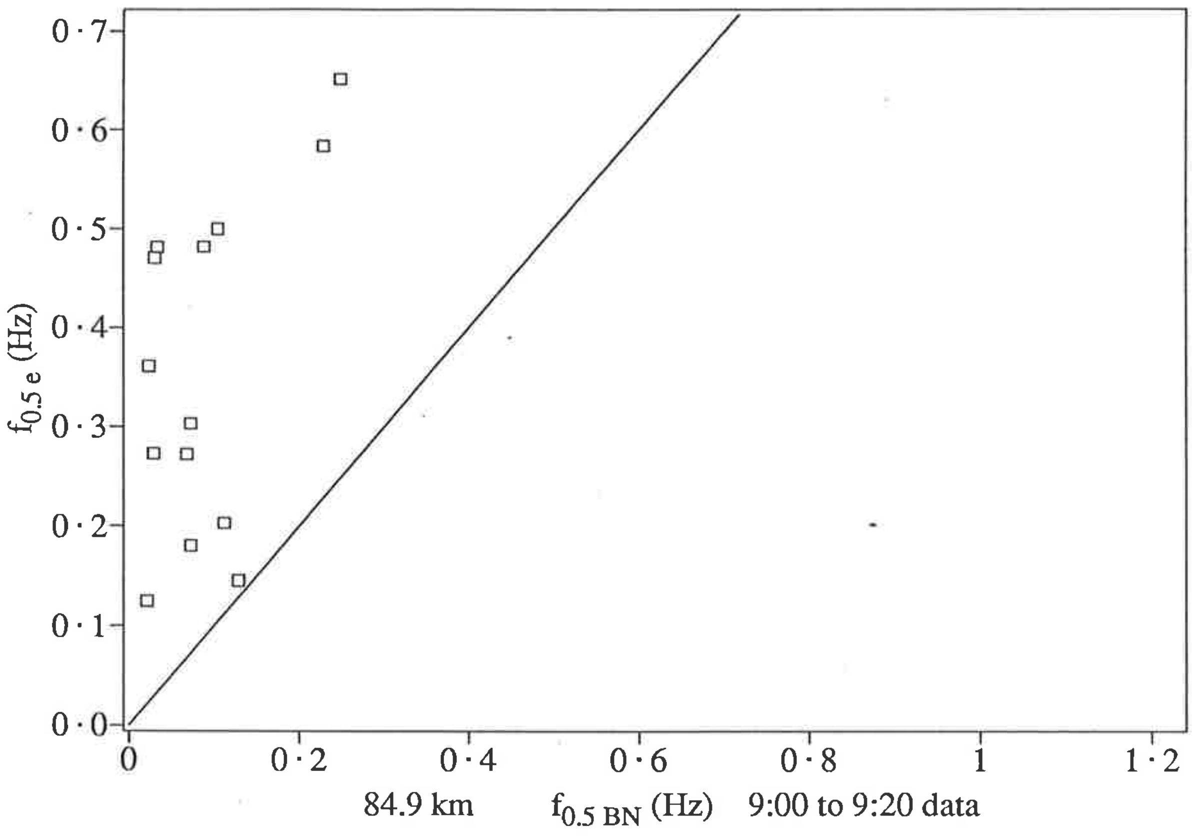

Figure 3.24: Scatter plot of measured spectral half-power half-width ($f_{0.5e}$) versus calculated half-power half-width due to beam broadening/narrowing ($f_{0.5BN}$), both in Hz for 9:00 to 9:20, baseheight 84.9 km data.

9:00 – 9:20, 84.9 – 86.7 km data.

The data shown in figures 3.24 and 3.25 suggest that turbulence information is obtainable. Both the time series in figures 3.26 and 3.27 have gaps due to chisquare rejection or the unavailability of horizontal wind data. The latter part of figure 3.27 however shows some quite large spectral width values.

8:30 – 8:50, 86.1 – 86.7 km data.

Figure 3.28 shows that beam broadening/narrowing dominates in a few points however turbulence information is still available. This data set (see figure 3.29) is characterised by a decrease in vertical velocity with some small-scale fluctuations around it. The corrected spectral half-width becomes large for two 3Z2T samples around 8:40.

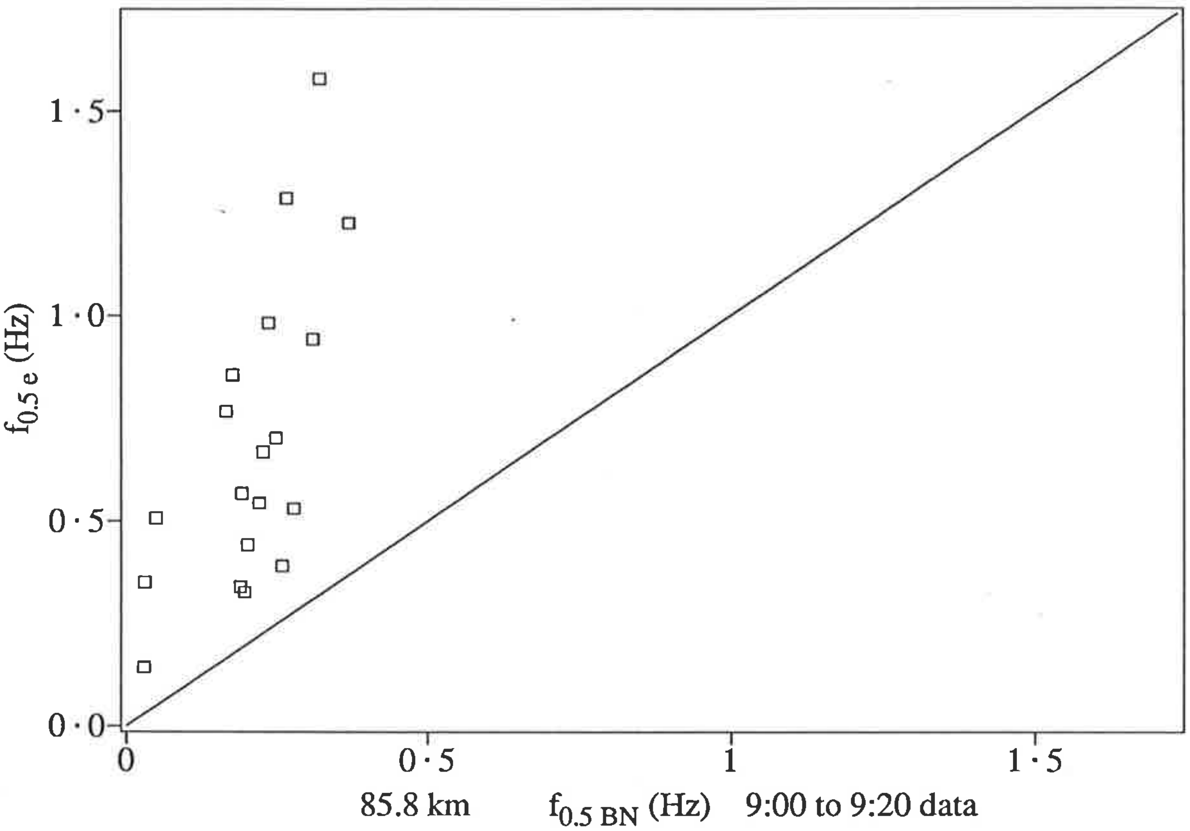

Figure 3.25: Scatter plot of measured spectral half-power half-width ($f_{0.5e}$) versus calculated half-power half-width due to beam broadening/narrowing ($f_{0.5BN}$), both in Hz for 9:00 to 9:20, baseheight 85.8 km data.

Summary of corrected half-widths squared			
Time	Baseheight	Mean (Hz^2)	Median (Hz^2)
11:00–11:20	84.6 km	0.476	0.380
	85.5 km	0.451	0.384
14:00–14:20	84.0 km	0.180	0.132
	84.9 km	0.188	0.163
13:00–13:20	84.3 km	0.193	0.132
9:00–9:20	84.9 km	0.143	0.087
	85.8 km	0.560	0.284
8:30–8:50	86.1 km	0.325	0.151

Table 3.4: Summary of the mean and median values of the corrected spectral half-width squared in Hz^2.

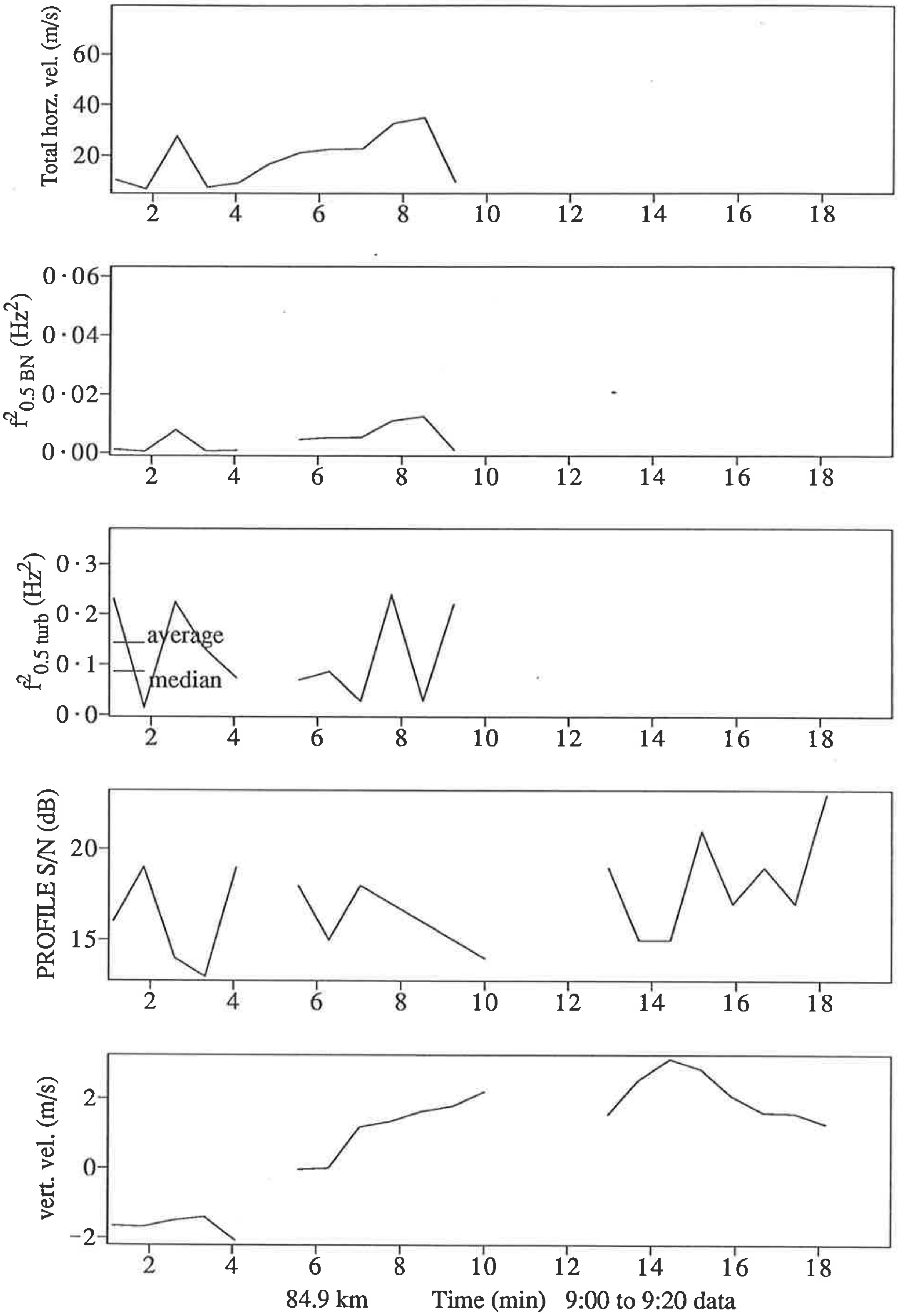

Figure 3.26: Spectral half-power half-widths and associated information for the 9:00 to 9:20, baseheight 84.9 km data. See text for details.

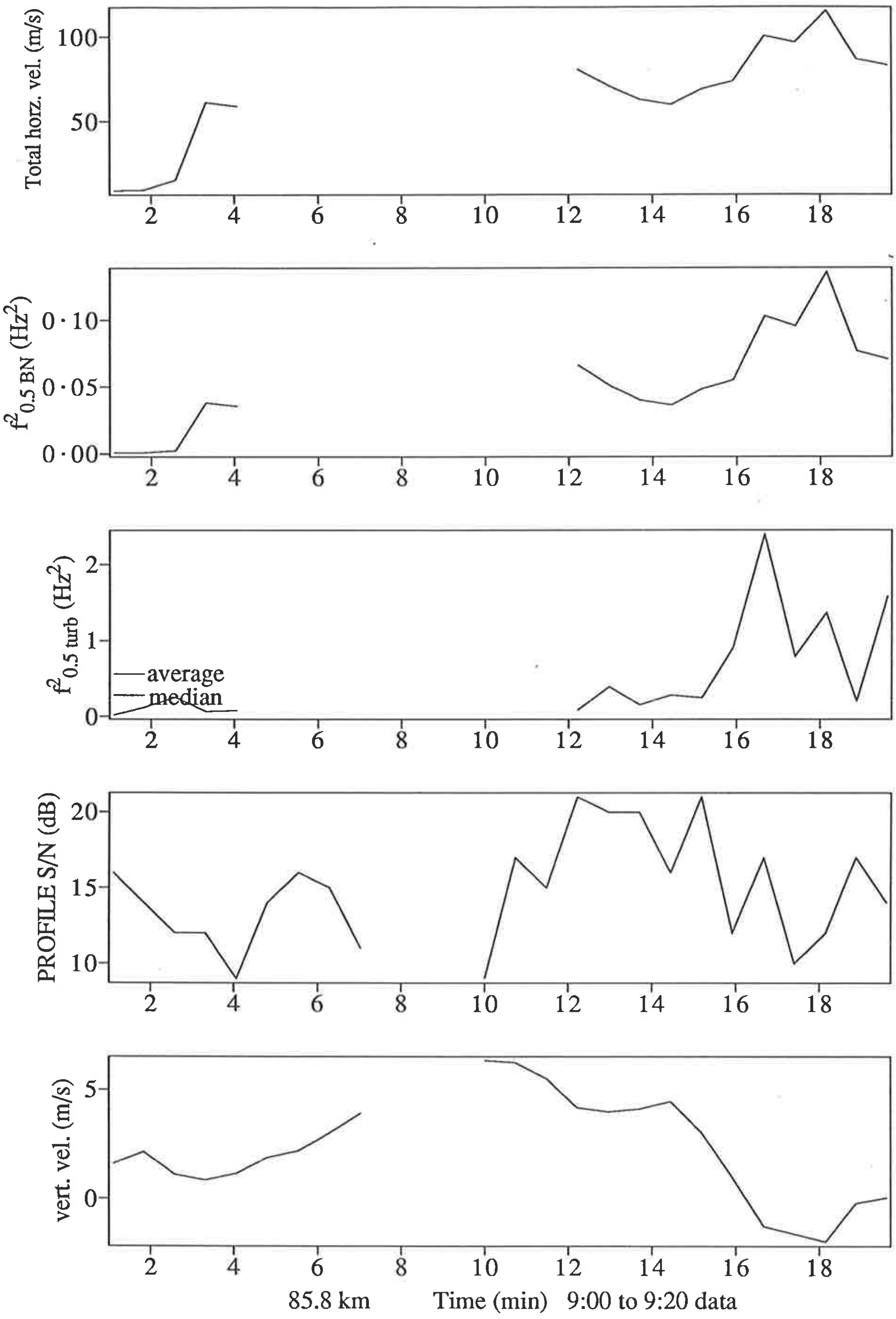

Figure 3.27: Spectral half-power half-widths and associated information for the 9:00 to 9:20, baseheight 85.8 km data. See text for details.

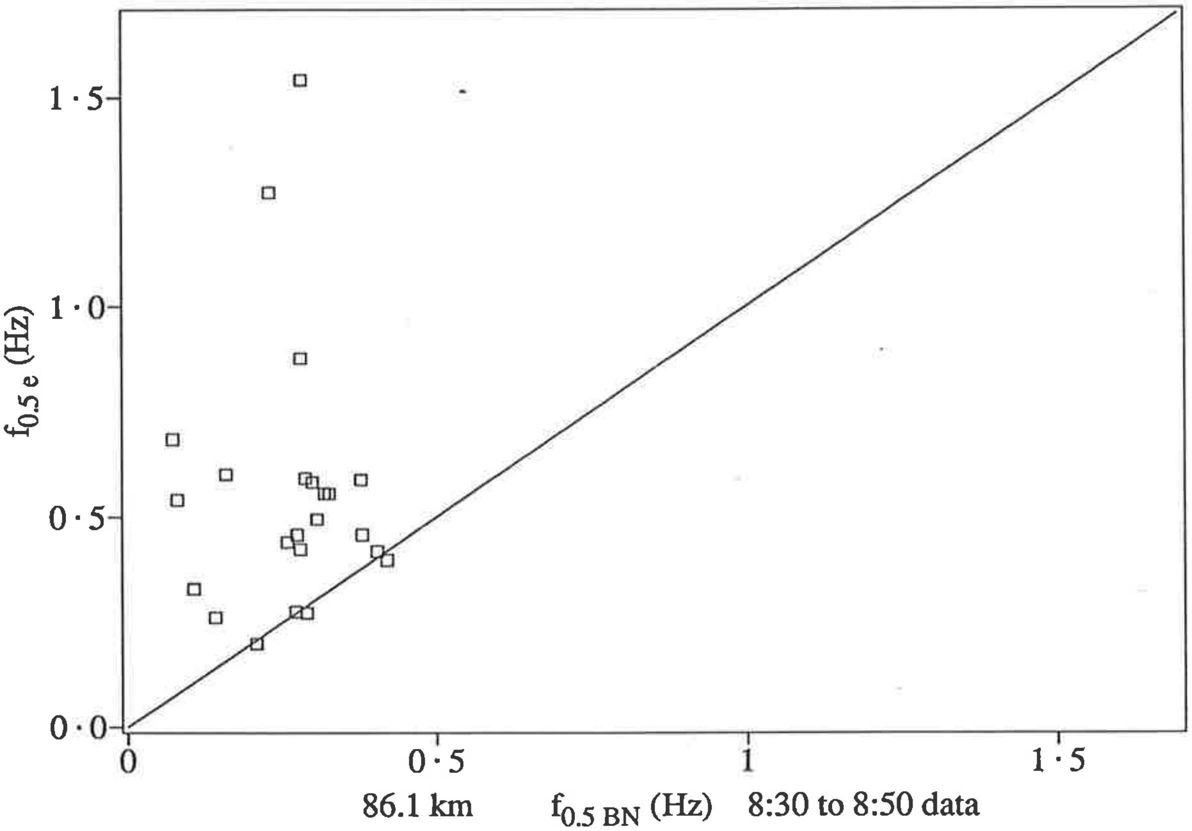

Figure 3.28: Scatter plot of measured spectral half-power half-width ($f_{0.5e}$) versus calculated half-power half-width due to beam broadening/narrowing ($f_{0.5BN}$), both in Hz for 8:30 to 8:50, baseheight 86.1 km data.

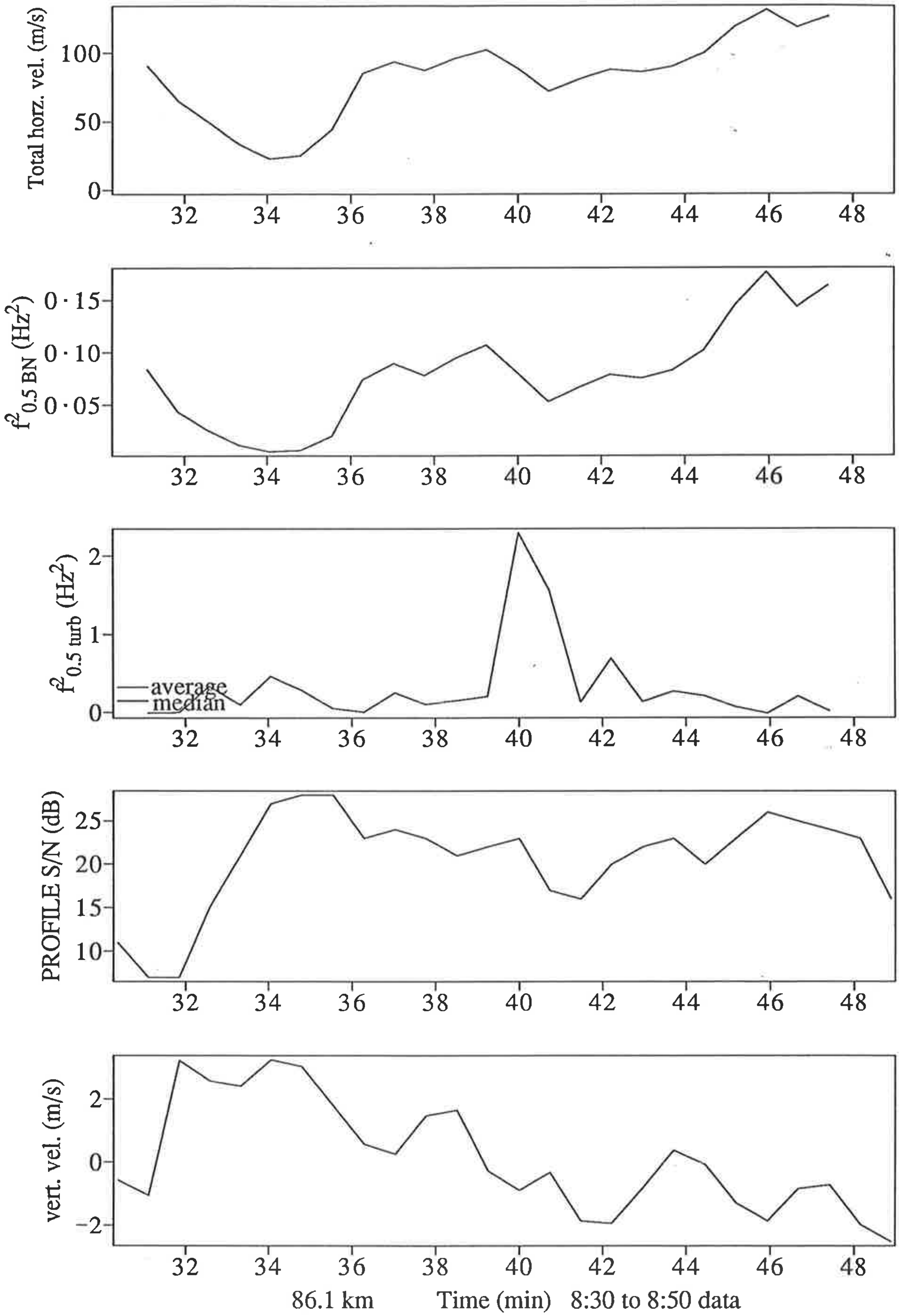

Figure 3.29: Spectral half-power half-widths and associated information for the 8:30 to 8:50, baseheight 86.1 km data. See text for details.

3.3 Discussion

The first two data sets presented in the previous section, i.e. those for 11:00–11:20 and 14:00–14:20, show moderate amplitude oscillations in vertical velocity which are assumed to be due to gravity waves. Using the ratio Y_i (see equation 3.5) it is shown that contamination of the spectral widths due to gravity waves occurred at sampling times of 165 and 55 s. respectively. The other data sets, however, were not affected for sampling times up to 200 s. Thus gravity wave contamination of spectral width measurements can occur. The equation derived by Hocking(1988) (equation 3.13) was shown to give a good estimate of this contamination for monochromatic waves and could be used to make an approximate correction to spectral-width estimates *if the period and amplitude were known.* However if the instrument is able to resolve the period, it is unlikely that this contamination will be a serious problem. This experiment has shown that VHF radars can be used to obtain uncontaminated data; however MF radars, with their longer fading times and resultant longer sampling times, could be seriously affected.

Hocking(1988) carried out a statistical study of gravity-wave contamination in data obtained using the Buckland Park HF/MF radar. By changing the sampling time between 102 s and 205 s, Hocking was able to confirm the presence of gravity wave contamination in spectral-width measurements. To correct the energy dissipation rate measurements however, all that could be done was to assume that 5 min was the dominant contaminating period.

The spectral widths, corrected for gravity-wave contamination, can be used to obtain the energy dissipation rate (ε) and methods for doing this (as outlined previously) require a knowledge of the relationship between the spectral width and ε. As the constants that should be used are subject to some debate, these calculations will be avoided in the discussion of the character of the time variations of spectral widths (and thus ε) that is to follow. These time variations are shown in figures 3.16, 3.17, 3.20, 3.21, 3.23, 3.26, 3.27 and 3.29.

The possibility of a correlation between the phase of a gravity wave and ε is considered first. The 11:00 to 11:20 data set (figures 3.16 and 3.17) contains the most well behaved oscillation and it is assumed to be due to a gravity wave with a ground based period of around 300 s. (The Brunt-Väisälä period in that region is of the order of 265 s (Groves 1987).) An oscillation in the total horizontal velocity vector is seen to be in antiphase with that in the vertical velocity. Although this could feed back into the corrected spectral widths via the beam broadening/narrowing term, this does not seem to be occurring here. The data for the 84.6 km baseheight (figure 3.16) and the 85.5 km baseheight (figure 3.17) both suggest a peak in ε toward the end of the increasing vertical velocity segment of the wave.

A similar suggestion can be seen in the 14:00 to 14:20 data at the baseheight of 84.0 km (figure 3.20) although both the gravity wave and this effect are less clear. Of the 3 peaks in vertical velocity, the first (at around 14:07) and the last (near 14:17) seem to have preceding peaks in ε; however, the peak in w at 14:11 does not.

The peaks in ε for the baseheights 84.6 km and 85.5 km in the 11:00 to 11:20 data occur at the same time. This coherence is not displayed in the signal-to-noise ratio (SNR) data however. In fact the character of the time variations of SNR is quite different to that of the variations of spectral width, both in the 11:00–11:20 data, and the other data sets.

Contour plots of SNR are often used to indicate the presence of turbulence, however, the lack of correlation between SNR and spectral width seen here suggests that some care should be taken in the interpretation of SNR data. It is safe to assume that noise is essentially constant. Galactic noise is the major noise source at 50 MHz. If the beam being considered does not transit a radio star, short term variations in the noise will not be a problem. At Poker Flat, this transit would take less than 2 min and the data do not show signs that this is occurring. The potential refractive index structure constant, C_n^2, is proportional to returned power (the signal) for a single radar system at a fixed height. However the relationship between C_n^2 and ε is a complex one, viz:

$$\varepsilon = [\frac{C_n^2 \omega_B^2}{a^2 \alpha' c_2 M_n^2}]^{3/2} \tag{3.18}$$

(from the previous chapter) and many of the parameters in this expression are not constant. The most important in this case is probably M_n, the potential refractive index gradient,

$$M_n = \frac{\partial n}{\partial N}[N\frac{\omega_B^2}{g} - \frac{dN}{dz} + \frac{N}{\rho}\frac{d\rho}{dz}] \tag{3.19}$$

where n is the refractive index, N is the electron density, ρ is the density at height z, ω_B is the Brunt-Väisälä frequency and g is the acceleration due to gravity. The echoes considered here are thought to result from auroral particle precipitation; thus the form of dN/dz and $N(z)$, and hence the form of M_n, cannot be considered constant.

It is also worth noting that the spectral width method of measuring ε includes information from all scales in the range $\lambda/2$ (the Bragg scale) to L_B the inner scale of the bouyancy range. Bragg scale structures, acting as tracers, are advected around by larger eddies. The power method, however, relies on *the presence of* Bragg scale turbulence structures or in fact any structure of that scale. It has recently been suggested by Klostermeyer (1988) that parametric instabilities may be enhancing small-scale structure. If this is so, the power method will be affected by non-turbulent contributions.

Hoppe *et al.* (in preparation) conducted an experiment in which VHF and incoherent scatter radar techniques were used to study the summer polar mesosphere. As part of this, the mobile SOUSY VHF 53.5 MHz. radar (Czechowsky *et al.* 1984, Schmidt *et al.* 1979) was operated on the island of Andøya, Norway. In data obtained during June 1987, Hoppe *et al.* found cases of a correlation between vertical velocities and SNR as well as spectral width and SNR. They admit, however, that many cases exist that *do not* correlate well.

Røyrvik and Smith (1984), using the 50 MHz VHF radar situated at Jicamarca near the equator (11.95° S,76.87° W) looked for correlations between returned signal power (S) and the signal correlation time (C), which is inversely proportional to the spectral width. Their results varied as a function of height with a strong positive correlation between S and C below 75 km (negative correlation between power and spectral width) and a negative S/C correlation above 75 km (correlation between power and spectral width). These observations should be treated with caution however as the mechanisms causing the echoes in the summer polar mesosphere are thought to be quite different to those operating elsewhere.

Empirical calculations of the energy dissipation rate, ε, from the spectral width were carried out using the equation

$$\varepsilon = \mathcal{K}\overline{v^2}f_B \tag{3.20}$$

(see previous chapter) where f_B is the Brunt-Väisälä frequency in Hz, $\mathcal{K} = 3.1$ and $\overline{v^2}$ is the RMS vertical velocity. This is related to spectral width by $\overline{v^2} = f_T^2/2\ln 2$ where f_T is the spectral width due to turbulence only measured in ms^{-1}. As stated previously, the constant $\mathcal{K}$ is subject to some debate. Weinstock (1981) suggests $\mathcal{K} = 2.5$ whereas calculations by Hocking refining the Hocking (1983a) value of $\mathcal{K} = 2.8$ have resulted in the value used here of $\mathcal{K} = 3.1$ (Hocking 1988). These variations in the $\mathcal{K}$ value used need to be kept in mind when comparisons of ε values obtained by other authors are made.

Measured values of f_B at the time of the experiment were unavailable so model values had to be used. These were obtained from Groves (1987). As the date of the experiment was August the 1st. and the model supplied monthly values, those for July and August for 65° N were averaged together. Some interpolation was carried out to obtain a value for the centre of each height block (approximately); however in the light of the uncertainty in $\mathcal{K}$, this was probably overkill. All values were close to 0.0237 rad s¯1 or 0.00377 Hz.

The values of ε obtained from the median spectral widths are summarised in figure 3.30. In cases where it is warranted (i.e. those where there is a suitable amount of data), the time variation of ε is plotted in figure 3.31. The median of ε ranged from 0.007 Wkg^{-1} to 0.029 Wkg^{-1} (figure 3.30) however energy dissipation rates in excess of 0.15 Wkg^{-1} occur in figure 3.31.

As part of the STATE experiment, Watkins *et al.* (1988) calculated energy dissipation rates using the Poker Flat radar. The experiment was carried out in June 1983, at which time the radar was operated in a different configuration to that described previously in that the vertical beam width was 2.2°. The average ε calculated by Watkins *et al.*, using a $\mathcal{K}$ of 2.8 are larger but not inconsistent with the values presented here. The typical

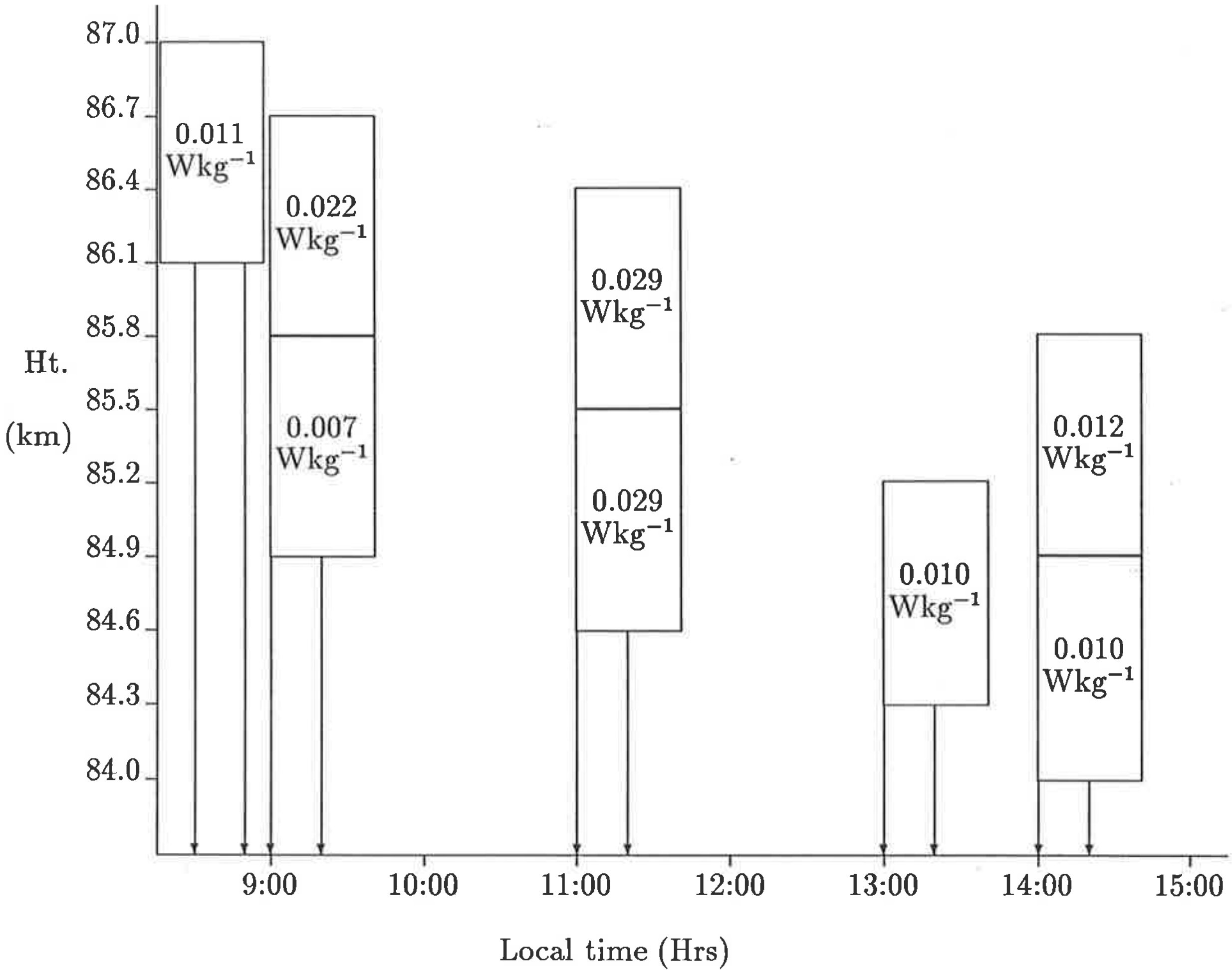

Figure 3.30: Summary of median energy dissipation rate values (ε)

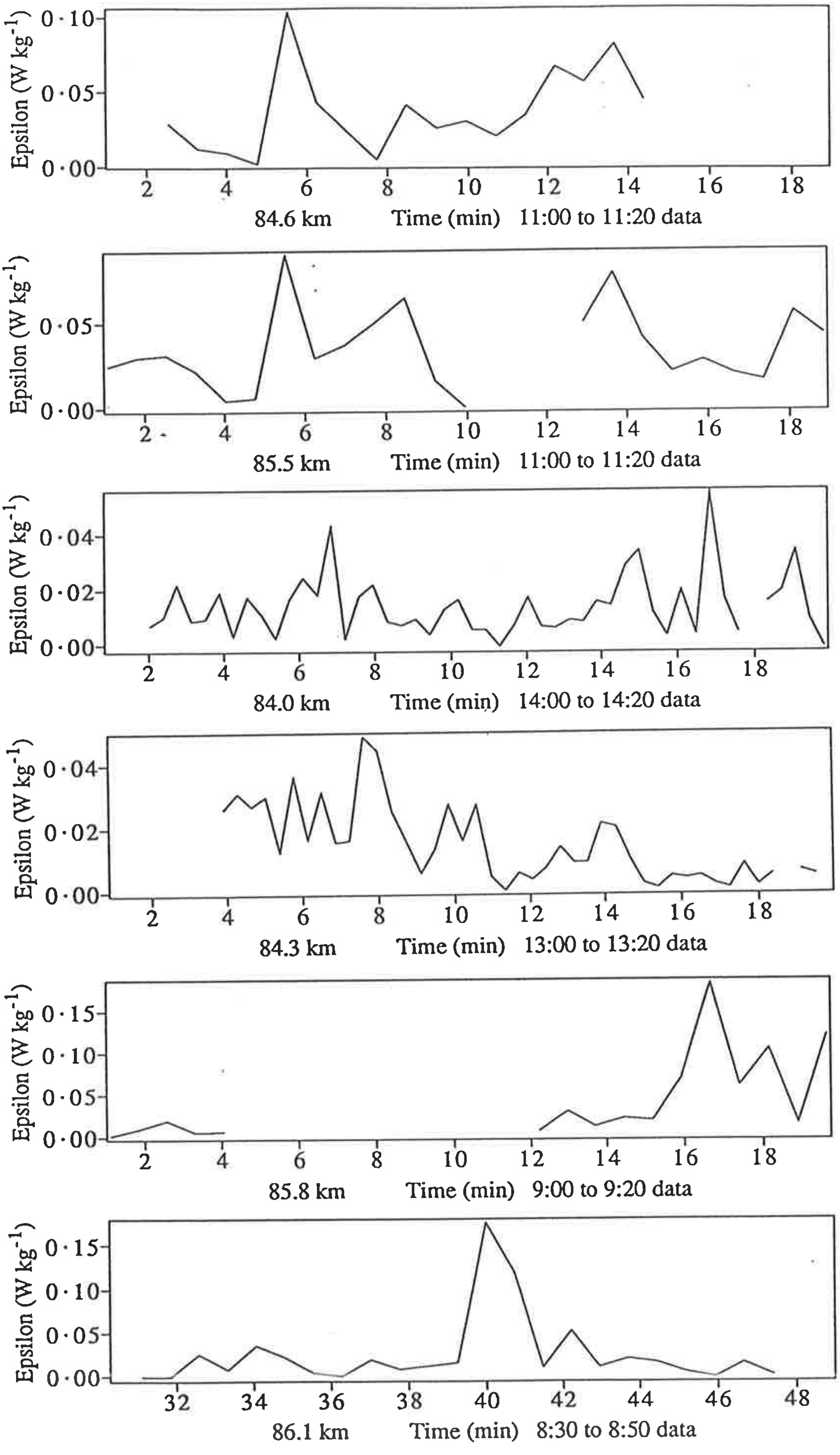

Figure 3.31: Energy dissipation rates (ε) as a function of time.

maximum values they found however are some 5–10 times greater than these values and are much larger than all the maxima seen in figure 3.31. The Watkins *et al.* (1988) work included correction for beam broadening and narrowing, but used a data aquisition time of 1 min. As was shown in figure 3.9, this could result in gravity wave contamination and may explain the larger ε values. A further consideration will be discussed shortly.

Røyrvik and Smith (1984) used the Jicamarca 50 MHz VHF radar to calculate ε in the equatorial mesosphere during February 1983 and obtained a value of 0.05 $\mathrm{Wkg^{-1}}$. Because of the difference in latitude and season, it is possible that this value should not be compared to those presented previously. Additionally, Røyrvik and Smith did not apply any correction for beam broadening/narrowing and, as they used an oblique beam, had to adjust for horizontal velocity contamination. Thus this value is cast into some doubt.

Hocking (1988) presented a two year study of ε using the Buckland Park HF/MF system (138.5° E, 35° S). In that study, Hocking showed that the long data aquisition time was causing contamination. The ε values obtained after some correction for this are of the same order or larger than those found here. However, as before, the difference in latitude may make comparison of the two inappropriate. It should be noted that in Watkins *et al.* (1988) and Røyrvik and Smith (1984), spike rejection and Gaussian fitting were not used. If spikes are present in the spectra, this will generally act to decrease the width value obtained. Accepting non-Gaussian spectra will probably be a greater problem though. If a gravity wave half-cycle is sampled by the radar, a spectrum that is a convolution of the turbulence spectrum with that shown in figure 3.5 will result. If the gravity wave has an amplitude of a few metres per second, a spectrum much wider than that due to turbulence alone would result, and without the restriction of a Gaussian fit will be interpreted as due to turbulence alone. These gravity waves are seen to exist (eg. the 14:00–14:20 data) above Poker Flat and could explain the large values of ε found on occasions by Watkins *et al.* (1988).

As a final comparison, Thrane (1985) used rocket measurements to obtain ε in the mesosphere over Norway in November 1980. The mean ε values presented there are in general agreement with the median values of figure 3.30.

3.4 Summary

In this chapter, an experimental study of the effect of gravity waves on the width of the Doppler spectrum was carried out. The data were obtained using the Poker Flat 50 MHz VHF radar. A parameter Y_i was used to describe the difference in the width of spectra sampled over a long period of time (τ_i) and that taken over a shorter time (τ_0). If Y_i is not significantly different to 1.0, no contamination is present. Non-unity values of Y_i were seen to exist in some cases where a gravity wave was present. The experimental data considered here were of a time resolution that allowed the period and amplitude of the contaminating gravity wave to be determined. A theoretical expression for gravity wave contamination proposed by Hocking (1988) was then tested and found to agree with measurements.

Having shown that the data blocks and sampling times selected were not contaminated by gravity waves, it was possible to use the spectral-width measurements to obtain the turbulent energy dissipation rates for these blocks. The time variation of spectral width was considered first and found to show a correlation with vertical velocity in the case of an almost monochromatic gravity wave. The peak in spectral width occurred as the vertical velocity approached its maximum upward amplitude. This effect was less clear for the case where the gravity wave was less monochromatic.

Median spectral width values were used to calculate energy dissipation rates and these values were seen to agree with values obtained by other workers. There was some discrepancy between typical maximum values found here and those calculated by others; however, these differences can be explained on the basis of the differences between the methods.

Chapter 4

Buckland Park

Equipment and basic analysis

The data considered in the remaining chapters of this thesis were obtained using the Buckland Park MF/HF (1.98/5.94MHz) radar. The antenna array was constructed between 1964 and 1967 and is situated approximately 40 km north of Adelaide at 35° 38′S, 138° 29′E. The name comes from the Buckland Park sheep station that is situated nearby and which once covered the area of the field site. The results presented in this thesis were obtained using only the 1.98 MHz mode of operation, so the 5.94 MHz mode will not be considered in this chapter. A 50 MHz ST radar has been constructed next to the MF/HF array. A plan of the Buckland Park site is presented in figure 4.1.

Although the Buckland Park radar system is unique, radars are in common use around the world. Their application, which was born of a desire to detect aircraft, has extended into many fields. Weather radars form a significant fraction of radar usage, and a considerable amount of radar expertise has resulted from their use. (For a review of weather radar methods, the reader is referred Doviak and Zrnić 1984.) Radar remote-sensing of the atmosphere and ionosphere has been able to draw on this knowledge as well as contribute new methods to it. For example, the technique used to obtain the first moment of a power spectrum that is described later in this chapter was developed by ionospheric investigators (Woodman and Hagfors 1969).

In this chapter, some details of the Buckland Park system and the analysis methods used on data obtained there are presented. The aim is to provide the reader, who already has some knowledge of radar techniques, with the information necessary to appreciate the limitations and advantages of the Buckland Park system that are pertinent to the work presented in the remainder of this thesis.

4.1 Transmission

The position of the transmitting array is given in figure 4.1. It consists of four folded dipoles arranged as shown in figure 4.2. The separation between the parallel dipoles is around 75 m giving a beam-width of approximately 40° half-width half-maximum. The dipoles are suspended at a height of 30 m. The configuration shown in figure 4.2 allows transmission of both right and left-hand circularly-polarised waves as well as enhancing, to some extent, the transmitted power that is directed vertically.

Switching between circular polarisations improves echo strength at various times of the day. During the daylight hours, E (or X) mode (left-hand circularly polarised in the southern hemisphere when looking from the source) is strongly absorbed before reaching 80 km; however, echo powers are enhanced by using E mode at night. O mode (right-hand circularly polarised) is used during the daylight hours.

The transmitter operates in a pulsed mode with a typical pulse repetition frequency of 20 Hz. Each pulse is a 1.98 MHz sine wave modulated by a Gaussian envelope. The half-width of this envelope is typically 25 μs. The transmitter peak power varies with condition of the valves, but is typically around 25 kW.

4.2 Reception

Returned echoes are received via a circular filled array with a diameter of 1 km . Its layout is shown in figure 4.1 (after Briggs *et al.* 1969). The array consists of two independent sets of 89 half-wave dipoles, one set aligned 4° off north-south, the other aligned 4° off east-west. The dipoles are 72 m in length and are strung from wooden poles at a height of 11 m. Each is connected to the patch board in the main hut by a

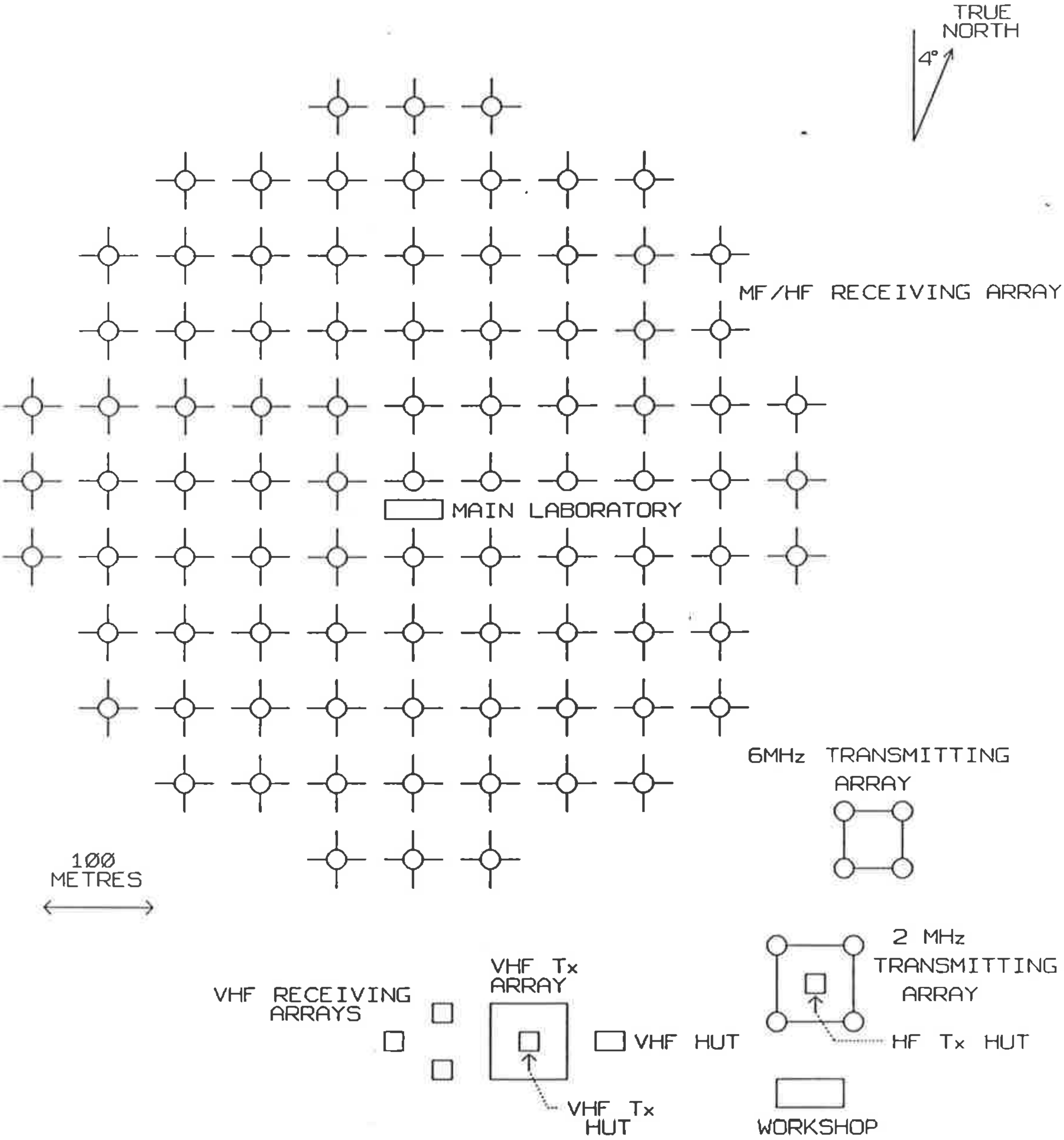

Figure 4.1: A ground plan of the Buckland Park site (after Briggs *et al.* 1969).

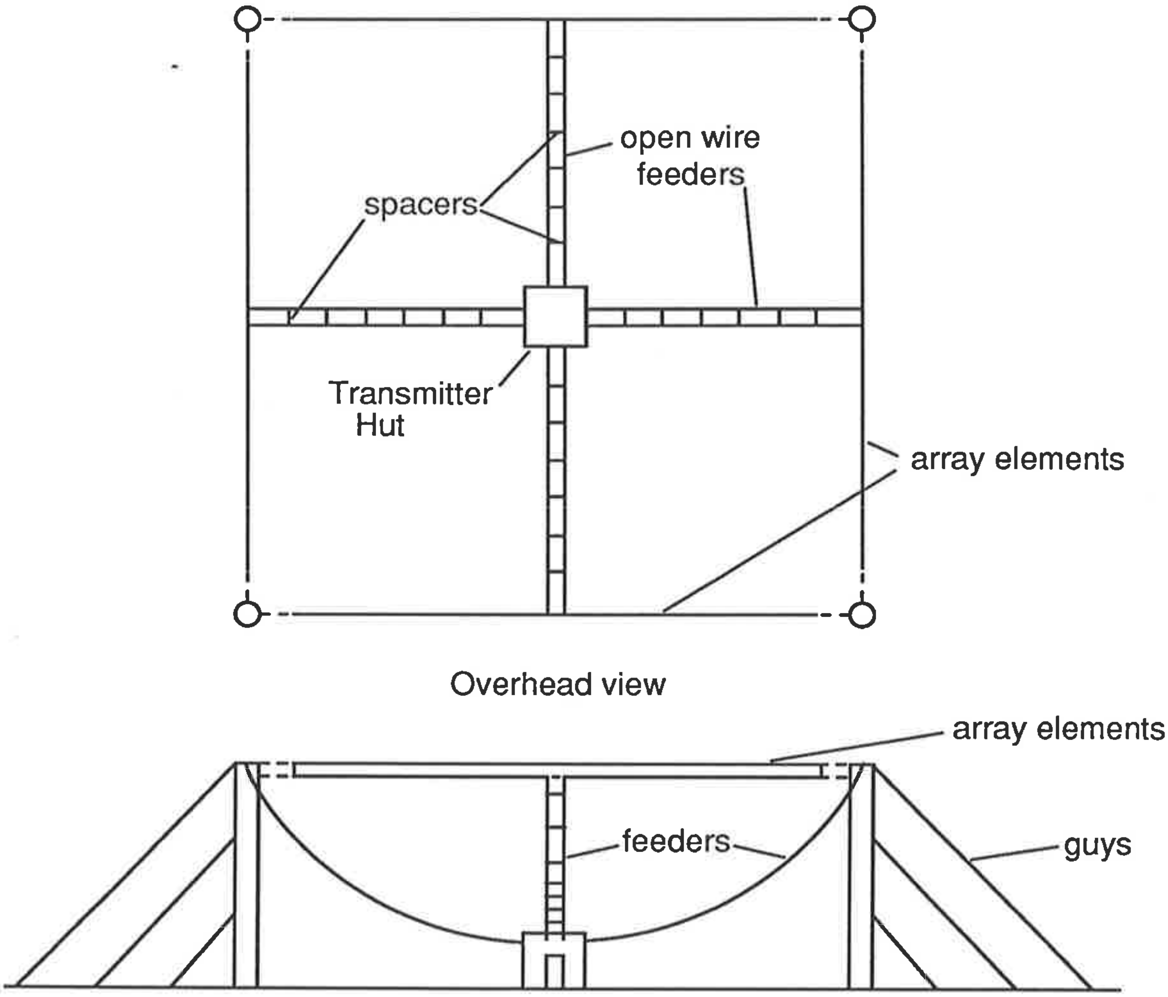

Figure 4.2: The layout of the Buckland Park transmitting array.

balun transformer and its own coaxial cable cut to an integer number of wavelengths (in cable). Thus each of the 2×89 dipoles is accessible in the main hut. Here they can be phased relative to each other to produce the desired beam configuration. (The phasing used for momentum flux measurements is described in a later section.) When all the north-south or east-west elements are connected as a broadside array, the polar diagram has a beam-width of approximately 5° half-width half-maximum. The first nulls lie at 11.6° from the vertical.

Eight receivers are available to amplify the 2 MHz signals from the array. The output from these receivers is passed to signal processors that take samples of the complex voltages. The in-phase and quadrature parts of the signal are sampled using an 8-bit analogue-to-digital converter and are passed to the controlling Eclipse S/120 mini-computer.

The echo height is calculated from the time between the pulse transmission and the time of sampling. This time interval $= 2z/c$ where c is the speed of light and z is the height from which a narrow transmitted pulse would have been reflected. The finite transmitted pulse width (here around 25μs) means that reflections occurring above and below this level arrive at the ground with this time delay. The practical result of this effect in this case is that the vertical height resolution is of the order of 4 km. Height samples are taken every 2 km thus successive height bins are not independent.

The averaging of the in-phase components and the quadrature components of the signal at successive times to give a representative in-phase, quadrature pair (coherent averaging) is used to improve the signal-to-noise ratio. For most of the data considered here, 8 samples separated by 0.05 s were coherently averaged to give a pair of data points every 0.4 s. A time series of 256 of these samples, lasting 102.4 s is stored for each available height.

The variation in the echo power with height, and the resulting changes in gain required by the receivers used here to compensate for this, make it impossible to sample over a height range of more than 20 km at one time. Generally these 20 km height blocks are switched between 60–78 km and 80–98 km for successive time intervals. At night,

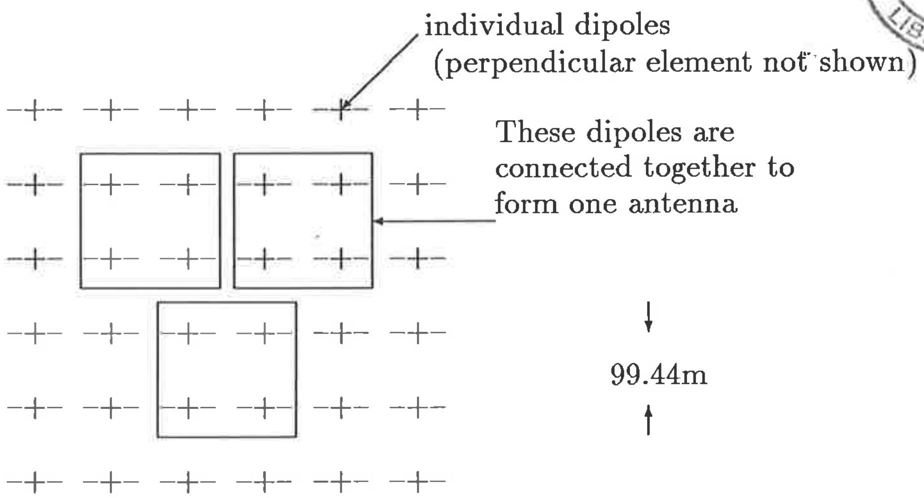

Figure 4.3: The antenna configuration used for spaced-antenna wind measurements.

however, the lower block is moved up to 70–88 km as no echoes occur below 70–80 km at this time.

4.3 Spaced antenna analysis

One mode in which the Buckland Park MF system can be operated is that utilising spaced antennas to measure winds (the SA method). For a full description of the method the reader is referred to Briggs (1984).

Three antennas are required for this method of analysis. At Buckland Park these are made up from combinations of either the north-south aligned or east-west aligned antennas. Either can be used as the echoes returning from the mesosphere are circularly polarised. Each of the three antennas is made up of four dipoles, adjacent to each other on the grid as shown in figure 4.3. The complex signals from these three antennas are recorded and analysed using correlation analysis.

The radio waves reflected from the mesosphere form a diffraction pattern on the ground. The movement of the scatterers with the wind causes this pattern to move so that by measuring the speed at which this pattern moves and the direction it is moving, the wind velocity and direction can be obtained. Given the variations in the signal at three vertices of a triangle, a cross correlation of the pairs of complex time series will yield information on the time required for the pattern to pass from one vertex to another. Then, given the distance between, and the positions of the three vertices, the components of the velocity can be obtained (Mitra 1949). This simple method, however, does not account for any systematic elongation of the pattern or for variations in the diffraction pattern as it moves. These changes will cause the above method to yield a velocity larger than the true velocity. The full correlation analysis (Briggs 1984) accounts for this factor and it is this analysis that is used on the spaced-antenna data treated in this thesis.

A theoretical treatment of the errors of the SA technique was carried out by May (1988). It was found, however, that the rejection criteria used in the SA technique made experimental determinations of the error more applicable. An experiment was conducted which used two separate sets of receiving antennae to make two independent determinations of the horizontal velocity and obtain an estimate of the statistical error of the SA technique. May found root-mean-square differences between the two velocities of between 6 and 21 ms^{-1} which translate to an error in each reading of between 1.7 and 3.2 ms^{-1}. These measurements were made in the mesosphere with wind speeds of greater than 70 ms^{-1}.

The full correlation analysis provides information on other aspects of the scatterers. In particular, the pattern scale, which describes the size of the diffraction pattern on the ground, is obtained from the spatial correlation function. It is assumed that the spatial correlation function has elliptical contours and the parameters that describe the $\rho = 0.5$ ellipse, namely the axial ratio, length of semi-major axis and orientation of the ellipse, are calculated in the full correlation analysis.

4.4 Doppler analysis

Another method whereby radars can be used to obtain the velocity of motion of a medium is the Doppler method. As stated previously, the Doppler method has been applied to weather studies for some years and has undergone extensive development in that time. A small subset of these developments that are relevant to middle atmosphere studies is presented now. For further information, the reader is referred to (eg.) Doviak and Zrnič (1984).

Radio waves transmitted at a carrier frequency ω_t are backscattered by irregularities in refractive index in the radar sampling volume. If these irregularities are moving, the returned radio waves are shifted in frequency by an amount ω_d that satisfies $\omega_d = 2V\omega_t/c$ where V is the velocity of the scatterer radial to the radar and c is the speed of light. Thus by measuring ω_d, the radial velocity of the scatterer can be determined.

In practice, random motions in the atmosphere and its bulk motion produce a spectrum of returned frequencies and it is the mean of this spectrum that is used to obtain the velocity. This mean value can be obtained using approaches that use the spectrum, or by applying the Fourier shift theorem and using the autocorrelation function of the time series from which the spectrum was obtained. One of the former methods was used in Chapter 3 to obtain spectral widths. The discussion here will begin with the time-series (covariance) based methods used on the Buckland Park data. Other possible methods will then be discussed

In the case where the atmosphere is stationary, but contains some zero-mean random motions, a Doppler power spectrum of the returned echoes $S_s(\omega)$ would be centred on the radar frequency. The sampling method used at Buckland Park has the effect of moving this to zero frequency, leaving the spectrum centred on zero. By the autocorrelation or Wiener-Kintchine theorem (see e.g. Bracewell 1978, p115) the Fourier transform of this power spectrum is the autocorrelation function $\rho_s(\tau)$ of the original time series.

If the atmosphere is in motion, the power spectrum $S_s(\omega)$ will be shifted to (say) ω_d. If we define the shifted spectrum $S(\omega) = S_s(\omega - \omega_d)$ then its Fourier transform can be found using the shift theorem and is as follows:

$$S(\omega) \leftrightarrow \rho(\tau) = \rho_s(\tau)e^{i\omega_d\tau} \tag{4.1}$$

$\rho(\tau)$ being an autocorrelation function and $\leftrightarrow$ denoting a Fourier transform. If we assume that $S_s(\omega)$ is symmetrical (i.e. an even function), then $\rho_s(\tau)$ will be purely real.

Thus the phase of the autocorrelation function, $\phi(\tau)$, in the expression

$$\rho(\tau) = |\rho(\tau)|e^{i\phi(\tau)} \tag{4.2}$$

will be due to the shift in the spectrum only. This implies that $\phi(\tau) = \omega_d\tau$ or $\omega_d = \phi(\tau)/\tau$. This result was obtained by Woodman and Guillen (1974), Rastogi and Woodman (1974), however, they used slightly different reasoning.

In principle, this could be calculated at any value of τ. Values close to zero are preferred in practice, however, because noise and departures from symmetry can make the phase less reliable at large lag values. With the complex time series obtained at Buckland Park, the value of the phase of the autocorrelation function at one discrete lag is calculated to give ω_d. This method is sometimes termed the pulse pair (PP) technique.

It was noted that this treatment assumes that the power spectrum, if computed, would be symmetric. This may not be so in practice. The gravity-wave effects discussed in chapter 3 could make the spectrum asymmetric. For off-vertical beams, leakage of power into the beam from the vertical could increase the power near zero frequency causing asymmetry. "Specular spikes" could also bias the spectrum; thus it is possible that this symmetry assumption is not satisfied. For this work, however, the computational efficiency of this widely-accepted method made it preferable.

The error in the velocities obtained when this method is applied to Buckland Park data was considered by Vincent and Reid (1983). The results of independent velocity determinations from narrow Doppler beams pointed in the *same direction* were compared and the mean-square difference was found to be around 0.5 m^2s^{-2}. The error in a single determination of velocity was given as $0.7ms^{-1}$. This value is consistant with that obtained when the theoretical treatment of Doviak *et al.* (1979) is applied with typical values of spectral width and signal-to-noise ratio (Reid 1984).

Another time-series based method of obtaining velocities (termed the poly-pulse pair technique) utilises the phase of the autocorrelation function at various lags and computes a weighted average of these to obtain the slope of the phase function at zero lag. The error involved in the pulse pair, poly-pulse pair and various spectrum-based techniques

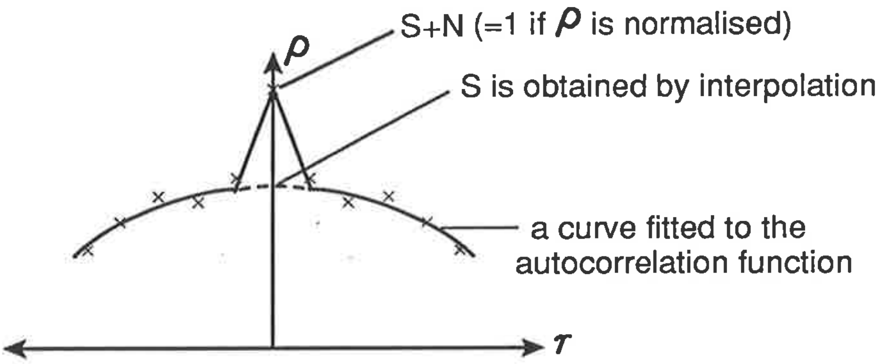

Figure 4.4: Interpolation back to the zero lag value of the autocorrelation function gives the signal-to-noise ratio.

was calculated by May *et al.* (1989) and compared with the results of simulations and some tropospheric radar observations. They concluded that the pulse-pair technique was best for data with a good signal-to-noise ratio.

The signal-to-noise ratio can also be obtained from the complex time series. The noise will be uncorrelated at the first lag and will therefore appear in the autocorrelation function at zero lag. At non-zero lags the correlation function will be largely unaffected by noise. Thus by calculating the amplitude of the autocorrelation function at zero and (say) one, three and five lags, the correlated signal at zero lag can be determined by interpolation from greater lags and compared with the actual zero lag value to give the signal-to-noise ratio. This process is described in figure 4.4; it gives the signal to noise as a power ratio.

4.5 Phasing the Buckland Park array

The Doppler method just described is most often applied to data obtained using narrow off-vertical beams. It is necessary to have a narrow beam to enable the off-zenith angle to be accurately determined and to minimise any variations in this angle which might occur. This requirement is applied to the Buckland Park array through the use of all 89 of the north-south or east-west aligned dipoles. The off-zenith angle is set through the use of phasing cables.

The momentum flux measurements that are considered in the remainder of this thesis require two orthogonal pairs of off-vertical beams. The procedure required to produce one pair of off-vertical beams is now described.

The signals from each of the 89 north-south aligned (say) dipoles are available in the receiving hut at Buckland Park. These are arranged in 11 rows, each having between 3 and 11 dipoles as seen in figure 4.1. The dipoles in each row are connected in parallel (and transformed to maintain a constant resistive load) to form eleven outputs, one from each row. The signals from each of these rows are then split with power splitters into two identical sets of eleven signals. These can then be phased to swing the beam in a direction perpendicular to the rows of antennas.

The off-vertical angle utilised at Buckland Park is 11.6°. This is the angle of the first nulls of the polar diagram of the whole array when it points vertically. When the array is tilted to 11.6°, one of these nulls point vertically, reducing the scatter leaking into the beam from overhead. This configuration was found to be optimum by Hocking (1979).

To achieve this off-vertical angle, a phase delay is introduced between sucessive rows using various lengths of coaxial cable. A schematic diagram of this arrangement is given in figure 4.5. The lengths of the cables are given in table 4.1. With this arrangement, signals due to a plane wave coming from 11.6° off-zenith (as indicated in figure 4.5) will arrive at the output to the receiver in phase.

Because the transmitted pulse used at Buckland Park contains many cycles of the transmitted frequency, it is possible to truncate any cables that are longer than one wavelength (in cable). This can be seen in table 4.1 between cables l_9 and l_{10}. The beam on the other side of zenith to the one just described is obtained in the same way as this one, however, the order of this set of cables is reversed. Where one output from the power splitters may have a cable of length l_i, the other will have l_{12-i}. This procedure is also repeated for the set of dipoles that are aligned perpendicular to the first set, however, the rows in this case are connected in a direction perpendicular to that used for the first pair of beams. Thus four independent radar beams are available.

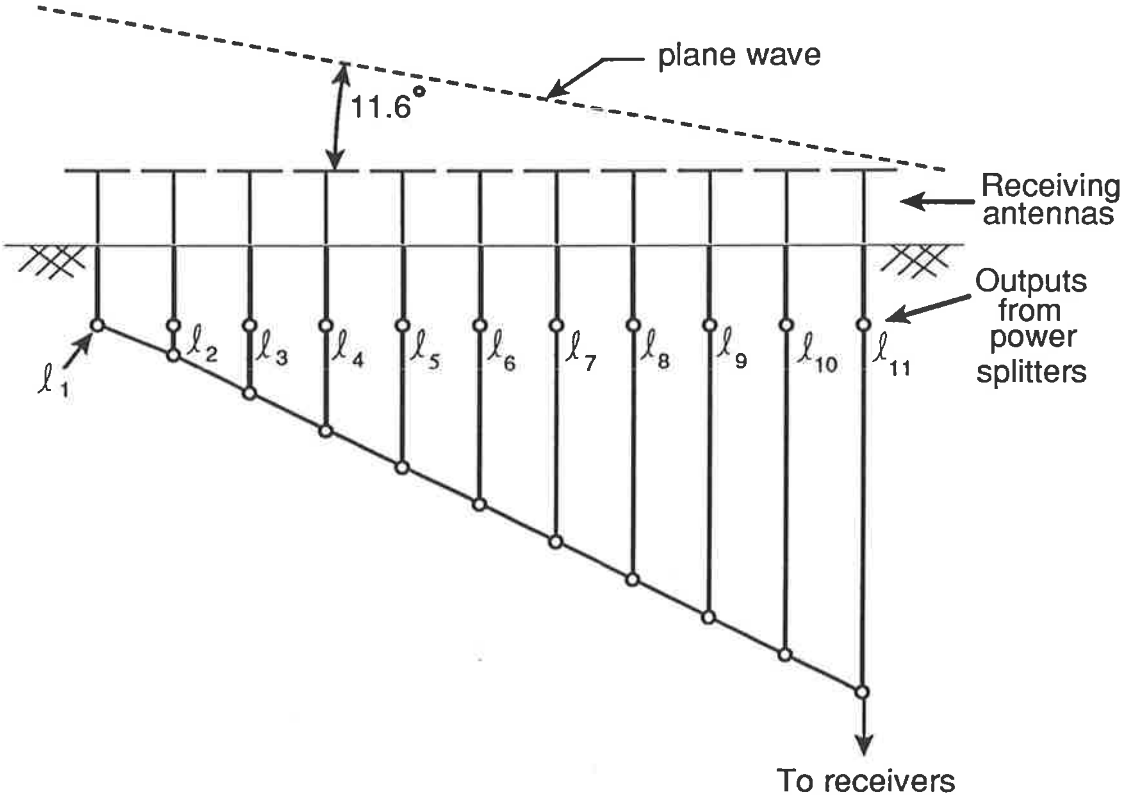

Figure 4.5: The phasing cables used to obtain an 11.6° off-vertical beam.

i	l_i
1	0m
2	11.6m
3	23.2m
4	34.8m
5	46.3m
6	57.9m
7	69.5m
8	81.1m
9	92.7m
10	7.7m
11	19.3m

One wavelength in cable = 96.6m

Table 4.1: The cable lengths used to phase the Buckland Park MF array for an 11.6° off-vertical beam.

It is noted that this arrangement allows the data for the momentum flux experiments to be obtained concurrently. This differs from the experimental arrangement used at some other radar installations where one beam is pointed in different directions at different times (e.g. Poker Flat, Fritts and Yuan 1989).

4.6 Summary

In this chapter, some aspects of the Buckland Park MF/HF array have been presented. Methods of data analysis for various types of experiment as well as some aspects of the hardware configuration have been summarised. For reasons of brevity, however, the scope of the chapter has been limited to concepts that are of importance in discussions of the experiments and data processing presented in the rest of this thesis.

Chapter 5

Beam pointing angles and the Buckland Park array

It was suggested by Vincent and Reid (1983) that their momentum flux measurements underestimated the true momentum flux because the effective pointing angle of the radar beams was closer to the zenith than that defined by the antenna phasing. Fritts and Vincent (1987) estimated the effective pointing angle by comparing root-mean-square (RMS) velocities obtained using spaced-antenna and Doppler modes of analysis. As a precursor to the momentum flux analyses that are the subject of this thesis, a study of pointing angles, how they can best be calculated, and how they vary with time as well as height is now presented.

Nominal and effective pointing angles (θ) for the Buckland Park system are generally within 12° of zenith. In this range, $\sin\theta$ and θ are very close to being linearly related (or equal if θ is expressed in radians). It is therefore common in this chapter to consider $\sin\theta$ even though the parameter ultimately required is θ. It is also common to use the term "height" where "range" would be a more precise term. Once again, with θ within 12° of zenith and a sampling volume approximately 4 km in height, the difference between height and range is not critical.

5.1 Methods of ascertaining the pointing angle

If a very narrow beam is directed at an angle θ from the vertical, then the instantaneous radial velocity measured through this beam will be given by

$$v_{rad} = v_{hor} \sin\theta + w \cos\theta \tag{5.1}$$

where w is the vertical velocity in the radar sampling volume and v_{hor} is the component of horizontal velocity in the plane of the zenith and the radar beam. For θ small (say less than 15°), $\cos\theta \approx 1$ so that to a good approximation

$$v_{rad} = v_{hor} \sin\theta + w. \tag{5.2}$$

Rearranging gives

$$\sin\theta = \frac{v_{rad} - w}{v_{hor}} \tag{5.3}$$

The two velocities v_{rad} and v_{hor} can be measured by the Doppler and spaced-antenna methods. In order to use equation 5.3 to obtain θ, it is necessary also to know w. One way of obtaining this information is to have a second radar beam directed vertically. Assuming that the vertical velocity in the sampling volume overhead is the same as that in the sampling volume of the off-vertical beam, w can be obtained and used in the above expression. An alternative approach is to assume that w is zero, giving

$$\sin\theta = \frac{v_{rad}}{v_{hor}}. \tag{5.4}$$

The quality of the assumptions leading to equations 5.3 and 5.4 can sometimes be enhanced by averaging over a period of time such that v_{rad}, v_{hor} and w refer to average velocities. The root-mean-square variation around that average can then be computed and it was this method that was used by Fritts and Vincent (1987). This root-mean-square variation can be substituted for the velocities in equation 5.4 to find a constant $\sin\theta$. A discussion on the application of this method is presented in a later section.

How often the assumptions made above will be satisfied is difficult to say. It is conceivable that w will be small if averaged over a suitable period of time but large values are possible over short time scales. For example, vertical velocities as large as

10ms^{-1} were seen in the polar mesospheric data presented in figure 3.6 of chapter 3. It is important that this be kept in mind and considered in relation to each set of data.

The above discussion assumes a very narrow beam, that is, a beam that has little scope for pointing angle variations. The effective polar diagram of a radar will be the product of the transmitting, receiving and scattering polar diagrams and as suggested by Röttger (1981), if both the transmitting and receiving polar diagrams are broad, variations in the scattering polar diagram will change the effective polar diagram. The effective pointing angle θ_{eff} will then be the angle at which this polar diagram has maximum gain. Then θ_{eff} will replace θ in equation 5.3 and 5.4.

Models for obtaining this effective pointing angle have been presented by Whitehead *et al.* (1983), Hocking *et al.* (1986), Reid (1988) and Hocking (1989). Hocking (1989) assumes polar diagrams of the form $P_s(\theta) \propto e^{-\frac{\sin^2\theta}{\sin^2\theta_s}}$ for the scatterers and $P_R(\theta,\phi) \propto e^{-\frac{(\sin\theta\sin\phi)^2+(\sin\theta\cos\phi-\sin\theta_T)^2}{\sin^2\theta_0}}$ for the radar beams combined. Here ϕ is the azimuthal angle and θ_s and θ_0 are parameters that describe the width of the scatterer and radar beam polar diagrams respectively. Finding the position of the maximum of these polar diagrams yields

$$\sin\theta_{eff} = \sin\theta_T\left[1+\frac{\sin^2\theta_0}{\sin^2\theta_s}\right]^{-1} \tag{5.5}$$

where θ_T is the pointing angle of the two-way radar beam only. This approach is different to that of the other workers mentioned above in that it utilises the correct form of the radar polar diagram of a tilted beam. The expressions that had been used previously contained no dependence on ϕ and thus could only describe a vertical beam correctly. An annular ring instead of a narrow off vertical beam resulted when a tilt angle was included in these expressions. Both approaches, however, yield equation 5.5.

The above polar diagrams assume that the distribution of the returned power is azimuthly symmetric. Information provided by the spaced-antenna analysis, however, suggests that this may not actually be the case. The full correlation analysis (Briggs 1984) allows azimuthal asymmetry to the extent that contours of constant autocorrelation can be elliptical. With the assumption of a Gaussian form the spatial autocorrelation function contours will then have the form

$$\rho(\xi,\eta) = \exp\left(-\left[\frac{\xi^2}{\xi_1^2} + \frac{\eta^2}{\eta_1^2}\right]\right) = \text{constant} \tag{5.6}$$

as shown in figure 5.1(a). ξ_1 and η_1 are the e^{-1} lengths of the spatial correlation function and ξ, ξ_1, η and η_1 are all expressed in wavelengths. The distances to the half-correlation points are calculated by the full correlation analysis and are related to the e^{-1} values by $(\xi_1)_{0.5} = \sqrt{\ln 2}\,\xi_1$ and $(\eta_1)_{0.5} = \sqrt{\ln 2}\,\eta_1$. Briggs (private communication 1989) pointed out that equation 5.6 is in fact the Fourier transform of the angular power spectrum of the echoes (see e.g. Ratcliffe, 1956). This result can be used to obtain, not only $W(S_1, S_2)$, the angular power spectrum, but the effective pointing angle as well. The method used to do this, which is presented in detail in appendix C, is now outlined.

The angular power spectrum will have the form

$$W(S_1,S_2) = W_0 \exp(-\left[\pi\xi_1^2 S_1^2 + \pi\eta_1^2 S_2^2\right]) \leftrightarrow \rho(\xi,\eta). \tag{5.7}$$

Here, S_1 and S_2 represent $\sin\theta$ on two orthogonal axes and "$\leftrightarrow$" denotes a Fourier transform. An example is given in figure 5.1 (b).

As noted earlier, the effective polar diagram of the radar is the product of the transmitting, scattering and receiving polar diagrams. At Buckland Park, the transmitting polar diagram is broad and it is the combination of the polar diagrams of the scatterers and receiving antenna that determines the effective polar diagram and the effective pointing angle. If the receiving beam is phased to point in the direction $S_1 = a_1$, $S_2 = a_2$ and is assumed to have the form $P(S_1,S_2) \propto \exp - \left[\frac{(S_1-a_1)^2+(S_2-a_2)^2}{S_0^2}\right]$, (as shown in figure 5.1 (c)) the resulting polar diagram will have an effective pointing direction that is given by

$$(S_1)_{eff} = \frac{a_1}{1+S_0^2\xi_1^2\pi^2}, \quad (S_2)_{eff} = \frac{a_2}{1+S_0^2\eta_1^2\pi^2}. \tag{5.8}$$

This polar diagram is represented in figure 5.1 (d).

Thus far, the S_1, S_2 axes have not been aligned with the N-S, E-W directions. This is because the orientation of the autocorrelation ellipse need not be along these axes. The full correlation analysis gives the angle ϕ between the semi-major axis of the

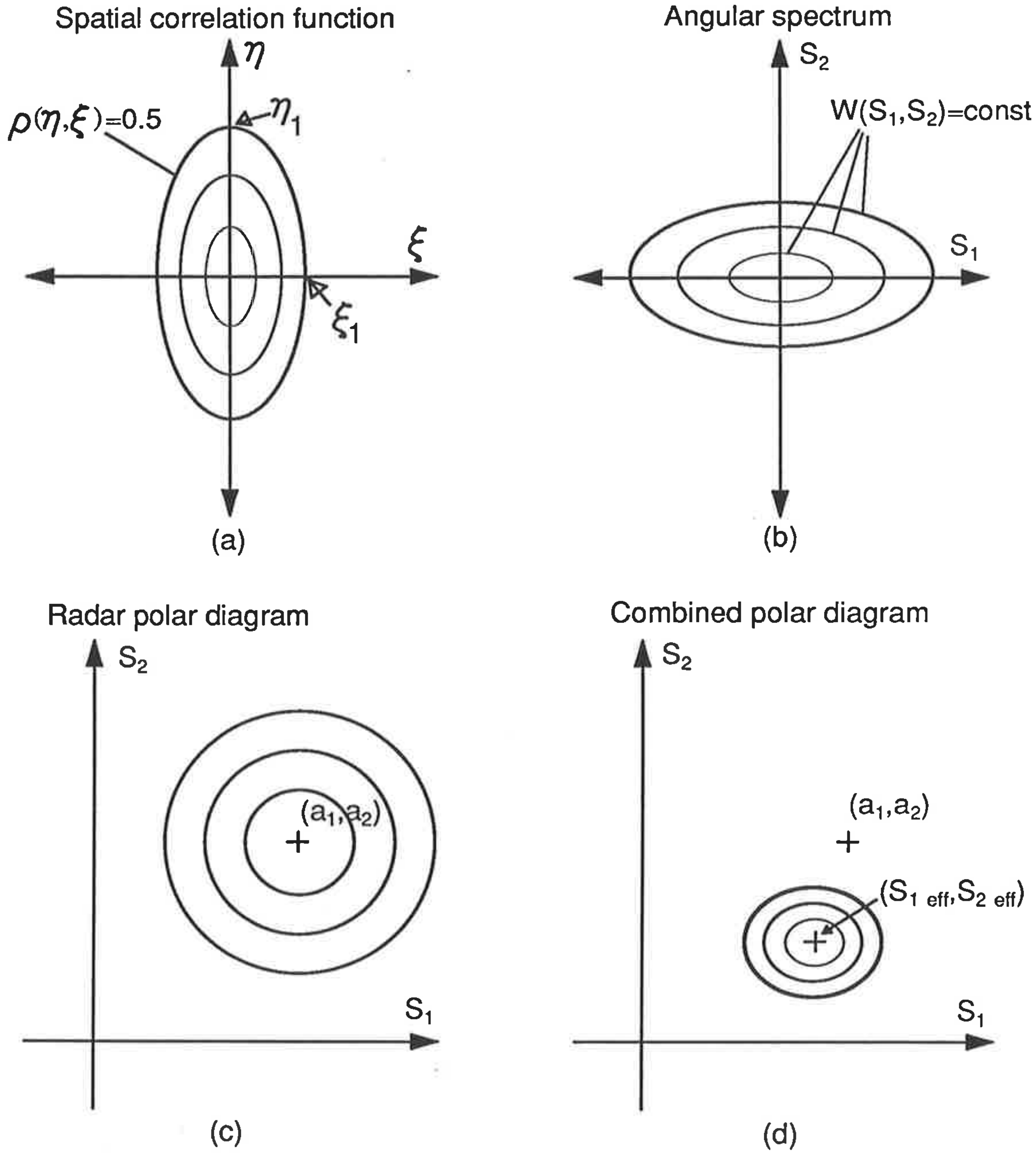

Figure 5.1: The correlation ellipse (a), its Fourier transform, the angular power spectrum (b), the radar polar diagram (c) and the effective polar diagram of the scatterers and radar combined (d).

spatial correlation half-width ellipse and North (ϕ must be between 0 and 180 degrees). Therefore the axes in the above treatment need to be rotated through an angle ϕ. If this is done and the appropriate values of a_1 and a_2 are included for a beam phased to point 11.6° off-zenith toward the east, the result is

$$(S_1')_{eff} = \frac{\sin 11.6^\circ \sin^2\phi}{1+\frac{S_0^2\pi^2(\eta_1)_{0.5}^2}{\ln 2}} + \frac{\sin 11.6^\circ \cos^2\phi}{1+\frac{S_0^2\pi^2(\xi_1)_{0.5}^2}{\ln 2}} \tag{5.9}$$

and

$$(S_2')_{eff} = \frac{\sin 11.6^\circ \sin\phi\cos\phi}{1+\frac{S_0^2\pi^2(\eta_1)_{0.5}^2}{\ln 2}} - \frac{\sin 11.6^\circ \sin\phi\cos\phi}{1+\frac{S_0^2\pi^2(\xi_1)_{0.5}^2}{\ln 2}}. \tag{5.10}$$

In these primed coordinates, S_1' is toward the east and S_2' is toward the north. Therefore, using the parameters calculated using the full correlation analysis, the effective pointing direction can be obtained.

The above derivation assumes a scattering polar diagram that is centred on the zenith. Although this has been thought to be acceptable in general, some authors (whose work will be discussed later) have reported the need for an angular distribution of scattered power that peaks away from the zenith. If this were the case, a translation in S_1 and S_2 would be necessary. For an angular spectrum with a maximum at $S_1 = b_1$, $S_2 = b_2$ the translation

$$a_1 \rightarrow a_1 - b_1$$

$$a_2 \rightarrow a_2 - b_2$$

would be necessary before the rotation was applied. For the data considered later in this chapter, however, b_1 and b_2 are unknown making it impossible to carry out this translation.

The difference between the velocity and the polar-diagram-based methods of determining θ_{eff} should be noted. The radial velocity is a measure of the mean of the power spectrum which in turn results from the integrated effect of the velocities in the radar sampling volume, weighted by the effective polar diagram. If this effective polar diagram is asymmetric, (for example where the backscatter polar diagram is not circularly symmetric) the power spectrum may also be asymmetric. The velocity represented by the mean would then differ from the one that would be obtained if the wind was projected onto a narrow beam pointing in the direction θ_{eff}. Browning and Wexler (1968) and Hocking (1989) note this but Hocking suggests that the difference will not be great.

5.2.1 A comparison of Doppler and spaced-antenna-derived velocities on short time-scales

For a week in June, 1984, the Buckland Park array was operated in such a way that it collected time series using three spaced antennas, one narrow vertical beam and one narrow off-vertical beam directed 11.6°off zenith toward the east. The data were stored on magnetic tape. The narrow beams utilised the full array and gave data suitable for Doppler analysis. The other three time series were subjected to the full correlation analysis (Briggs 1984) mentioned in chapter 4. A similar experiment is described in Reid (1988), although in Reid's work the spaced antenna and Doppler data were not concurrent. This limited the conclusions that could be drawn from the experiment, but a tendency for the Doppler value to be less than the spaced antenna value was noted. In the data presented here, the time series used in both methods of analysis were obtained simultaneously and comparisons of the two methods are subject to fewer assumptions.

Optimally, analysis of these time series would yield two measures of velocity for each height and time sample. Unfortunately, the rejection criteria applied in each method remove some data points from each set. This necessitates the removal of points which do not have values in *both* data sets to maintain the simultaneity of the data. This is important because there may be a systematic rejection of points in one of the methods which will bias the results when averaging is applied. The test used required that Doppler data in one of the beams (including two of the wide spaced-antenna beams) but not necessarily all of them, be available with each spaced antenna point.

The first data sets considered are made up of 4 min averages of the data. During the day, each 4 min bin contains one point for each height. However, at night, an overlap in the height multiplexing means that two points per 4 min sometimes occur between 80 and 88 km inclusive. Data exists between around 70 and 98 km but the data acceptance rate below approximately 80 km limited the usefulness of the data in that region. Similarly, the E-region seemed to affect the 98 and 96 km data so that only the data between 80 and 94 km is considered in detail.

Firstly, the existence of a problem with pointing angles should be confirmed. This is done in figures 5.2 and 5.3 where the eastward component of the wind obtained using the spaced antenna (SA) analysis is plotted with the horizontal velocity inferred from the radial velocity measured with an eastward pointing, nominally 11.6°, off-vertical beam. An 11.6° effective pointing angle and no vertical velocity are assumed. Only heights of 94, 90, 86 and 82 km are plotted in the interest of brevity. It can be seen that there is a systematic difference between the SA and Doppler derived velocities. This suggests that the effective pointing angle is not 11.6°.

Equations 5.3 and 5.4 are used to obtain $\sin\theta_{eff}$. The results of these calculations are presented in figures 5.4, 5.5, 5.6 and 5.7. Values from near 0.2 ($= \sin(11.6°)$) to around 0.1 ($= \sin(11.6° - 4.5°)$, 4.5° being the beam half-width) would be expected and do exist, but there are also values vastly different from these. At all heights, using both methods, values less than zero occur. These correspond to effective pointing angles on the opposite side of zenith to the beam and are difficult to explain. At 94 and 90 km, values close to or even greater than 1.0 can be seen. These are impossible to interpret and show a breakdown in the analysis. The error analysis that follows helps to explain this breakdown.

Inspection of equations 5.3 and 5.4 suggests that large values of $\sin\theta_{eff}$ would result if V_{hor} was small. If standard error analysis is applied to equation 5.4, the absolute error in $\sin\theta_{eff}$ can be found using the expression

$$\Delta \sin\theta_{eff} = \sqrt{\frac{(\Delta V_{rad})^2}{V_{hor}^2} + \frac{V_{rad}^2(\Delta V_{hor})^2}{V_{hor}^4}} \qquad (5.11)$$

assuming that the covariance between V_{rad} and V_{hor} is zero. These measurements are made separately and are thus independent so that the covariance term can be taken as zero. Although in reality they are related by $\sin\theta_{eff}$, here we are allowing V_{rad} and V_{hor} to take any value and are considering the error in $\sin\theta_{eff}$ due to random errors in the velocity measurements.

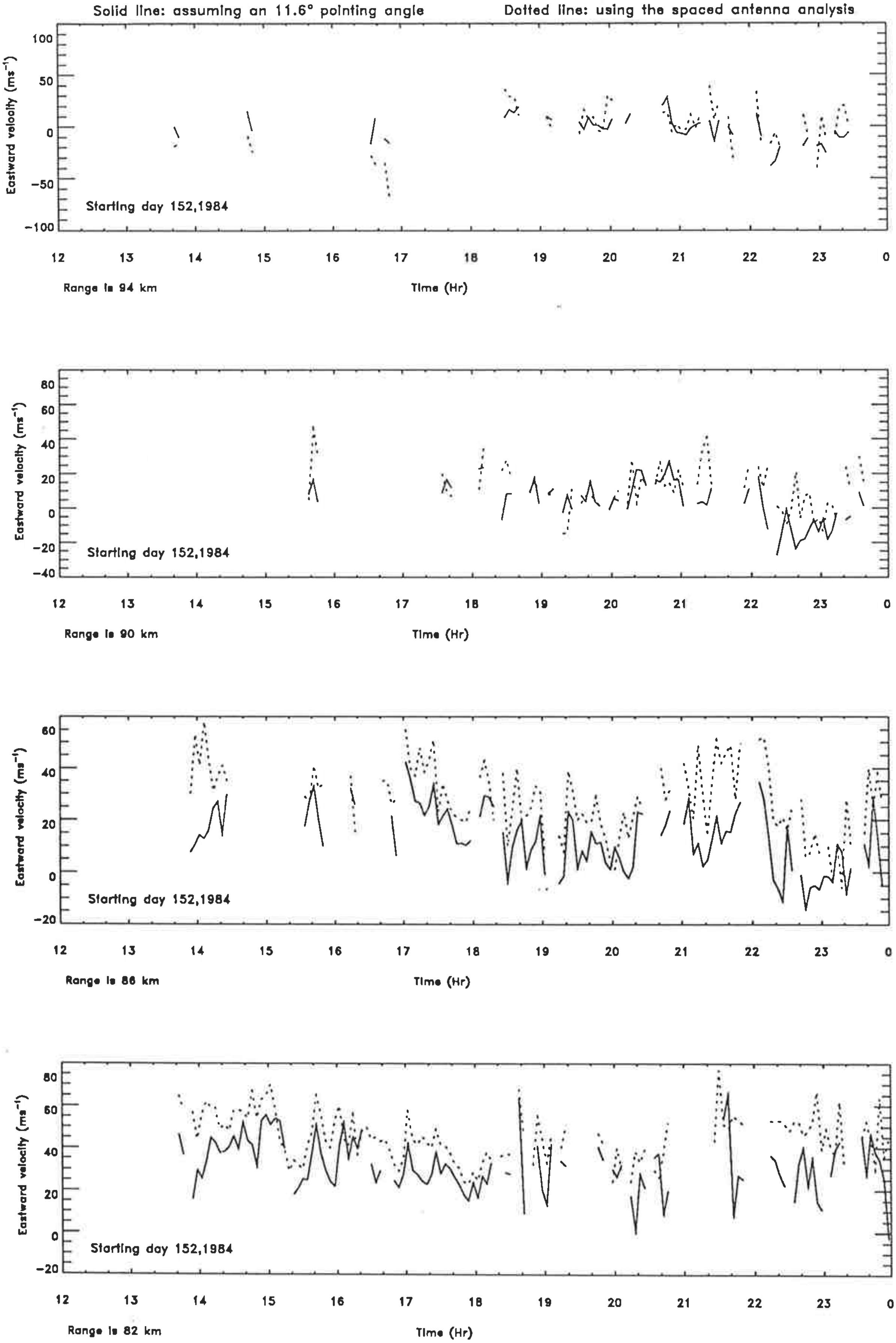

Figure 5.2: A comparison of SA derived eastward velocities (dots) and Doppler derived eastward velocities assuming an effective pointing angle of 11.6° and zero vertical velocity for day 152, 12:00–24:00.

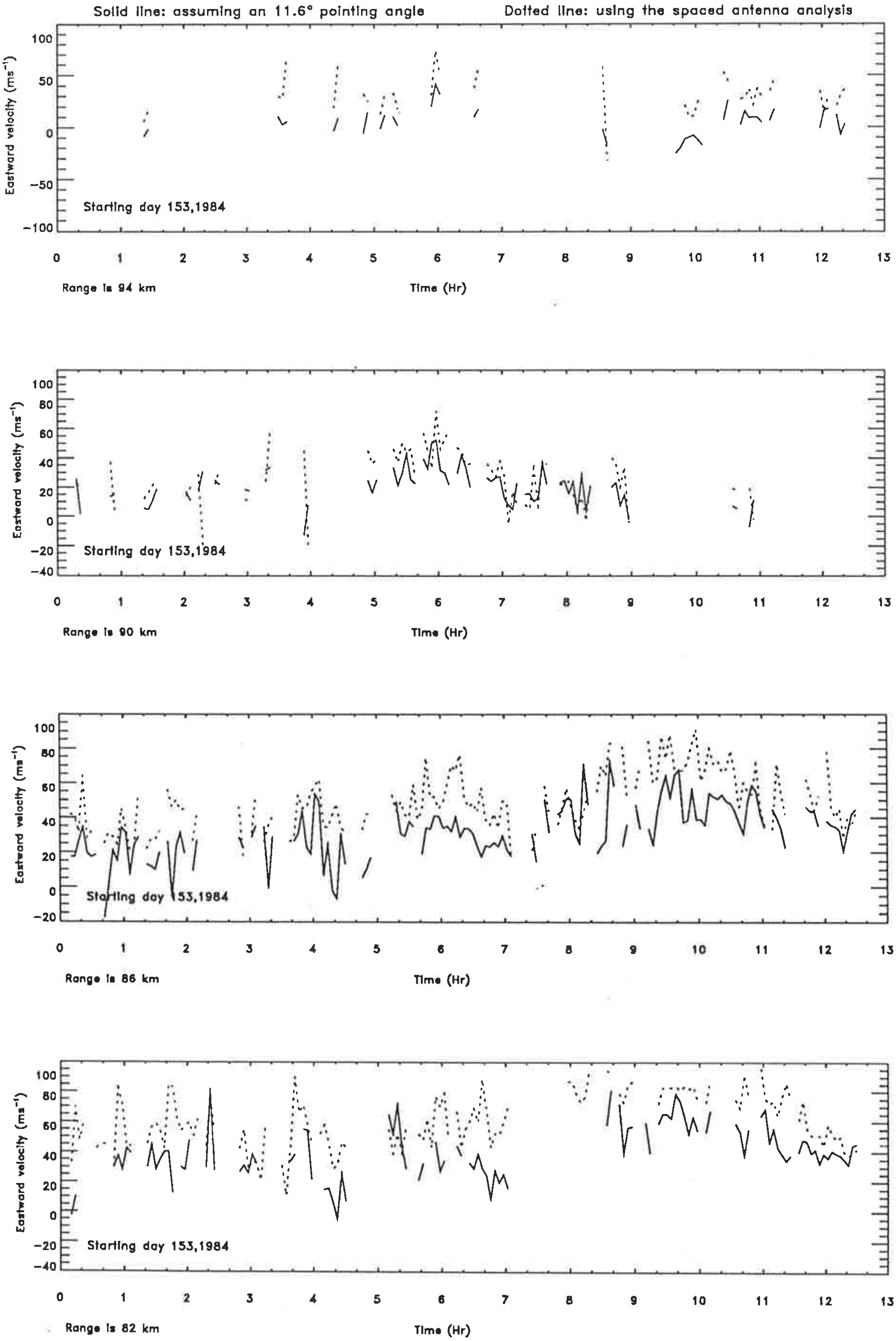

Figure 5.3: A comparison of SA derived eastward velocities (dots) and Doppler derived eastward velocities assuming an effective pointing angle of 11.6° and zero vertical velocity for day 153, 0:00–13:00.

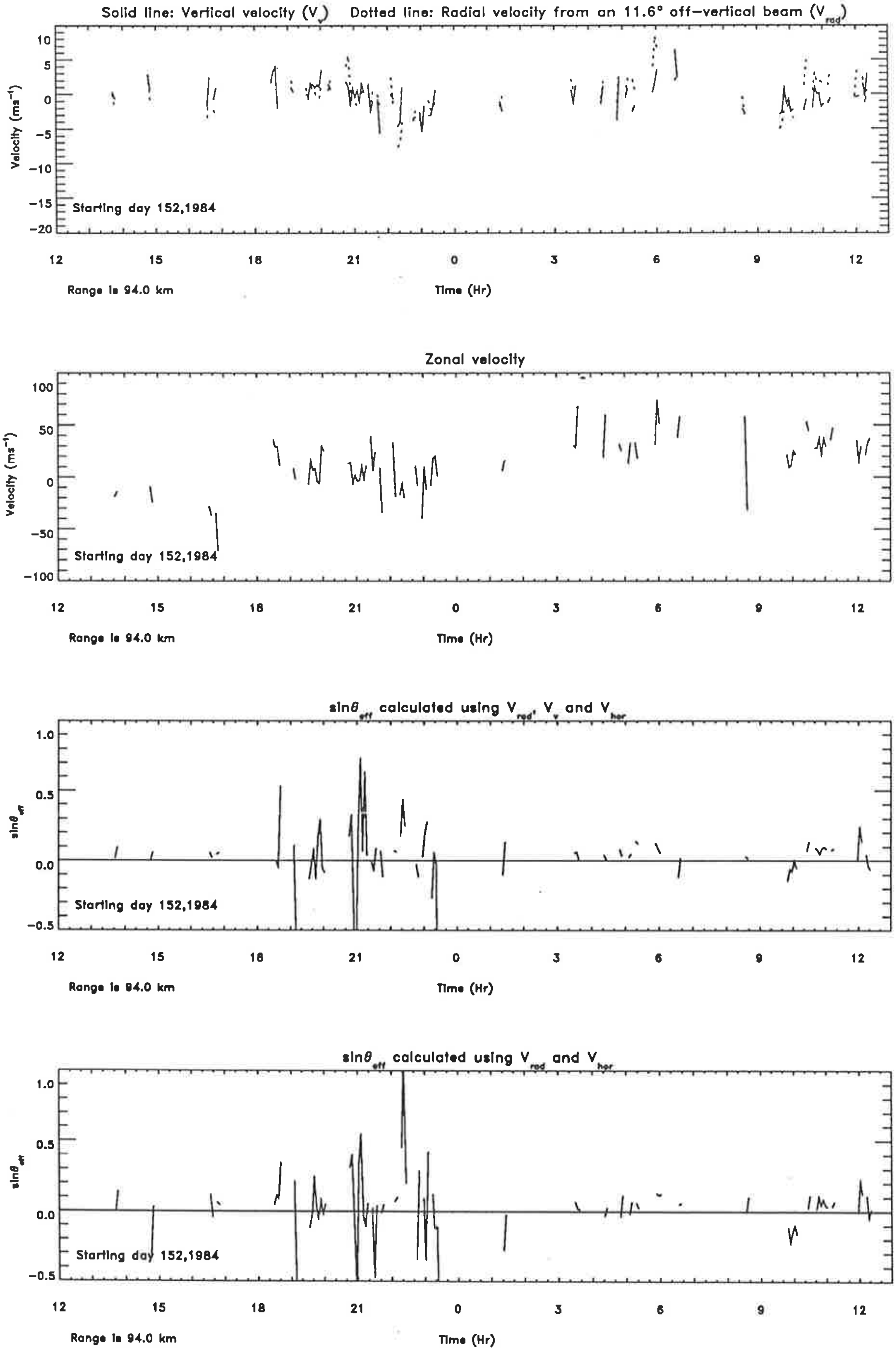

Figure 5.4: Velocities and the $\sin\theta_{eff}$ values obtained from them for the 94 km data.

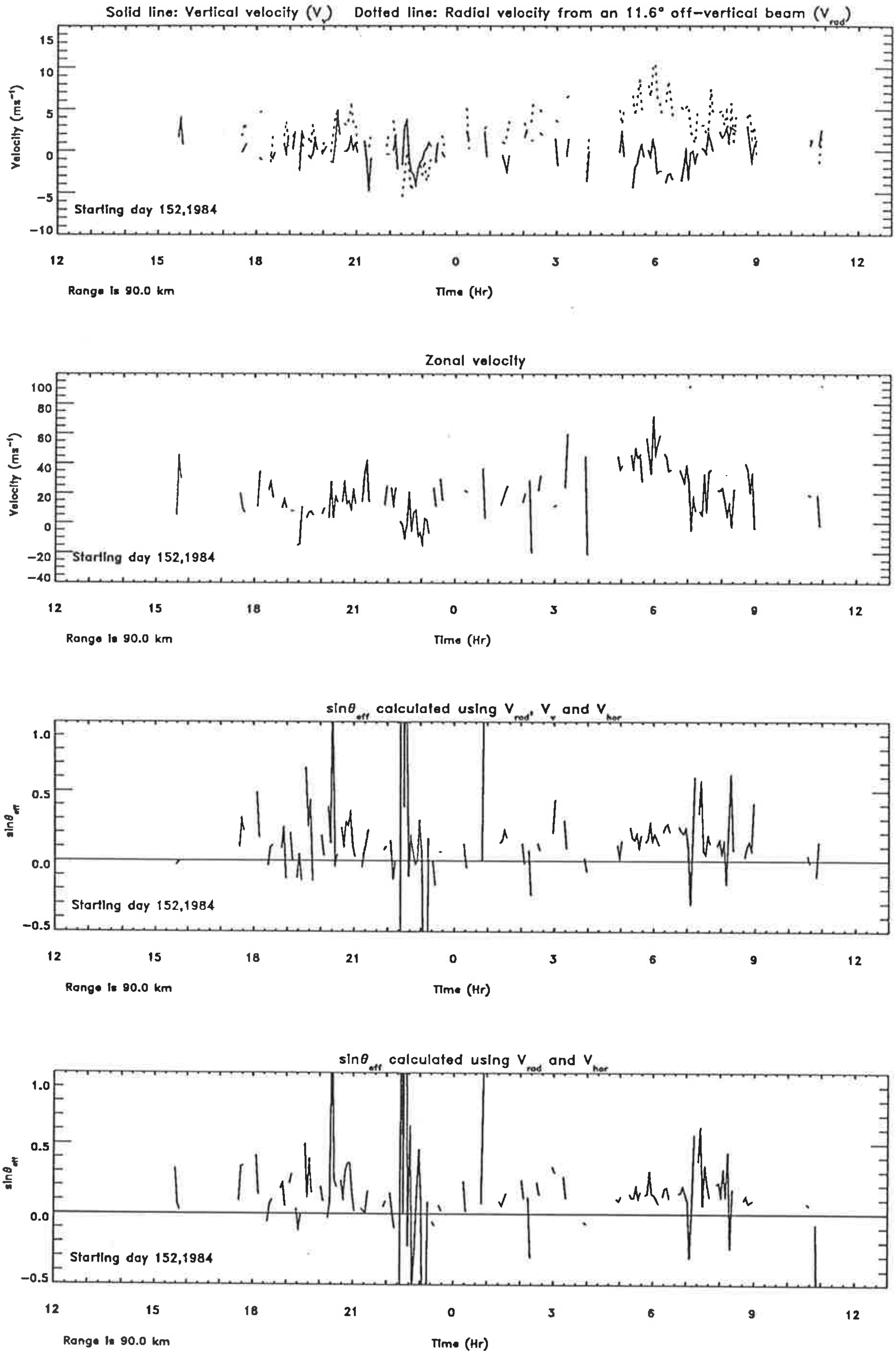

Figure 5.5: Velocities and the $\sin\theta_{eff}$ values obtained from them for the 90 km data.

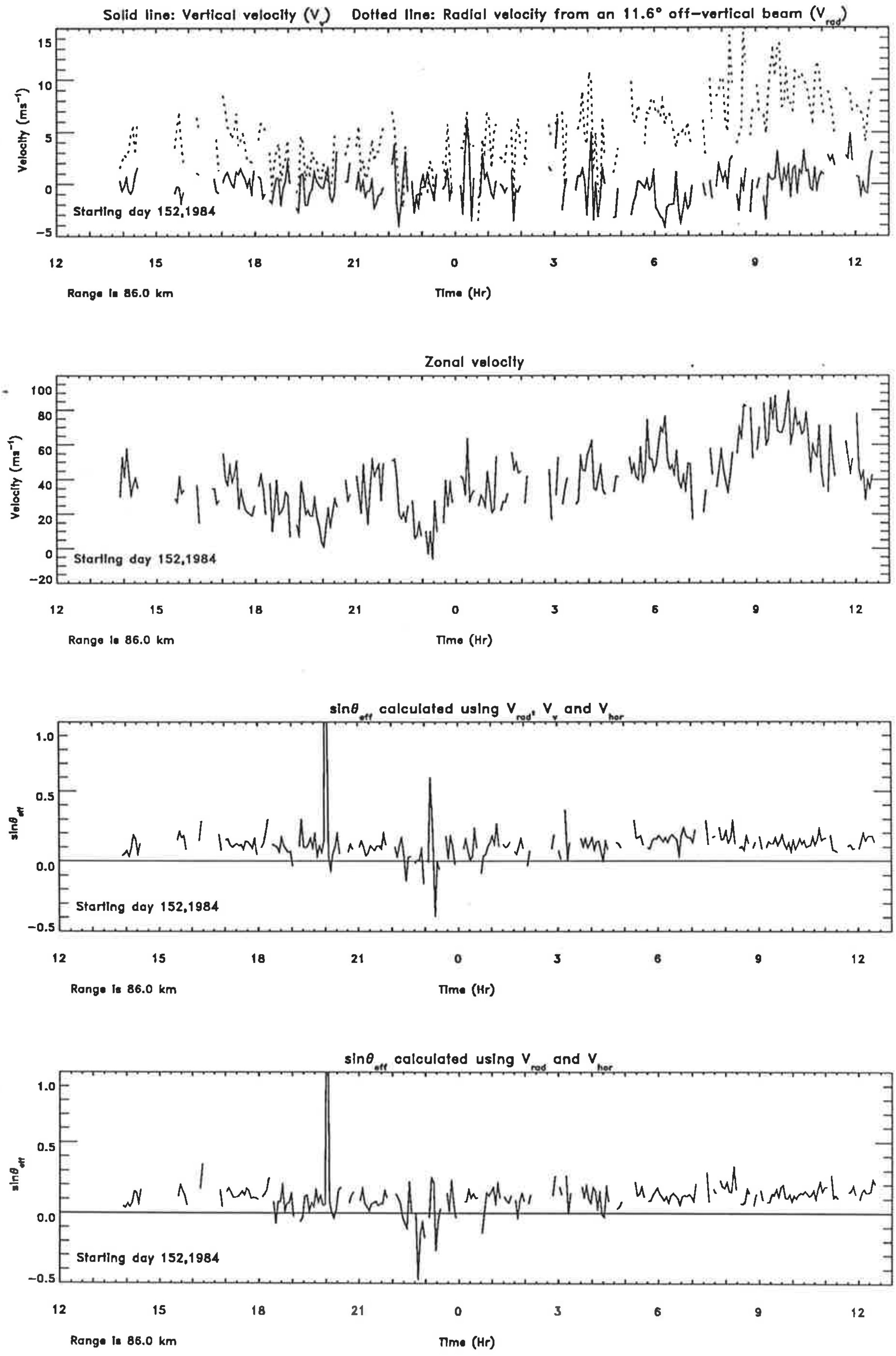

Figure 5.6: Velocities and the $\sin\theta_{eff}$ values obtained from them for the 86 km data.

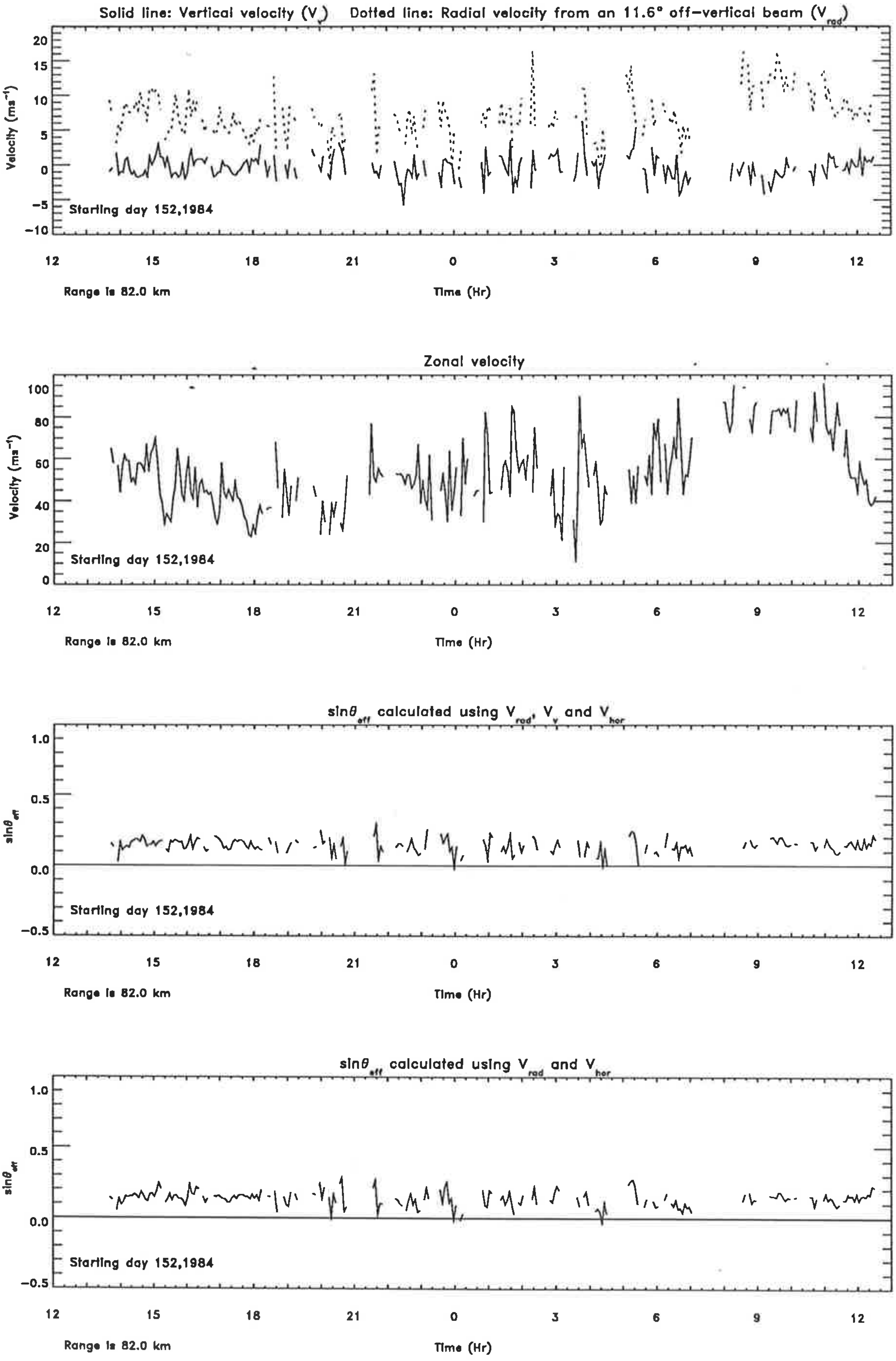

Figure 5.7: Velocities and the $\sin\theta_{eff}$ values obtained from them for the 82 km data.

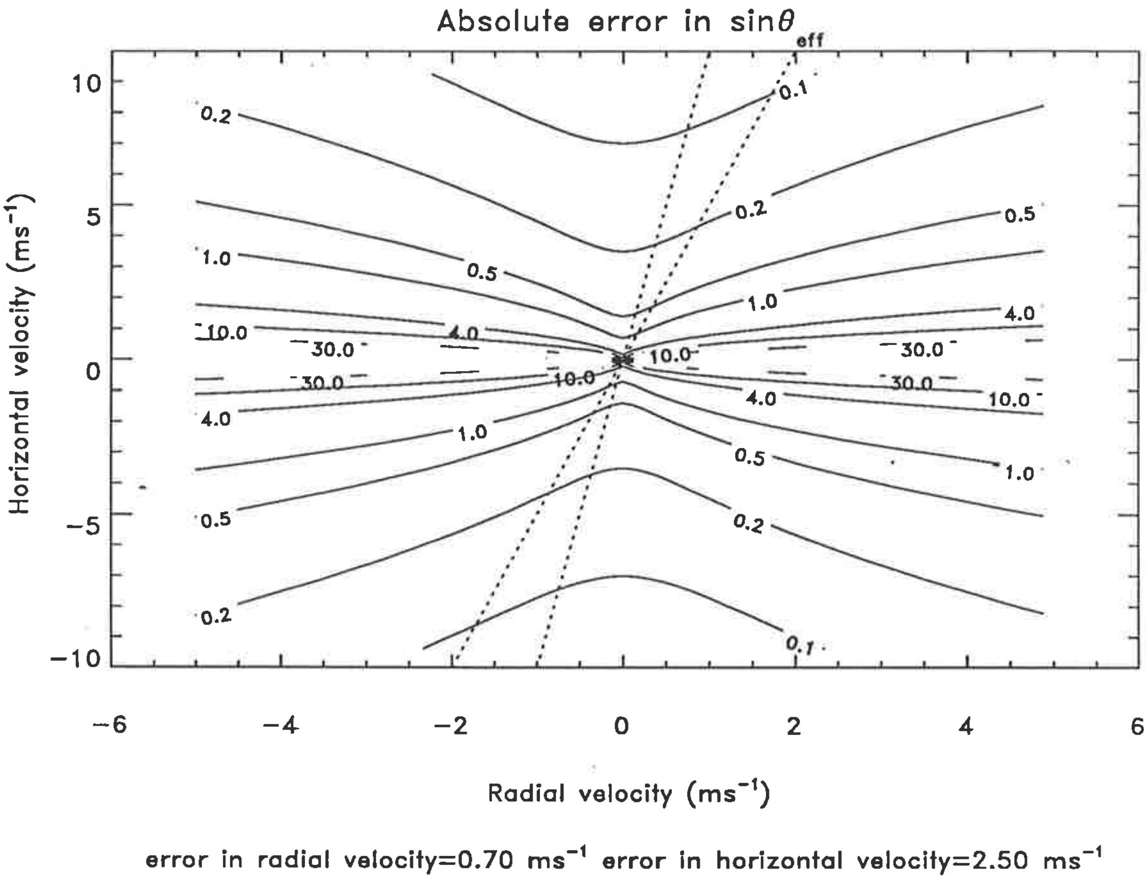

Figure 5.8: Contour plot of the error in $\sin\theta_{eff}$ where $\sin\theta_{eff}$ is obtained using equation 5.4.

Contours of this function for values of ΔV_{hor} =2.5ms^{-1} and ΔV_{rad} =0.7ms^{-1} are plotted in figure 5.8. The value of 2.5ms^{-1} used for ΔV_{hor} falls in the middle of the range of uncertainties deduced from May (1988). The error estimate for V_{rad} comes from Reid and Vincent (1987). The dependence of V_{hor} on V_{rad} can now be introduced by considering the points that lie in the region $V_{rad} = (0.1 \text{ to } 0.2)V_{hor}$. It can be seen that in this region errors in $\sin\theta_{eff}$ of the order of 0.1 exist in the range $|V_{hor}| < 10\text{ms}^{-1}$. This suggests that only values of $V_{hor} > 10\text{ms}^{-1}$ (at least) should be used.

The values of $\sin\theta_{eff}$ obtained using equation 5.4 with values where $|V_{hor}|$ <10ms^{-1} removed are given in figure 5.9. (Recall that V_{hor} is the component of horizontal velocity in a plane containing the zenith and the radar beam.) Fewer large values of $\sin\theta_{eff}$ exist but there are still some negative values. Most importantly though, at some heights the number of data points has been reduced considerably. Applying this rejection to values

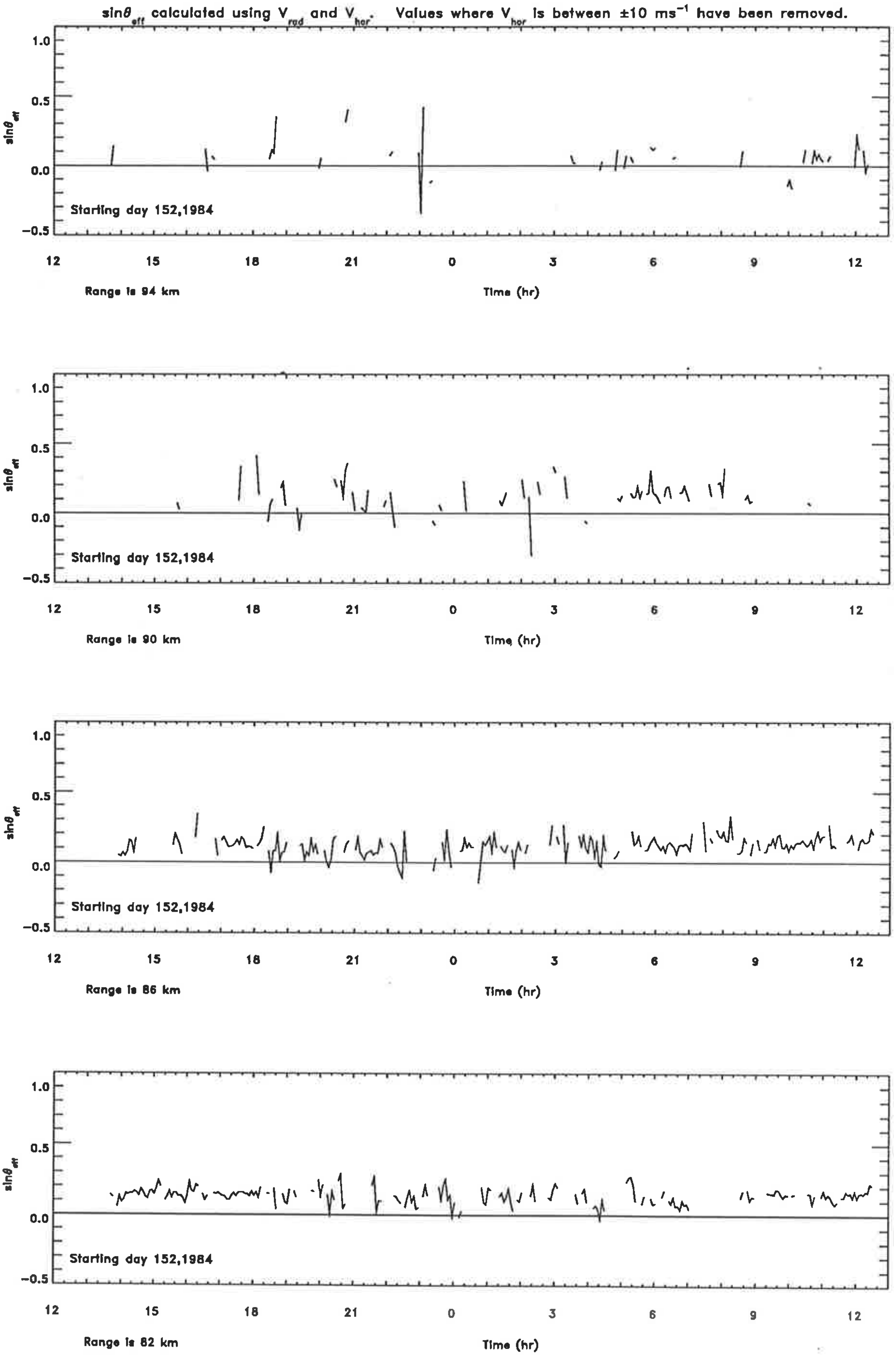

Figure 5.9: The $\sin\theta_{eff}$ values obtained using equation 5.4 with values where $|V_{hor}|$ <10ms^{-1} removed.

obtained using equation 5.3 yields similar results. Thus, at least at short time scales, the velocity method of obtaining $\sin\theta_{eff}$ is unsuitable.

Another possible method, where $\sin\theta_{eff}$ is obtained using the pattern scale from the full correlation analysis was, presented earlier in this chapter. Equation 5.9 was used to obtain the values of $\sin\theta_{eff}$ for the data obtained on day 152/153 and the results are presented in figure 5.10. Some variation in $\sin\theta_{eff}$ is still present (the fluctuations are of greater magnitude at night) but a well-behaved data set results. These were used in equation 5.4 to obtain the horizontal velocities (under the assumption that the vertical velocity is zero) and these are compared with the spaced-antenna velocities in figure 5.11 and 5.12. It can be seen that the agreement is now much better than when an 11.6°off-zenith beam was assumed. This is quantified through the average differences of the two velocities presented in figure 5.13.

The presence of outliers should be noted (e.g. just prior to 04:00 on day 153 at 82 km and at around 00:40 on day 153 at 86 km). Investigations of these points show values of radial velocity and $\sin\theta_{eff}$ that are moderately consistent with those around them. Their ratios, however, are quite unrealistic and they were therefore removed from the data set. Their cause is uncertain although a specular event (where one echo is much stronger than the others contributing to the power spectrum and causes a biasing of the mean of the spectrum) in the Doppler beam may be to blame.

As this velocity difference does not involve any squaring or moduli, both positive and negative values are possible. It can be seen that at almost all heights in the region of interest, the pattern-scale method of obtaining the effective pointing angle gives Doppler results that are more consistent with the spaced-antenna velocities. The average zonal velocities in figure 5.13 show that the minimum difference occurs at an altitude where the zonal velocity is a maximum. This suggests that the variations in the average difference are not simply due to variations in the average zonal velocity and that a real improvement in the agreement between the two methods has been obtained.

Although these results show a better agreement between the pattern-scale-corrected Doppler velocities and the spaced-antenna velocities, there does still seem to be a sys-

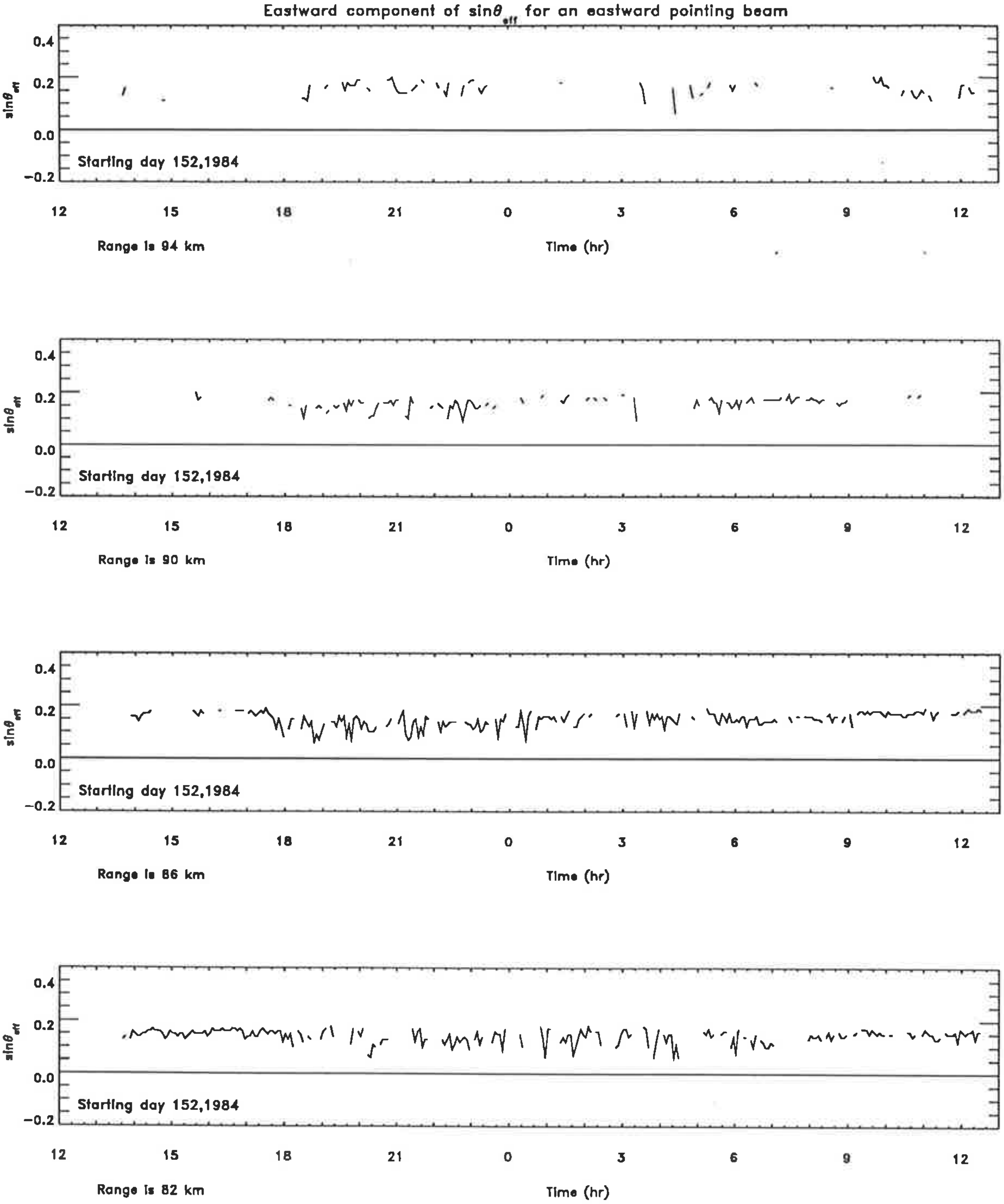

Figure 5.10: Values of $\sin\theta_{eff}$ obtained from the pattern scale for heights 94,90,86 and 82 km.

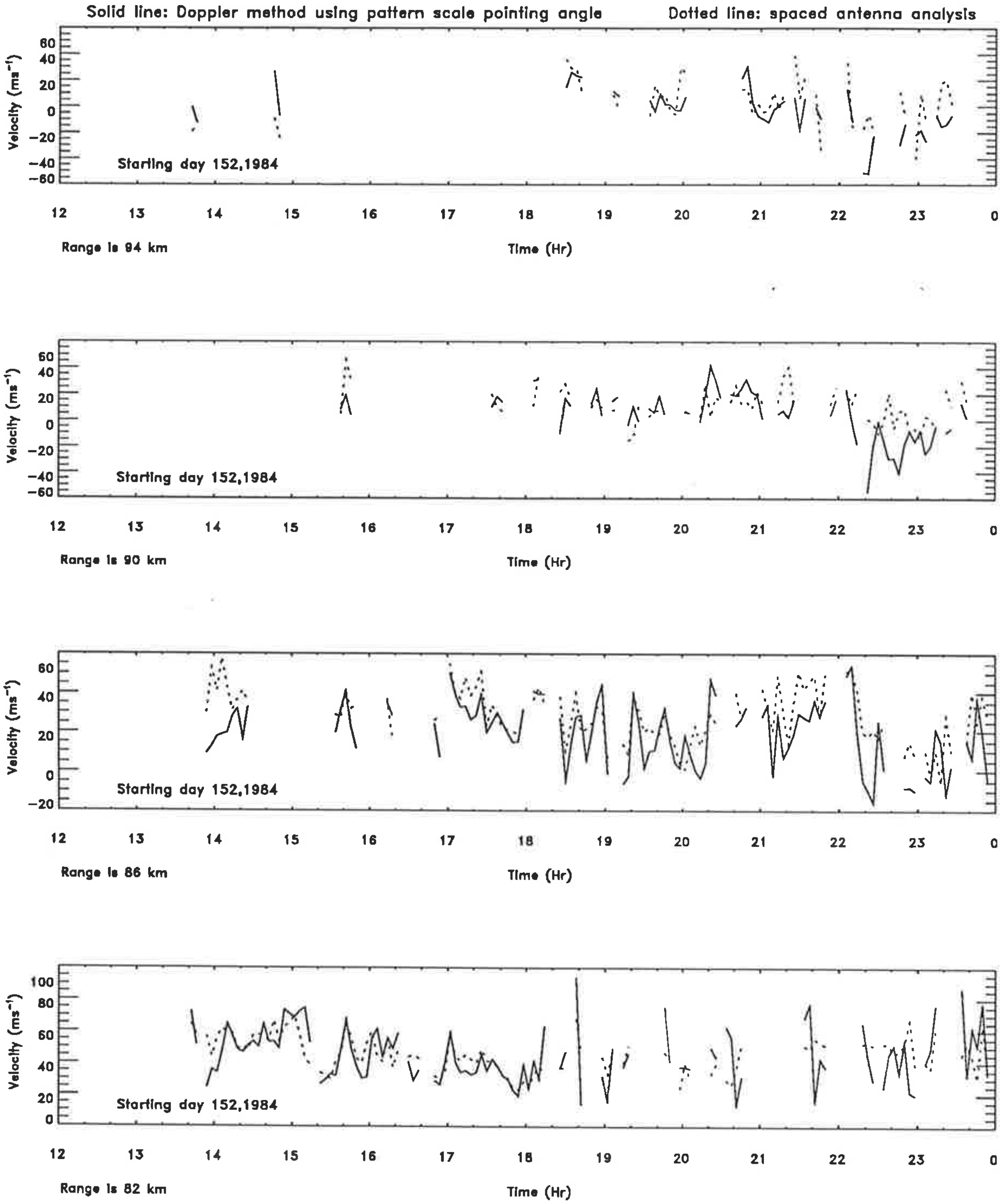

Figure 5.11: Spaced antenna winds (dotted lines) and Doppler winds using pointing angles derived from the pattern scale, for heights 94, 90, 86 and 82 km. (Day 152 data.)

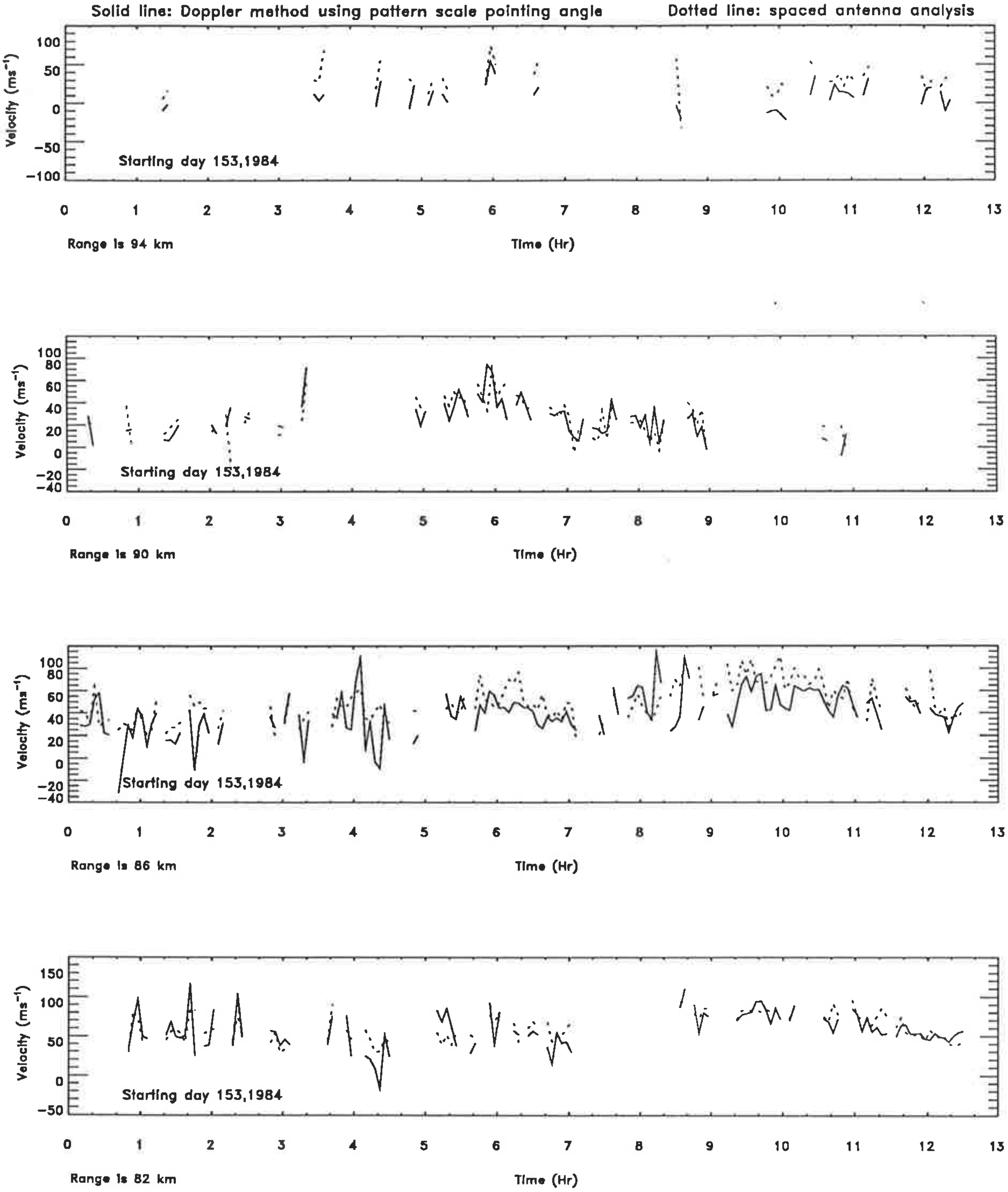

Figure 5.12: Spaced antenna winds (dotted lines) and Doppler winds using pointing angles derived from the pattern scale, for heights 94, 90, 86 and 82 km. (Day 153 data.)

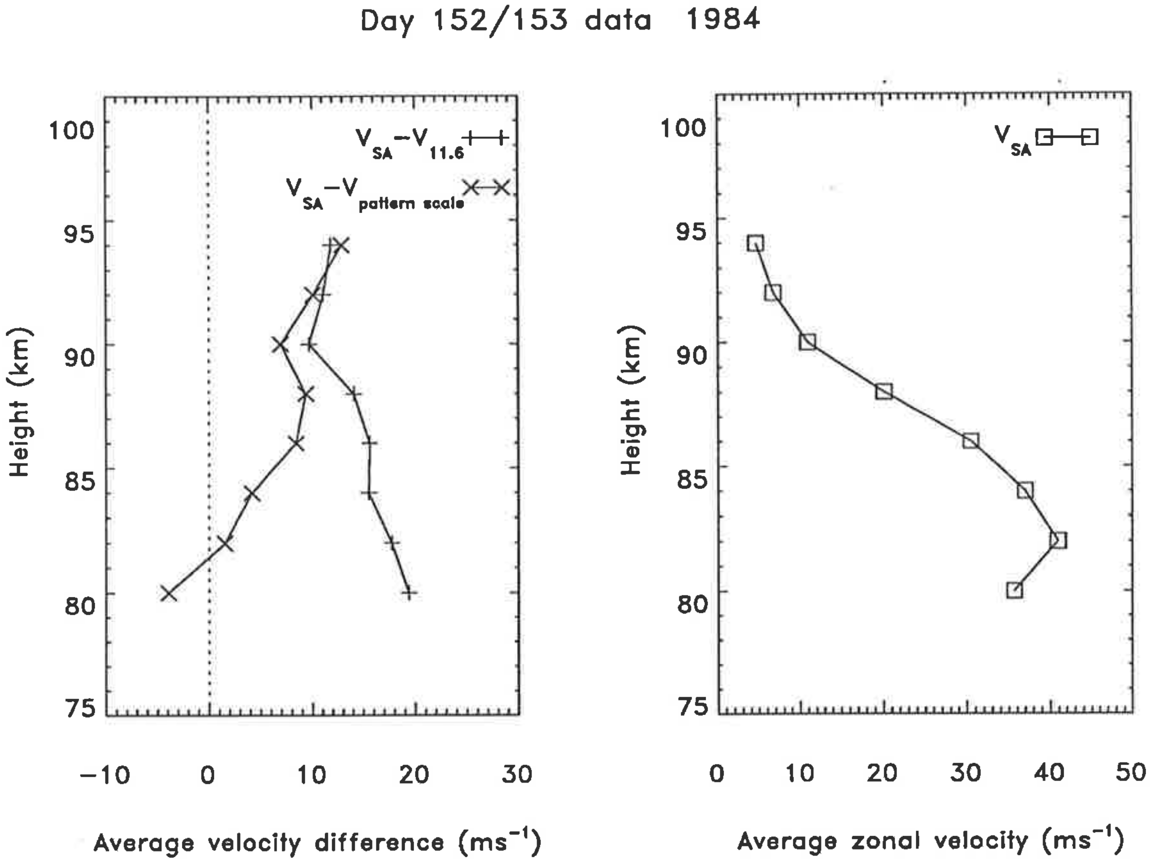

Figure 5.13: The average velocity difference and the average zonal velocity as a function of height for the day 152/153 data, 1984

tematic difference. Vertical velocities could cause this difference on short time scales. However, as the difference statistics were compiled from almost a full day of data, any vertical velocity component of the difference would have averaged to a value close to the mean on this time scale. This mean is widely thought to be of the order of tens of cms^{-1} (see e.g. Rüster and Reid 1990) and cannot account for the differences seen here.

Radial velocity data from a "narrow vertical" beam are available and *could* be used in this analysis to take out the effects of vertical velocity, however, some questions about these data that were raised by Murphy (1984) cast doubt on this course of action. These included the susceptibility of these measurements to contamination by horizontal velocities. Velocities from wide beams (such as one of the spaced-antenna beams) are probably less susceptible to this problem because their Doppler spectra will be much broader, but their sampling volumes cover a larger altitude range. The wide-beam and narrow-beam vertical velocities do in fact differ but the uncertainties in whether either or neither of them are correct make it best to avoid their use where possible.

Another possibility is that the polar diagram of the scatterers is not centred on the zenith. The differences seen in figure 5.13 could perhaps be explained by a shift from zenith of the order of 1 or 2 degrees, which is not inconceivable. This shift would not change the amplitude of the spatial correlation function but would introduce a phase variation. The phase of the spatial correlation function is not necessary in the full correlation analysis and is not measured with the Buckland Park system. Thus it is difficult to see if a phase variation across the array is occurring. Consideration of data from beams pointing at equal off-vertical angles on either side of the zenith may be instructive, so some dual-beam data taken on days 168/169 of 1984 will be considered shortly.

It may also be possible that there is a systematic error in the spaced-antenna method. Some sources of systematic error are discussed in Hocking *et al.* (1989), the most relevant being that proposed by Røyrvik (1983). Variations in vertical velocity over the sampling volume would cause the diffraction pattern on the ground to move, over short time scales, in a manner that does not represent the bulk motion of the atmosphere. Røyrvik presented some parameters of the gravity waves that would be of greatest concern but little is known about how often they occur. Meek *et al.* (1985) suggested that a peak in the power spectrum of spaced-antenna velocities near the Brunt-Väisälä frequency was evidence for some contamination of the data by vertical velocities but noted that this peak occurred rarely in their spectra. Simulations conducted by Meek and Reid (1984) concluded that gravity-wave vertical velocities did not affect spaced-antenna measurements, however, the sampling times that they used were considerably longer than those utilised at Buckland Park. This would tend to average out the source of error proposed by Røyrvik. In general, atmospheric motion appears to be quasi-random in nature and the assumption of a wind field that is uniform over the sampling volume is a satisfactory one. Given this assumption, the effects of vertical velocities and effective pointing angle variations being considered here are not considered a problem in the spaced-antenna method making it a suitable bench-mark for this study. Previous studies in which the spaced-antenna method was compared with direct wind observations using rocket techniques (Vincent *et al.* 1977) showed that if it is biased at all, it is in the sense of the velocity being slightly too small. This is the wrong sense to explain the present velocity differences.

Data collected on days 168 and 169 of 1984 (June 16th and 17th, about two weeks after that presented previously) consisted of spaced-antenna winds and radial velocities from an eastward-pointing and a westward-pointing Doppler beam. Both these beams were phased to point at 11.6° from the zenith. As before, equation 5.9 was used to calculate an effective pointing angle. This was used to obtain a horizontal velocity value for each data point and each beam. The westward-beam velocity was then folded over (by changing its sign) to compare it with the eastward-beam value. Half-hour averages of these data are presented in figure 5.14 for heights 82, 86, 90 and 94 km. It can be seen that the two horizontal velocities that are inferred from the radial velocities mirror each other fairly well. The spaced-antenna value often falls between these two velocities but at times does not. Some possible causes of this behaviour will now be considered.

Given the beam configuration presented in figure 5.15, and the assumption of a

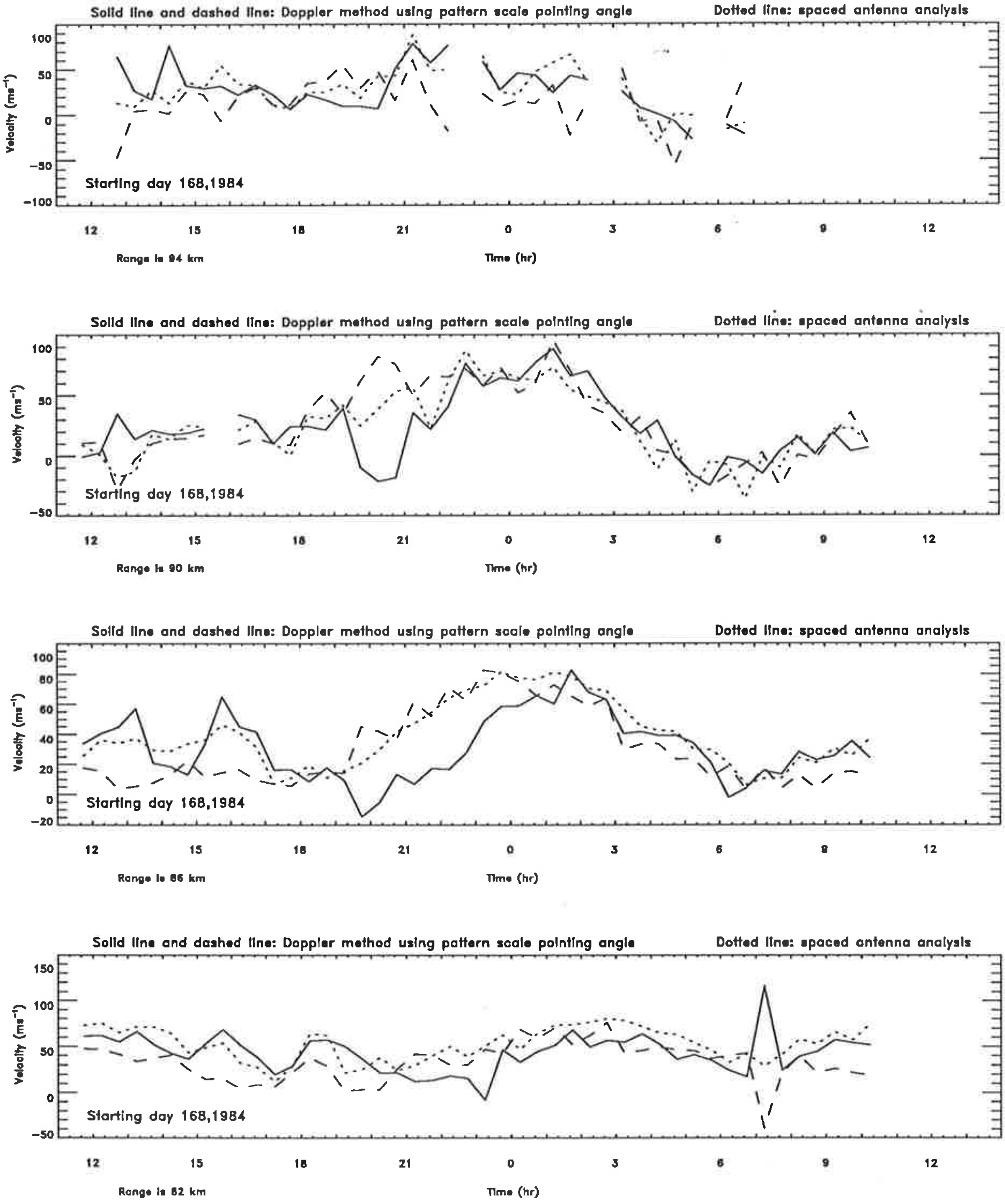

Figure 5.14: Half-hour averages of the horizontal velocities inferred from eastward (solid line) and westward (dashed line) beam data and of the spaced antenna velocity for days 168/169 of 1984.

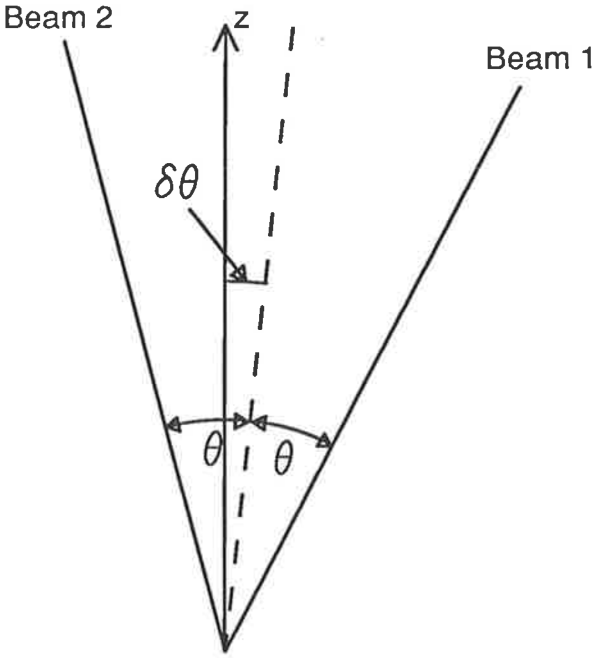

Figure 5.15: Effective beam configuration for a pair of off-vertical beams in the presence of a scattering polar diagram that is centred off zenith.

uniform velocity field, the radial velocities measured in each beam will be

$$V_1 = V_{hor}\sin(\theta - \delta\theta) + w\cos(\theta - \delta\theta) \tag{5.12}$$

$$V_2 = -V_{hor}\sin(\theta + \delta\theta) + w\cos(\theta + \delta\theta). \tag{5.13}$$

Assuming that $\theta + \delta\theta$ is small, this can be approximated by

$$V_1 = V_{hor}(\theta - \delta\theta) + w \tag{5.14}$$

$$-V_2 = V_{hor}(\theta + \delta\theta) - w \tag{5.15}$$

where θ and $\delta\theta$ are expressed in radians. The negative sign on V_2 makes the expression more comparable to figure 5.14. V_1 and V_2, however, are radial velocities whereas those in figure 5.14 are horizontal velocities. They are expressed in this form to allow comparison with spaced-antenna velocities but they should be thought of as $V_1/\sin\theta_{eff}$ and $V_2/\sin\theta_{eff}$ in this discussion.

If we set $\delta\theta$ to zero and consider the effect of vertical velocities, V_1 and $-V_2$ become

$$V_1 = V_{hor}\theta + w$$

$$-V_2 = V_{hor}\theta - w.$$

It can be seen that a vertical velocity will cause the lines in figure 5.14 to move away from a common point. This movement, however, will be equal in both beams (given the assumption of a uniform velocity field) but in opposite directions because V_{hor} is the same in both expressions.

If $\delta\theta$ is non-zero, but $w = 0$ we get

$$\begin{aligned} V_1 &= V_{hor}\theta - V_{hor}\delta\theta \\ -V_2 &= V_{hor}\theta + V_{hor}\delta\theta. \end{aligned}$$

Once again the lines in figure 5.14 will move away from a common point. Thus only symmetric departures from a common point are possible when the effective polar diagram of the scatterers is not centred on the zenith or vertical velocities are non-zero.

These effects can explain the "mirroring" that is seen in the radial beam horizontal velocities of figure 5.14. The extent to which each effect contributes to the mirroring cannot be determined because $\delta\theta$ and w are unknown.

The fact that the spaced-antenna velocities do not always fall exactly between the eastward-beam and westward-beam values cannot be explained by the above effects. In order to reconcile *these* values, one of the spaced-antenna or radial velocities, or the values of $\sin\theta_{eff}$ must be in doubt. Although all are possible, problems with $\sin\theta_{eff}$ are considered most likely. The full correlation analysis assumes that the amplitude of the spatial correlation function is Gaussian making the angular spectrum of the scatterers Gaussian as well. If this is not the case then the pattern scale parameter used in this analysis will not be an appropriate measure of the pattern scale, and the value of $\sin\theta_{eff}$ will be in error.

Some studies of the angular spectrum of mesospheric echoes have been carried out. Haug and Pettersen (1970) computed the angular spectrum from the autocorrelation function by assuming that the diffraction pattern does not change rapidly with time. As their method precludes a maximum scatter from the zenith, however, their results are difficult to interpret. Vincent and Belrose (1978) required an angular distribution of scattered powers with a decrease at the zenith to explain some of their results but noted that this angular distribution could come about if a strong scattering layer was situated just below a range gate when measured overhead. The intersection of the curved sampling volume with this scattering layer would enhance the off-vertical scatter giving a peak in the scattering power at an angle away from the zenith.

Murphy (1984) correlated the horizontal winds measured using the spaced-antenna method at Buckland Park with the Doppler winds from a "vertical" beam over three 12 week periods in 1984. The direction of maximum correlation between horizontal and vertical winds suggested that the scattered power was centred on a point between 0.4° and 1.0° off zenith depending on azimuth, height and season. Variations of this magnitude cannot explain all of the "mirroring" seen previously but it should be noted that these variations may be larger on shorter time scales.

Although the Gaussian form of the angular distribution $P_s(\theta)$ is easy to manipulate algebraically, it suggests that the scattered power goes to zero at large scattering angles. The work of Czechowsky *et al.* (1988) at VHF suggests that a constant should be added to this Gaussian to allow scatter from isotropic irregularities at large zenith angles. This idea is consistent with the findings of Hocking (1979) who compared mesospheric echo powers at 1.98MHz from a vertical and an 11.6° off-zenith beam. Hocking found that significant returns at large off-vertical angles occurred above 80km. The changing nature of the echoes as a function of height that Hocking observed is of interest and was noted in the work of Lindner (1975). Lindner found that echoes from near 80 km had a smaller angular spread than those from above that region. This would explain why the method of obtaining $\sin\theta_{eff}$ from the pattern scale works well at some levels but is less accurate at others. It suggests that this method of obtaining $\sin\theta_{eff}$ is more suited to narrow angular spectra. It is conceivable that, for these spectra, the additive constant proposed by Czechowsky *et al.*(1988) will be small compared to the peak power and the Fourier transform of this will be mainly Gaussian. The increasing importance of this constant at greater heights will introduce a spike into the spatial correlation function and affect the parameters obtained from it.

The pattern-scale values used in this work have been taken as correct. Although it is likely that they will have an error associated with them, the magnitude of this error is unknown. It is hoped that some planned modelling studies (D. Lesicar, private communication 1989) will provide estimates of the error in this and other spaced-antenna parameters.

5.2.2 Obtaining effective pointing angles from averaged data.

It was stated earlier that the effective pointing angle could be obtained from the root-mean-square (RMS) velocities but the method presented assumed that $\sin\theta_{eff}$ was a constant. There is now evidence that this is not the case and as a result of that, the methods of obtaining $\sin\theta_{eff}$ from RMS values must be changed. As the basic theory to be used here involves the relationship between the variances of different distributions, it is variance data that will be considered rather than the RMS values.

Given the expression

$$\sin\theta_{eff} = \frac{V_{rad}}{V_{hor}} \quad or \quad S = \frac{R}{H} \tag{5.16}$$

(where S, R and H are used for ease of subscripting) then the variances of the distributions of S, R and H are related by

$$\frac{\sigma_S^2}{S^2} = \frac{\sigma_R^2}{R^2} + \frac{\sigma_H^2}{H^2} - 2\frac{\sigma_{HR}^2}{HR} \tag{5.17}$$

where σ^2 denotes a variance and σ_{HR}^2 is the covariance between H and R. This can be rearranged to give an expression for S.

This expression differs from that used by Fritts and Vincent (1987) in that σ_S^2 and σ_{HR}^2 are non-zero. If these terms are ignored, the results are as shown in figure 5.16. The average of the values of $\sin\theta_{eff}$ from the pattern scale are also shown. It can be seen that the results of the two methods are quite different. Reid (1988) also compared the pointing-angle profile of Fritts and Vincent to those of other workers at Adelaide and found that they differed. An attempt is now made to explain these differences.

Until now, the effective pointing angle has not been allowed to vary with time in theoretical treatments aimed at obtaining its value. Thus there has been an *a-priori*

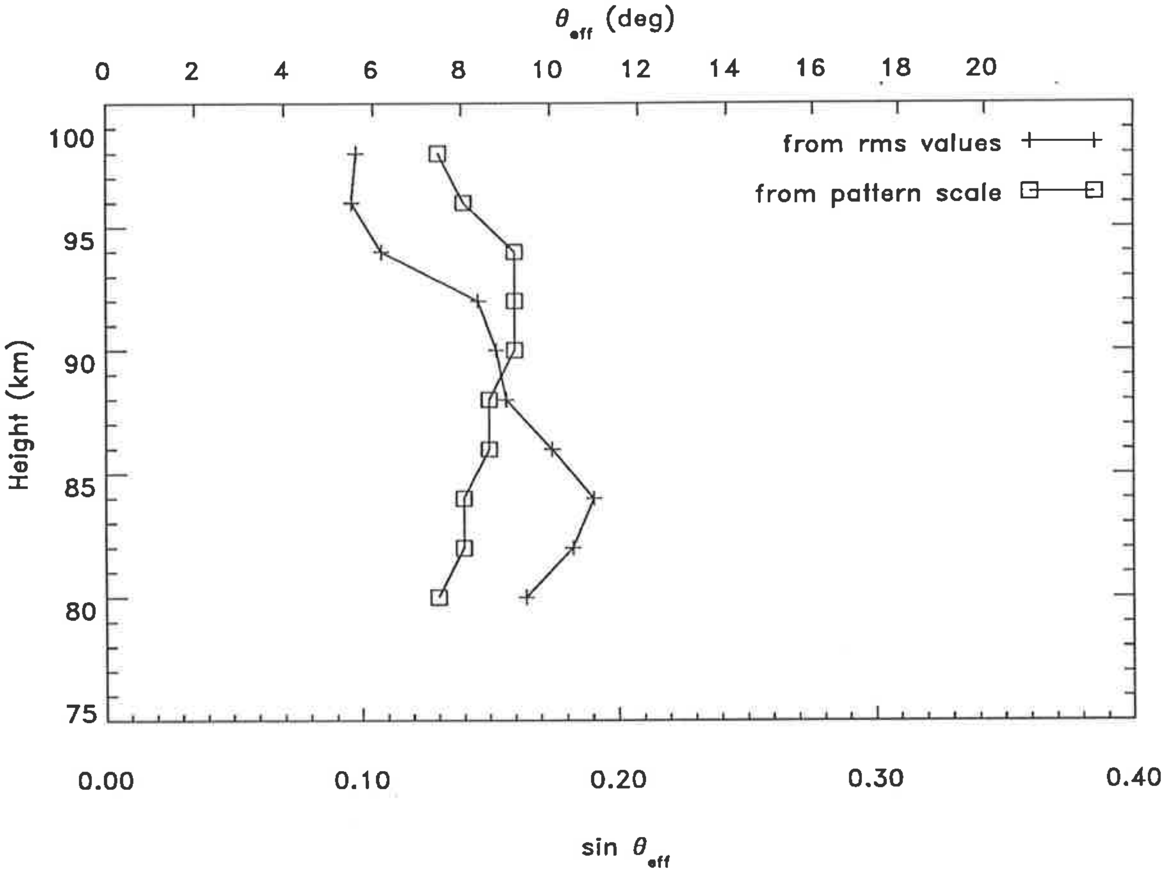

Figure 5.16: The effective pointing angle, following Fritts and Vincent (1987) and from the pattern scale.

assumption that $\sigma_S^2 = 0$. The work presented in this chapter has shown that this is not so. Therefore, in order to use equation 5.17 an estimate of σ_S^2 must be obtained. The σ_{HR}^2 term is also non-zero as there will be a correlation between the radial velocity and the horizontal velocity. The radial velocity will also have an independent component due to vertical velocities. Therefore it is difficult to estimate what the value of σ_{HR}^2 will be.

Some attempts were made to obtain $\sin\theta_{eff}$ in this way by assuming various levels of correlation between H and R; however, this method seemed quite unreliable. When applied to the dual beam data of days 168/169, two $\sin\theta_{eff}$ profiles that were not only different to each other but different to the pattern scale profile resulted.

5.3 Obtaining the pointing angle profile for momentum flux analysis.

In this chapter so far, a number of methods have been considered for obtaining the effective pointing angle for an off-zenith beam in the Buckland Park 2MHz radar system. The purpose of this was ultimately to improve estimates of momentum flux considered later in this thesis.

The method which utilises the scale of the spatial correlation function will be used. Although it seems more suitable at some levels in the mesosphere, it still gives acceptable results at others. It also has the advantage of allowing for any azimuthal asymmetries in the angular spectrum that may exist.

Much of the data to be considered in this thesis do not have concurrent spaced-antenna data associated with them. In these cases, the spaced-antenna data obtained before and after the momentum flux run will be used to obtain a pointing angle profile.

5.4 The effect of pointing angle variations on the momentum flux analysis

The analysis method proposed by Vincent and Reid (1983) assumes that the pointing angle remains constant with time. Results presented earlier in this chapter, however, suggest that this is not the case. It is therefore necessary to gauge the effect of pointing angle variations on the Vincent-Reid analysis.

To do this, a computer model has been constructed. A spatially uniform but time-varying two-dimensional wind field is set up and a pair of finite-width radar beams are replaced in the simulation by two coplanar infinitely narrow beams pointing at an angle of θ_{eff} from the vertical on either side of zenith. The wind velocity at any one time is then projected onto each beam to produce two radial velocities. Variations in the wind field as a function of time result in a radial-velocity time series for each beam. This can be used to calculate $\overline{u'w'}_{exp}$ using the Vincent-Reid analysis. The true $\overline{u'w'}$ ($\overline{u'w'}_{true}$) can also be calculated by averaging the product of the instantaneous velocity components for the duration of the times series. In an ideal situation, these quantities would be exactly the same. In this case, the effective pointing angle θ_{eff} has been allowed to vary as a function of time making a difference between $\overline{u'w'}_{true}$ and $\overline{u'w'}_{exp}$ possible.

The variations in the pointing angle are modelled using distributions of ϕ, the angle between the semi-major axis of the correlation ellipse and North, $r(=\eta_1/\xi_1)$, the axial ratio of this ellipse and η_1, its semi-major axis length (in metres). Distributions of these parameters were obtained from the spaced-antenna data presented earlier in this chapter. It was then necessary to generate values of ϕ, r and η_1, that have distributions like those observed in the spaced-antenna data. This is not an easy thing to do in general, however, if these distributions had been Gaussian, this could have been done using the equation

$$X = \sigma\sqrt{-2\ln r_1} \times \sin(2\pi r_2) + \mu$$

where r_1 and r_2 are random numbers in the range (0,1), σ and μ are the standard deviation and mean of the Gaussian distribution respectively and X is one value from

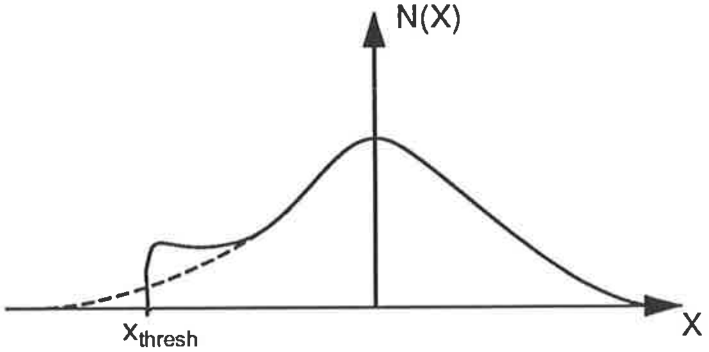

Figure 5.17: An example of folding a Gaussian distribution

the distribution. This is known as the *Box-Muller* method. (see e.g. p202, Press *et al.* 1986) The distributions of ϕ, r and η_1 were not Gaussian but it was found that they could be approximated to a suitable standard by folding a Gaussian distribution about x_{thresh} as illustrated in figure 5.17. This involves the following:

$$\text{If } X < x_{thresh},\ X \rightarrow x_{thresh} + (x_{thresh} - X).$$

By varying σ, μ and x_{thresh}, a variety of distributions are available. In generating r and η_1 the values of μ, σ and x_{thresh} that were used were

$$\text{for } r: \quad \mu_r = 1.3, \quad \sigma_r = 0.5, \quad x_{thresh} = 1.0;$$
$$\text{for } \eta_1: \quad \mu_\eta = 300, \quad \sigma_\eta = 125, \quad x_{thresh} = 175.$$

Values of ϕ were taken to be evenly distributed between 0° and 180° and the equation, $\phi = r_3 \times 180$ was used where r_3 is a random number in the range (0,1). The distributions for r, η and ϕ that these equations produce, and those that they seek to imitate are given in figure 5.18.

The ϕ, r and η_1 values obtained in this way are combined to produce a value of $\sin\theta_{eff}$ using equation 5.9 of the previous section. This approach assumes that the covariance between ϕ, r and η_1 is zero. Whether or not this is so could be determined from the spaced-antenna data presented earlier; however, it was found that the time

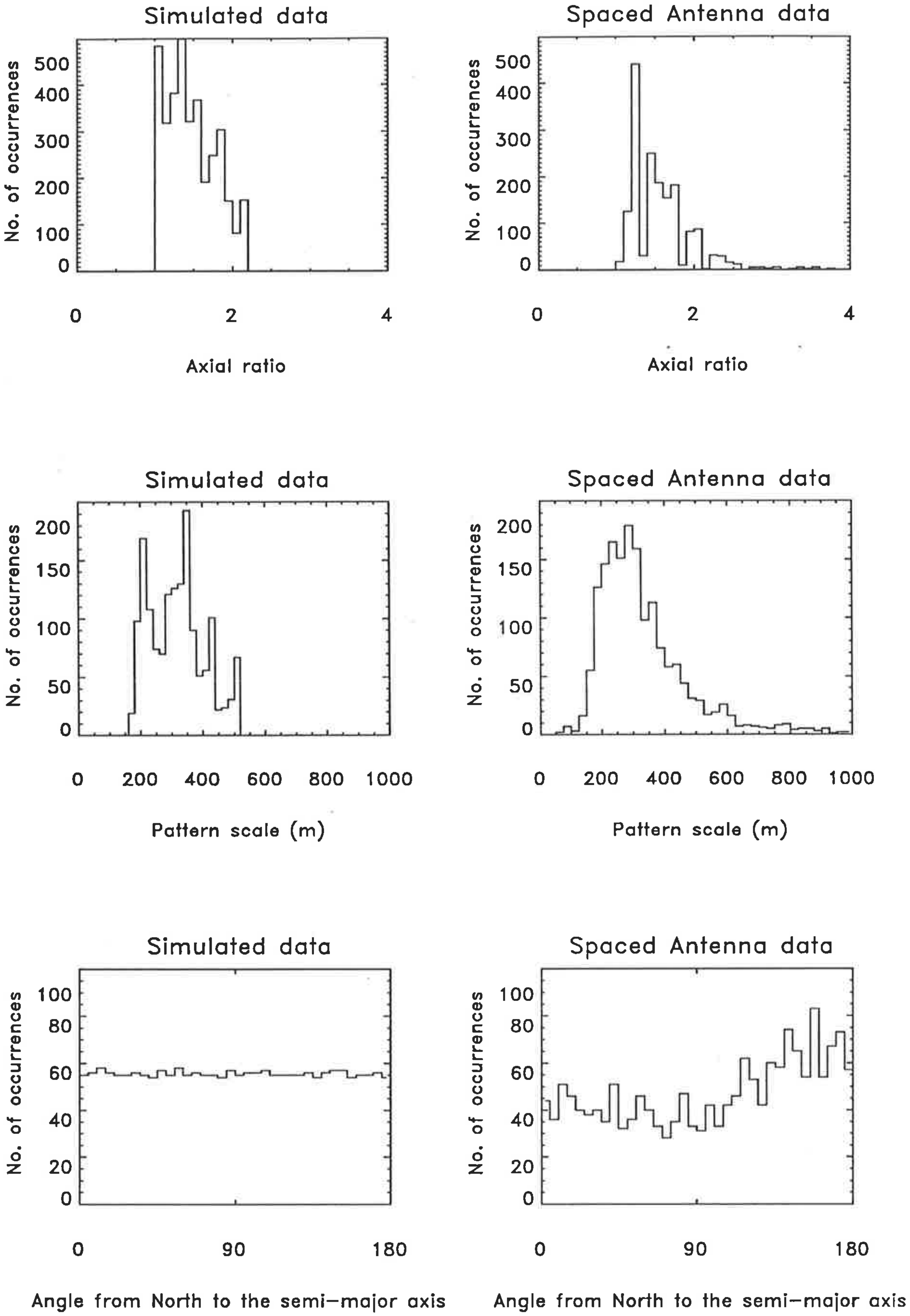

Figure 5.18: Distributions of the values of axial ratio, length of the semi-major axis and the angle from north to the semi-major axis of the correlation ellipse obtained from the simulation and from some spaced-antenna data

series of $\sin\theta_{eff}$ obtained in the way described above were of similar character to those given in the previous section. Thus ϕ, r and η_1 were taken as independent in the interest of simplicity. Apart from being used in the calculations of radial velocity for the two beams, the values of $\sin\theta_{eff}$ are also averaged to produce a value of θ_{eff} for the Vincent-Reid analysis.

With beams pointing near to the vertical, small variations in pointing angle will affect the radial velocity resulting from the projection of horizontal velocities onto the radar beam to a greater extent than the radial velocity due to the vertical velocity projection. It would therefore be useful to consider the effect on $\overline{u'w'}$ of wind fields where either one of the vertical or the horizontal velocities dominate. Short period gravity waves have predominately vertical parcel motions whereas longer-period waves have a more significant horizontal velocity component. Therefore a set of wind fields made up of monochromatic gravity waves of different periods should make it possible to gauge the effect of pointing angle variations under a suitable variety of circumstances. To this end, the following process was adopted. A gravity-wave period was chosen in the range 10 to 480 min and the horizontal-velocity amplitude of a gravity wave at that period was calculated from a power spectrum taken from Vincent (1984). The amplitude of the vertical velocity was then obtained from the gravity-wave polarisation relations (Hines 1960). This gave a two-dimensional velocity vector (u', w'). The amplitude of this vector was varied sinusoidally with time between the limits (u', w') and $(-u', -w')$, and projected onto the radar beams at $\pm\theta_{eff}$ from zenith. It should be noted that under the assumptions outlined above, it was not necessary to introduce the *spatial* variation in velocity that would be typical of a gravity wave. Therefore in the interest of simplicity, this was not done in this model. Samples of radial velocity were taken at equally-spaced intervals from a time series ten times the wave period in length, and $\overline{u'w'}$ was calculated using the Vincent-Reid analysis. This was repeated for different periods and therefore for wind fields of different character.

A graph of the percentage error in $\overline{u'w'}$ as a function of gravity-wave period is presented in figure 5.19. The percentage error is calculated using the expression 100 ×

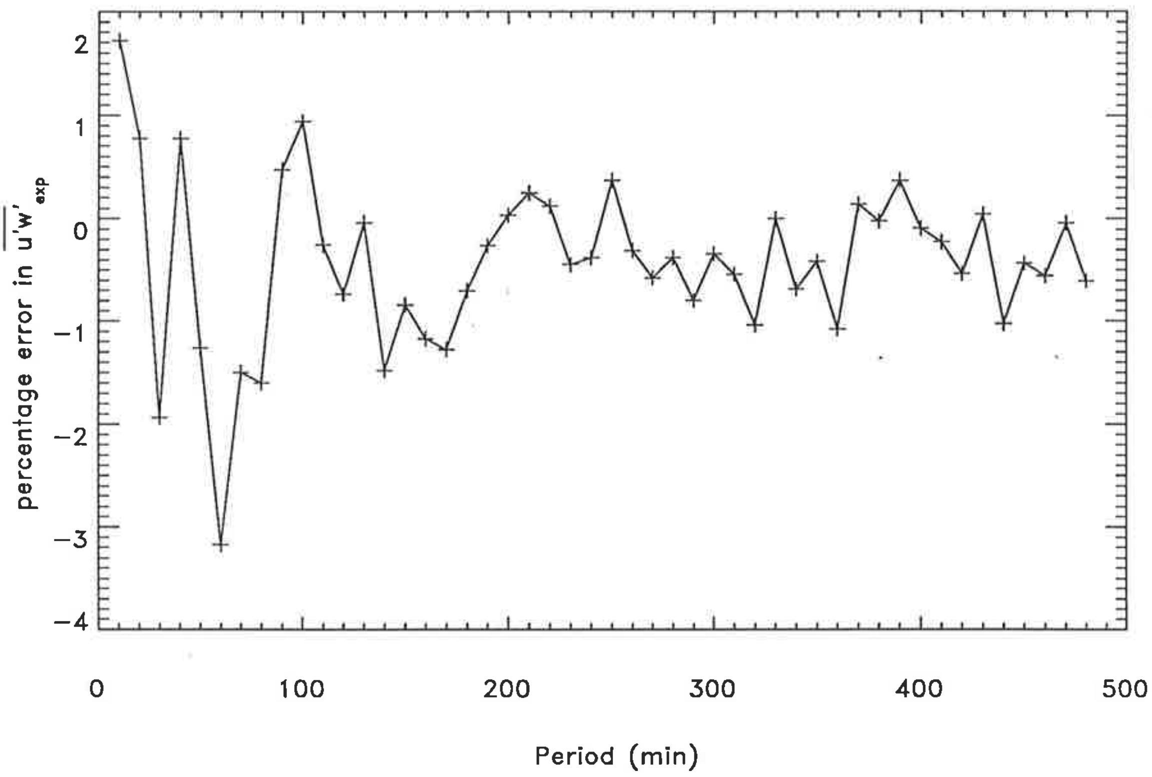

Figure 5.19: The error in $\overline{u'w'}$ as a function of gravity-wave period expressed as a percentage

$(\overline{u'w'}_{exp} - \overline{u'w'}_{true})/\overline{u'w'}_{true}$ where $\overline{u'w'}_{exp}$ is the value obtained using the Vincent-Reid analysis and $\overline{u'w'}_{true}$ comes from the instantaneous u' and w' values. It can be seen that in general an error of less than 1 percent is the result of the pointing-angle variations although at shorter periods the errors are as large as 3 percent. This is in contrast with the arguments about horizontal and vertical velocities presented above and is due to the fact that, to remain consistent with the momentum-flux analysis methods to be used in this thesis, a time separation between simulated data points of 4 min was chosen. This undersampling seems to have a more significant effect at these shorter periods and in fact is less pronounced when a time step of 2 min is used. In any case, an error of 3 percent or less is quite acceptable.

This model has made it possible to estimate the magnitude of the error in $\overline{u'w'}$ due to short time-scale variations in the beam pointing angle. Other sources of error in $\overline{u'w'}$

exist and some of these can be quantified. It is now possible to compare these errors with that due to pointing angle variations. A further discussion of the Vincent-Reid analysis will be presented in the following chapter.

5.5 Summary

Previous applications of the Vincent-Reid analysis to produce $\overline{u'w'}$ using MF radar data (Vincent and Reid 1983, Fritts and Vincent 1987, Reid and Vincent 1987) gave results whose magnitudes were somewhat uncertain. This was due to an erroneous or inexact estimate of the effective pointing angle (θ_{eff}), a parameter required by the Vincent-Reid analysis.

Attempts to overcome this problem have been described in this chapter. A method of obtaining effective pointing angles from simple pattern scale parameters and the application of diffraction theory has been presented and tested. It produced results that ranged from significant improvement to little improvement over methods used previously.

Some of the methods that have been used in the past were reviewed and found to be inappropriate. In particular, the presence of variations in θ_{eff} on short time-scales made methods involving comparison of horizontal and radial velocity variances to find the effective pointing angle less reliable than previously thought.

The possibility that these short term variations in θ_{eff} may introduce a significant error in measurements of $\overline{u'w'}$ obtained using the Vincent-Reid analysis was considered. Through the use of a simple model it was found that errors of the order of a few percent were typical as a result of this effect making it far less important than correctly estimating the mean value of θ_{eff}.

Chapter 6

Momentum flux analysis

The importance of momentum transport in balancing the mesospheric momentum budget was demonstrated in chapter 1. It was suggested there that gravity waves were the most likely process of transporting momentum from the energy-dense troposphere into the mesosphere and that some quantitative measurements of the gravity-wave momentum flux would be of great value. In this chapter, a method of measuring gravity-wave momentum flux using the Buckland Park radar system is presented. The quantity that is measured, $\overline{u'w'}$ (and $\overline{v'w'}$) is considered in a simple example as an introduction to the analysis method, however, this quantity is fundamental in some complex formulations of atmospheric dynamics. Before the analysis method is presented, some origins of $\overline{u'w'}$ will be discussed.

One interpretation of $\overline{u'w'}$ stems from an analogy with statistical mechanics. If a plane in a fluid (gas or liquid) is considered, then the fluid on one side of the plane will exert a force per unit area (a stress) on the fluid on the other side of the plane. If the fluid is inviscid, this force will only act normally to the plane. If, however, the fluid is viscous, motions parallel to the plane will be transferred across the plane by viscosity and a stress parallel to the plane will result. Thus, viscosity is transferring momentum across the plane. If this concept is extended to three dimensions by considering three mutually perpendicular planes, each plane will have associated with it stresses which have three components, one normal to the plane and two mutually perpendicular components that are parallel to the plane giving nine stress components in all. A convenient notation for these components is a tensor (e.g. Reif 1965). It is possible to draw an analogy between the viscosity above (molecular viscosity) and similar effects due to turbulence. In this analogy, the tensor described above is called the "Reynolds stress tensor" and it has the form $\psi_{ij} = -\rho\overline{v_i v_j}$ where $v_i, v_j \in (u', v', w')$ (Gossard and Hooke 1975). A further analogy to the cross-products of gravity-wave perturbation velocities is often drawn as well so that the quantities $\overline{u'w'}$ and $\overline{v'w'}$ are termed elements of the Reynolds stress tensor.

The equations governing the dynamics of the atmosphere require a balance of quantities such as momentum, heat flux and mass flux. The coordinate system in which these equations are derived can only change the form of the equations and not the physical processes that they represent. Therefore, it is possible to alter the form of the equations in a manner that may emphasise and illuminate particular aspects of the dynamics they describe. Two possible coordinate systems include the Lagrangian and the Eulerian systems. The Lagrangian system follows the motion of a particular fluid element where the Eulerian system describes the properties of a fluid at a fixed point in space. A derivation of this latter system, known as the transformed Eulerian mean (TEM) system is of some utility in studies of the momentum budget. When the momentum balance is considered, a quantity $\nabla \cdot \vec{F}$ appears on the right-hand side of the equation (see e.g. Andrews *et al.* (1987), p128). The $\vec{F}$ in this expression is known as the Eliassen-Palm flux. The usefulness of this quantity lies in the fact that it depends on basic physical properties of the flow. The workers after whom the flux is named, Eliassen and Palm (1961), showed that for steady linear waves on a zonal flow, which was a function of latitude and height only, with no frictional or diabatic effects, $\nabla \cdot \vec{F} \equiv 0$. In the case of (shorter-period) gravity waves, $\vec{F} = (0, -\rho_0\overline{u'v'}, -\rho_0\overline{u'w'})$. Thus the result $\rho_0^{-1}(\rho_0\overline{u'w'})_z = 0$ (i.e. that the mean-flow acceleration is zero) for this class of waves, is a result from the Eliassen-Palm theorem. The utility of this approach and extensions of it does not lie in it's treatment of simple cases like the one above, but in its application to more complicated situations. For example, non-steady waves are treated in the *generalised Eliassen-Palm theorem* of

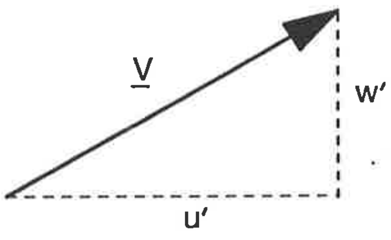

Figure 6.1: Components of velocity $\underline{V}$

Andrews and McIntyre (1976, 1978).

6.1 Momentum Flux

Consider a wind vector $\underline{V}$ as shown in figure 6.1. In this case the components, denoted u' and w' correspond to the horizontal and vertical velocities, the primes denoting perturbations from a mean. The following discussion is applicable to non-perturbation velocities but is applied in this thesis to data that has had low-frequency components removed. Hence the prime notation is used.

If the atmospheric density is ρ, the quantity $\rho u'$ is the horizontal momentum per unit volume. Under the influence of a vertical velocity w', the amount of some quantity crossing an area A in unit time is $w'A$. Combining these concepts, it becomes clear that $\rho u'w'$ =the amount of horizontal momentum per unit volume crossing unit area in unit time or the vertical flux of horizontal momentum. This quantity has been called the momentum flux. The significance of this quantity lies in its variation with height. If the momentum passing through one level differs from that at another level, a force must exist to account for this difference. The variations of momentum flux with height and the associated forces will be discussed further in the next chapter.

In order to obtain the quantity $u'w'$, all we need do is obtain the orthogonal components u' and w' of the velocity vector $\underline{V}$. This is shown schematically in figure 6.2a. To obtain these projections using radars, however, it is necessary to have two separate systems aimed at a common sampling volume. A more practical arrangement is

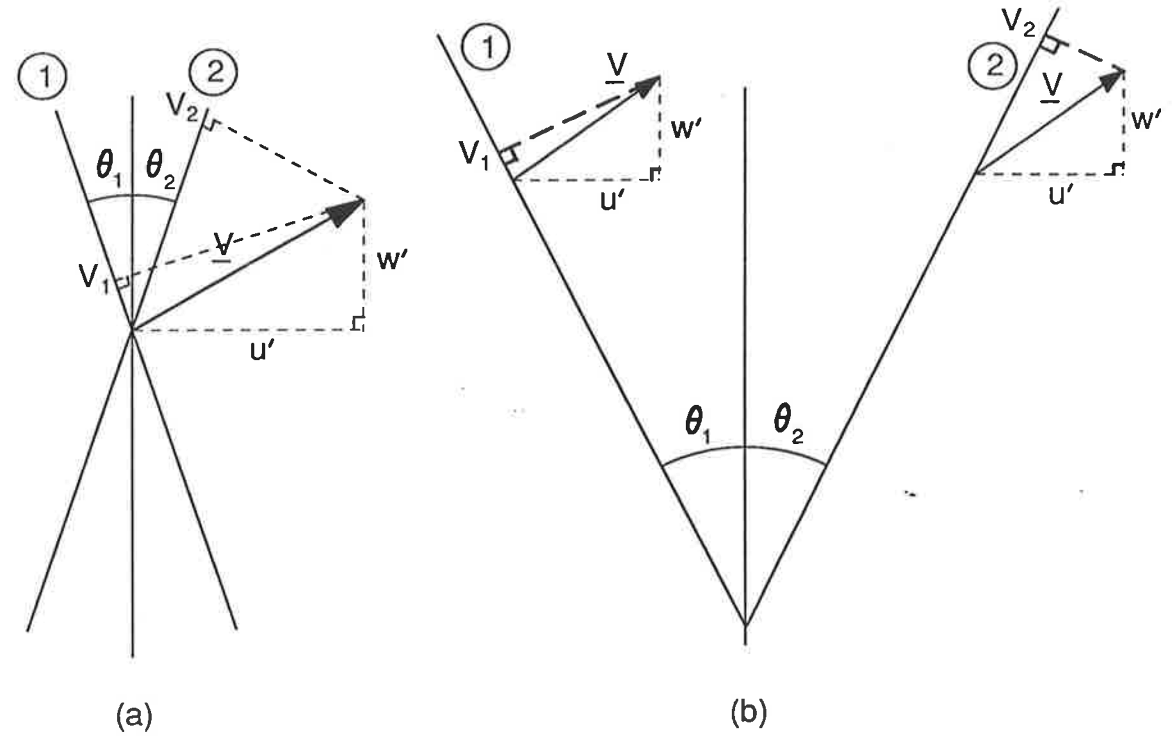

Figure 6.2: Projections of the velocity vector $\underline{V}$ onto two axes

shown in figure 6.2b where the velocity projections in two separate sampling volumes are obtained with one monostatic radar system. It is not reasonable to assume that the instantaneous velocities in the two sampling volumes are the same. Thus, in order to use this configuration, it is necessary to make the assumption that the statistical properties of the atmosphere at one height are spatially invariant in a horizontal plane. It is then possible to obtain $\overline{u'w'}$, where the overbar denotes a time average. This method was presented by Vincent and Reid (1983) and involves the use of the expression

$$\overline{u'w'} = \frac{\overline{V_2^2} - \overline{V_1^2}}{2\sin 2\theta} \tag{6.1}$$

where $\overline{V_1^2}$, $\overline{V_2^2}$ are the variances of a time series of the components of velocity for beams 1 and 2, and $\theta = \theta_1 = \theta_2$ is the (effective) off-zenith pointing angle of the radar beams being used.

In the general case, the velocity vector $\underline{V}$ is three dimensional, i.e. $\underline{V}(u', v', w')$. It is possible to obtain $\overline{u'w'}$, the vertical flux of zonal momentum and $\overline{v'w'}$, the vertical flux of meridional momentum using a pair of radar beams in the east-west plane and a pair of radar beams in the north-south plane respectively. It is noted that the radar beams at Buckland Park are actually aligned 4° off the north-south and east-west planes. It was found that the effect on $\overline{u'w'}$ and $\overline{v'w'}$ of a rotation of 4° was negligible, and it has been assumed that the measured values of momentum flux are $\overline{u'w'}$ and $\overline{v'w'}$.

6.2 Data analysis

6.2.1 Filtering the data

The momentum fluxes to be measured here are thought to be due to the action of waves of a continuum of frequencies. It is therefore instructive to obtain momentum flux values for various (ground-based) frequency or period bands. These bands were chosen as follows.

Short period	Period from the Nyquist period (here 8 min) up to 1 hour
Medium period	Period from 1 hour to 8 hours
Long period	Period from 8 hours to the inertial period ($\approx$21 hours at Adelaide)

The method of separating the contributions from these bands is that used by Fritts and Vincent (1987). The lower limits of each period range were set by averaging the data. For example, the short-period data, which had either one or two points per 4 minutes, was averaged into 4 minute blocks. This gave a Nyquist period of 8 minutes. The upper limit was then set by taking, in this example, 15 points or one hour of data to give a maximum period of one hour. Similarly, an 8 hour block of half-hour averaged points gave the medium-period band and a 24 hour block of 4 hour averaged points gave the long period band. In the latter case, the upper limit is actually set geophysically by the inertial period rather than by the data processing.

Although a one-hour data block (say) cannot be used to obtain information on oscillations of period greater than one hour without ambiguity, it is still possible for these oscillations to affect the data. To minimise the potential of this effect, the variances required by equation 6.1 are not calculated around the mean but around a line of arbitrary slope and intercept fitted to the data. In the medium and long period data, a diurnal and semidiurnal oscillation is fitted to the data and removed before the straight line fit is carried out.

6.2.2 Outlier rejection

The Vincent-Reid method of estimating momentum flux involves the difference between two quantities which are similar in magnitude. The quantities that are being differenced are variances and these are susceptible to the effects of outliers. If a bad data point occurs and lies some distance d from the line of best fit, its contribution to the variance sum d^2, could easily dominate the contributions of the good data points. It is therefore important to remove the outliers from the data.

A number of methods were tried in order to achieve this. The first involved taking a block of radial velocity data (at one height and for one channel) and calculating the mean and standard deviation of that block. The data in the block that fell outside a range centred on the mean and extending a predetermined number of standard deviations from the mean were then rejected. In this method, the final variance of the data was not being set artificially as the standard deviation of the data could have any value. In order to ensure that a significant number of points contributed to the mean and standard deviation, the data blocks needed to be as long as possible. However, if their length became comparable to half the period of the semi-diurnal tide, it was conceivable that the tidal variation of the velocity could lead to some good data points near the tidal maxima and minima being rejected. The block length chosen on the basis of these arguments was three hours.

In the above method, the original calculation of the standard deviation contains values due to data that are destined to be rejected. This has the potential to bias the standard deviation calculations. Because of this, an initial pass over the data rejecting only values that are well away from the mean (say 2 or 3 standard deviations) should be executed to remove the really bad points. Further passes over the data can then be made with more confidence in the statistics being used.

The question arises: How do we know if the outlier rejection is working? Little is known about momentum flux, the quantity we are trying to measure, therefore we cannot know if the outlier rejection has been successful. This question, and its solution, led to another outlier rejection method and this method was used on the short-period data.

Each of the fifteen four-minute average data points that make up a one-hour block of the short-period data makes a contribution to the variance sum $\sum_i (v_i - \overline{v_i})^2$ where v_i is the ith data point and $\overline{v_i}$ is the value of the line of best fit at the ith data point. If one point lies much further away from the line of best fit than the others, its contribution to the variance sum will dominate those due to the other points. The variance then reflects the value of this one point and ignores the character of all the other points in the data block. Should this one point be kept in favour of the others in the block? Given that there is a chance that this data point may be in error, the answer to this question must reasonably be no, and the point in question should be removed.

If a point that fitted the above description existed in each data block, it would be a simple programming task to remove that point. In practice, there are sometimes no points that should (using the dominance criterion above) be rejected and sometimes two or three points. Because of this, it was not possible to automate this outlier rejection philosophy. Instead a manual approach had to be adopted. This involved displaying a series of the data points on a computer screen. Points could be removed by positioning the cursor on a data point and pressing a mouse button. When the current set of points was considered acceptable, the next set was displayed and the process was repeated. This program formed the basis of the outlier rejection or "weeding"[1] process carried out on the short-period data.

Weeding of the data was carried out in two phases. The first involved making a cursory inspection of the data, at each channel and each height, on the computer screen and removing points that were clearly outliers. Some examples of these are given in figure 6.3a and b. In this diagram, time is plotted on the top axis and an index number (the number of points from the begining of the data set) is plotted on the lower axis. In

---

[1] Weed - to rid of weeds or of inferior parts or members. Pocket Oxford Dictionary

figure 6.3a two points, one near 0:30 (index 145) and one near 2:20 (index 169) would clearly dominate the variance sum and should be removed. Similarly in 6.3b, the point at index 40 should be removed. The datum at index 41 is more marginal but should probably be rejected on the basis that it seems to be affected in the same way as the point at index 40.

Phase two of the weeding process involved calculating the variance of each one hour block. Blocks that satisfied the following criteria were flagged for further inspection.

- Large variance. The variance was greater than approximately $30\mathrm{m}^2\mathrm{s}^{-2}$.
- Variance different to partner. If the variance of the data from one beam is more than twice that from the beam on the other side of zenith, the block was marked for inspection. This test was only applied to variances that were greater than approximately $8\mathrm{m}^2\mathrm{s}^{-2}$.

The data blocks that were marked were then inspected once more. Points that dominated the variance sum in the way described above were then removed. These criteria tended to indicate blocks such as that between 0:00 and 0:56 in figure 6.3c. The point at 0:12 (index 138) in this data block should be removed.

Some aspects of this weeding process should be noted. Firstly, if a block was marked for further inspection, this did not mean that some points *had* to be removed. It may just be that the variance was large (say) in that data block. Secondly, although removing bad points from a data block will always act to decrease the variance, $\overline{u'w'}$ and $\overline{v'w'}$ are free to increase or decrease. This is because the momentum flux is proportional to the difference between two positive-definite quantities (the variances). This difference can increase or decrease as a result of the weeding process so that the weeding is not biassing the momentum flux toward zero. Importantly though, any large magnitude values of momentum flux that do result, which have a greater potential for biassing a mean momentum flux, can be accepted with some confidence because of the attention paid to them in phase two. Finally, this possibly subjective approach to outlier rejection has a "safety net". Short-period values of momentum flux are only calculated if at least

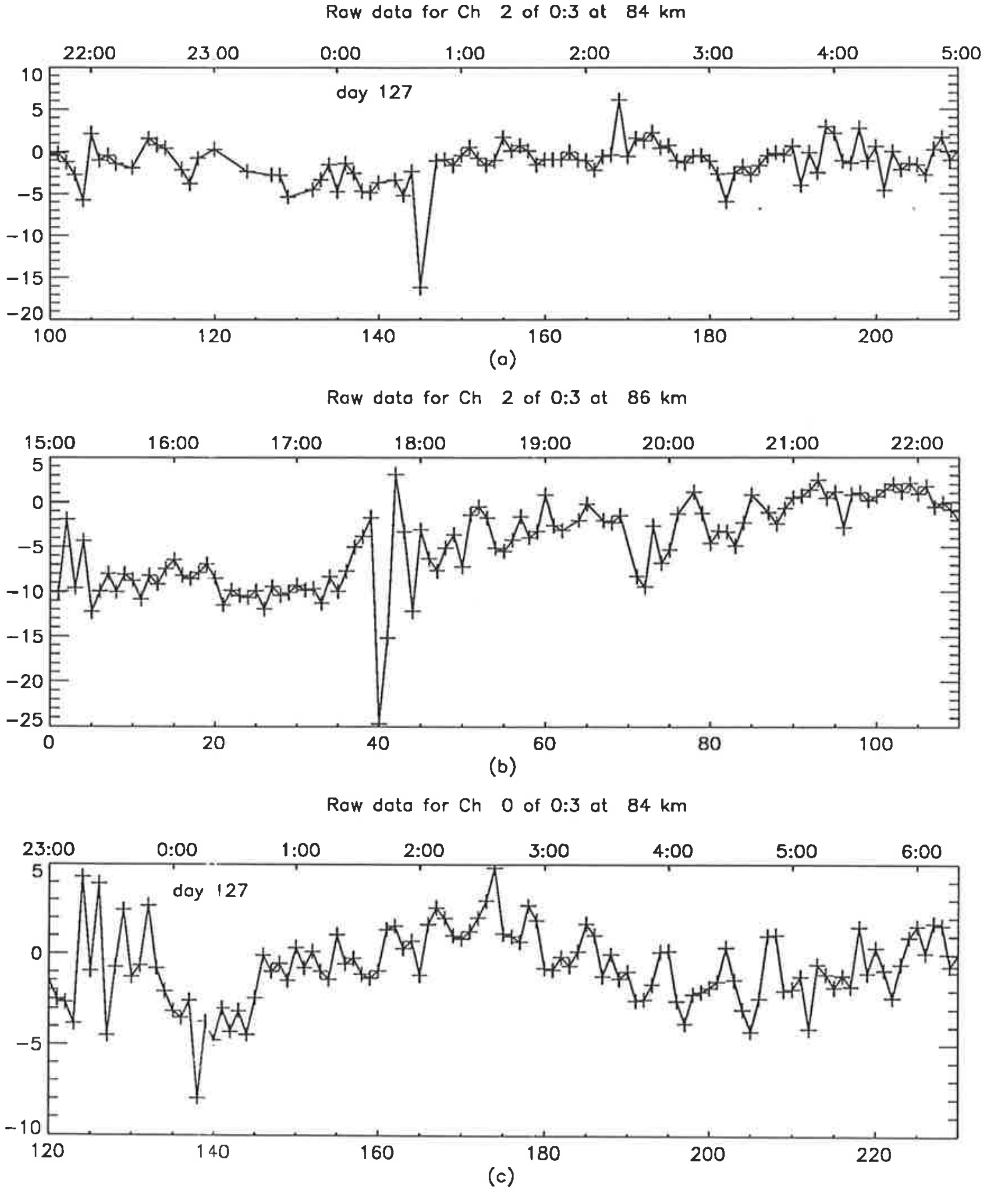

Figure 6.3: Some examples of the outliers in the velocity data.

ten of the fifteen available points per block exist in each beam. Weeding removes values from the wings of the distribution of velocities, but because at least 66% of the data must remain, there is little potential for significant changes to the body of the distribution and confidence in the variance values remains.

This weeding process was applied to the short-period data only. Ideally, this weeded data would then be averaged into half-hour and four-hour blocks for the medium-period and long-period data analysis, but this could not be done because of an incompatability in the format of the data. Instead, phase one was replaced with two successive outlier rejection passes over the raw (unaveraged) data, filtering three-hour data blocks to 2.5 standard deviations as described previously. It was not possible (or considered necessary) to imitate phase two because the data points used for the medium and long-period analyses were half-hour and four-hour averages of the filtered data respectively and were thus less affected by smaller-scale variations of individual points. Thus, the raw data was filtered to 2.5 standard deviations, this filtered data was then filtered to 2.5 standard deviations, averaged appropriately and then analysed to obtain the momentum flux. A flow chart summarising the outlier rejection, averaging and momentum-flux analysis for the three period bands is given in figure 6.4.

The outlier rejection method used in this work has been based on the effect that individual data points have on the variance. Points that were rejected on the basis of the dominance criterion discussed previously occured in all four channels and at all heights. They were both greater than and less than the bulk of the data points around them. Although the reason why some data points were bad has not been considered in detail, no characteristics of the occurrence of these points were noted that would suggest a cause. Some possible causes include poor signal-to-noise ratio and variations in the pointing angle. It was found, however, that outliers often occurred during periods of 100% data acceptance rate for that height suggesting that the signal-to-noise ratio was good. Variations in the pointing angle could not be investigated because details of the spatial correlation function were unavailable for these data sets.

Although the question of cause has been considered beyond the scope of this the-

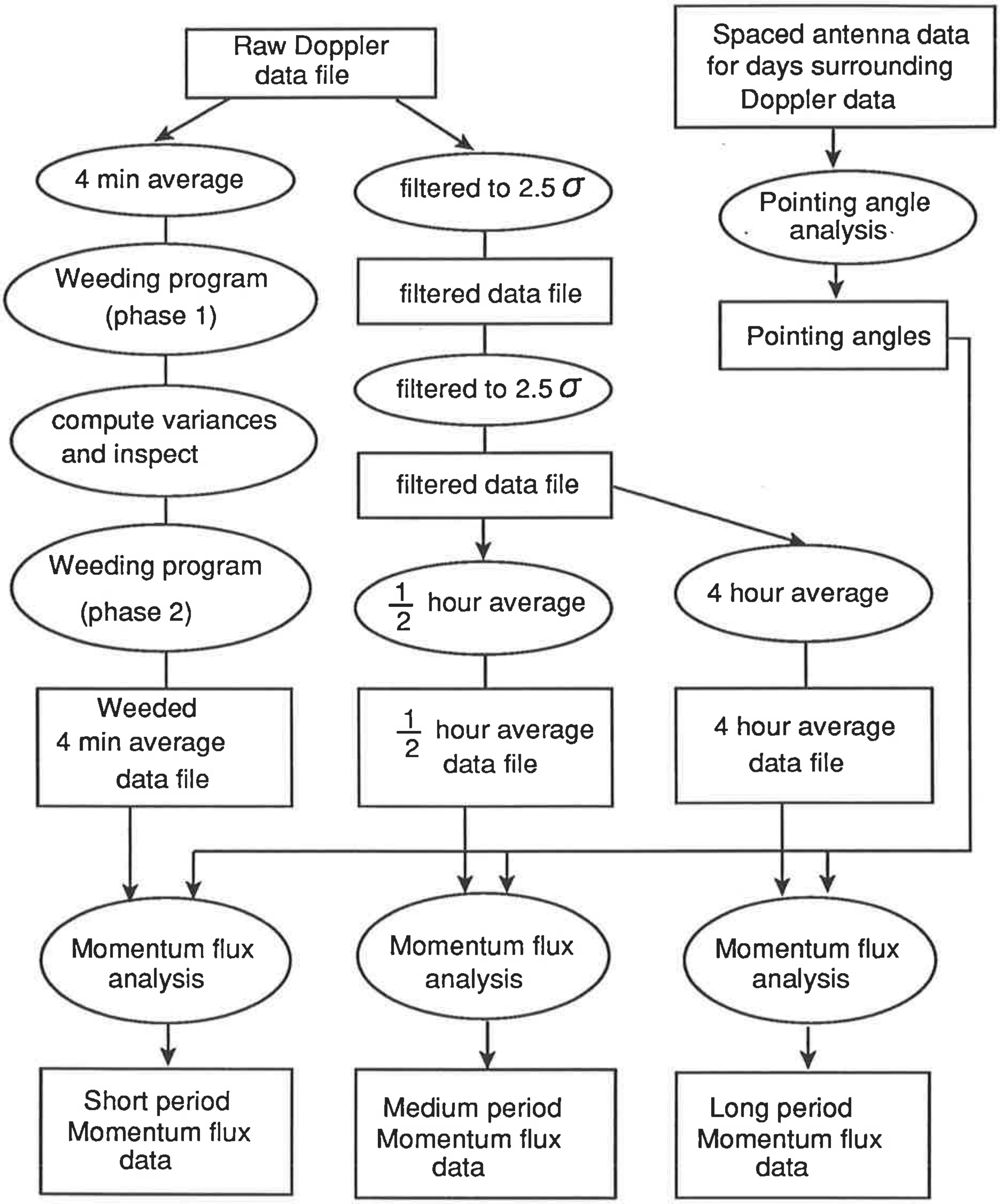

Figure 6.4: A flow chart summarising the momentum flux analysis.

sis, some statistics of the data points that were removed have been stored on file for later analysis. Further, the concept of a display, where the Doppler spectrum could be inspected, combined with the display of the velocity data used for weeding is noted as a powerful extension of the current system. It would also be instructive in finding the cause of the bad points. Unfortunately the computing facilities available here would not allow a system of this kind.

6.3 The effect of outlier rejection

One of the twelve data sets obtained during 1985/86 was selected at random for a comparison between data that were subjected to the outlier rejection methods just described and data that were not. These data were obtained over four days from 5 August to 9 August, 1985.

As stated previously, little is known of the parameters $\overline{u'w'}$ and $\overline{v'w'}$. This makes comparison between filtered and unfiltered data difficult to interpret and limits the conclusions that can be drawn from such a comparison. Some of the points that can be noted are now considered.

Figure 6.5 shows average short period momentum flux values obtained by averaging over the four days of (hourly) values at each height between 80 and 94 km. This height range is selected because the data above 94 km appear to be affected by the ionospheric E-layer and those below 80 km are only present during part of the day. Both the raw data and the weeded data are represented. It can be seen that weeding has a significant effect on the data at the lower heights causing a change in $\overline{u'w'}$ of approximately $40\text{m}^2\text{s}^{-2}$ and $10\text{m}^2\text{s}^{-2}$ in $\overline{v'w'}$ at 80 km. In general the effect is of the order of 2 or $3\text{m}^2\text{s}^{-2}$ in $\overline{u'w'}$ and $1\text{m}^2\text{s}^{-2}$ or less in $\overline{v'w'}$.

Medium-period data are presented in figure 6.6. Here we have data that have been subjected to no outlier rejection (unfiltered data), data that have had one pass of a 2.5 standard deviation three-hour block filter (filtered data - 1 pass) and data where these one pass values have been filtered again to 2.5 standard deviations (filtered data

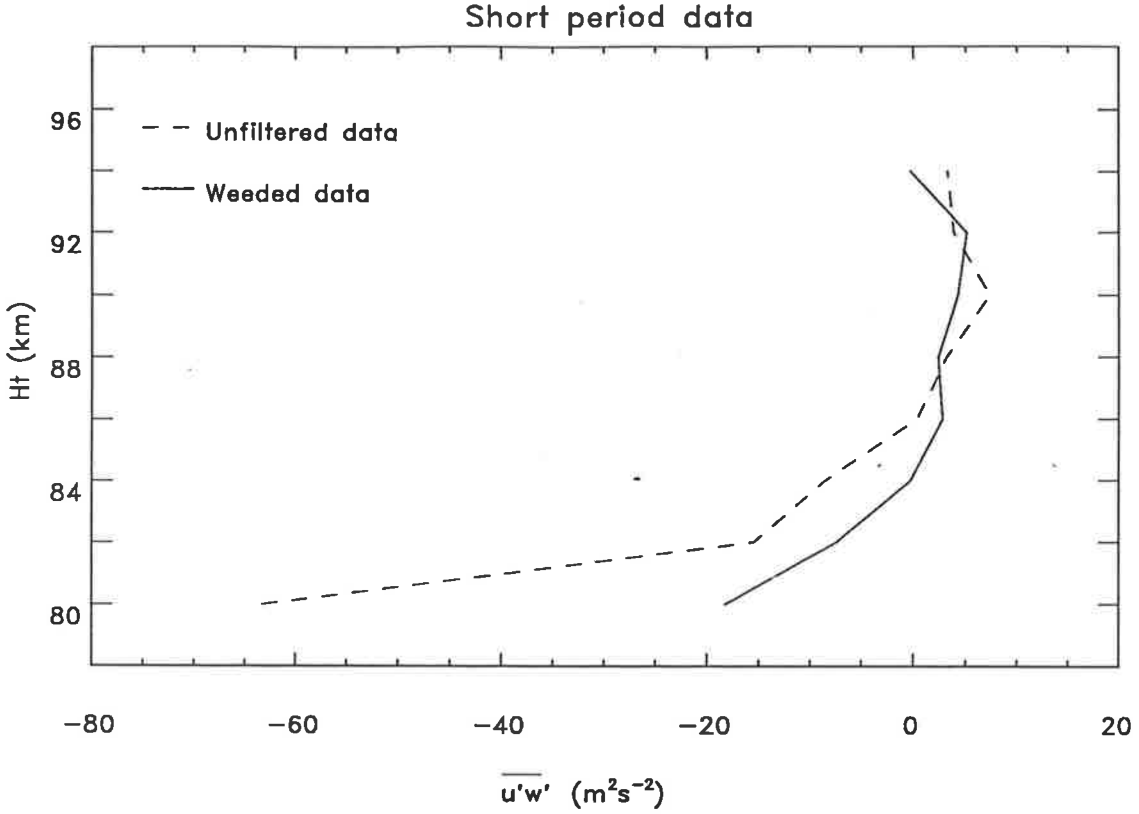

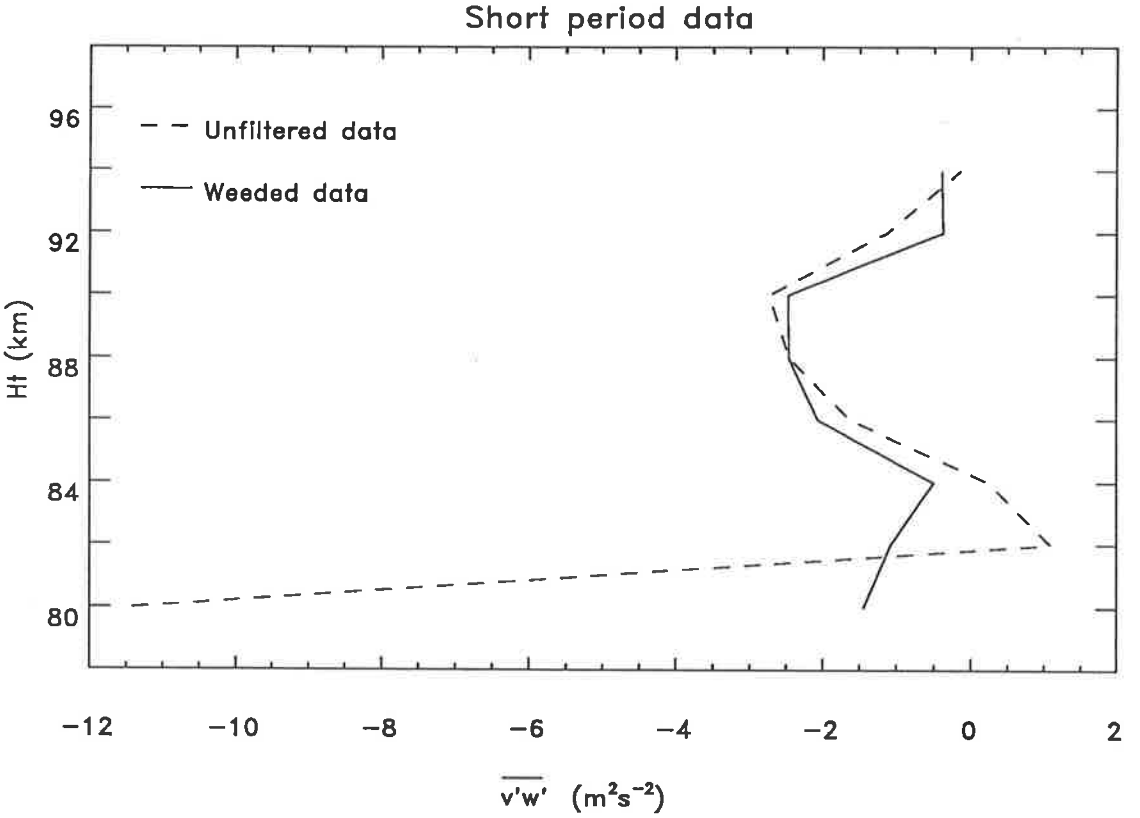

Figure 6.5: Comparison of the outlier rejection techniques applied to the short-period data

- 2 passes). Once again, the most significant changes occur at 80 km. Elsewhere, the filtering causes changes in the four day average of less than $1\mathrm{m}^2\mathrm{s}^{-2}$ in both $\overline{u'w'}$ and $\overline{v'w'}$.

In the long-period data of figure 6.7, it can be seen that the filtering has no effect at 80km. This suggests that the four-hour averages used to obtain the long-period momentum flux values are not affected by outliers. There is, however, some small effect at 86km in $\overline{u'w'}$ and above 86km in $\overline{v'w'}$.

6.4 Sources of error in the momentum-flux analysis

The outlier rejection methods just described allow greater confidence in the momentum-flux analysis but there is still some error involved in the measurements. These errors are now considered.

A basic assumption of the Vincent-Reid analysis is that the statistical properties of the atmosphere do not vary horizontally. This assumption was tested in Vincent and Reid (1983) and found to be a reasonable one. Given this assumption, if the true variances in each beam are obtained, then equation 6.1 will give the exact value of $\overline{u'w'}$. However, to obtain the true variance, it is necessary to determine the radial velocity distributions in each beam exactly. In a statistical context, this means that the *parent* radial velocity distribution must be obtained. This is, of course, impossible and the best that can be obtained in practise is a good estimate of the variance from the sample of the radial velocity distribution that is available.

In order to find the sources of error in $\overline{u'w'}$ and $\overline{v'w'}$ then, it is necessary to establish what aspects of the experiment could cause the sample variance to differ from the true variance. One possibility is that there are too few radial velocity points to adequately describe the true (or parent) distribution. Thus, it is important to keep the number of samples per variance calculation as high as possible. In practise, this is limited by the upper limit of the desired period band on the one hand and either the lower limit of the period band or the time taken to obtain a Doppler spectrum (and therefore a velocity

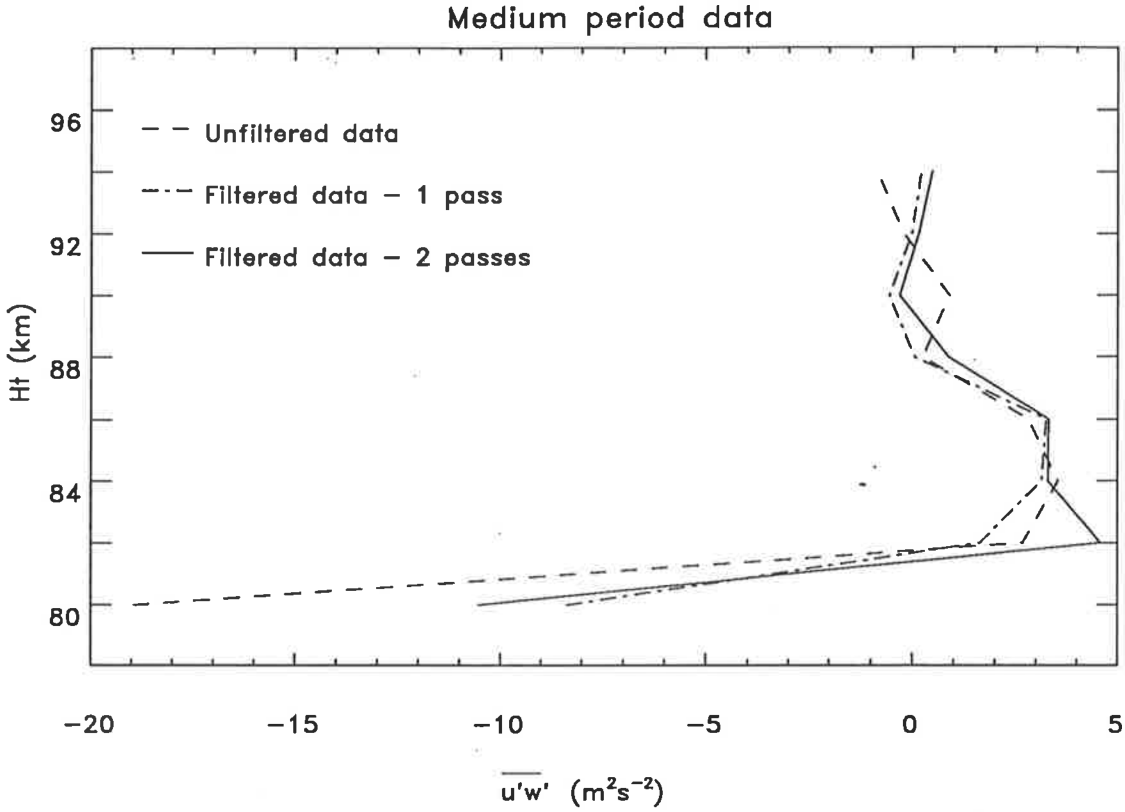

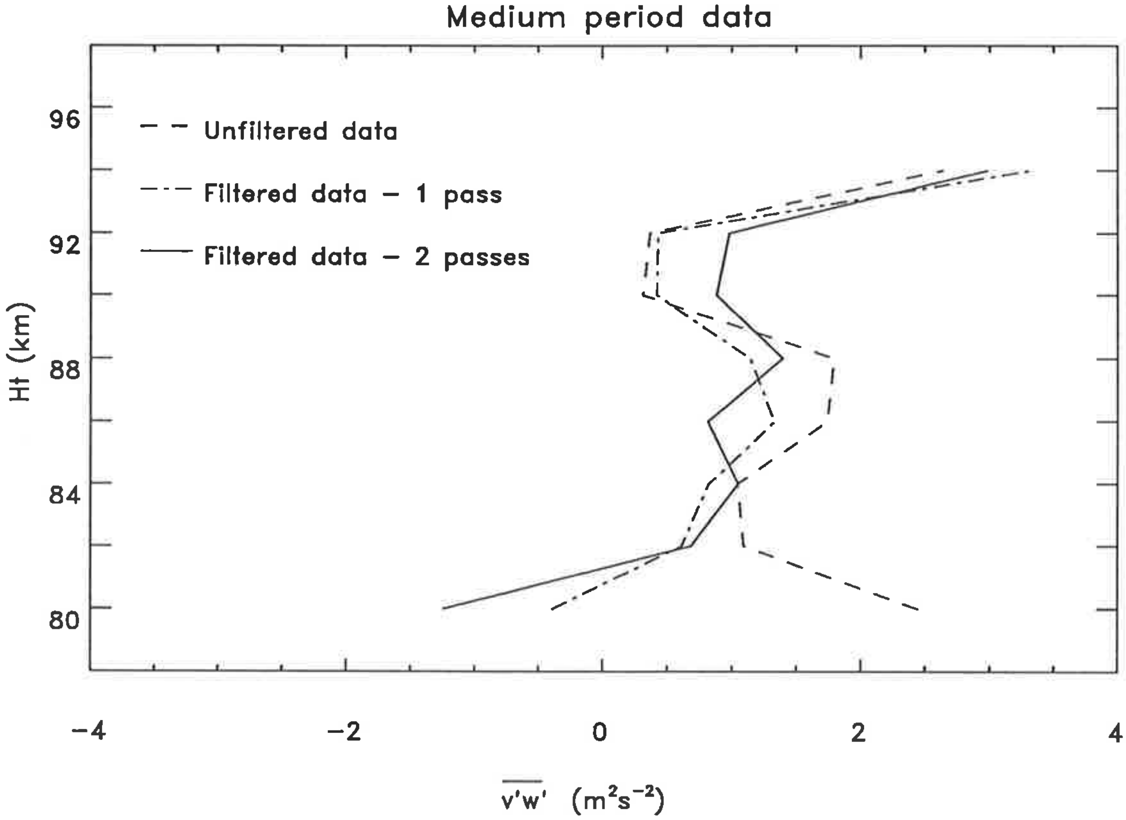

Figure 6.6: Comparison of the outlier rejection techniques applied to the medium-period data

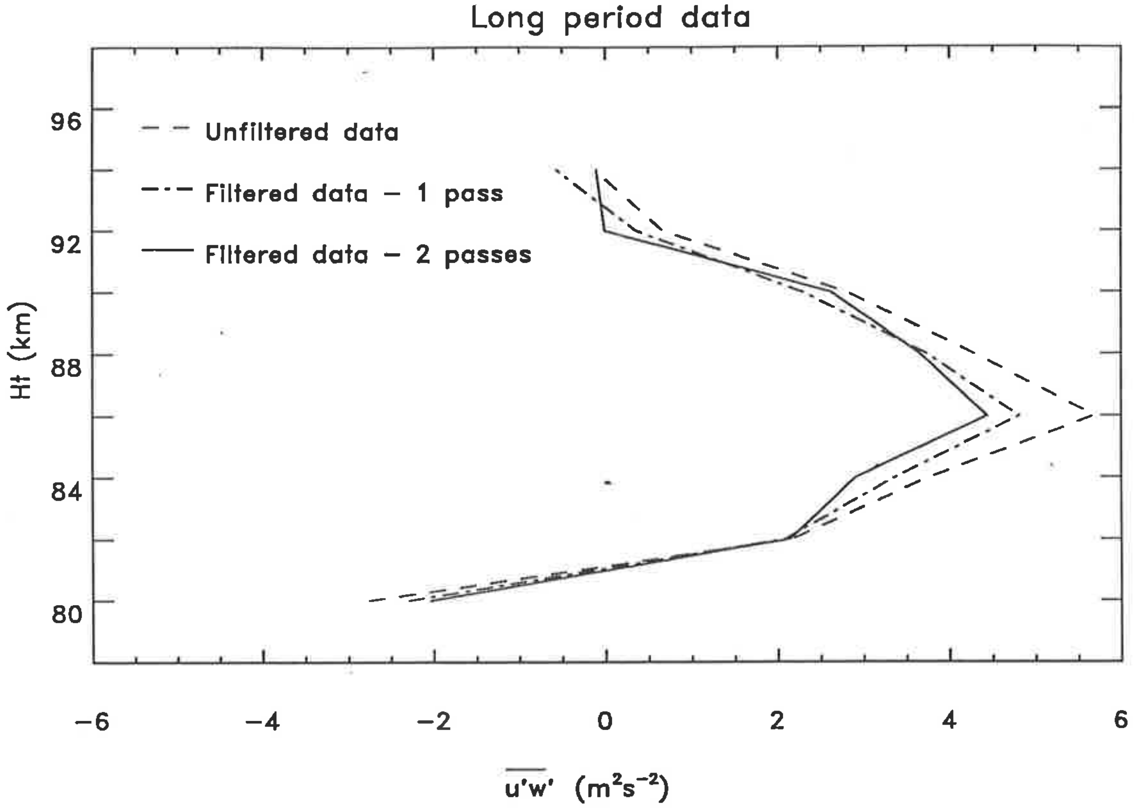

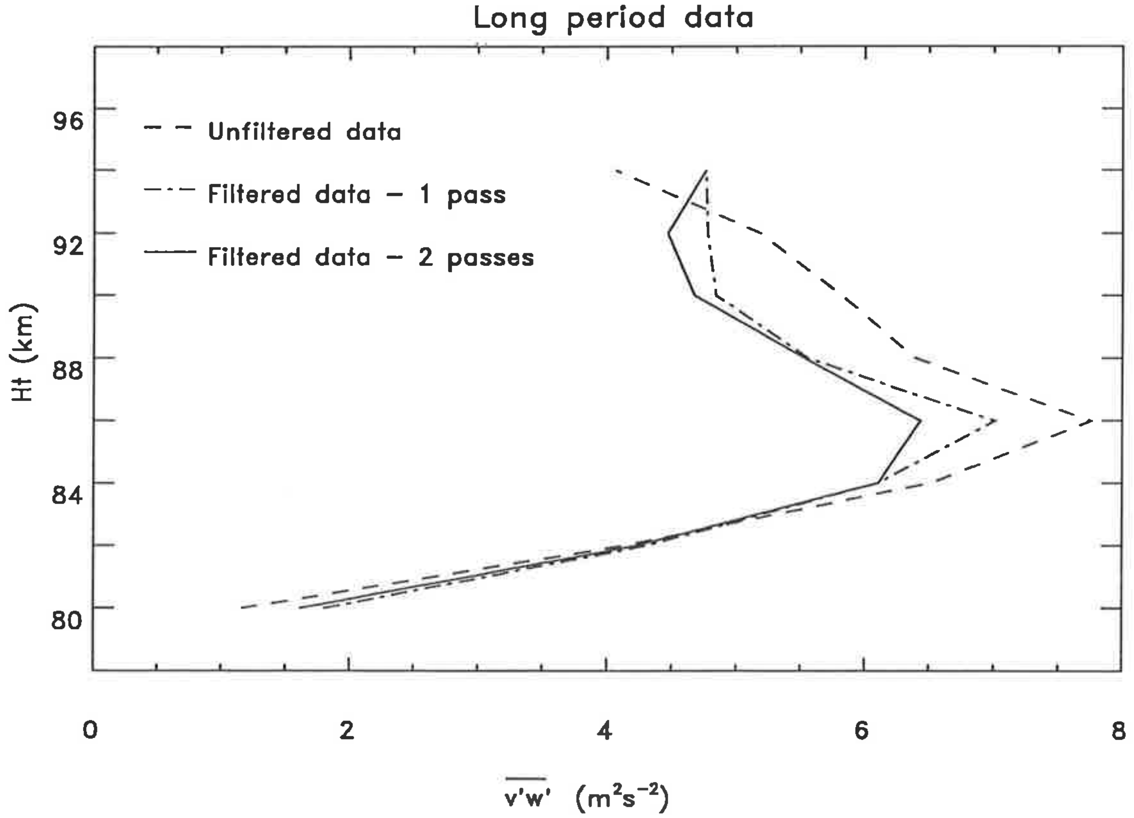

Figure 6.7: Comparison of the outlier rejection techniques applied to the long-period data

measurement) on the other. In the analysis just described, it was these factors that determined the number of samples per data block. The criteria where data blocks with data acceptance rates less than around 66% were rejected ensured a good representation of the radial velocity distribution was present. (It is noted that if the height range over which the data were taken was contracted from 40 to 20 km, a radial velocity data point would be possible every two minutes. However, when the experimental data considered in this thesis was collected, it was hoped that data below 80 km could be obtained.)

Random errors in the velocity measurements could also affect the sample variance although this would be a function of the magnitude of the variance itself. Vincent and Reid (1983) estimated the intrinsic error due to signal-to noise ratio and sample length in a single radial velocity measurement to be 0.7 ms^{-1}(or 0.5 m^2s^{-2}). If the true variance were much greater than this, then these random errors would have little effect on the sample variance. Each velocity sample is likely to be within 0.7 ms^{-1} of the true value but each has an equal chance of being above or below the true velocity value. Because the variance involves a sum of *squared* deviations, the effect of random errors will not average out to zero but it will be smaller than the (0.7 $ms^{-1})^2$. If the true variance was small, however, random errors could set a lower limit on the sample variance. At the lower heights, sample variances occasionally get as low as 0.6–0.7 m^2s^{-2} which could mean that the corresponding momentum fluxes are underestimates of the true momentum flux value. If numerous momentum flux values are averaged, however, this effect will be reduced because it is likely that small values will occur in both beams.

The variation of the variance with time due to geophysical effects make it difficult to gauge how good an estimate of the true variance the sample variance is. If it were possible to oversample the velocity time series, the variance of subsets of this data set containing various numbers of points could be compared. Because of the longer fading times at MF in the mesosphere, this oversampling would be difficult to obtain (although a 2 min sampling time may achieve this). At VHF, however, such a comparison of variance may be possible.

6.5 Other momentum flux analyses

So far in this thesis, some problems associated with measurements of momentum fluxes using dual-beam-Doppler radar techniques and an MF radar system have been dealt with. The basic methods used to obtain momentum fluxes, however, can be applied using numerous other systems. Some examples of these are now presented.

The work presented by Vincent and Reid (1983) was the first application of the dual-beam-Doppler technique in the mesosphere. In that paper, it was noted that the Vincent-Reid method was in fact a special case of the analysis required for Velocity-Azimuth-Display (VAD) radars. These radars measure the radial velocity using beams that have fixed zenith angles but that are swept through 360° in azimuth and had been used in meteorological studies. A review of the principles of VAD radars is presented in Wilson and Miller (1972) where the following chronology is noted. Browning and Wexler (1966) showed that a Fourier-decomposition technique could be applied to VAD data to obtain information on wind divergence and deformations. Lhermitte (1968) noted that the variances of the VAD radial velocities could be used to obtain the covariance between the horizontal and vertical winds. Wilson (1970) then used estimates of these variances to obtain (among other things) momentum fluxes. These early applications used weather radars operating in the lower part of the lower atmosphere.

The dual beam and VAD techniques of obtaining momentum fluxes have been applied elsewhere as well. A Doppler lidar scattering off atmospheric aerosols has been used in a VAD mode to obtain momentum fluxes in the lower atmosphere (Eberhard, Cupp and Healy 1989). Later work by Lhermitte (Lhermitte and Poor 1983) saw the application of the dual beam technique to Doppler sonar studies of tidal-flow turbulence in water channels. This work is of note in that it differs from other applications in a fundamental way. Lhermitte and Poor use the variance of the Doppler spectrum (rather than the variance of the radial velocity time series) to obtain the momentum flux within the pulse volume. This concept is being applied to mesospheric data to obtain turbulence-momentum fluxes by Reid (private communication 1990)

Momentum fluxes have been measured using the Vincent-Reid technique at a variety of sites. The momentum flux in the polar mesosphere has been measured using the Poker Flat radar in Alaska by Fritts and Yuan (1989), Wang and Fritts (1990a), Wang and Fritts (1990b), and using the SOUSY radar situated at Andenes in Norway by Reid *et al.* (1988). The MU VHF radar system has also been used to make measurements of momentum flux in the mesosphere by Tsuda *et al.* (1990) and in the troposphere and lower stratosphere by Fritts *et al.* (1990) as has the Poker Flat radar (McAfee, Balsley and Gage 1989). The latter paper included a study of the effects of orography on momentum flux measurements and sounded a warning in this regard. It is noted that, flow over orography can introduce an additional vertical component of velocity to one Doppler beam and thus compromise the assumption of statistics that are invariant in a horizontal plane. It was shown that this can be a problem through much of the troposphere, but it is unlikely, given the mean wind variations that occur in the stratosphere, that this effect will be a concern in the mesosphere.

Applications of the Vincent-Reid technique at MF have been limited to Adelaide because of the narrow beam-width that is required. Experiments by Vincent and Reid (1983), Fritts and Vincent (1987) and Reid and Vincent (1987) have been presented in the literature.

Momentum fluxes have also been measured in other ways. Smith and Fritts (1983) identified individual gravity waves in the mesosphere over Poker Flat and measured $\overline{u'w'}$ directly. Meyer *et al.* (1989) used foil clouds to estimate the mesospheric momentum flux in northern Scandinavia and Meek and Manson (1989) combined radial velocities from a vertical Doppler beam with spaced antenna horizontal velocities to obtain momentum fluxes. This latter work is susceptible to error through possible contamination of the vertical velocity measurement by horizontal winds. Some attempt was made to correct for this but the adequacy of this correction is difficult to gauge.

The radar beam configuration used by Vincent and Reid (1983) is not the only "non-VAD" radar configuration that can be used to obtain measurements of momentum flux. Other possible configurations and their relative merits for measuring the momentum fluxes of gravity waves are presented by Reid (1987). It is found that the Vincent-Reid configuration is optimal, however, if more beams are included, further useful parameters can be measured.

6.6 Summary

In this chapter, the methods of filtering the data into short, medium and long-period ranges are presented. The presence of outliers is then considered and the methods used to remove them from the data are discussed. Possible causes of error in momentum flux are then discussed. This is followed by a review of measurements of momentum flux.

Chapter 7

The mesospheric momentum budget

In the preceding chapters, techniques for dealing with two important aspects of the momentum flux analysis method of Vincent and Reid (1983), namely the estimation of the effective pointing angle and the treatment of outliers, have been considered. It is now possible to apply these ideas to the analysis of a data set obtained during 1985/86.

The spatial and temporal coverage of measurements of mesospheric momentum fluxes is rather limited. The data set to be presented in this chapter represents a significant extension of this data base and it is now possible to consider aspects of momentum fluxes that could not be studied until now. Seasonal variations (like those noted in $\overline{u'w'}$ by Reid and Vincent (1987)) can be used to improve modelling studies of the mesospheric momentum budget and can provide clues as to the sources of gravity waves and the filtering processes that they are subject to.

In this chapter, the data set will be presented and some characteristics of it will be summarised and discussed. These characteristics will include the variation of momentum flux on long (seasonal) time scales in both $\overline{u'w'}$ and $\overline{v'w'}$, the partitioning of the total momentum flux into period ranges and the importance of their contributions throughout the year. The capacity for gravity wave momentum fluxes to balance the mesospheric momentum budget will also be considered through calculations of the mean-flow acceleration and comparison of these results with Coriolis torques.

7.1 A climatology of mesospheric momentum fluxes

7.1.1 Momentum fluxes during 1985/86

Between March 1985 and February 1986, the Buckland Park MF radar was used to obtain momentum flux data on twelve occasions. Each campaign lasted for four days (except one, which had to be terminated due to a system failure). This duration was the same as that used in the GRATMAP or GRAvity waves And Tides in the Middle Atmosphere Program series of experiments and the campaigns considered here either coincided with those in GRATMAP or fell in a week either side of a GRATMAP run. The start and end times and dates are presented in table 7.1. (Note that the number in the run code represents the start day of the year, and the year of the run.)

The array was phased in the manner described in chapter 4 to produce northward, southward, eastward and westward pointing beams, each at a nominal 11.6° off zenith. This configuration allowed the measurement of $\overline{u'w'}$ and $\overline{v'w'}$. The results of the analysis described in the flow chart of figure 6.4 are presented in the following 12 figures. These figures show a time average over the data set for each height. The horizontal bars indicate the standard deviation of the individual momentum-flux values. These should not be interpreted as measures of the uncertainty of the data. $\overline{u'w'}$ (and $\overline{v'w'}$) shows a significant amount of systematic variation as a function of time (Fritts and Vincent 1987). The repeatability of this variation suggests that it is larger than the uncertainty in the momentum flux. Thus, the standard deviation reflects the momentum flux variability more than it does the error. N, the number of momentum flux values contributing to the average, is printed next to the right-hand axis of each figure.

It should be noted that the ranges of the x-axes (momentum fluxes) varies from graph to graph. This makes comparisons between the graphs more difficult, however, specific comparisons of the data will be carried out in the next section where appropriate subsets of the data will be reproduced.

Start time	Start date	Start day	End time	End date	Run code
13:08	4/3/85	day 63	11:58	8/3/85	gmr06385
15:24	15/4/85	day 105	13:56	19/4/85	gmr10585
15:04	6/5/85	day 126	3:02	11/5/85	gmr12685
13:38	27/5/85	day 147	11:12	31/5/85	muc14785
12:54	8/7/85	day 189	15:30	12/7/85	muc18985
11:34	5/8/85	day 217	13:16	9/8/85	gmr21785
12:32	16/9/85	day 259	6:34	18/9/85	gmr25985
11:08	7/10/85	day 280	15:16	11/10/85	gmr28085
11:58	18/11/85	day 322	11:38	22/11/85	gmr32285
14:04	9/12/85	day 343	13:06	13/12/85	gmr34385
11:06	6/1/86	day 6	9:06	10/1/86	gmr00686
9:34	9/2/86	day 40	11:00	13/2/86	gmr04086

Table 7.1: The start and end times and dates for the momentum flux experiments carried out between March 1985 and February 1986

The experiment that began on day 259 of 1985 (gmr25985) was terminated prematurely by a system fault. Because the resulting data set was less than two days long, it was not possible to carry out the medium and long-period data analysis. Thus figure 7.7 contains only short-period momentum fluxes. In cases where only one point contributes to the mean momentum flux, the standard deviation is not calculated and the error is set to zero. It can be seen in some cases that the data acceptance rate at the lower heights is much lower than those above approximately 88km.

The pointing angles that were used to obtain these data are presented in figures 7.13 and 7.14. As discussed in chapter 5, these were obtained using spatial-correlation-function information from the spaced-antenna analysis. The profiles are averages of the pointing angles during two full days prior to and two full days following each run. The numbers on the right hand side of each profile indicate the number of points contributing to the average at that height.

Finally, height profiles of the total momentum flux over all periods between 8 min and 24 hr are of interest. These are calculated by summing the profiles presented in figures 7.1 to 7.12. The standard deviation, that is plotted as a horizontal bar, is the square root of the sum of the squares of the standard deviations in each of the three original period bands. If less than a day of data was included in the average for any of the three period bands, then the summed momentum flux value was rejected. Because the GMR25985 data set contained only short period data, this data has been omitted from the total momentum flux computation. The results are presented in figures 7.15, 7.16 and 7.17, 7.18.

7.1.2 Long term variation in momentum flux

With a set of average momentum flux values spread throughout the year at hand, it is possible to look for any long term (seasonal time scale) trends that may exist. That is, of course, if each data set is representative of the time around it, i.e. if the 4 days of the data set reflect the characteristics of momentum fluxes in the 15 or so days before and after. Because the GRATMAP data presented in the previous section is made

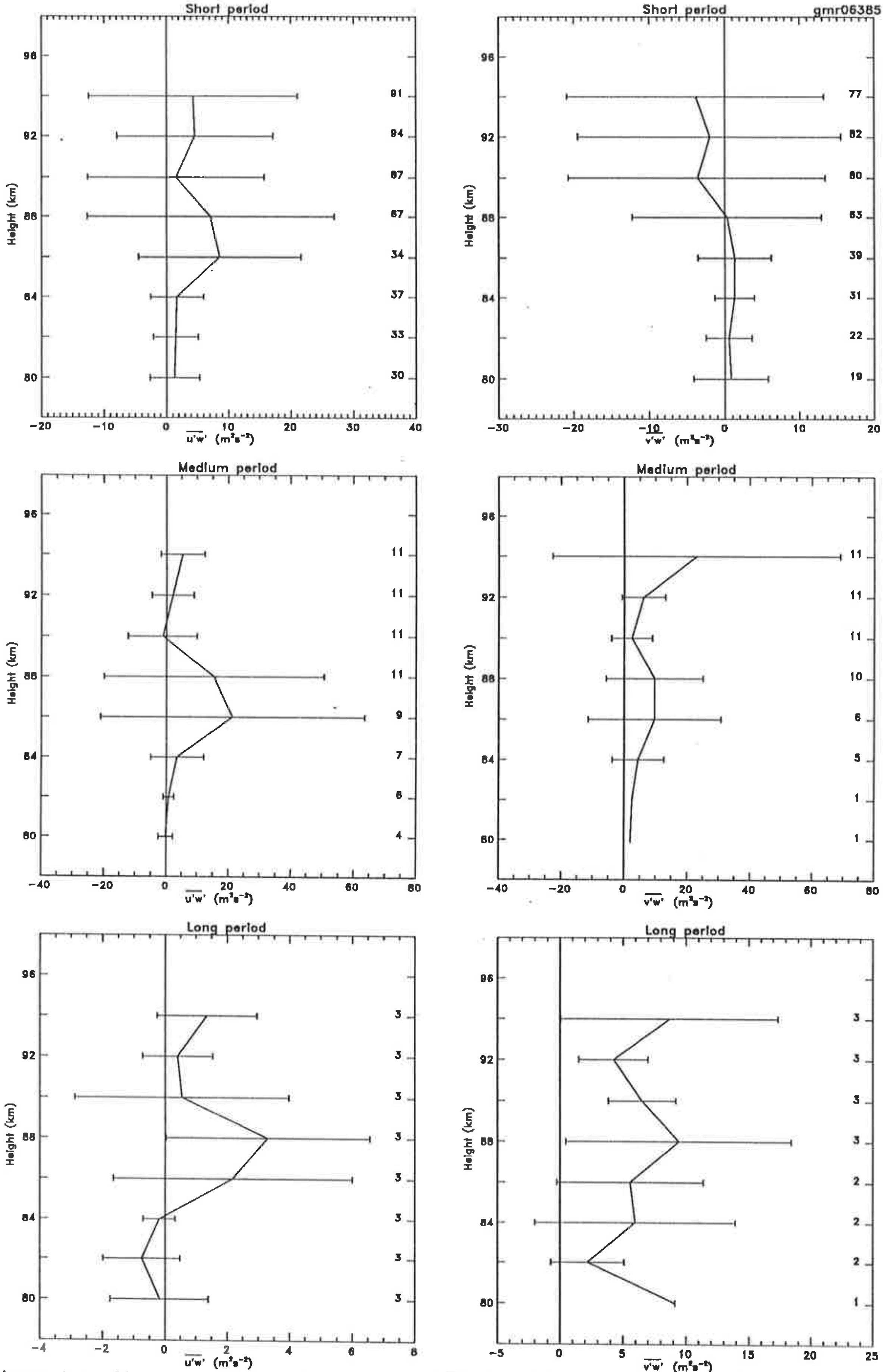

Figure 7.1: Short, medium and long-period $\overline{u'w'}$ and $\overline{v'w'}$ data averaged over the run beginning on day 63 (4 March), 1985. One standard deviation is indicated by the horizontal bar.

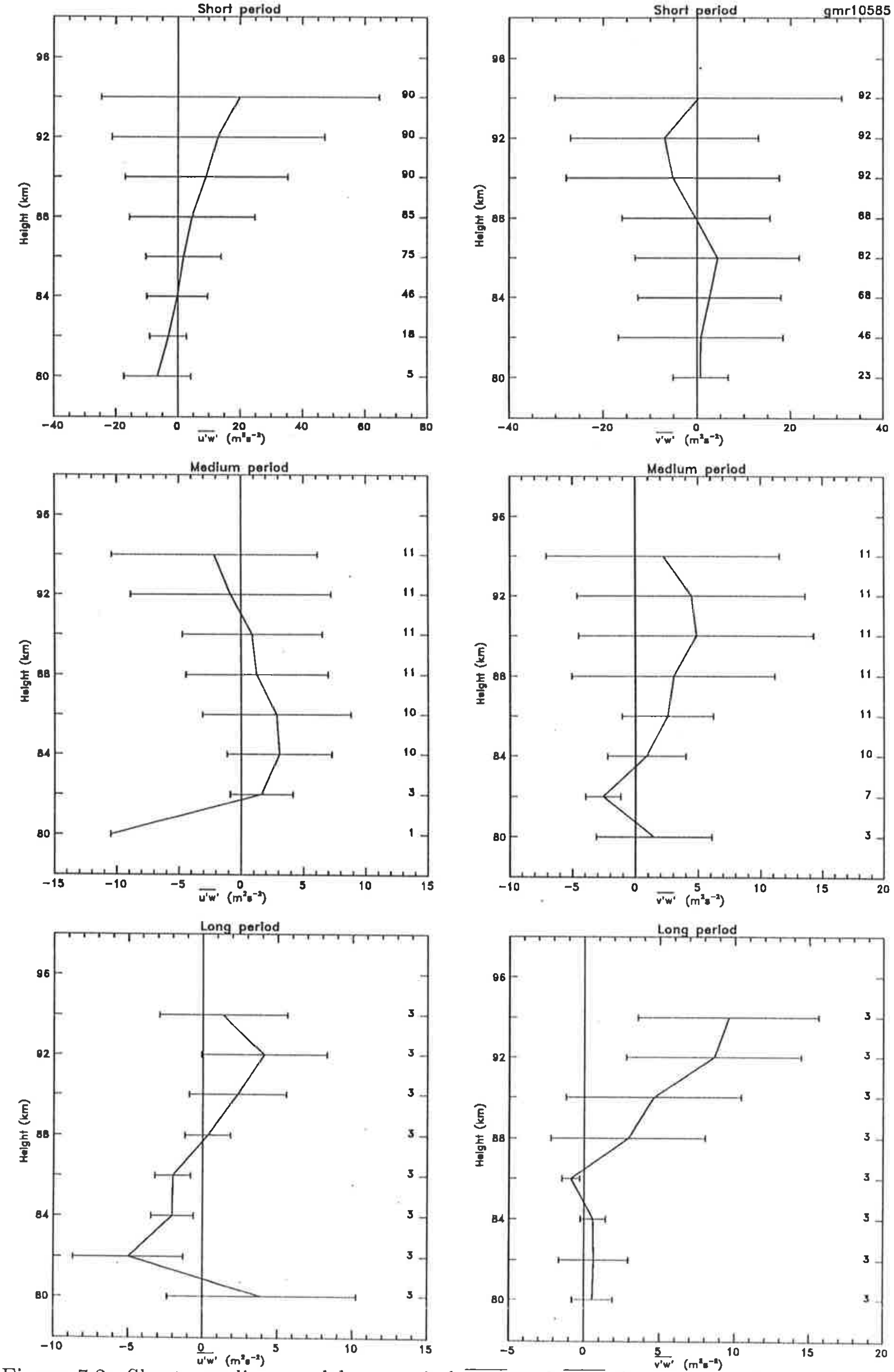

Figure 7.2: Short, medium and long-period $\overline{u'w'}$ and $\overline{v'w'}$ data averaged over the run beginning on day 105 (15 April), 1985. One standard deviation is indicated by the horizontal bar.

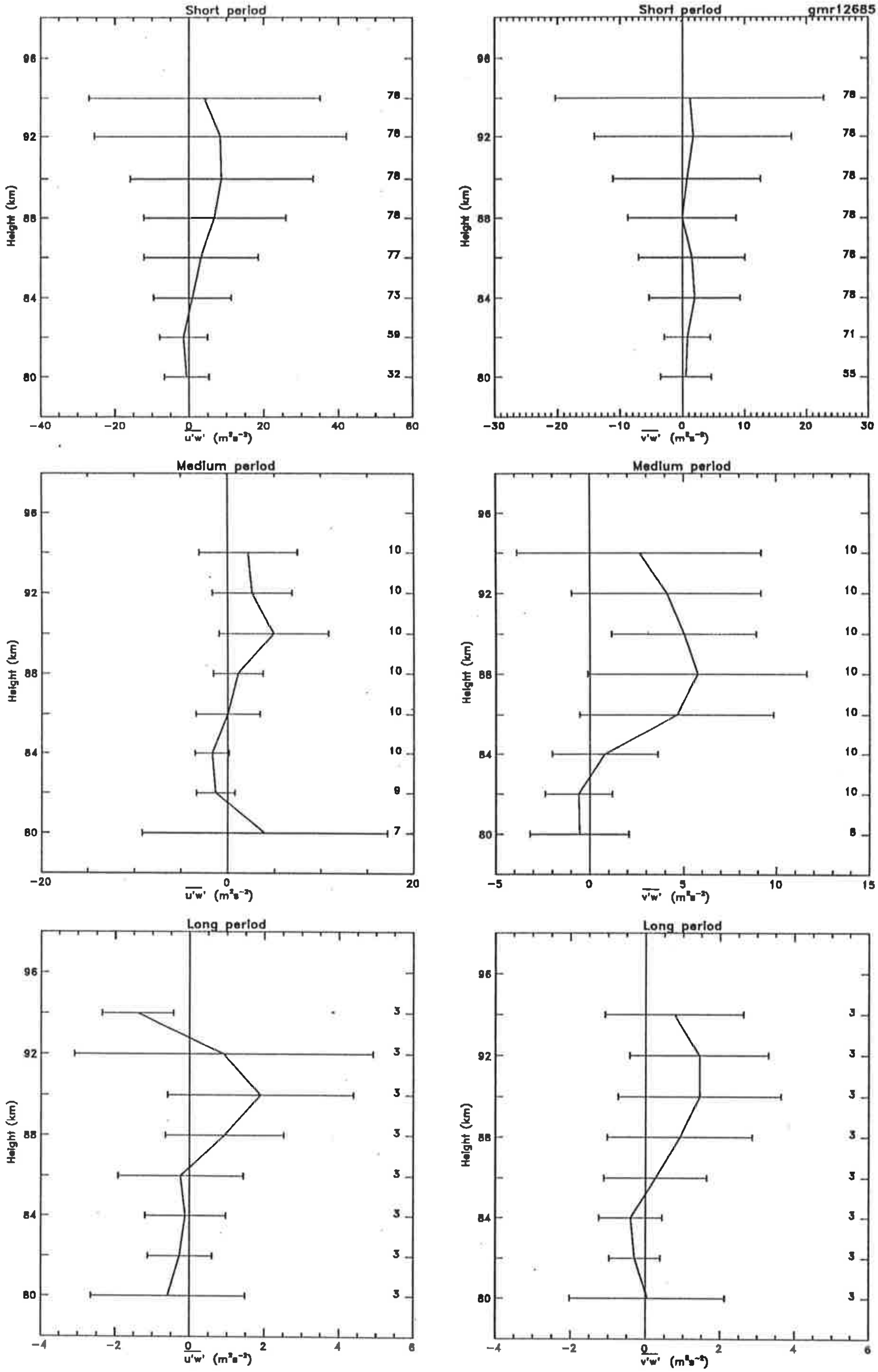

Figure 7.3: Short, medium and long-period $\overline{u'w'}$ and $\overline{v'w'}$ data averaged over the run beginning on day 126 (6 May), 1985. One standard deviation is indicated by the horizontal bar.

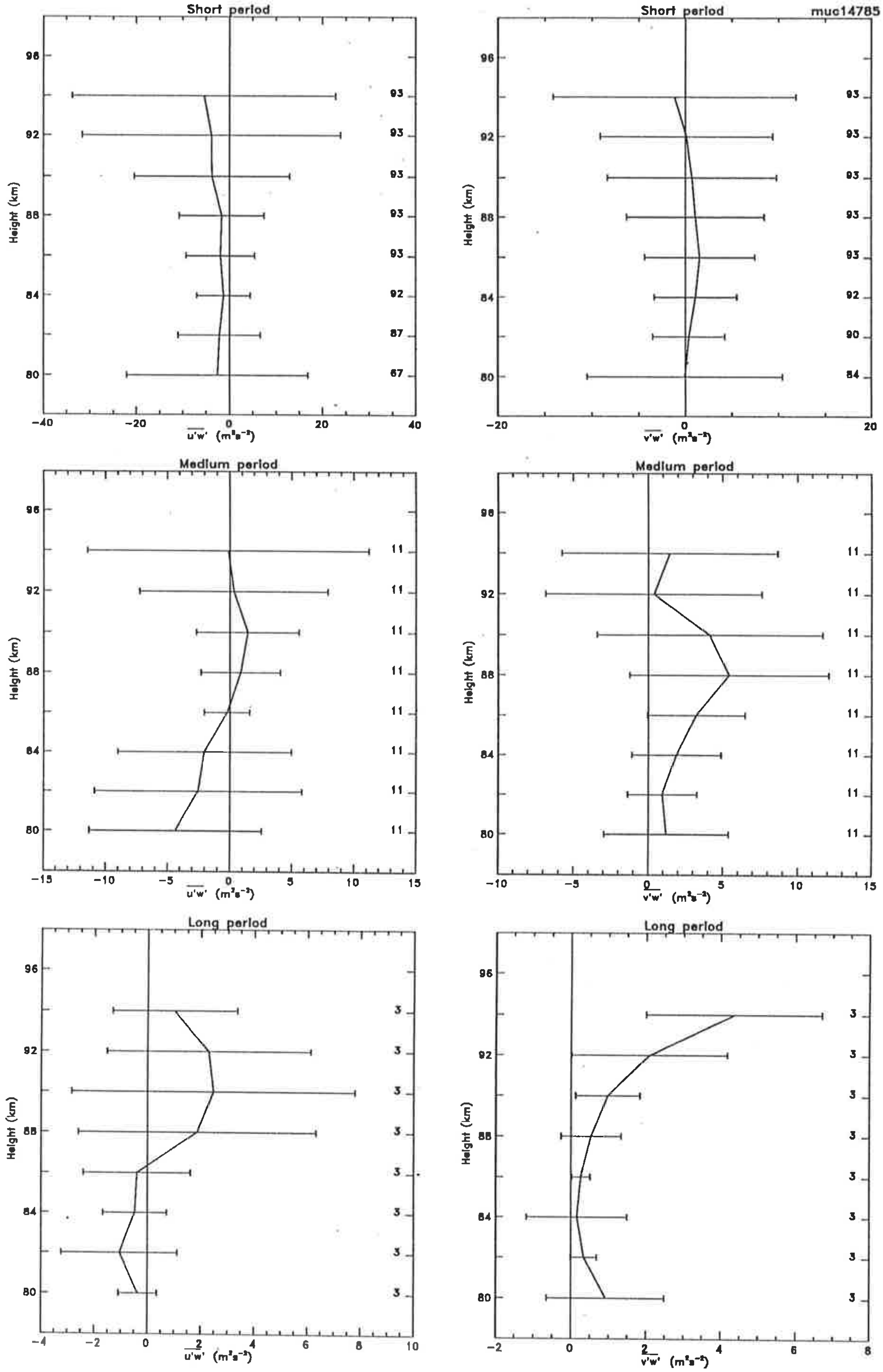

Figure 7.4: Short, medium and long-period $\overline{u'w'}$ and $\overline{v'w'}$ data averaged over the run beginning on day 147 (27 May), 1985. One standard deviation is indicated by the horizontal bar.

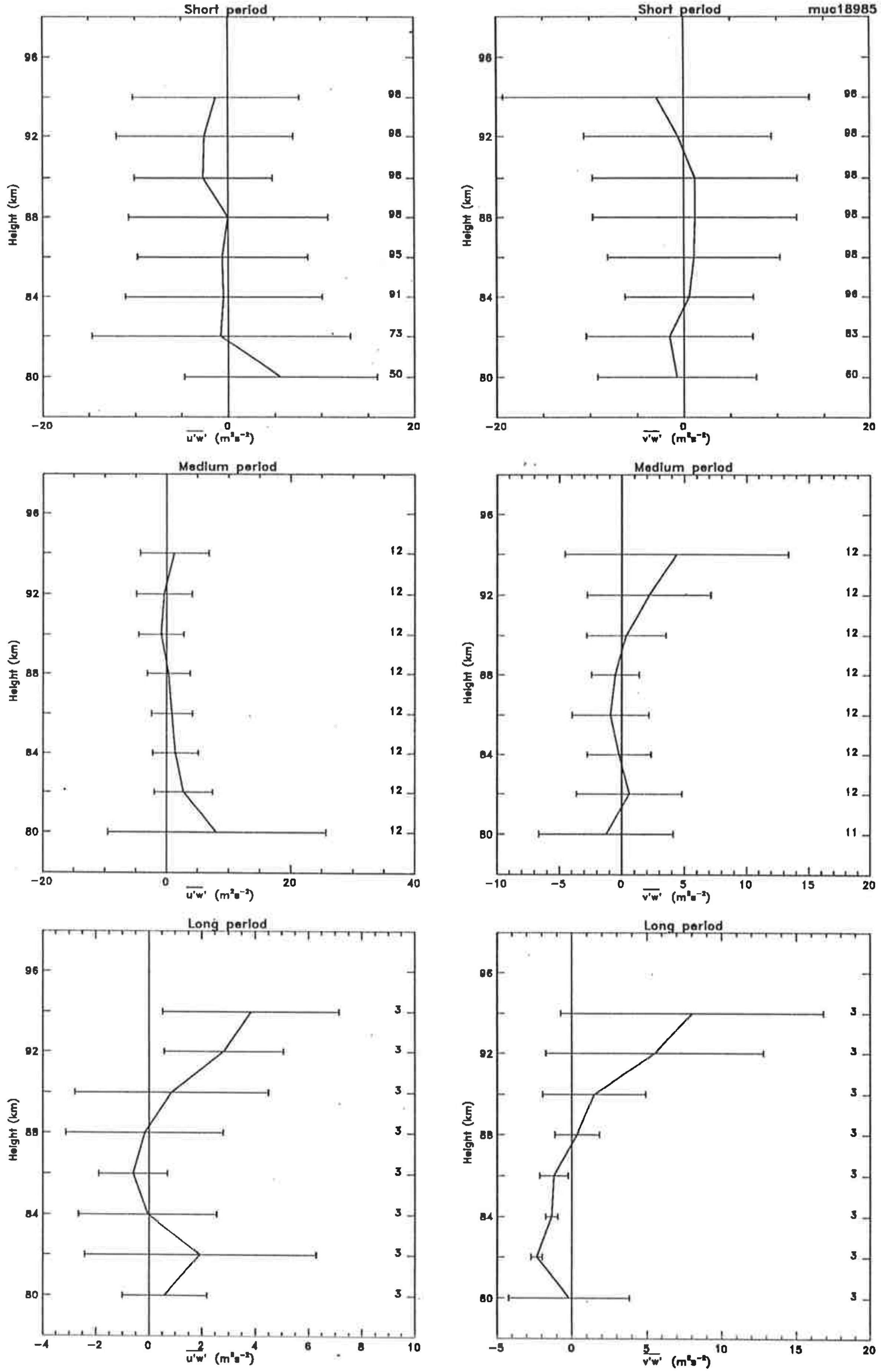

Figure 7.5: Short, medium and long-period $\overline{u'w'}$ and $\overline{v'w'}$ data averaged over the run beginning on day 189 (8 July), 1985. One standard deviation is indicated by the horizontal bar.

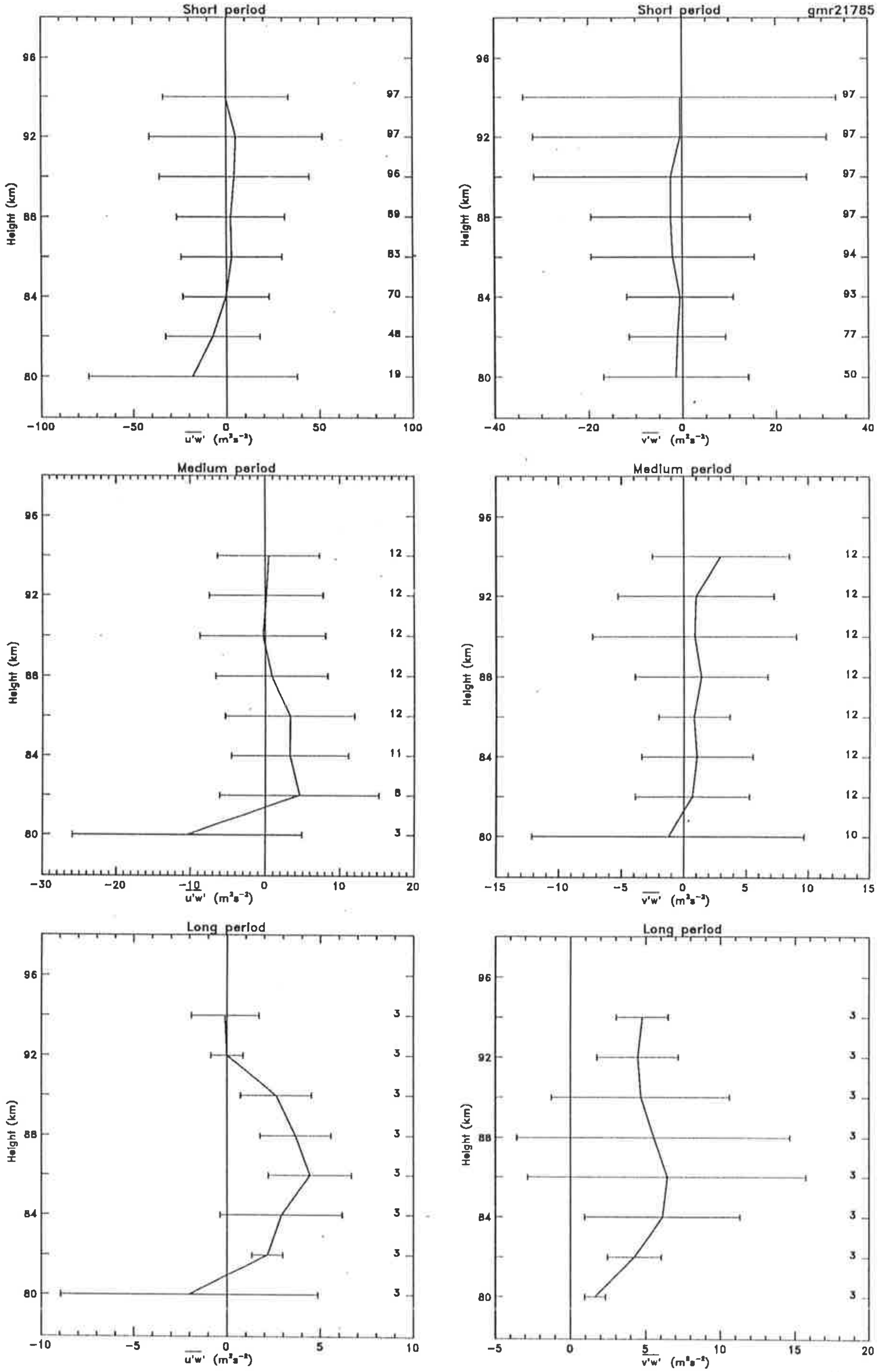

Figure 7.6: Short, medium and long-period $\overline{u'w'}$ and $\overline{v'w'}$ data averaged over the run beginning on day 217 (5 August), 1985. One standard deviation is indicated by the horizontal bar.

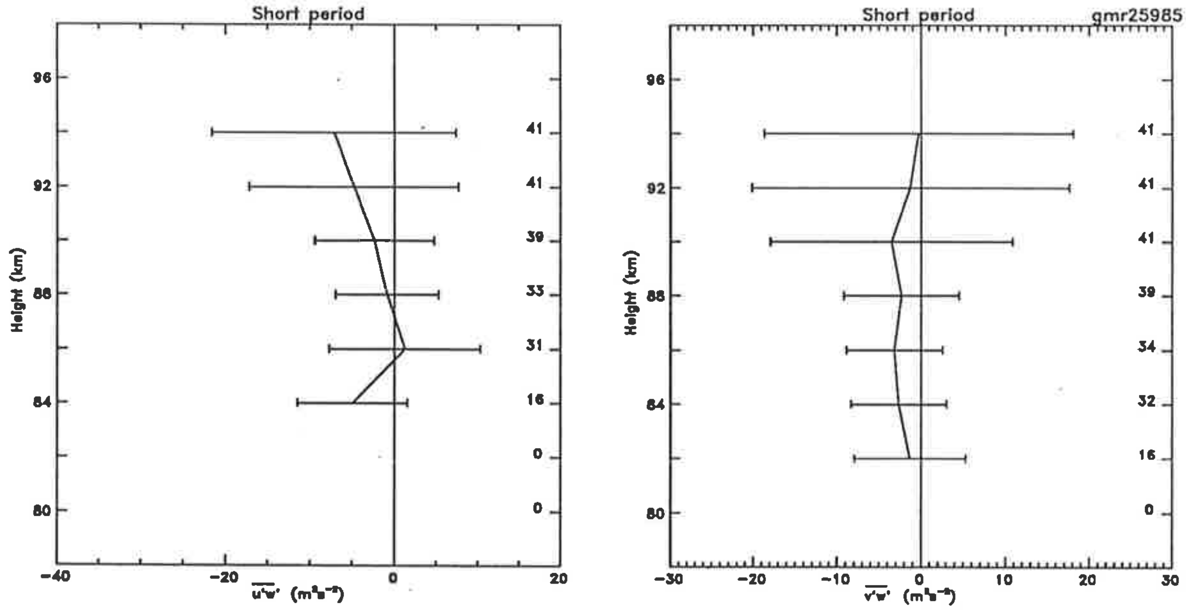

Figure 7.7: Short-period $\overline{u'w'}$ and $\overline{v'w'}$ data averaged over the run beginning on day 259 (16 September), 1985. One standard deviation is indicated by the horizontal bar.

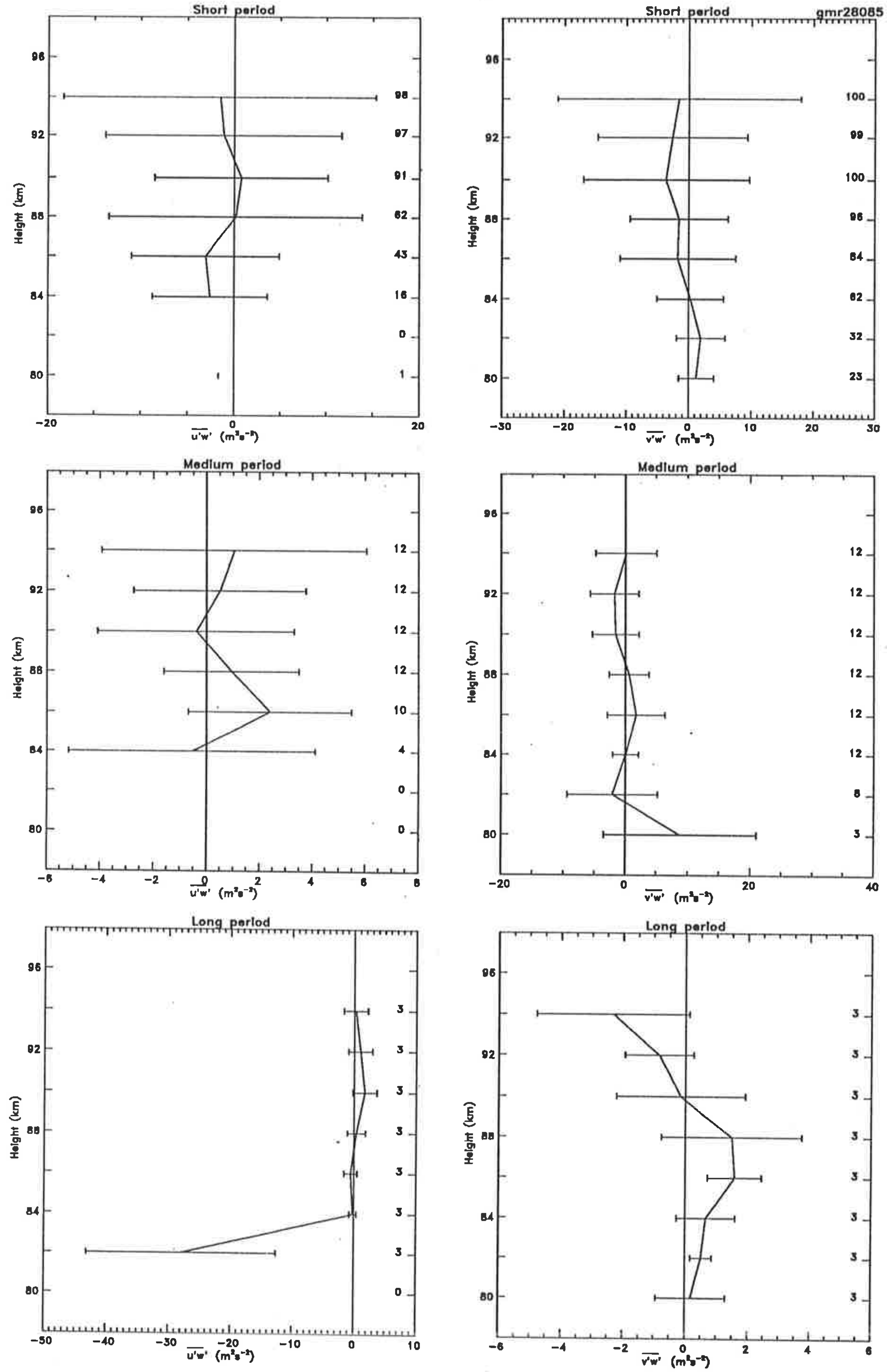

Figure 7.8: Short, medium and long-period $\overline{u'w'}$ and $\overline{v'w'}$ data averaged over the run beginning on day 280 (7 October), 1985. One standard deviation is indicated by the horizontal bar.

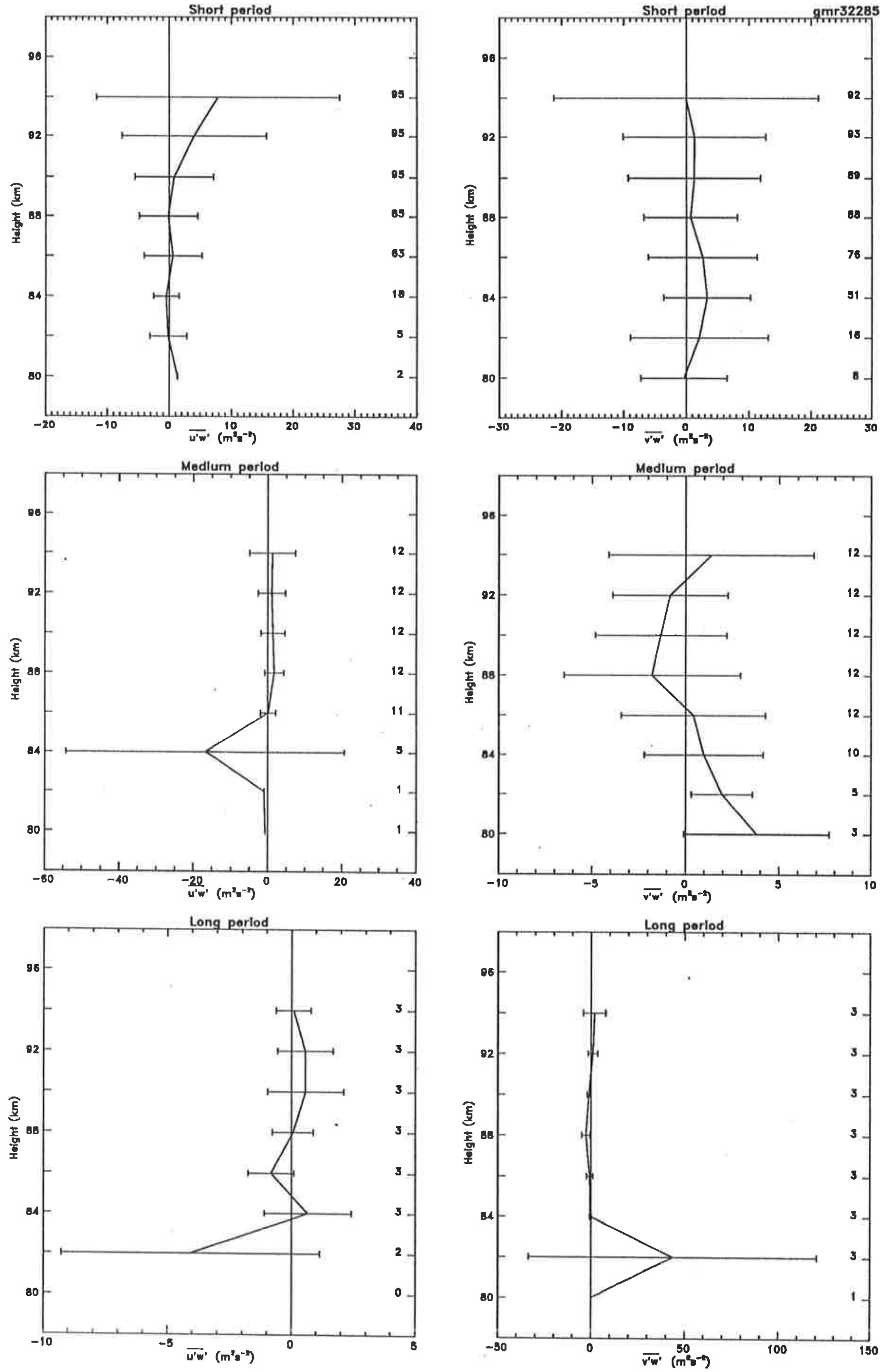

Figure 7.9: Short, medium and long-period $\overline{u'w'}$ and $\overline{v'w'}$ data averaged over the run beginning on day 322 (18 November), 1985. One standard deviation is indicated by the horizontal bar.

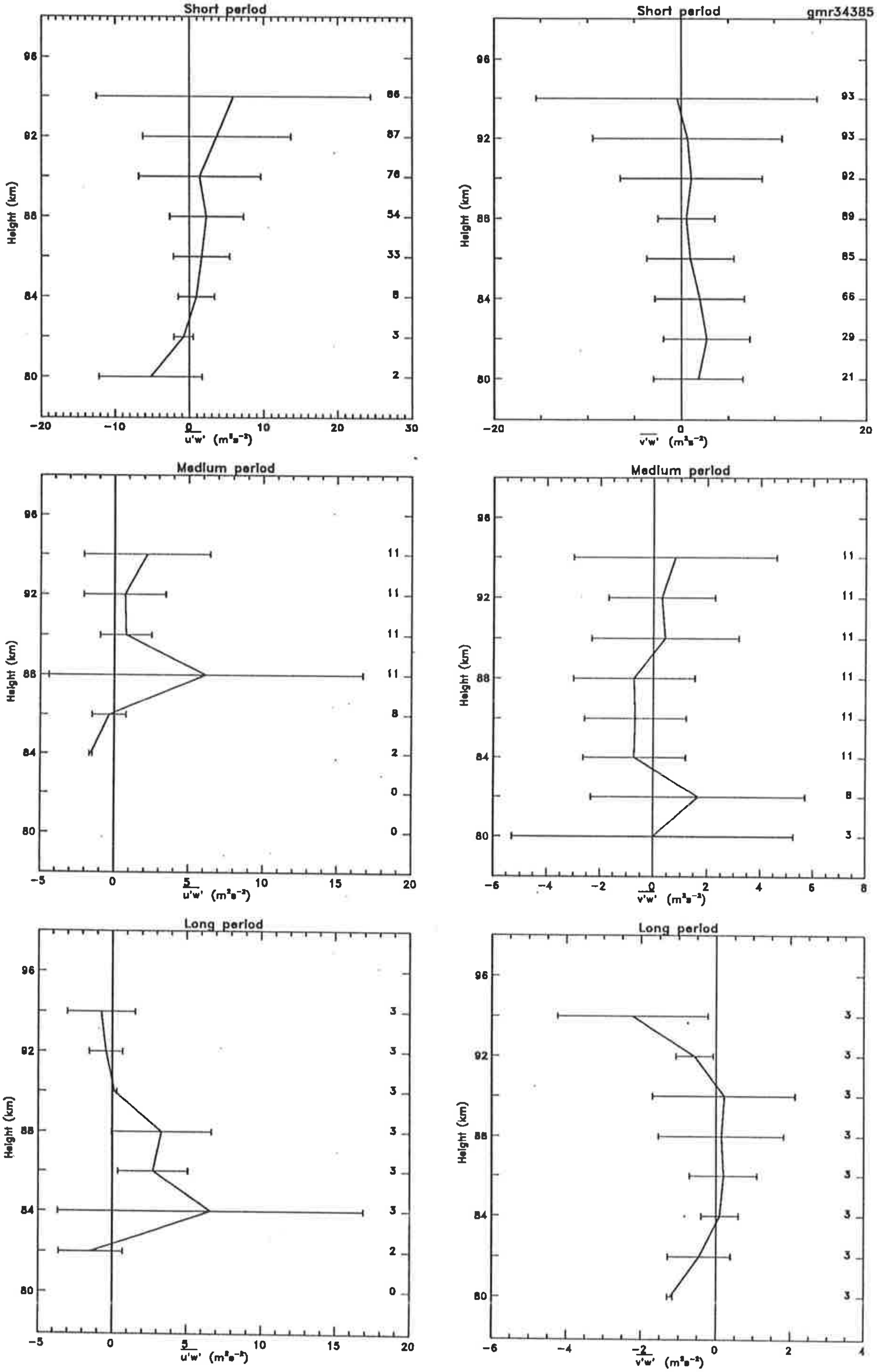

Figure 7.10: Short, medium and long-period $\overline{u'w'}$ and $\overline{v'w'}$ data averaged over the run beginning on day 343 (9 December), 1985. One standard deviation is indicated by the horizontal bar.

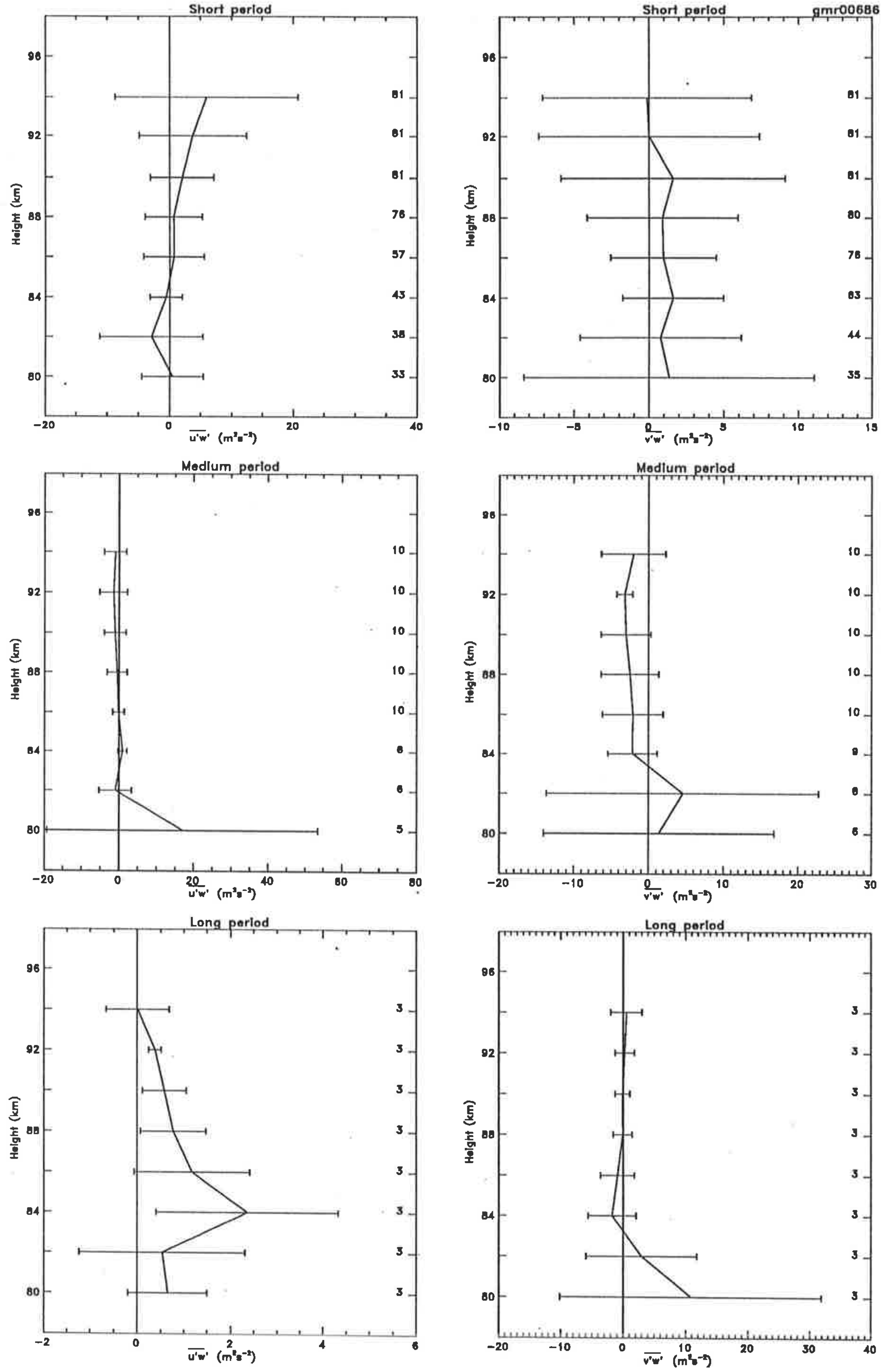

Figure 7.11: Short, medium and long-period $\overline{u'w'}$ and $\overline{v'w'}$ data averaged over the run beginning on day 6 (6 January), 1986. One standard deviation is indicated by the horizontal bar.

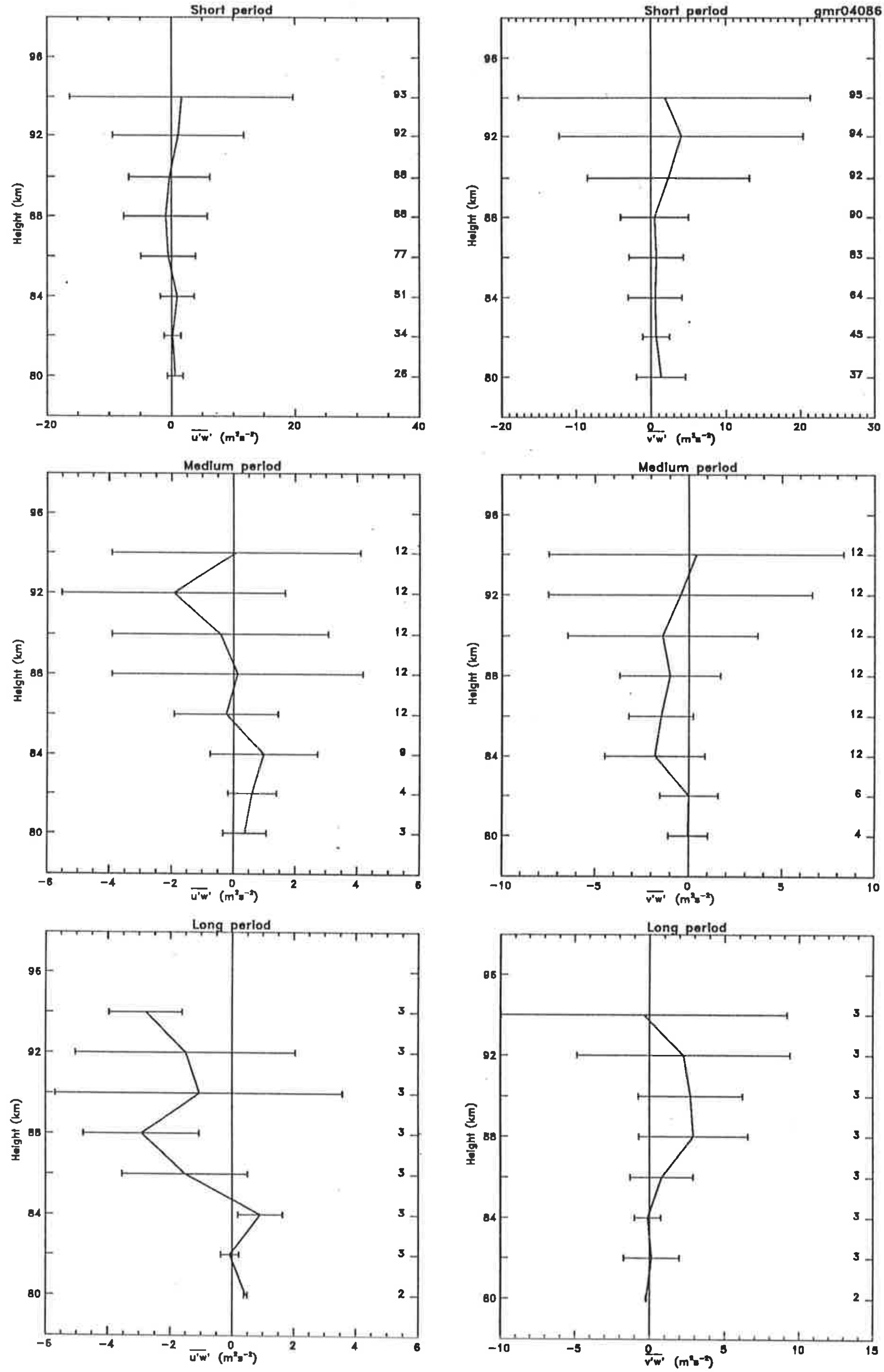

Figure 7.12: Short, medium and long-period $\overline{u'w'}$ and $\overline{v'w'}$ data averaged over the run begining on day 040 (9 February), 1986. One standard deviation is indicated by the horizontal bar.

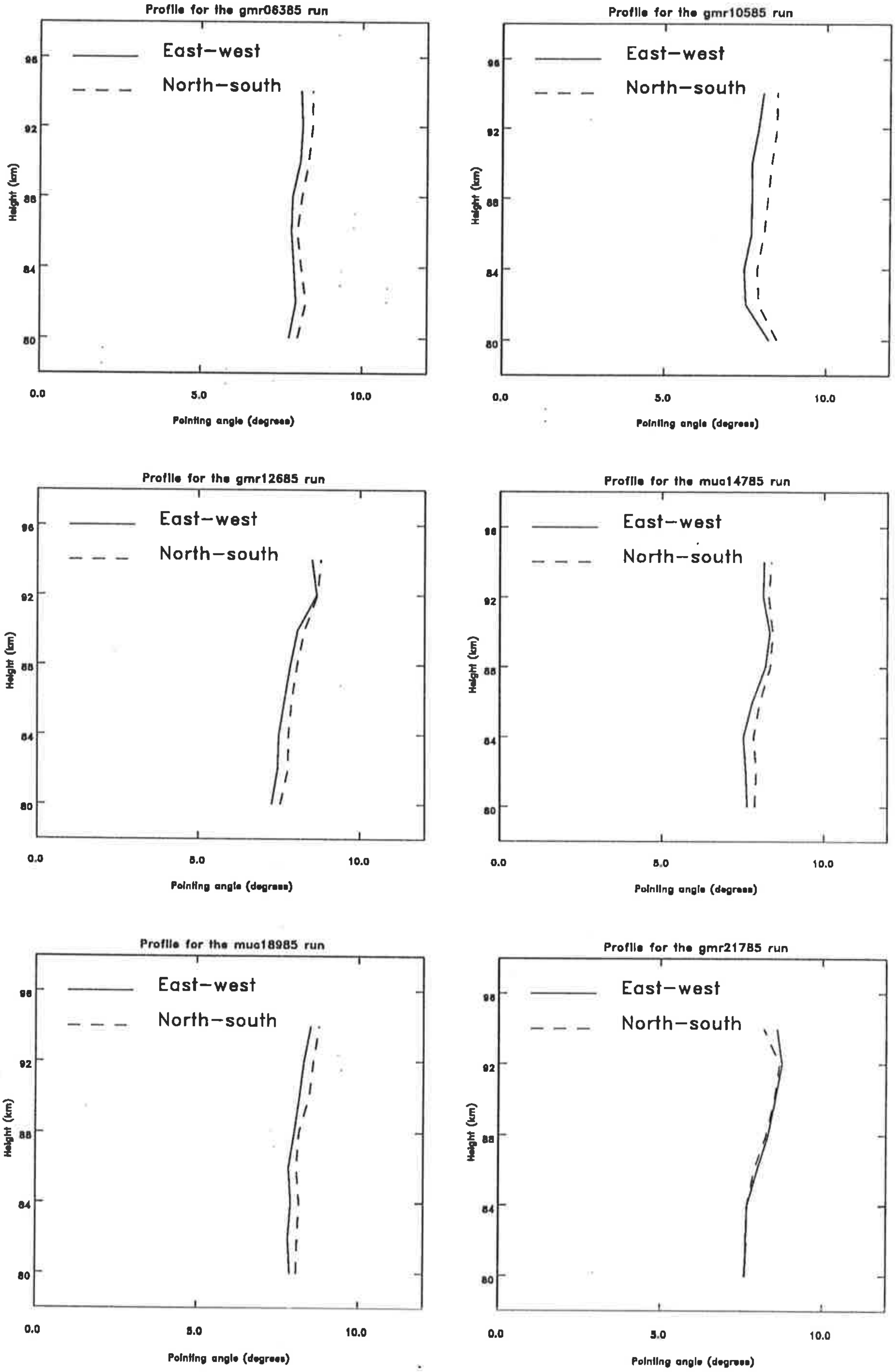

Figure 7.13: Pointing angle profiles for the six data sets up to gmr21785

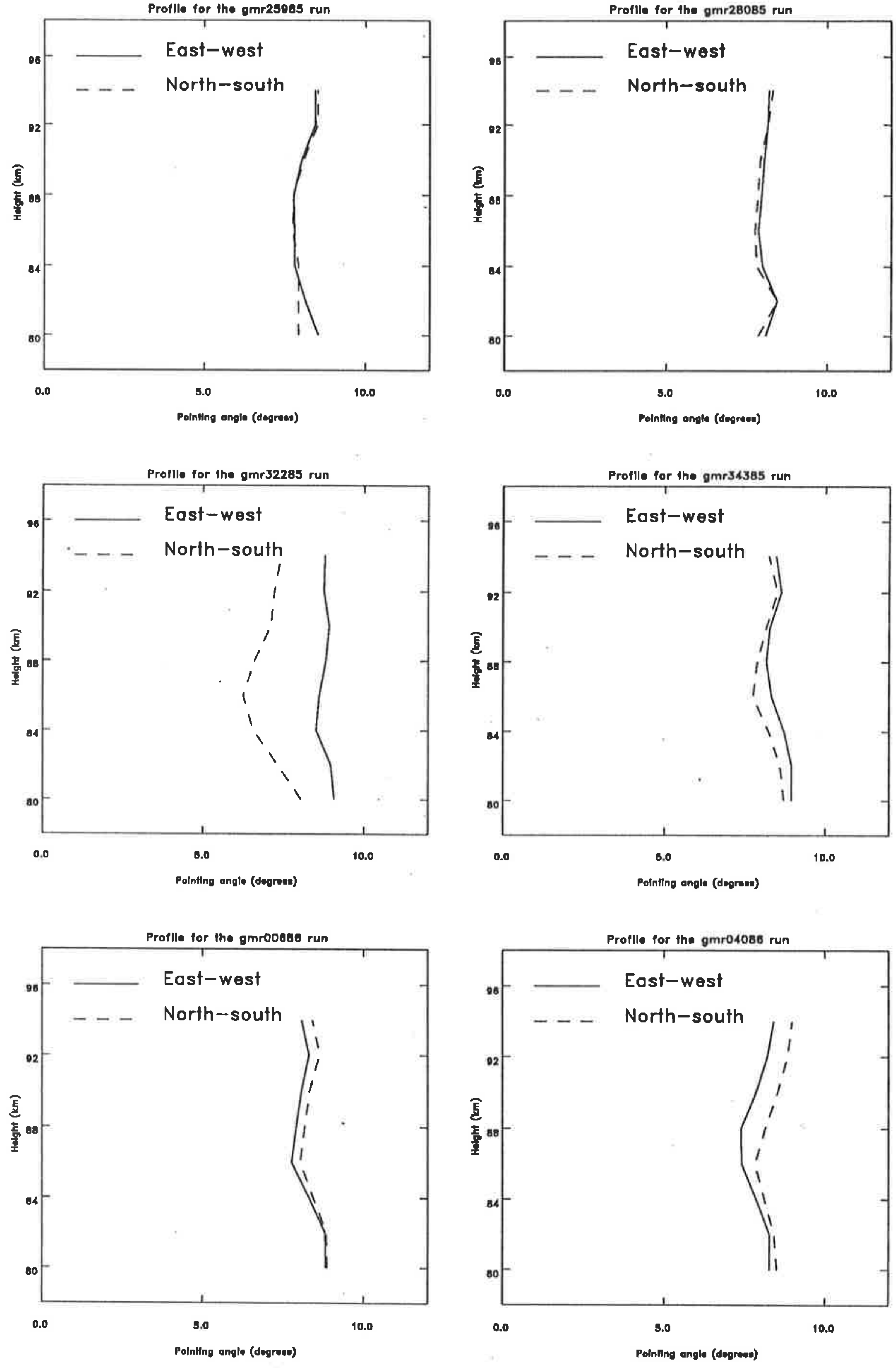

Figure 7.14: Pointing angle profiles for the six data sets up to gmr04086

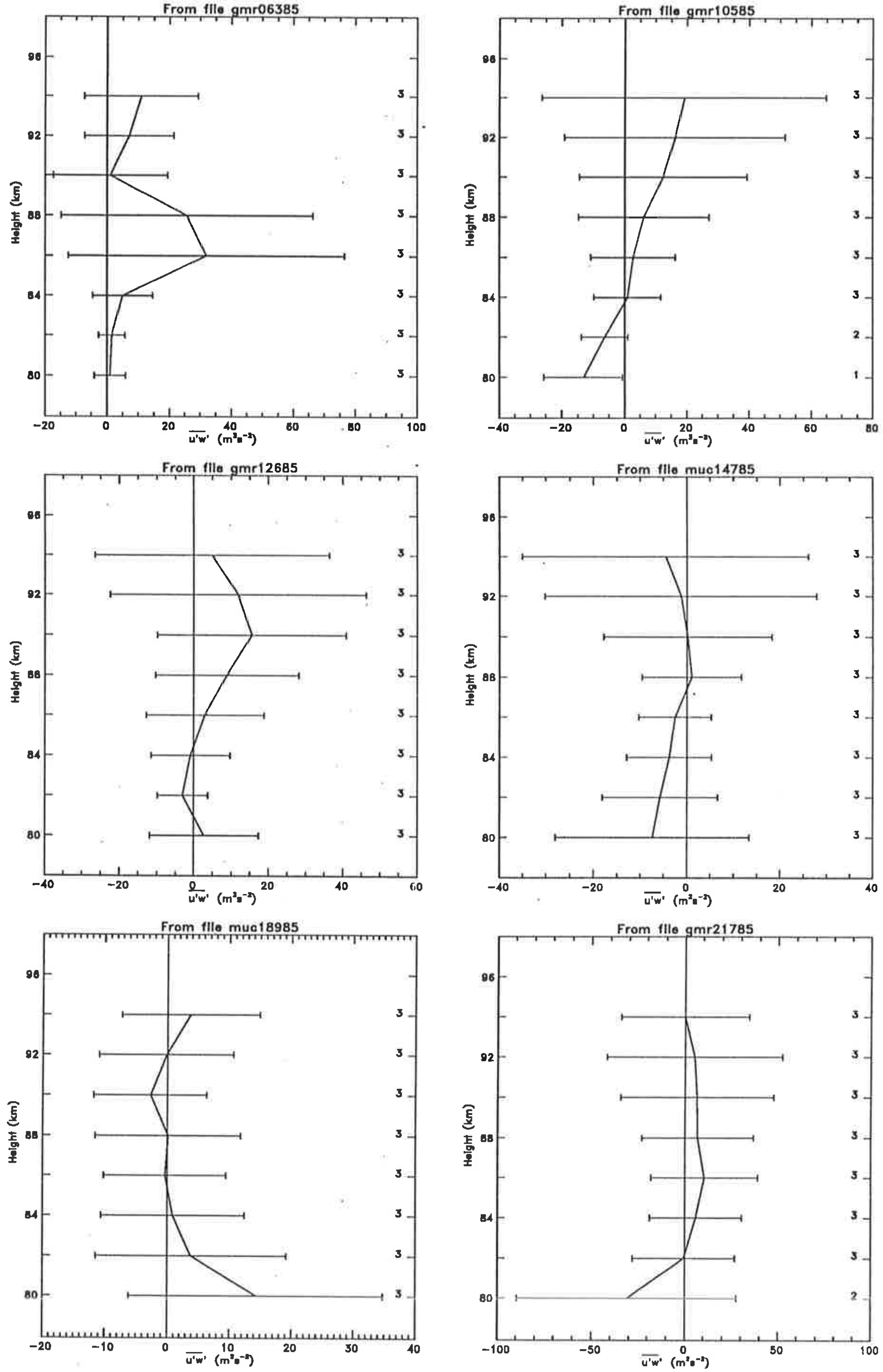

Figure 7.15: Momentum flux ($\overline{u'w'}$) for all periods (gmr06385 to gmr21785). One standard deviation is indicated by the horizontal bar.

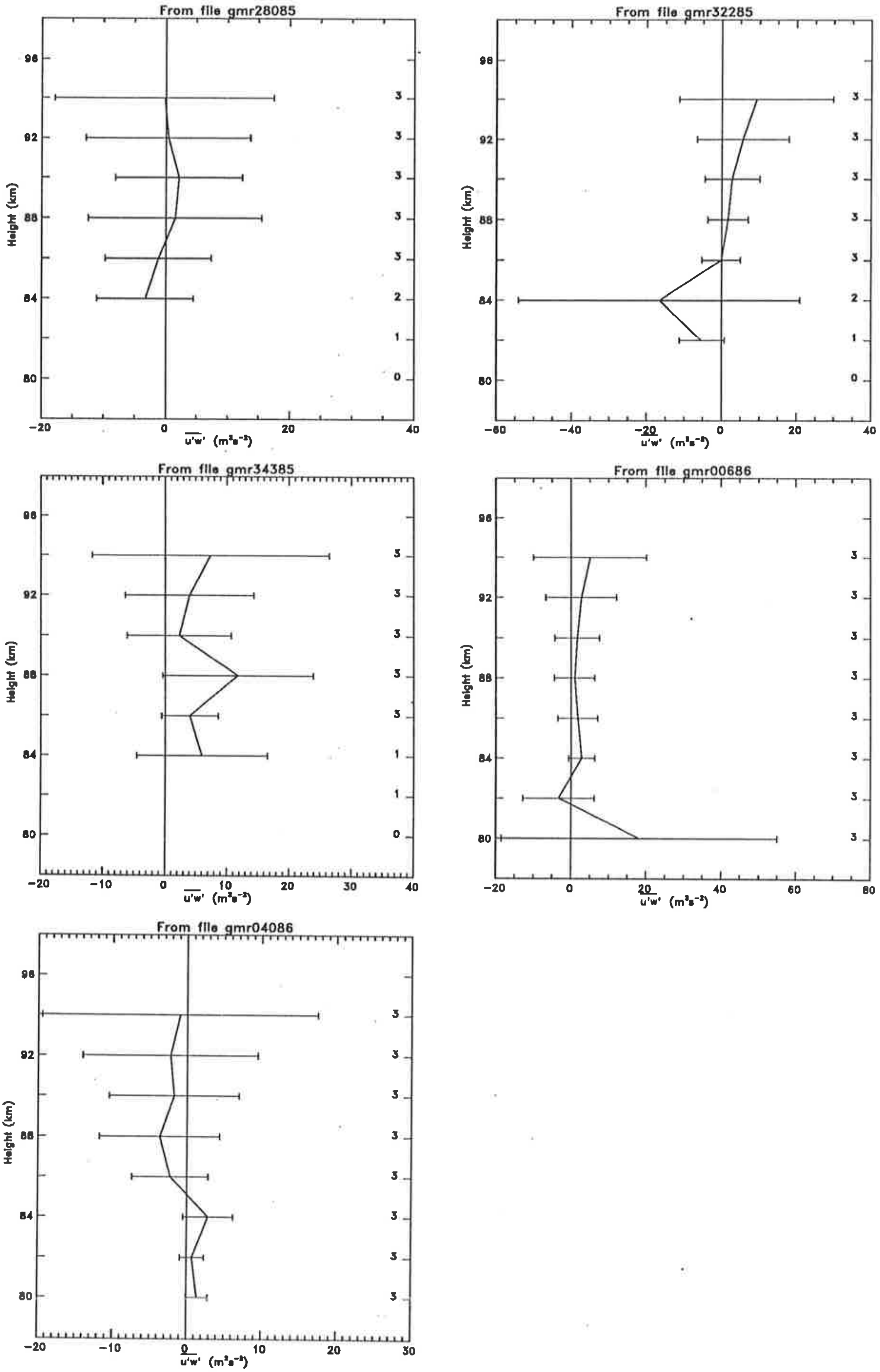

Figure 7.16: Momentum flux ($\overline{u'w'}$) for all periods (gmr28085 to gmr04086). One standard deviation is indicated by the horizontal bar.

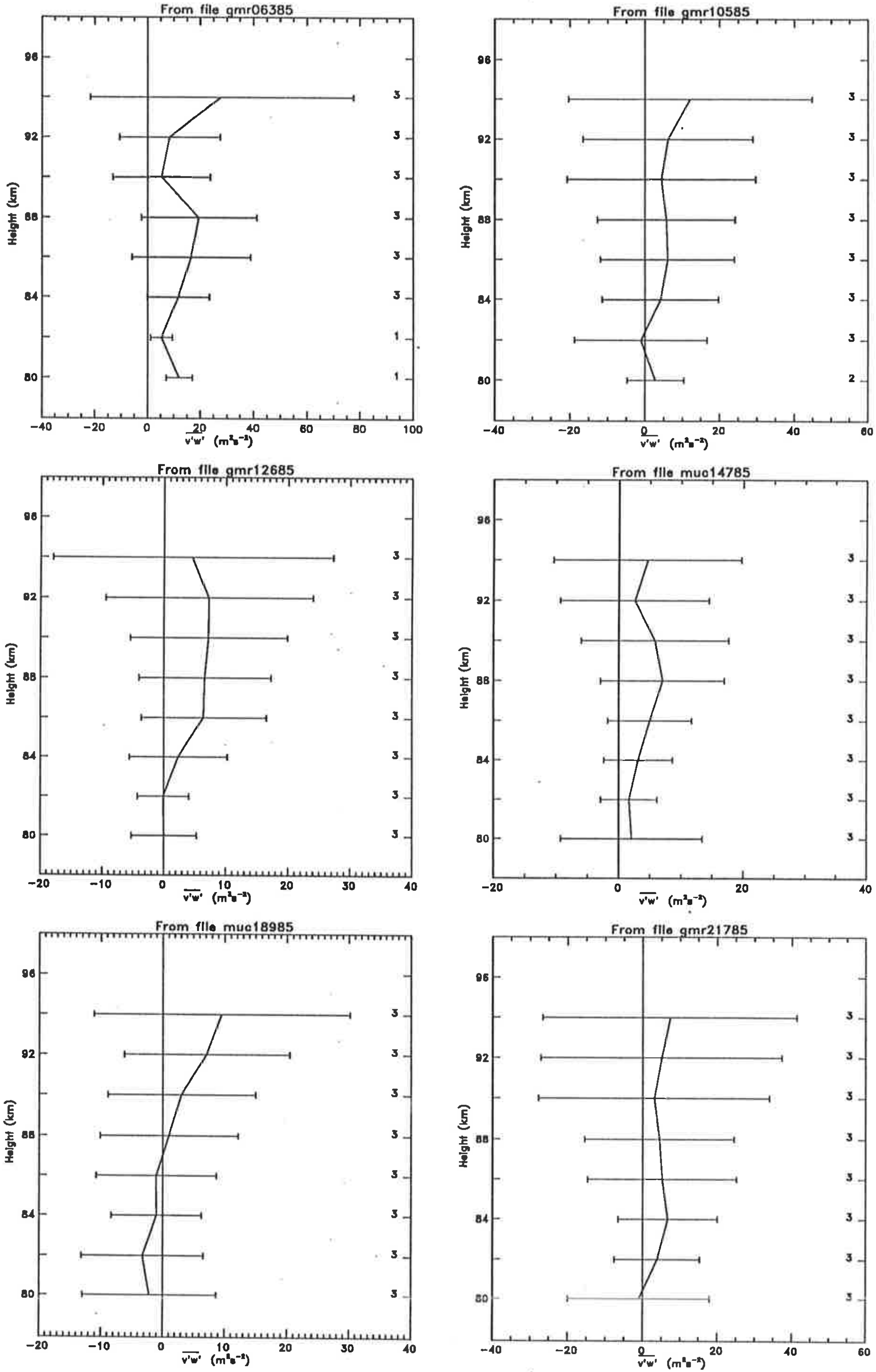
From file gmr06385

From file gmr10585

From file gmr12685

From file muc14785

From file muc18985

From file gmr21785

Figure 7.17: Momentum flux ($\overline{v'w'}$) for all periods (gmr06385 to gmr21785). One standard deviation is indicated by the horizontal bar.

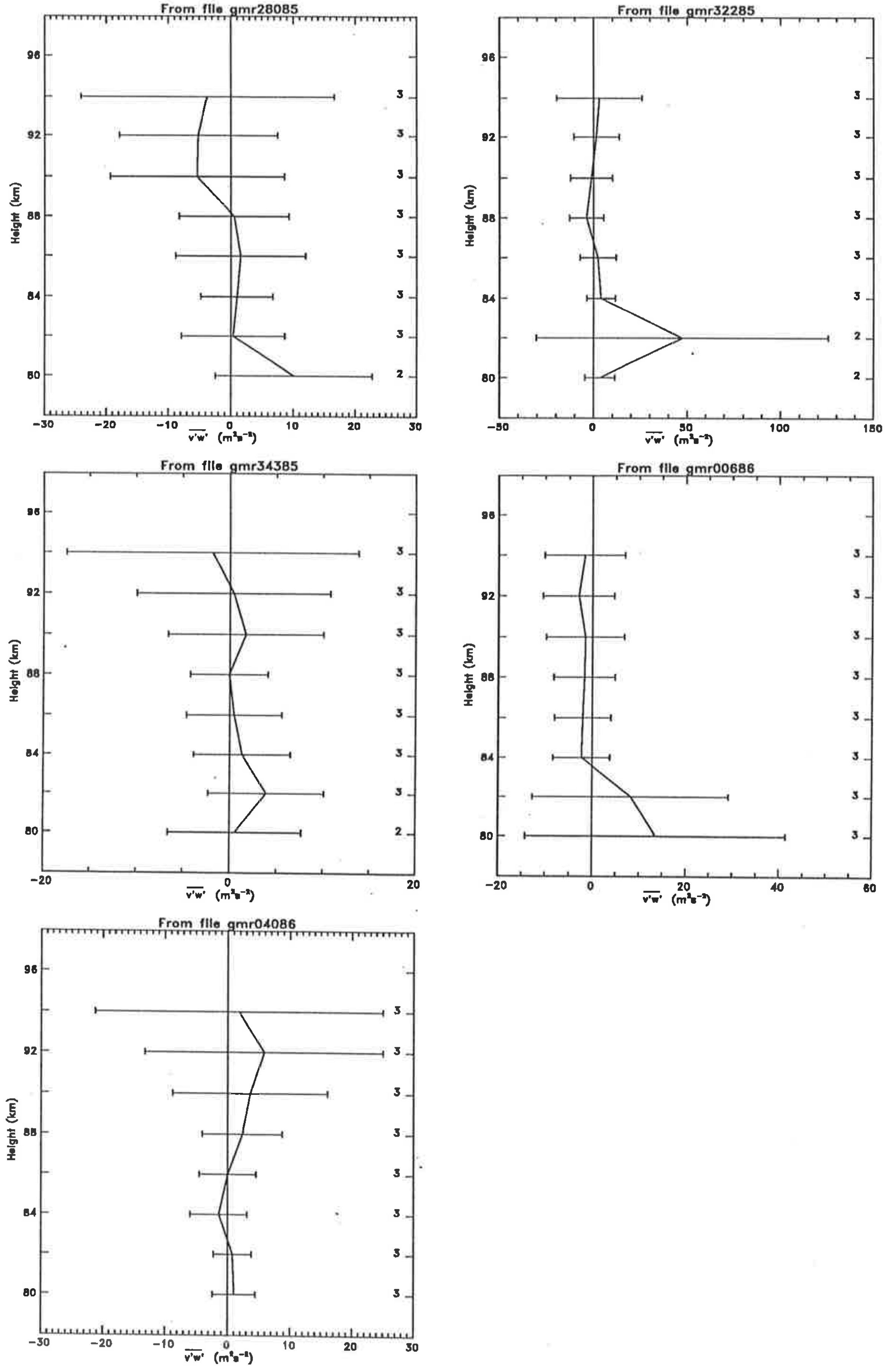

Figure 7.18: Momentum flux ($\overline{v'w'}$) for all periods (gmr28085 to gmr04086). One standard deviation is indicated by the horizontal bar.

up entirely of 4 day campaigns spaced by approximately one month, it is difficult to decide if the data is truly representative of the time around it. Data taken at Adelaide and presented by Reid and Vincent (1987), however, does give some insight into this question. In their case, $\overline{u'w'}$ data taken between 30 June and 16 July 1982 and $\overline{v'w'}$ data taken between 6 July and 16 July has been split up into intervals of between 2.4 and 3.9 days. Some variation in the character of the $\overline{u'w'}$ profiles can be seen and there is an even greater variation in the $\overline{v'w'}$ profiles. Of the 5 $\overline{u'w'}$ profiles, 3 look quite similar to each other, 1 a little different and the other quite different. In $\overline{v'w'}$, the 3 profiles available are each quite distinct. Thus some care needs to be taken in assuming that each data set is characteristic of a longer time period. Conversely, though, the height profile of $\overline{u'w'}$ presented by Reid and Vincent for the period 5–8 October 1982 (see p 448 of that paper) and that presented here for the period 7–11 October (gmr28085) are strikingly similar, suggesting that the momentum flux during early October is moderately uniform in character. Thus a cautionary note is sounded but it is not considered imprudent to proceed with a study of seasonal variations of momentum flux characteristics.

In order to consider the character of the momentum flux through the year, it is necessary to parameterise the momentum flux in some way. The simplest parameter, and that used in figure 7.19, is the mean. Thus, the average momentum flux over the height range 80–94 km for each data set is presented. In figure 7.19, all the periods between 8 min and 24 hr (recalling that the diurnal and semi-diurnal tides have been removed) are included. Figures 7.20, 7.21 and 7.22 give the short-, medium- and long-period height-averaged momentum fluxes.

The average $\overline{u'w'}$ values for "all periods" show some suggestion of a seasonal variation with a minimum around September, October, November (local spring) and possibly in February (1986) although the March (1985) value is quite large. Either of the February or March values may be due to the short term variation mentioned previously. The main contribution to the seasonal variation is that of the short period waves. A clear annual variation in $\overline{u'w'}$ can be seen in figure 7.20 with a minimum in (local) late winter-early spring and zero crossings in early-mid winter and late spring. Two local maxima occur

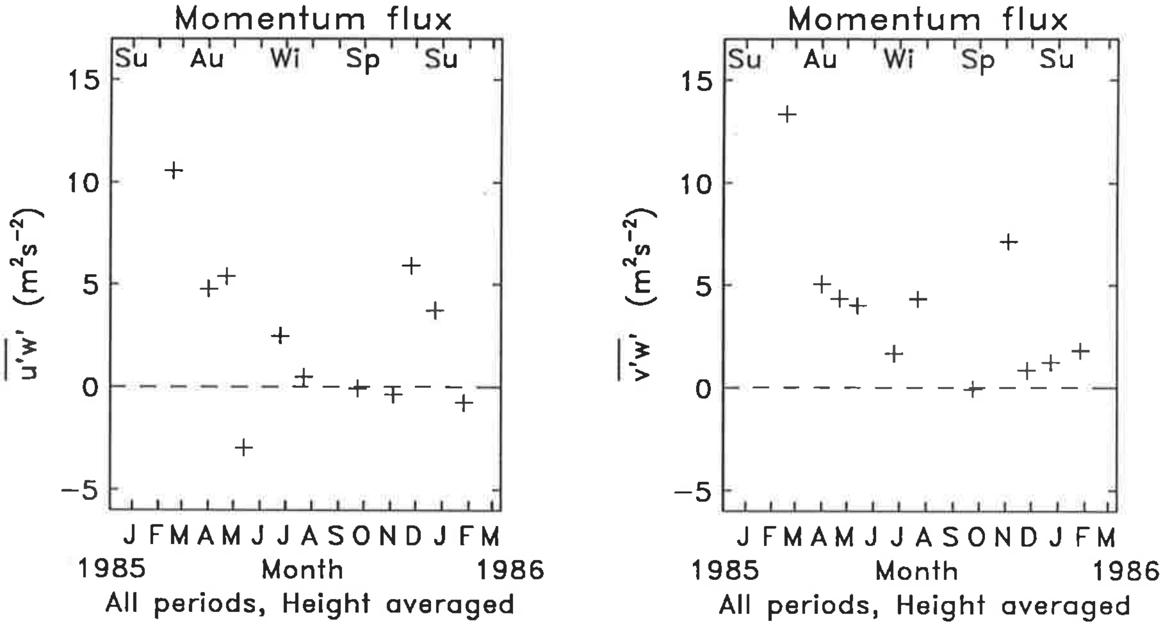

Figure 7.19: Momentum flux ($\overline{u'w'}$ and $\overline{v'w'}$) for all periods, averaged over the height range 80–94 km.

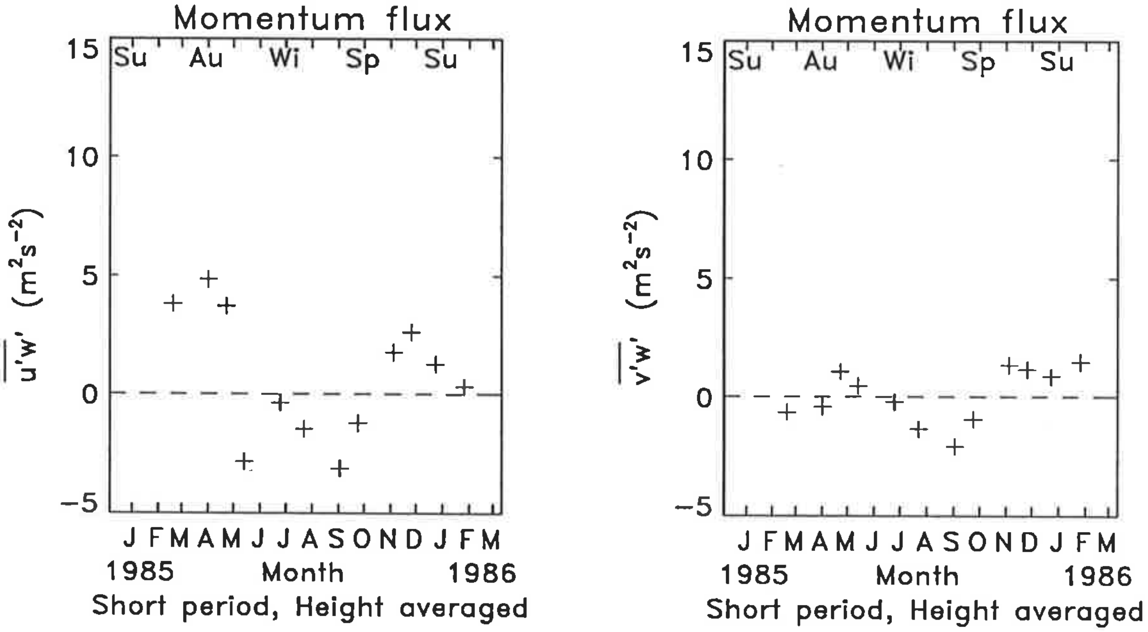

Figure 7.20: Momentum flux ($\overline{u'w'}$ and $\overline{v'w'}$) for short period data, averaged over the height range 80–94 km.

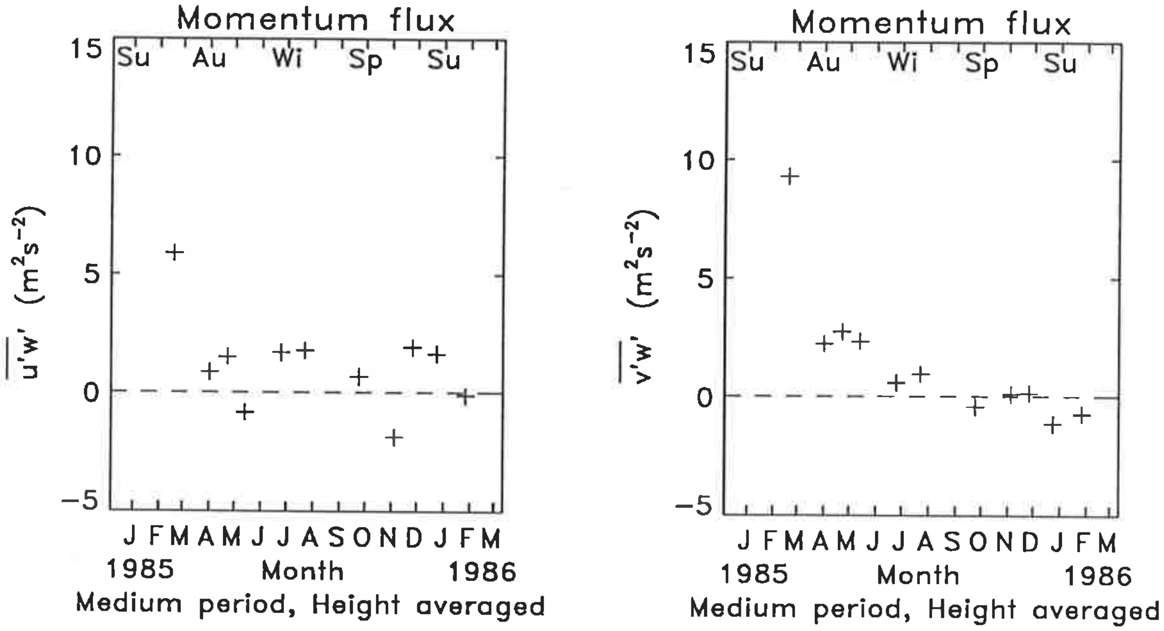

Figure 7.21: Momentum flux ($\overline{u'w'}$and $\overline{v'w'}$) for medium period data, averaged over the height range 80–94 km.

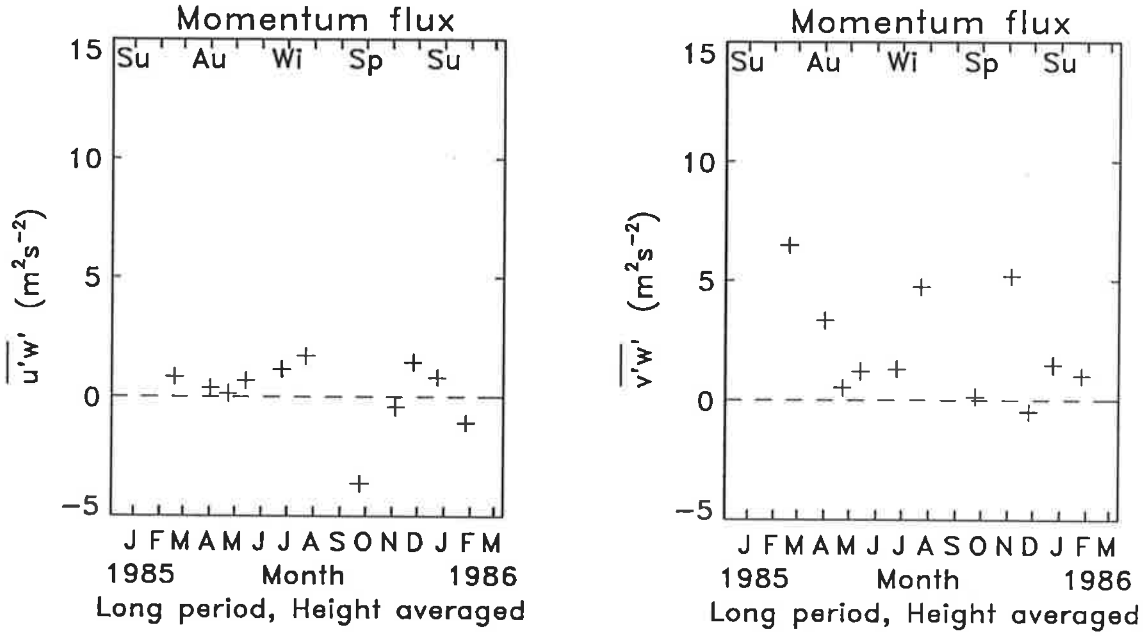

Figure 7.22: Momentum flux ($\overline{u'w'}$and $\overline{v'w'}$) for long period data, averaged over the height range 80–94 km.

at early summer and mid autumn with a local minimum between.

In $\overline{v'w'}$, there seems to be a tendency for the "all periods" values (figure 7.19) to be larger in autumn-winter than in spring-summer. A point in early March and one in November violate this trend. The medium period fluxes are probably the main contributions to this trend with some enhancement through a variation in the short-period $\overline{v'w'}$ values that is similar to that found in short-period $\overline{u'w'}$.

The relative amplitudes of the $\overline{u'w'}$ and $\overline{v'w'}$ components of the momentum flux are presented in figure 7.23. To obtain this figure, the absolute values of $\overline{u'w'}$ and $\overline{v'w'}$ were summed. The fraction of the sum due to $\overline{v'w'}$ was then shaded. Thus the sign of $\overline{u'w'}$ and $\overline{v'w'}$ is ignored. It is noted that, particularly in the case of the medium-, long- and all-period height averages, the contributions due to $\overline{v'w'}$ are of equal or greater importance to those due to $\overline{u'w'}$. An exception to this is the short period data where the $\overline{u'w'}$ values are more often of greater magnitude than the corresponding $\overline{v'w'}$ height averaged momentum fluxes.

The variation during the 4 days of each data set is crudely described by the standard deviation of the momentum flux. This quantity is presented as an horizontal bar in figures 7.1 to 7.12. Figures 7.24, 7.25, 7.26 and 7.27 contain height averages of the standard deviation between 80–94 km (including only those heights where there is enough data). The most striking feature of these figures is the large enhancement in Autumn of the standard deviation of the all-period zonal momentum flux. This enhancement is due to the short period waves (figure 7.25). There is also an extremely large value in August (the GMR21785 data of figure 7.6) which can also be attributed to short-period waves. The all-period $\overline{v'w'}$ values show considerable scatter due to the scatter in the short-period standard deviations. The minima in the $\overline{v'w'}$ standard deviations for all four graphs fall near the solstices (June and December).

The contribution of each period band is considered in figure 7.28. Each box within that figure contains segments whose size represents the fractional contribution of each period band to the sum of the absolute values of the momentum flux from each band. The grey and black shaded areas indicate the contribution due to medium- and long-

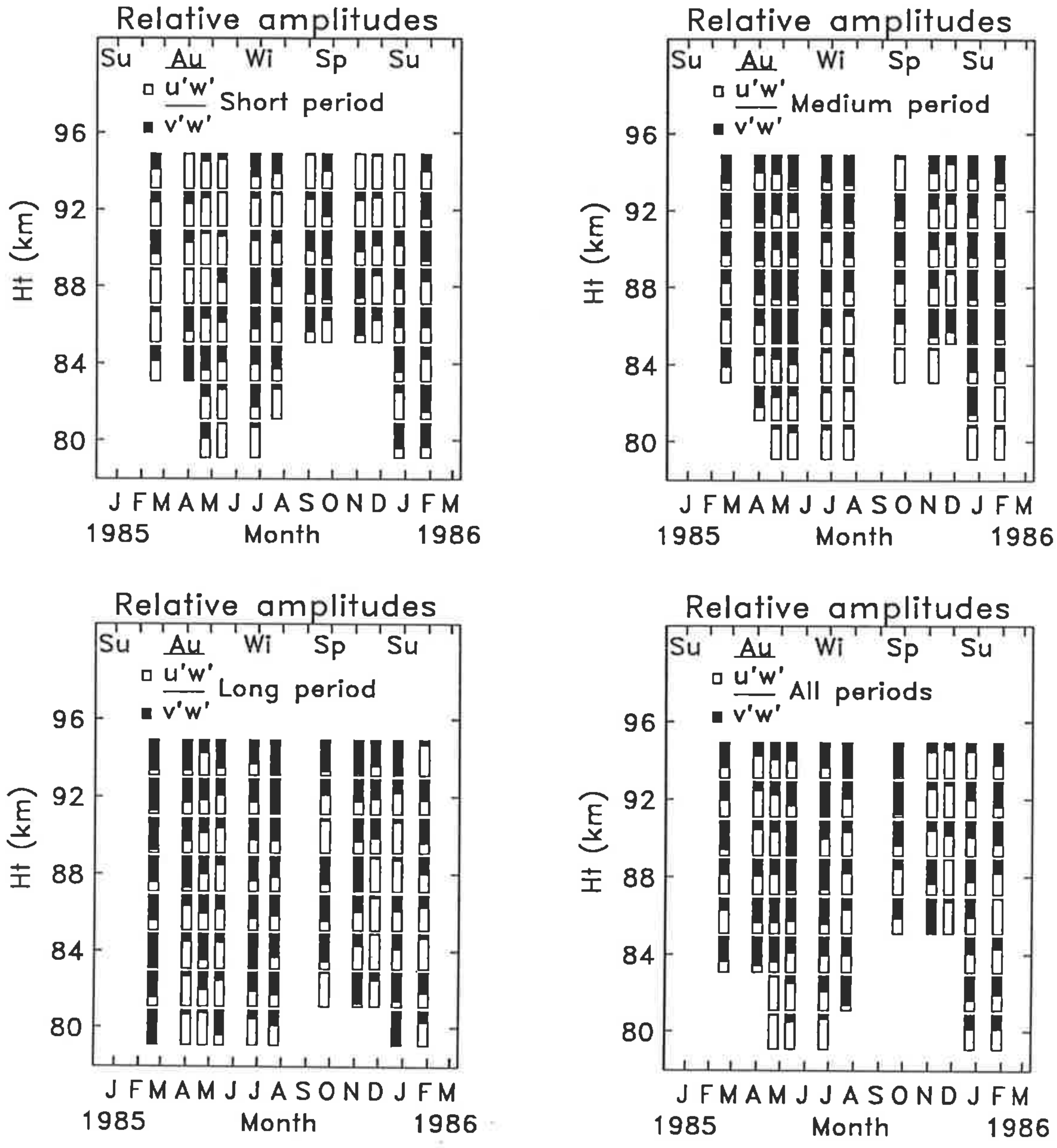

Figure 7.23: The relative amplitudes of $\overline{u'w'}$ and $\overline{v'w'}$ as a function of height and season

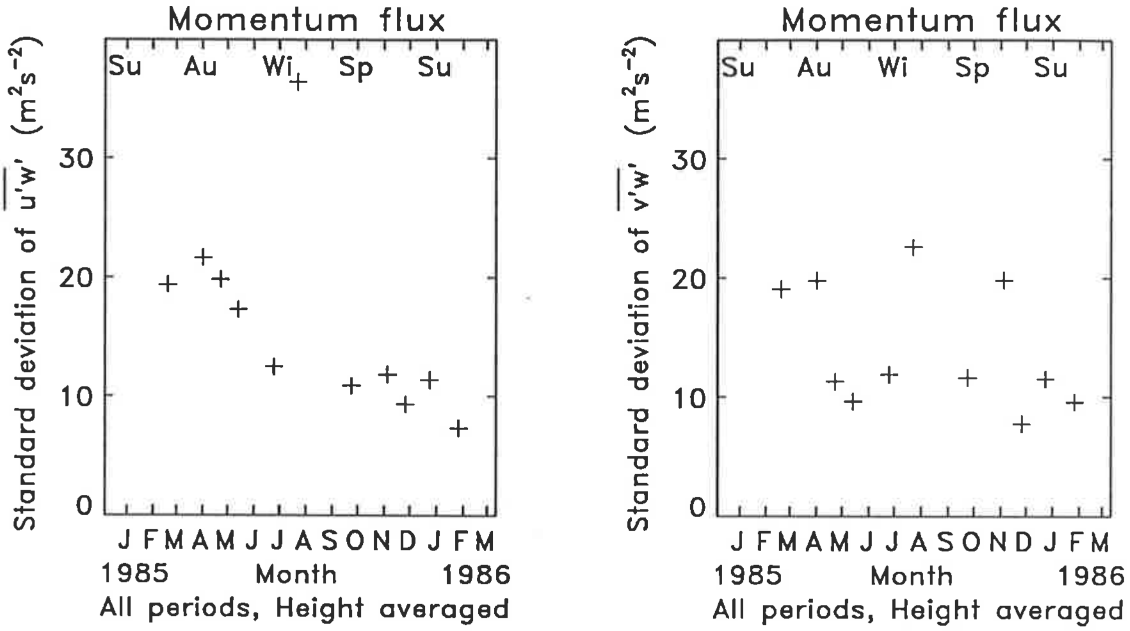

Figure 7.24: Variance of the momentum flux ($\overline{u'w'}$and $\overline{v'w'}$) for all-periods data, averaged over the height range 80–94 km.

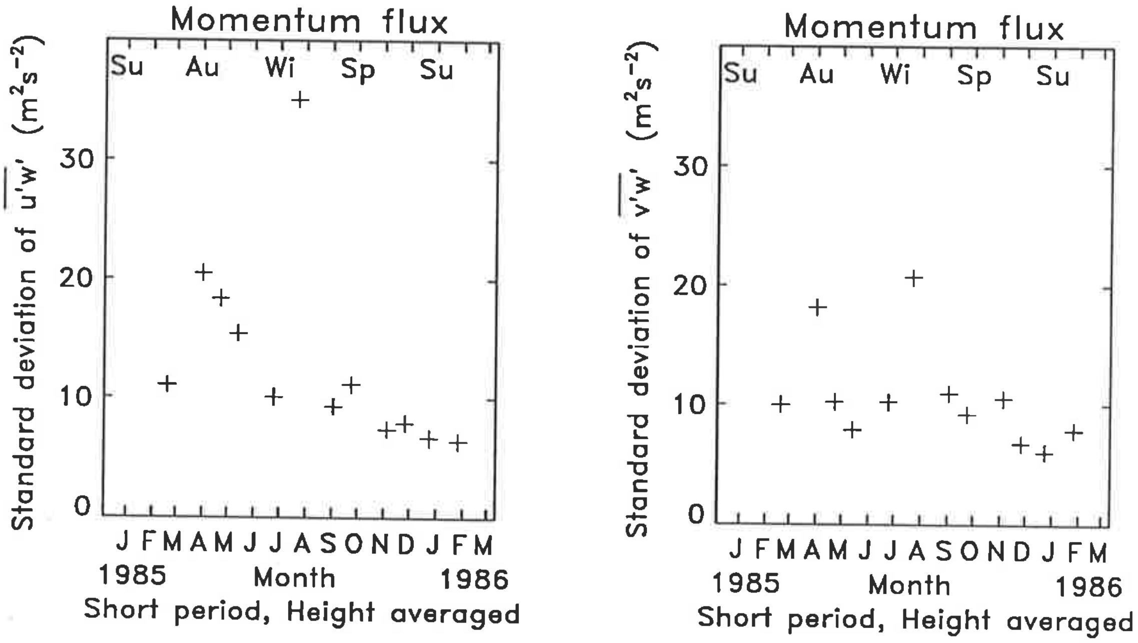

Figure 7.25: Variance of the momentum flux ($\overline{u'w'}$ and $\overline{v'w'}$) for short period data, averaged over the height range 80–94 km.

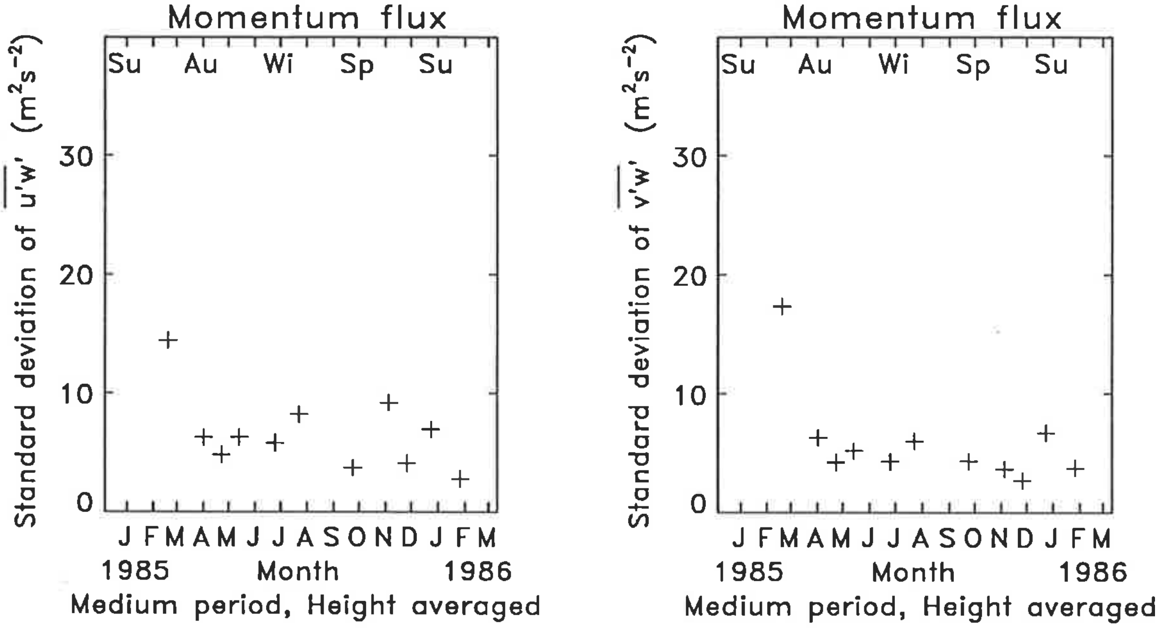

Figure 7.26: Variance of the momentum flux ($\overline{u'w'}$and $\overline{v'w'}$) for medium period data, averaged over the height range 80–94 km.

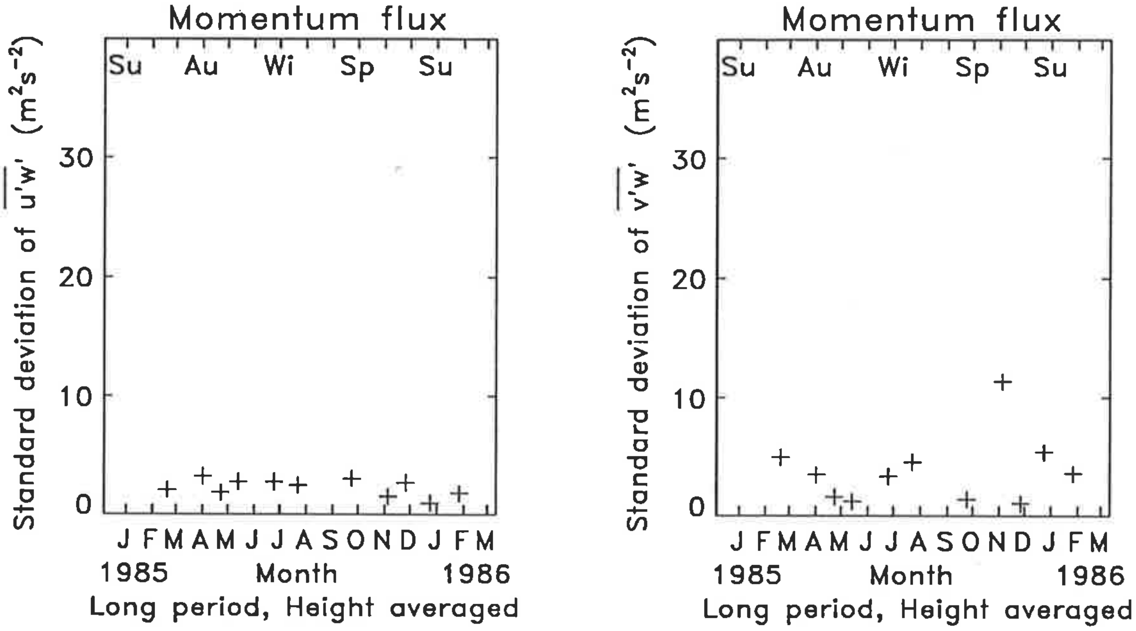

Figure 7.27: Variance of the momentum flux ($\overline{u'w'}$and $\overline{v'w'}$) for long period data, averaged over the height range 80–94 km.

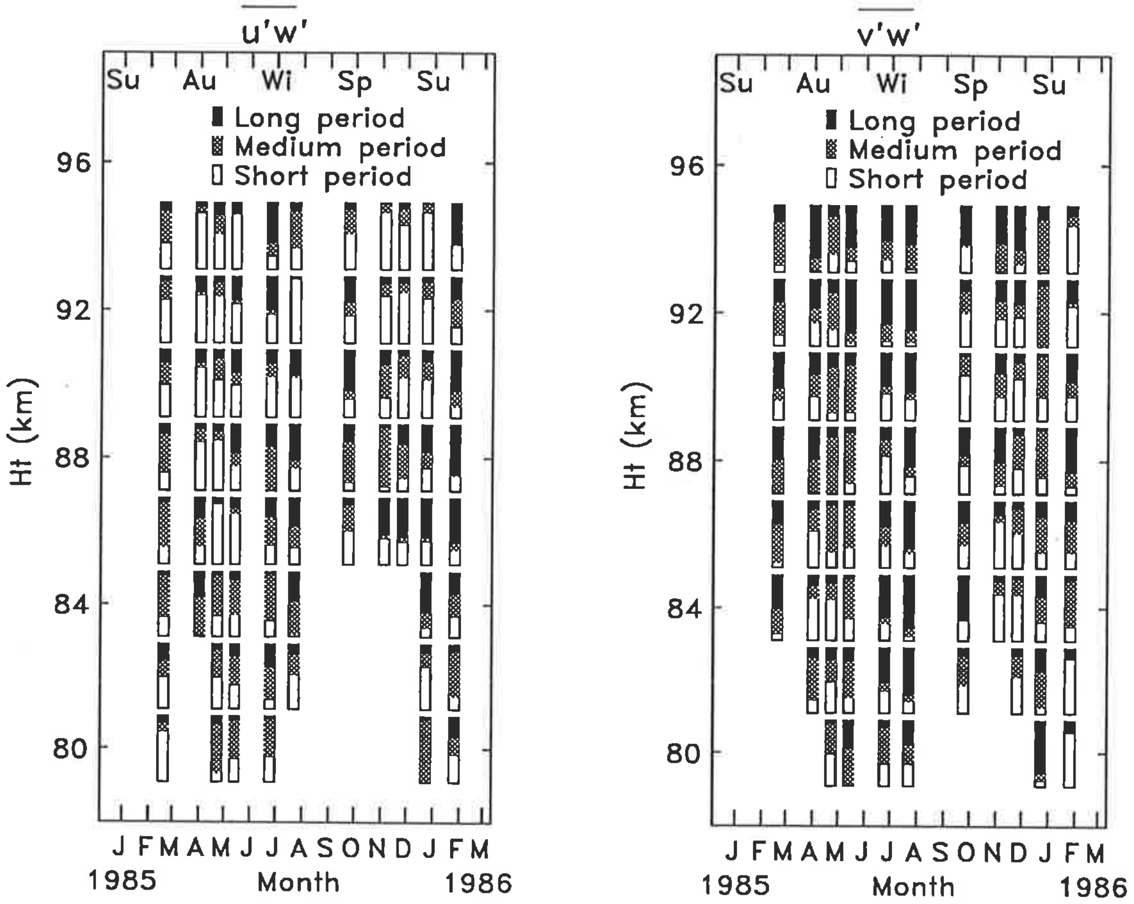

Figure 7.28: The relative contributions of the short-, medium- and long-period waves to the sum of the absolute momentum fluxes. The medium- and long-period contributions are shaded.

period waves respectively. Thus if the short period momentum flux dominates, much of the box will be clear and the shaded regions will occur near the top of the box. It can be seen that in some cases $\overline{u'w'}$ and in almost half the cases in $\overline{v'w'}$, the medium period values make a significant contribution.

Because the medium period range (1 hr to 8 hr) is quite broad and the wave periods contributing to the dominance of the medium-period band are uncertain, it was decided to reanalyse the data into period ranges 8 min–2 hr (short-medium period) and 2 hr–24

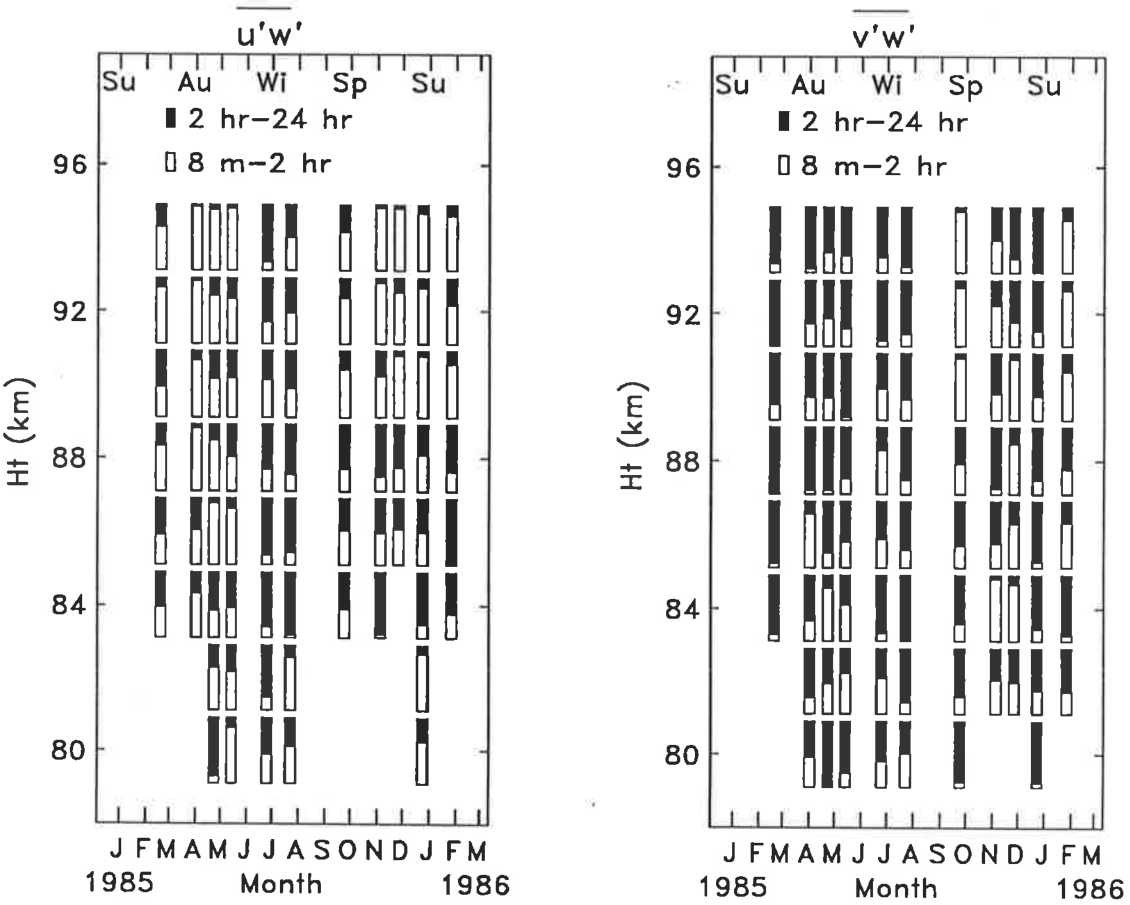

Figure 7.29: The relative contributions of the 8 m–2 hr and 2–24 hr period waves to the sum of the absolute momentum fluxes. The 2–24 hr period contribution is shaded.

hr (medium-long period), once again with the diurnal and semi-diurnal tides excluded. The results of this analysis are presented in figure 7.29. Here it is the contributions due to the 2–24 hr period waves that are shaded. Two points become clear in this figure. The first is that in $\overline{u'w'}$, the 2–24 hr period waves make their most significant contribution in winter, although below 90 km, this contribution continues on into the summer. Secondly, 2–24 hr period waves dominate $\overline{v'w'}$ almost all of the time. The main exception to this is above 88 km during October and at 90 km and below in December.

7.1.3 Discussion

The results of this analysis (which will be collectively referred to as the GRATMAP data) can be compared with those derived by other workers at Adelaide and data acquired at other sites. Data obtained at Adelaide are considered first. The data presented by Vincent and Reid (1983) for $\overline{u'w'}$ between 11–14 May, 1981 fall in the range -1 m^{2}s^{-2} (80 km) to -0.1 m^{2}s^{-2} (92 km). In contrast to this, the all-period data for a closely corresponding time in the data set presented here (6–11 May, 1985; gmr12685 data) has a range -3 m^{2}s^{-2} (82 km) to 16 m^{2}s^{-2} (90 km). The $\overline{u'w'}$ data presented in Reid and Vincent (1987) are averaged with height and compared to a height average of the GRATMAP all-period data in figure 7.30. It is noted that the GRATMAP results have a greater spread than those of Reid and Vincent. Fritts and Vincent (1987) present $\overline{u'w'}$ data for the period 9–17 June, 1984. The 8 min–24 hr data ranges from -3 m^{2}s^{-2} (82 km) to -5.5 m^{2}s^{-2} (90 km) in the 80–94 km height interval. The nearest GRATMAP data were taken between 27 and 31 May, 1985 (muc14785, 9 days prior to that of Fritts and Vincent) and has a maximum of 1 m^{2}s^{-2} (88 km) and a minimum of -7.5 m^{2}s^{-2} (80 km). A height average of the Fritts and Vincent (1987) data has been included in figure 7.30.

All the above works used somewhat different analysis methods. Vincent and Reid (1983) and Reid and Vincent (1987) applied a filtering algorithm that rejected data sets with more than 10% of the data missing but did not apply the manual rejection methods used here. The Fritts and Vincent (1987) and GRATMAP data analysis simply calculated the variance, around a linear trend, of the radial velocities. Visual inspection of the radial velocity time series was used to remove outliers in the Fritts and Vincent analysis as well as the GRATMAP analysis. In all cases, the diurnal and semi-diurnal tides were removed. Vincent and Reid assumed a pointing angle of 11.6 ° whereas Fritts and Vincent used a method (comparing root-mean-square velocities) that was questioned in chapter 5. Reid and Vincent used a pointing angle profile derived from a limited measure of the scatterers' polar diagram. These differences in the pointing angle profile can affect the magnitude of the momentum flux estimates but cannot change the

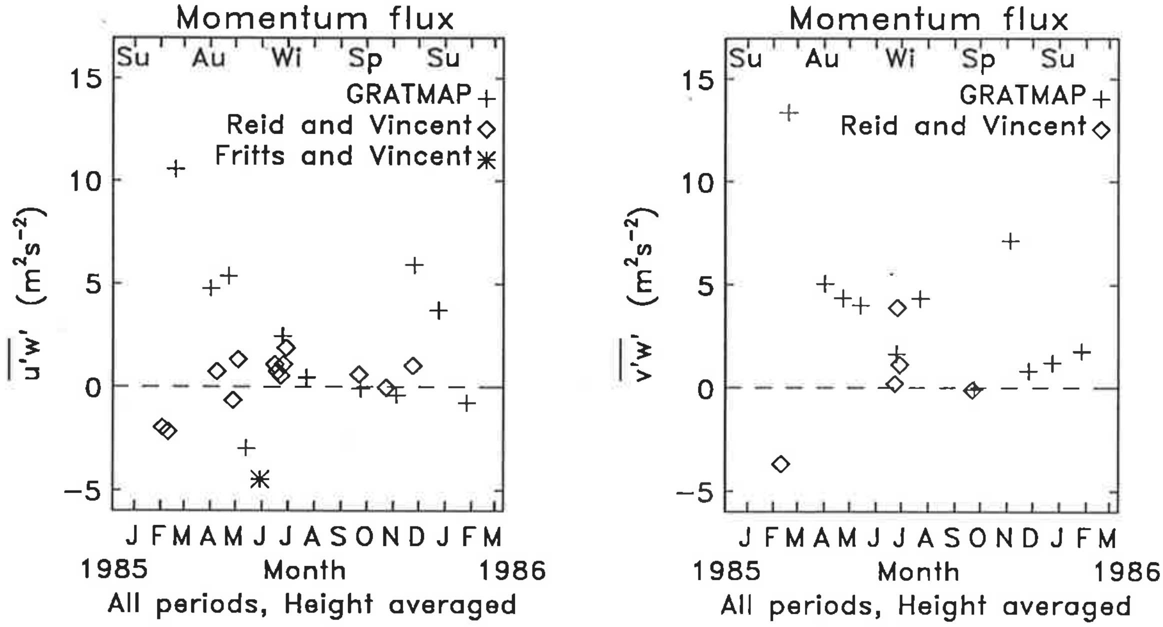

Figure 7.30: A comparison of the height averaged, all-period GRATMAP $\overline{u'w'}$ and $\overline{v'w'}$ data, with height averages of the Reid and Vincent (1987) $\overline{u'w'}$ and $\overline{v'w'}$ data and Fritts and Vincent (1987) $\overline{u'w'}$ data

sign. Despite these differences in analysis, the momentum flux measurements show general agreement.

Data obtained at Kyoto (35°N, 136°E) using the MU radar would be useful for comparison with the Adelaide data presented here because of the geographical conjugacy of the two sites. Tsuda *et al.* (1990) have presented a climatology of momentum fluxes. However, two points make comparison of the data sets from the two sites difficult. The first is that the MU radar data do not go above 80 km altitude whereas the GRATMAP data were not obtained below this level. Secondly, by virtue of the fact that the MU radar could only obtain data between 8:00 and 16:00 local time, the results of Tsuda *et al.* do not include contributions from waves of period greater than 2 hr. A comparison between GRATMAP short-medium period (say) data and the MU radar results could be considered, however, this too may be inappropriate. Fritts and Vincent (1987) showed that momentum flux in June of 1984 had a diurnal variation due to the large amplitude of the diurnal tide at Adelaide at that time of the year. They found that an enhancement of momentum flux values occurred between 0:00 and 6:00 local time, i.e. outside the sampling time of the MU radar data. The inability of VHF radars to obtain mesospheric velocities at night may then lead to a bias in averaged momentum flux data, at times when similar diurnal tidal conditions occur, because these radars will then only sample part of this momentum flux cycle. Although the zonal component of the diurnal tide is generally larger at Adelaide than it is at Kyoto (Vincent *et al.* 1988), in June 1984 this component was of the same magnitude at both sites. Therefore, at least at some times of the year, a limited sampling interval will be a problem. Conversely, though, the wind structure in the region below 80 km may differ from that above 80 km such that this diurnal modulation does not occur. Obviously, a data set with a full 24-hour coverage is required to resolve this question.

Fritts and Yuan (1989) calculated the momentum flux above Poker Flat, Alaska for 8 days in June 1986. (At this time and latitude, it was possible to obtain VHF echoes throughout the day.) Although they found values that were larger in magnitude than those of Vincent and Reid (1983) and Reid and Vincent (1987), the values presented by Fritts and Yuan are of similar magnitude to many of those presented in figures 7.15, 7.16, 7.17 and 7.18. The results of Rüster and Reid (1990) for a similar time at Andenes in northern Norway are smaller than those of Fritts and Yuan. Rüster and Reid, however, calculated the quantity $(\overline{u'w'} + \overline{v'w'})/\sqrt{2}$ because of limitations in the beam configuration. Thus a small $\overline{v'w'}$, like that found by Fritts and Yuan, could explain this difference.

The annual cycle that can be seen in the $\overline{u'w'}$ data of figure 7.20 could reflect a variation in the source distribution or in the filtering effects of the winds between the source and the mesosphere. This cycle is less clear in the all-period data which may explain the difference between the observations presented here and those presented by Reid and Vincent (1987) who found that the minima in the absolute value of the momentum fluxes occurred at the equinoxes. The long-period momentum fluxes presented here do not seem to be modulated in the same way as the short-period values so that their inclusion in the all-period data, both here and in the Reid and Vincent data, could act to make the position of the minimum less clear and explain the differences between the Reid and Vincent result and that presented here.

If it is assumed that the source distribution of gravity waves does not vary greatly through the year, an explanation for the character of the short period $\overline{u'w'}$ as a function of time can be tendered. If the polarisation relation for short period waves ($u' = -w'k/m$ where k and m are the horizontal and vertical wavenumbers respectively) is multiplied by w' and averaged, the result for a monochromatic gravity wave is that

$$\overline{u'w'} = -\frac{k}{m}\,\overline{u'^2}. \tag{7.1}$$

If it is assumed that wave fluxes are upward, then m will be negative so that

$$\overline{u'w'} = \frac{k}{|m|}\,\overline{u'^2}. \tag{7.2}$$

Thus the sign of $\overline{u'w'}$ will be the same as the only non-positive-definite quantity in the expression, i.e. k.

The above arguments suggest that when $\overline{u'w'}$ is positive, fewer negative phase-speed waves are not contributing to the mesospheric momentum budget. Little is known of the gravity-wave phase-speed distribution although it is often assumed that the phase velocity is symmetric in azimuth. Filtering effects are then thought to remove parts of this distribution as waves propagate upwards through the stratosphere.

A number of aspects of the short-period $\overline{u'w'}$ data presented in figure 7.20 are consistent with the ideas presented above. The mean zonal wind for 35°S from the Fleming *et al.* (1988) model are presented in figure 7.31 for a height range of approximately 0–80 km. It can be seen that the negative $\overline{u'w'}$ values (late-May, July, August, September and October) correspond to times when positive phase-speed waves will encounter a critical level in the stratosphere. Thus, negative phase speed waves will dominate the phase speed spectrum in the mesosphere and yield a negative $\overline{u'w'}$. Similar arguments can be applied to the November, December, January and February data if it is assumed that the phase-speed spectrum is symmetric in azimuth (at least in the east-west plane) just above the tropospheric jet. (This criterion avoids the filtering effects of the tropospheric jet itself.) The early-May value violates the above concepts and may be a result of the short term variations discussed previously.

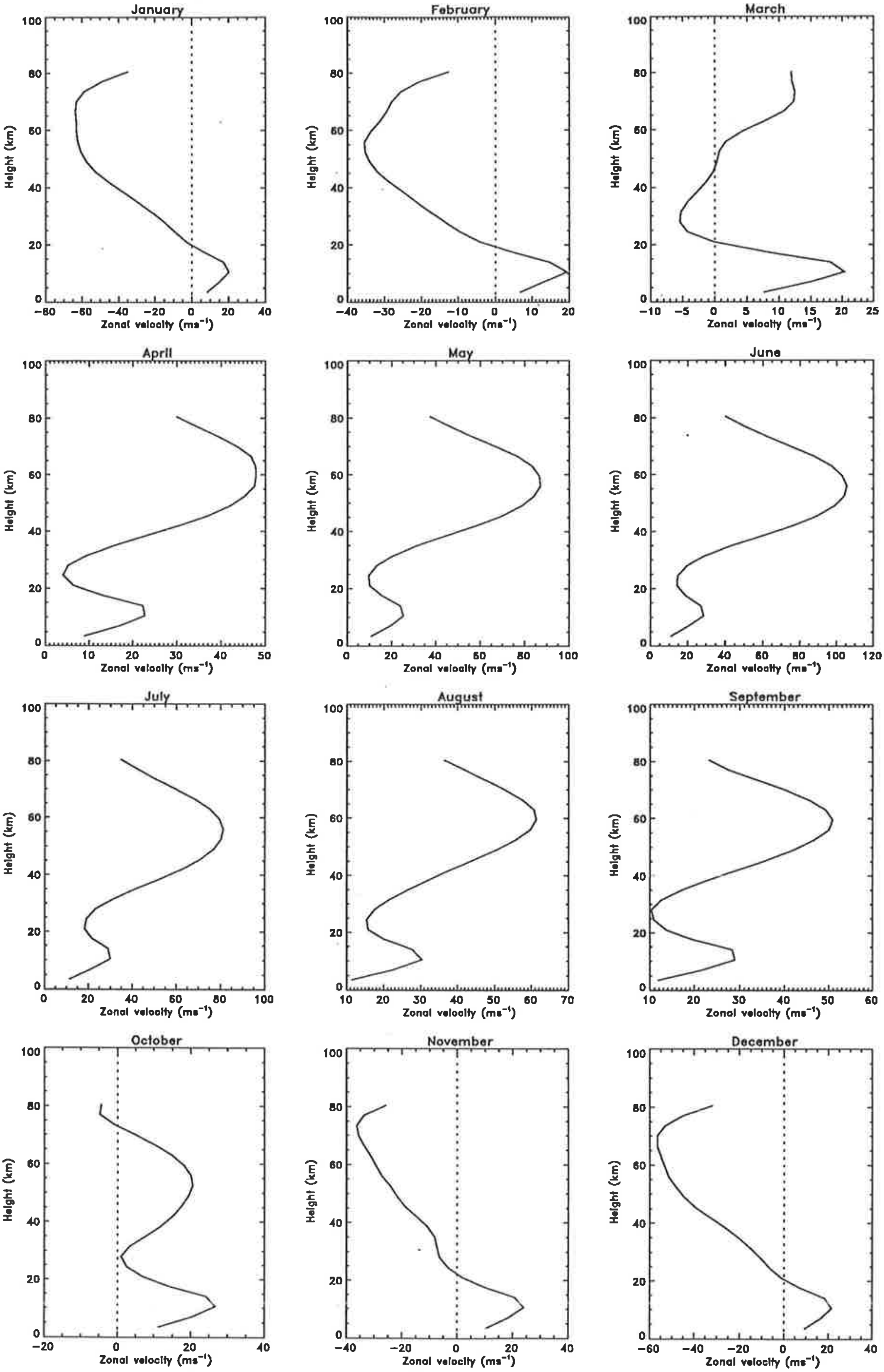

Figure 7.31: Profiles of zonal wind through the stratosphere for Adelaide (35°S)

Some comment can be made on the height averaged $\overline{u'w'}$ and $\overline{v'w'}$ standard deviation data presented in figure 7.25. If the wind field through which the gravity waves propagate is highly variable with time, then the mesospheric momentum flux will also vary with time (given a constant source distribution over the 4 day observation period). This variation can be quantified by calculating the standard deviation of the $\overline{u'w'}$ and $\overline{v'w'}$ values as has been done in figure 7.25. A possible cause of this variation is one or more of the solar tides. With this in mind, it is noted that the large standard deviation values for $\overline{u'w'}$ in the early half of 1985 (see figure 7.25) correspond in general to a time of the year when the zonal component of the diurnal tide has its largest amplitudes at Adelaide (Vincent *et al.* 1989). However, a smaller peak in the zonal diurnal tidal amplitude in October does not have a corresponding enhancement in height-averaged standard deviation. The large variation in the $\overline{u'w'}$ data at this time should be noted in the context of figure 7.30. The $\overline{u'w'}$ values in the early parts of the year show considerable scatter both within the GRATMAP data set and when the results of Fritts and Vincent (1987) and Reid and Vincent (1987) are included. This scatter corresponds to some extent to the time when the height averaged standard deviation in figure 7.25 is large.

Some attempts were made to present a "typical" summer and winter momentum flux profile. The variability in the data just discussed, however, make it difficult to represent the character of the summer momentum flux in one profile. In winter, however, the variability is much less. This is reflected in the standard deviation data, as well as in the fact that the height profiles of $\overline{u'w'}$ for 5–9 August (gmr21785) and 7–11 October (gmr28085) are quite similar. In conjunction with the similarity between the latter profile and one presented in Reid and Vincent (1987) for 5–8 October, it is concluded that the average momentum flux does not vary greatly at this time of the year and that the profiles just mentioned can be taken as typical for the late-winter early-spring period.

It has been noted by other authors that $\overline{u'w'}$ is dominated by contributions from short period waves (e.g. Fritts and Vincent) and this is supported by figure 7.29. The exception to this is, in general, during the winter. The $\overline{v'w'}$ data does not reflect this trend. In general, the contribution to the total momentum flux of waves of period less than 2 hr is less significant than that due to longer period waves.

7.2 Mean-flow acceleration

In chapter 1, the importance of a momentum source to balance the mesospheric momentum budget was discussed. Another "torque" was required to balance the Coriolis "torque" due to the meridional flow present at that level. (Note that the terms "torque", "body force" and "mean-flow acceleration" are used interchangeably in discussions of the momentum budget. The units of the quantity to be calculated here are those of acceleration so it is the latter term that will be used in this chapter.) The mean-flow acceleration can be calculated from the momentum flux using the expressions,

$$\overline{u}_t = -\frac{1}{\rho_0}\frac{\partial \rho_0 \overline{u'w'}}{\partial z}, \tag{7.3}$$

and

$$\overline{v}_t = -\frac{1}{\rho_0}\frac{\partial \rho_0 \overline{v'w'}}{\partial z}, \tag{7.4}$$

where ρ_0 is the mean density at height z. To balance the momentum budget, the mean-flow acceleration due to the Coriolis force should equal the mean-flow acceleration due to the zonal momentum flux divergence. The Coriolis acceleration is equal to fv, where f is the Coriolis parameter and v is the meridional velocity.

The above parameters can be calculated from the available Buckland Park data. The meridional velocity is obtained from the spaced-antenna data that is collected routinely at Buckland Park, however, this data is not available during the four-day intervals of the GRATMAP data. Instead, a period of four-days both before and after each GRATMAP run is averaged to obtain a height profile of v. To give a Coriolis acceleration in $\mathrm{ms^{-1}day^{-1}}$, the meridional velocities are multiplied by 7.29 day^{-1}. The densities are calculated using the Fleming *et al.* (1988) model atmosphere. Pressure and temperature for 30° S and 40° S are each interpolated to give a value at 35° S. The ideal gas equation is then used to obtain the density at heights between 75 km and 100 km. These are then interpolated (using a straight line fit to the log of density) to give densities every 2 km in the range 80km to 94 km.

In practise, the mean-flow acceleration due to momentum flux is a difficult parameter to calculate. Although based on a simple equation, the slope of $\rho_0\overline{u'w'}$ (say) as a function of height is subject to some uncertainty due to the uncertainty in each value of $\overline{u'w'}$. To overcome this, some smoothing is necessary, and this has been done by fitting a straight line to three consecutive (in height) points and calculating the slope of this line. The slope calculated using $\overline{u'w'}_{z-1}$, $\overline{u'w'}_z$ and $\overline{u'w'}_{z+1}$ is then allocated to the height z. The result is that no data is available for the heights corresponding to the lowest and uppermost acceptable data points. This loss of data would be greater if a fit to more than three data points was used.

It was noted in the previous section that most of the vertical flux of zonal momentum was due to waves of period less than two hours for most of the year. The sensitivity of the mean-flow acceleration to uncertainties in $\overline{u'w'}$ meant that the most reliable measures of $\overline{u'w'}$ had to be used in this calculation. Because of their contribution to the $\overline{u'w'}$ flux and their reliability, the 8 min–2 hr data was used in the calculation of the mean-flow acceleration. It should also be noted that calculation of the mean-flow acceleration due to longer period waves is complicated by the inclusion of a multiplicative factor $1-f^2/\omega^2$ (Fritts and Vincent 1987). Calculations of mean-flow acceleration from momentum flux data that include contributions due to long period waves are complicated because the value of ω is unknown. An upper limit to the mean-flow acceleration due to long period waves can be be calculated if this factor is ignored and the above equations for $\overline{u}_t$ and $\overline{v}_t$ are used.

The results of this analysis are presented in figures 7.32, 7.33, 7.34 and 7.35. The first two of these figures have the Coriolis acceleration for that time of the year superimposed onto the diagram. The sign of the Coriolis acceleration has been reversed so that, if the momentum fluxes balanced the momentum budget completely, the two lines in the figures would coincide. The diagrams presenting the mean-flow acceleration due to divergence of $\overline{v'w'}$ do not have a corresponding Coriolis acceleration.

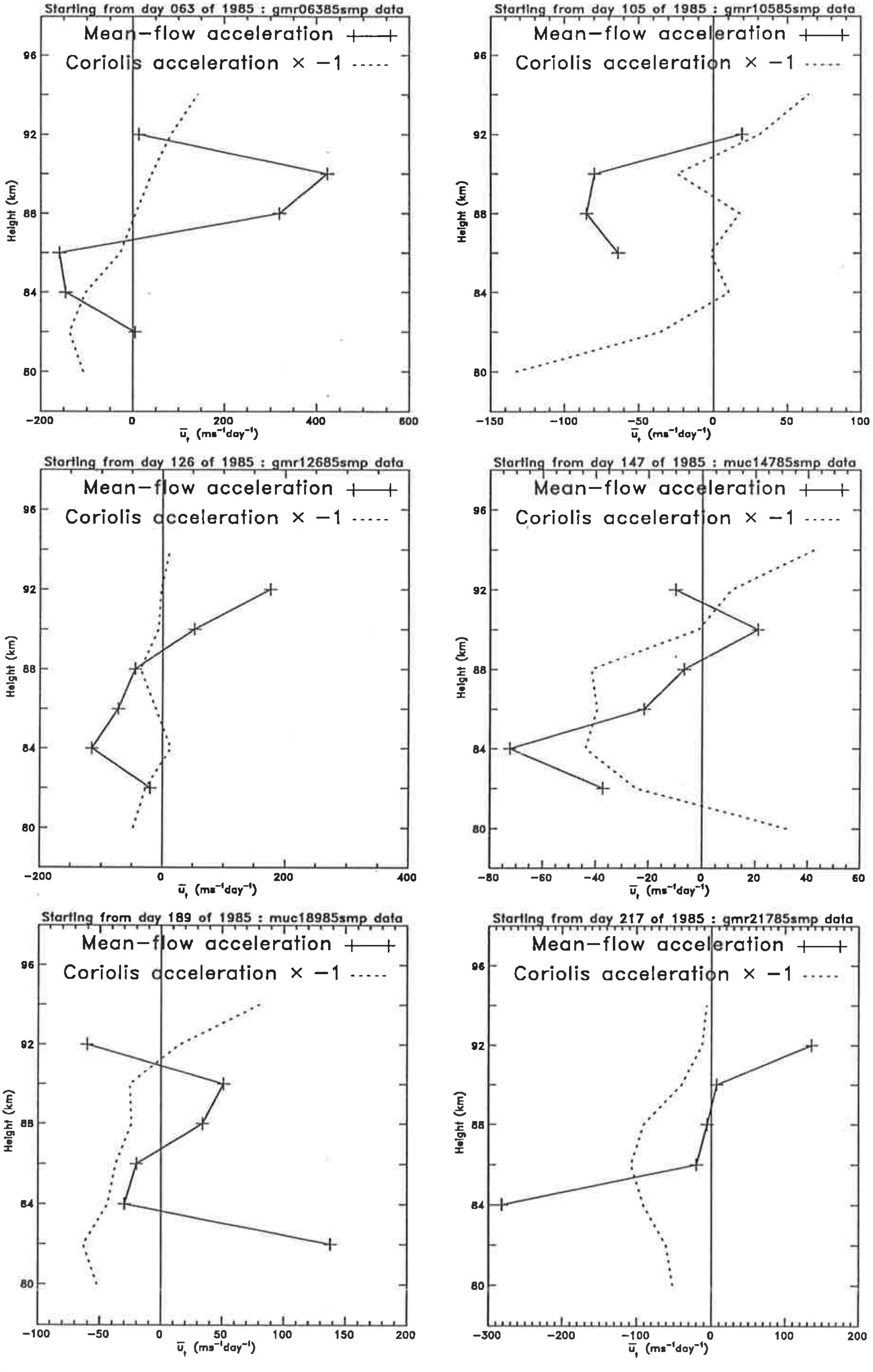

Figure 7.32: Zonal mean-flow acceleration as a function of height. The Coriolis acceleration has also been included

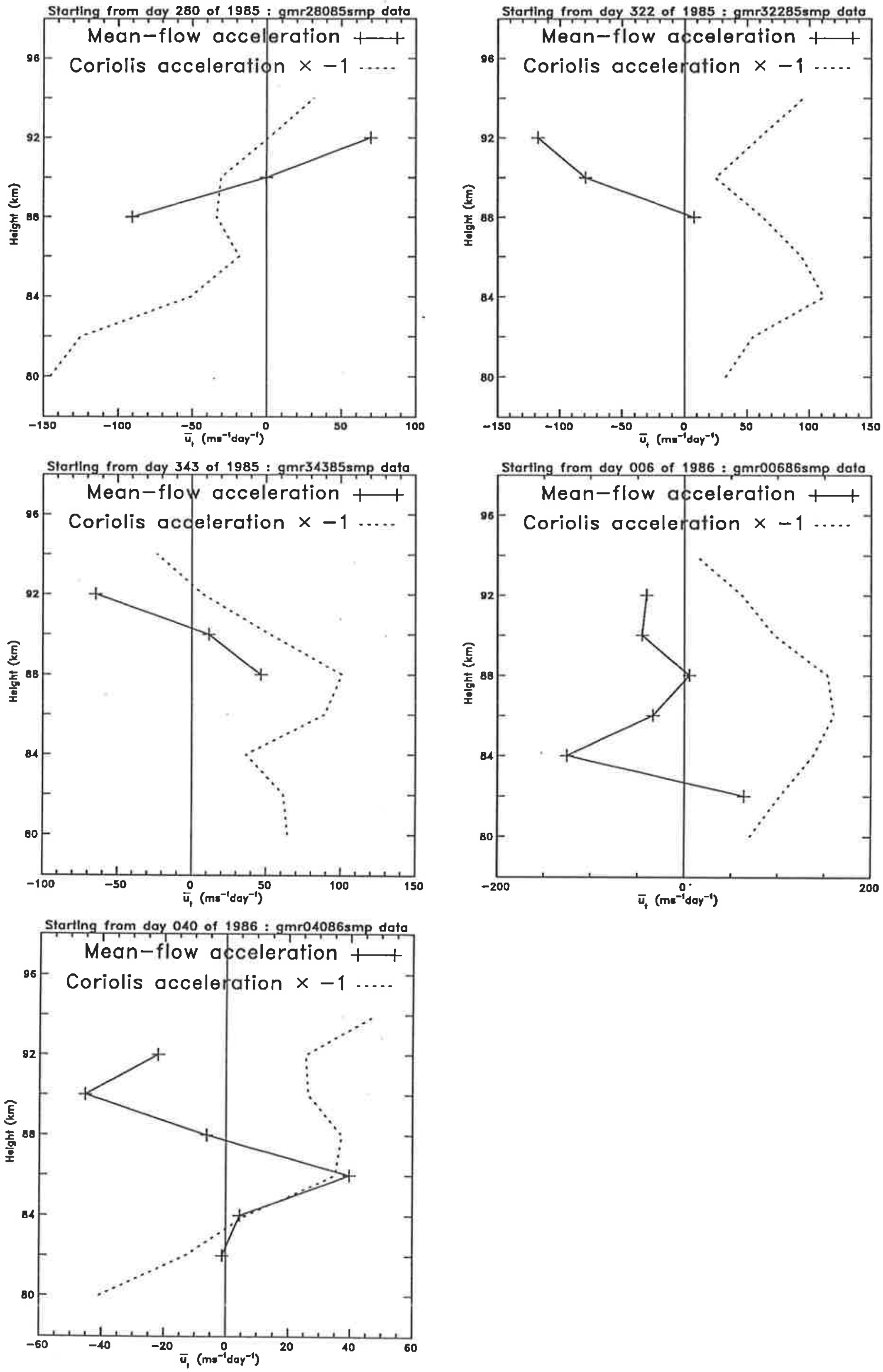

Figure 7.33: Zonal mean-flow acceleration as a function of height. The Coriolis acceleration has also been included

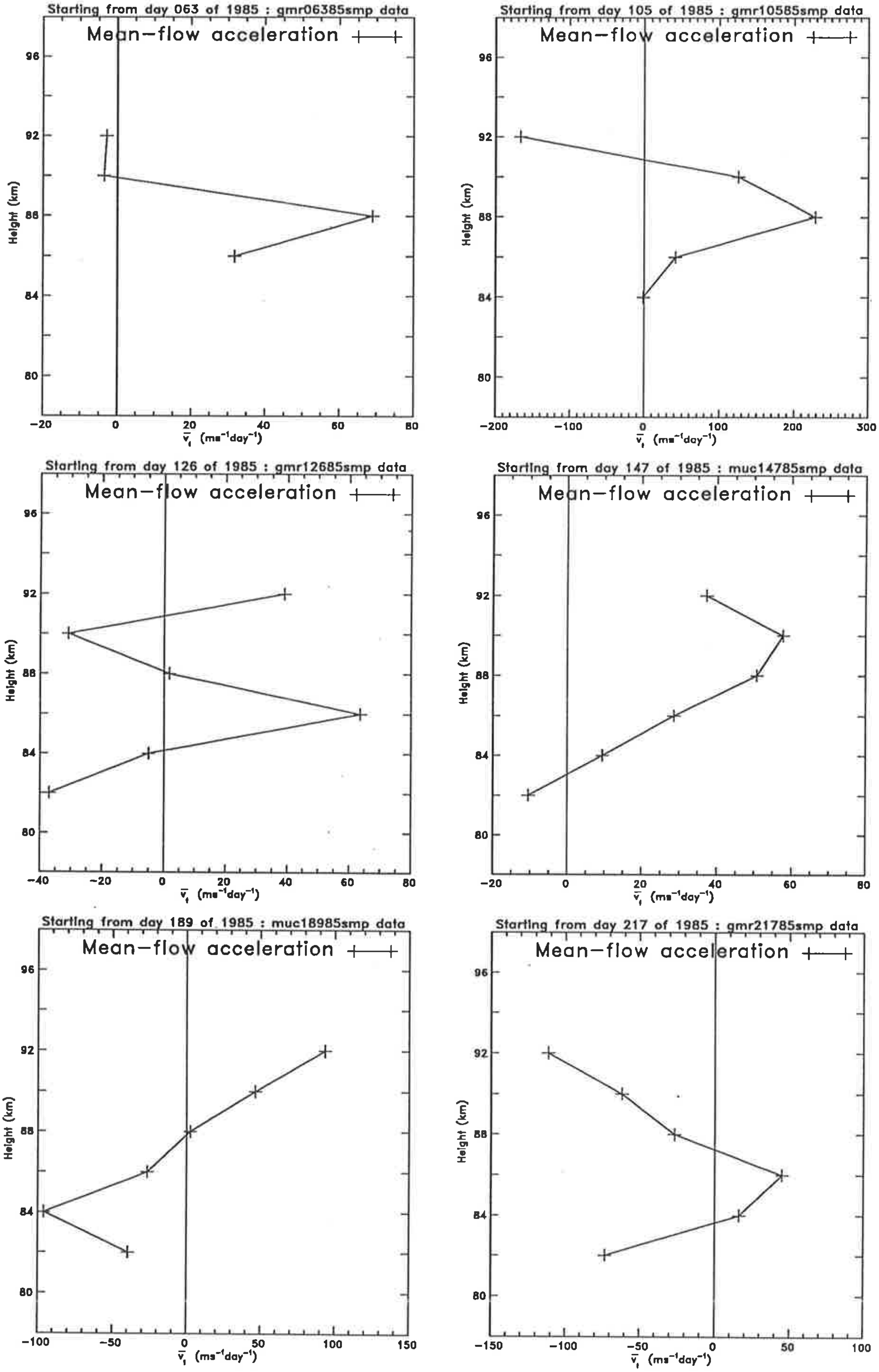

Starting from day 063 of 1985 : gmr06385smp data

Starting from day 105 of 1985 : gmr10585smp data

Starting from day 126 of 1985 : gmr12685smp data

Starting from day 147 of 1985 : muc14785smp data

Starting from day 189 of 1985 : muc18985smp data

Starting from day 217 of 1985 : gmr21785smp data

Figure 7.34: Meridional mean-flow acceleration as a function of height.

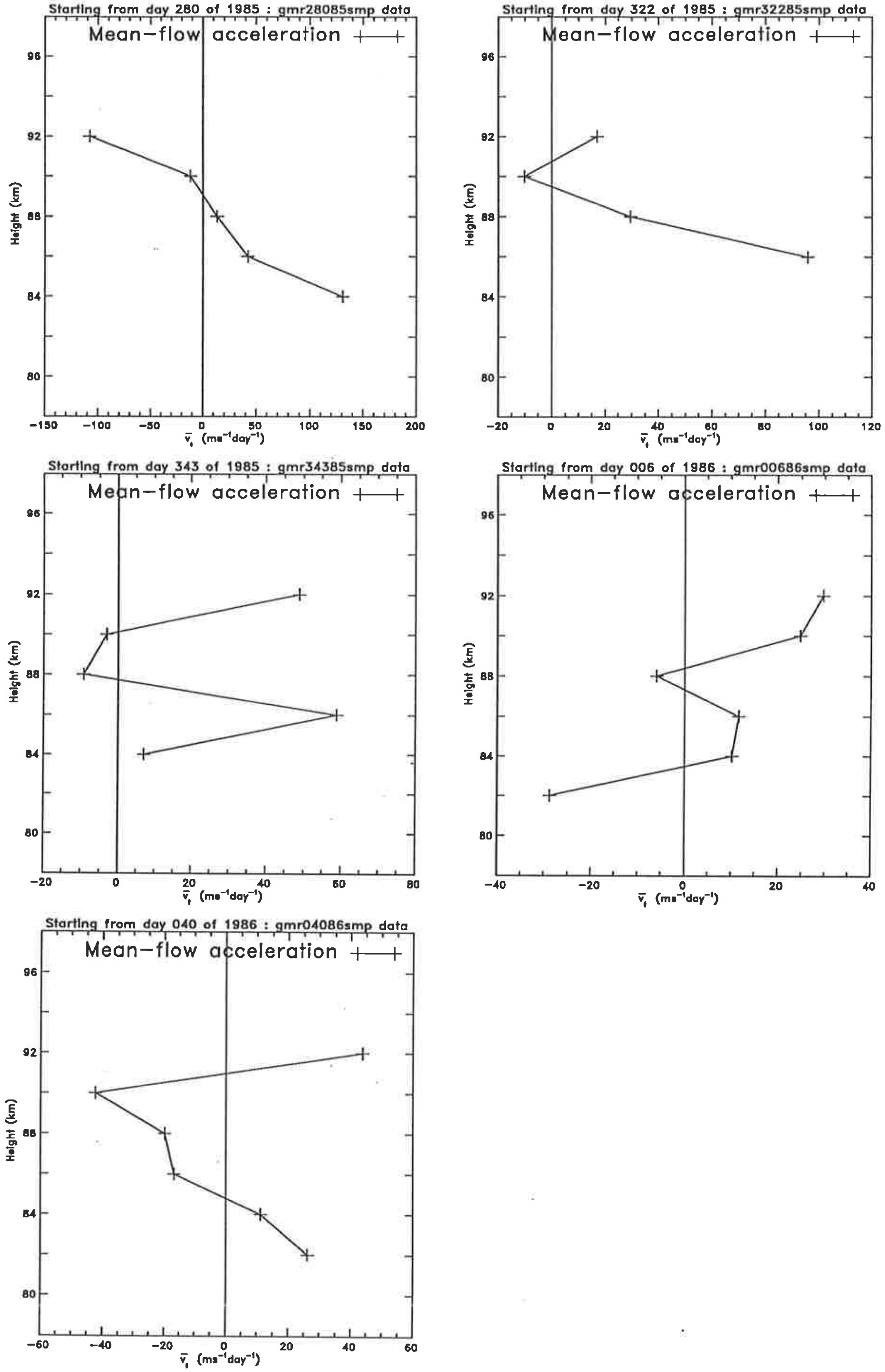

Figure 7.35: Meridional mean-flow acceleration as a function of height.

Despite the smoothing used in the mean-flow acceleration calculation, there is still some scatter in the results as a function of height with steps of hundreds of ms^{-1}day^{-1} occurring between successive heights at some time. An eyeball fit to the data is thought to be more meaningful in these cases. There is a reasonable agreement between the $\overline{u}_t$ values and the Coriolis acceleration in the data with starting days 63 (March), 105 (April), 126 , 147 (early and late May) and 189 (July). The other diagrams do not reflect a general agreement although those for day 280 (October) and day 343 (December) show some trends that agree with the Coriolis acceleration.

The $\overline{v}_t$ data of figures 7.34 and 7.35, although noisy, suggest a non-zero mean value of this quantity throughout much of the year. The $\overline{v}_t$ values are generally smaller than their $\overline{u}_t$ counterparts.

7.3 Summary

In this chapter, the momentum fluxes that were calculated using the methods developed in the previous chapters were presented. The seasonal variations of the vertical flux of zonal and meridional momentum were presented and discussed as were the partitioning of the amplitudes of these quantities between the various period bands. Some seasonal variation in short period $\overline{u'w'}$ was found and could be explained on the basis of stratospheric filtering effects. Some attempt was made to calculate the mean-flow acceleration although it was found that this calculation was very sensitive to uncertainties in the $\overline{u'w'}$ and $\overline{v'w'}$ data.

Chapter 8

Thesis summary and recommendations for future work

In chapter 1 of this thesis, some important properties of the middle atmosphere, in particular the mesosphere and lower thermosphere were presented and the background for the studies of momentum flux was set. It was shown that radiative equilibrium arguments, where local heating due to insolation is largely balanced by local cooling at infrared wavelengths, could be used to predict the thermal structure of the stratosphere. This predicted structure was found to agree well with that observed, particularly when accurate constituent profiles were used. These arguments could not, however, be extended to the mesosphere and lower thermosphere (termed the mesosphere for brevity in this work). The suggestion that a diabatic circulation brought about this departure from local thermodynamic equilibrium was supported with observations of a non-zero meridional flow. Considerations of the mesospheric momentum budget showed that this diabatic circulation could not be sustained without a source of momentum in the mesosphere. Gravity waves were shown to be a viable mechanism for transporting momentum from the troposphere upward to the mesosphere and processes that act to filter out part of the gravity-wave phase-speed spectrum as these waves propagate through the stratosphere were presented. Saturation of gravity waves and the resulting deposition of momentum into the mean flow was described using linear wave theory and it was shown that, if these filtering and momentum deposition processes were considered in conjunction with the stratospheric wind structure, a realistic model of processes that would explain the diabatic circulation could be constructed.

Chapter 2 was used to present the theoretical background for a separate but complementary study of energy deposition that used data from the Poker Flat VHF radar in Alaska. The relationship between the turbulence spectrum and the Doppler spectrum recorded by the radar was developed and it was found that the rate of dissipation of turbulence energy could be obtained from the Doppler spectrum. Some sources of contamination, that could cause this method to yield incorrect values of energy dissipation rate were presented including one that had, until now been little known and had never been considered experimentally. This contamination involved variations in the vertical velocity due to short period gravity waves, during the Doppler spectrum sampling interval. It was also shown that, under some circumstances, the power of the returned radar signal could be used to obtain measurements of the energy dissipation rate through turbulence.

The extent to which the vertical velocity could contaminate energy dissipation rate measurements was the subject of Chapter 3. Data with high time resolution from the Poker Flat radar were analysed to produce a measure of the width of each Doppler spectrum. This analysis involved fitting a Gaussian function to each function that satisfied a minimum chisquare (goodness of fit) condition. It was possible to obtain information on the radial velocity and signal-to-noise ratio as well, using this method. The effect of gravity waves on the data was considered by taking five segments of the entire data set, characterised by the presence of clear wave motions (or in one case, just a ramp in velocity), and applying the following analysis.

The data set was made up of Doppler power spectra obtained from short duration time series. To simulate a longer time series it was possible to sum successive power spectra and calculate the spectral width of the result. A similar concept can be applied to simulate the height of the sampling volume. In general, three successive height gates were summed to give one time spectrum. An index of contamination, denoted "Y_i", which was essentially the ratio of the variance (another measure of spectral width) of the simulated long duration Doppler spectra to the variance of the short duration was calculated for various simulated time samples. This index could also be used to test a model that predicts, quantitatively, the effect of a monochromatic gravity wave on the spectral width, for some of the data segments being considered. It was found that, for sampling times in common usage on VHF and MF radars, there was potential for contamination of spectral width measurements and therefore some energy-dissipation rate measurements by short- (ground-based) period gravity waves. This should be considered in experiments that seek to measure energy-dissipation rate accurately in this way. The sampling time that the experiment should use should be as short as is possible while maintaining a suitable reliability in the spectra.

With a set of uncontaminated spectral widths available, it was possible to calculate turbulence energy-dissipation rates. After the various sources of contamination (beam and shear broadening as well as that due to vertical velocities) were removed, this calculation was carried out and compared to other dynamics quantities such as vertical velocity. A suggestion of a correlation between the energy dissipation rate and the phase of the gravity wave was evident. The energy dissipation rate was also calculated from the Doppler spectrum power for this data and compared to the spectral-width energy dissipation rates. These values did not correlate well and it was suggested that the potential refractive index, a quantity that is necessary in the power energy-dissipation rate calculation, may in fact vary in an environment where auroral precipitation is thought to be responsible for the electron density. This would invalidate the use of the power calculation of energy-dissipation rate at this site and at this time.

The remainder of this thesis involved the analysis of data obtained using the Buckland Park radar near Adelaide. The radar, and some aspects of the analysis methods that are used to obtain horizontal winds and radial wind velocities are described in Chapter 4. The way in which the radar beams are pointed off-vertical for the momentum flux experiments that were conducted, is also described.

The Buckland Park array polar diagram has a half-width half-maximum of approximately 5°. The effective pointing direction of a radar is the product of the radar polar diagram *and* the polar diagram of the scatterers. Thus, in practise, there is some potential for variation in the effective pointing direction of the array. This is particularly true in situations where the radar beam is pointed at and angle from the zenith. The scatterer polar diagram is thought to be centred close to the zenith, drawing the effective off-zenith pointing angle from the direction in which the array was phased, toward the vertical. The Vincent Reid (1983) analysis requires a knowledge of this off-vertical pointing angle and chapter 4 is a study of methods that can be used to obtain this angle.

Some analyses that have been used by other workers to obtain the pointing angle were reviewed. These generally involved comparisons of velocities obtained with and without tilted radar beams. An alternative method, where the characteristics of the spatial correlation function of the returned echoes are related to the scatterer polar diagram and used to correct the array polar diagram is also presented. To test these analyses, a comparison of concurrent spaced antenna and tilted beam Doppler velocities was carried out. It was shown that the radar pointing angle due to the phasing did not give good agreement between these two velocities and a pointing angle closer to the zenith would be more suitable. Attempts to obtain this angle from individual velocity measurements were found to give unreasonable results, largely because of the statistical errors associated with the velocity measurements and the propagation of these errors through the pointing angle calculation. The scale of the spatial autocorrelation function (the pattern scale) was then used to obtain the pointing angle with considerably greater success. The pointing angle values time series contained only a few outliers and the agreement between spaced-antenna velocities and Doppler velocities projected onto the horizontal using this pointing angle was improved at most heights. Some further investigation suggested that tilting of the scatterers' polar diagram away from zenith was probably not the cause of the remaining difference.

The use of the echo characteristics obtained from the correlation function was recognised as a powerful tool for obtaining the effective pointing angle at some heights, however, at other heights, it is less effective. This is attributed to the changing nature of the echo mechanism as a function of height and the resulting change in the scatterer polar diagram. Unfortunately, the spaced-antenna analysis in its present form attempts to fit a Gaussian function to the spatial correlation function at each height. Although entirely acceptable at some heights, this leaves little scope for changes in the scatterers' polar diagram at other heights and therefore may not yield parameters that adequately describe the true spatial correlation function. The possibility of using a Gaussian plus a constant (say) in the spaced antenna analysis to allow for some of this variation in the scatterer polar diagram is recommended.

The variances of segments of the velocity time series obtained using the spaced antenna and Doppler methods have also been compared in the past, in order to obtain an effective pointing angle. The study of pointing angles presented in chapter 5 showed that the pointing angle can vary on a short time scale. This has the effect of introducing another component to the variance and introduces some extra terms into the expression that should be used to carry out this calculation. It was found that this method of obtaining the effective pointing angle was unsuitable.

The short term variations in the pointing angle mentioned above have the potential to affect the momentum flux values calculated using the method of Vincent and Reid (1983). In order to examine the extent to which these values will be affected, a model, with a semi-random pointing angle variation (based on the characteristics of the spatial correlation pattern) was set up to measure the momentum flux due to various wind fields. It was found that the error in $\overline{u'w'}$ induced by these pointing angle variations was less than around 3 percent.

Chapter 6 of this thesis describes the analysis methods applied to the radial velocity data collected at Buckland Park. In the data analysis, the data was filtered so that contributions due to three period bands could be isolated. This was done quite simply by averaging the data to give the lower limit of the period and by analysing blocks of data whose length define the upper limit of the period. The most difficult aspect of the analysis involved the removal of outliers. For unknown reasons, spuriously large radial velocity values occur from time to time in the data. The momentum flux analysis method of Vincent and Reid (1983) is extremely sensitive to these occurrences, firstly because this analysis involves differencing two large quantities and secondly, because these quantities are variances. Outliers have the potential to dominate the variance sum and therefore should be removed. A number of automatic methods were tried and one where the mean and standard deviation of three hour blocks of data were used to remove any points more than a predetermined number of standard deviations away from the mean of that block was adopted. Two passes, each rejecting a relatively small number of points were used in preference to one pass rejecting many points because the bad points also affect the rejection levels. This method, however, could only be applied to the data that was to be averaged into blocks of at least half an hour duration. The analysis applied to short-period data had to be quite different and, in the end, quite time-consuming.

In the short period analysis, the data was averaged into four minute blocks. Each of these blocks generally contained one radial velocity data point but at some times of the day and at some heights they contained two. Therefore, this averaging had little potential for removing the effects of outliers. A computer graphics program was written to display a time series of these radial velocities on a screen. It was then possible to remove data points by placing the cursor over the offending point and pressing a mouse button. This removed that point from the data set and wrote some of its characteristics to a file so a data base on the outliers could be compiled at a later time. In this way, the radial velocity data time series for each channel and each height were visually inspected. The choice of whether or not to reject was based on the following philosophy. If one data point has a value which means that, in calculating the variance sum, (i.e the sum of the squares of the deviations from the mean) the other points in the data block will not contribute significantly to the variance sum, then keeping that point in the block essentially ignores the character of the other points. That one point, then, must be considered an outlier and removed from the data set. This philosophy was applied in a two stage process and some limits on the acceptable number of points that can be missing per block (here 66%) decreased the potential for bias due to cases where the rejection of an outlier was not a clear-cut decision.

To measure the effect of the outlier rejection, "weeded"data (as the data subjected to the above philosophy were called) were analysed and compared to data where no outlier rejection was applied. The data that were subjected to the three-hour-block filtering were also compared in this way.

The method of outlier rejection applied to the short period data described above has a number of drawbacks. It is time-consuming and labor-intensive but most of all, it did not contribute to investigations of the cause of these outliers. Once the cause is found, it would be possible to incorporate rejection of these data points into the primary velocity analysis. If it has been possible to inspect the Doppler spectrum of the outliers, it may have been possible to suggest a cause for the occurrence of these points. This was beyond the capacity of the system developed here but could be integrated into a more elaborate outlier rejection/inspection system. This is suggested as the next step toward finding the cause of these outliers.

Although the application of the Vincent-Reid method of obtaining estimates of momentum flux at MF has some problems that do not occur at VHF, (e.g. the need to calculate an effective pointing angle) one important point makes the pursuit of solutions to these problems worthwhile. That is that, in general, VHF radars cannot measure radial velocities in the mesosphere (and therefore momentum fluxes) throughout the 24 hours of a day. The scattering mechanism at VHF is weak at night making it impossible to obtain momentum fluxes at this time. Diurnal variations of momentum flux have been noted by some authors (Fritts and Vincent, 1987) and these can only be investigated on a system that is capable of obtaining results throughout the diurnal cycle.

The pointing angle profiles calculated using the methods described in chapter 5 and the data analysis methods presented in chapter 6 were applied to a set of four beam radial velocity data spread throughout the period March 1985 to February 1986. This data consisted of twelve four-day data sets each approximately a month apart. They corresponded either closely or exactly to a series of times when global experiments on gravity waves and tides in the middle atmosphere were carried out and have been termed the GRATMAP data. In chapter 7 the data was summarised and some characteristics of it were presented. The data was also compared to other momentum flux estimates that have been made by other workers and at other sites and a general agreement was noted. It was found that the vertical flux of zonal momentum, $\overline{u'w'}$, varied on a seasonal basis and that this variation was mainly due to a corresponding variation in the short-period $\overline{u'w'}$ values. This variation could be explained on the basis of filtering of a tropospheric (or perhaps tropopausic) gravity wave source distribution by stratospheric winds. It was also noted that, at least for momentum fluxes due to medium- and long-period waves, the vertical flux of zonal momentum was not negligible and was often of similar or greater magnitude to the corresponding $\overline{u'w'}$ value. In $\overline{u'w'}$ it was found that waves of periods less than two hours were the main contributors to the momentum flux outside of winter but that in the $\overline{v'w'}$ data, these periods generally only made a small contribution to the total flux.

The mean-flow acceleration was calculated from the $\overline{u'w'}$ and $\overline{v'w'}$ profiles. It was found, however, that this quantity was very susceptible to the uncertainties in the momentum flux values and that the results of this calculation showed considerable scatter. A broad agreement between the Coriolis acceleration and the zonal mean-flow acceleration was observed and non-zero values of meridional mean-flow accelerations were also present.

The short term variability in the momentum flux means that calculations of mean-flow acceleration are difficult to carry out. This quantity, however, is of key importance in balancing the mesospheric momentum budget. It is suggested that longer data sets will give more information on this short-term variation and will improve estimates of the mean-flow acceleration. Four day data sets, like those used here, were used in experiments aimed at studying tides in the middle atmosphere (ATMAP) and were also found to be too short. Longer data sets may not be feasible with the manual method of data rejection used in this thesis but could be feasible if an automated data rejection algorithm was developed.

Appendix A

The Doppler spectrum due to a gravity wave.

In Chapter 3, the effects of gravity waves on the VHF Doppler spectra recorded at Poker Flat were considered. In this appendix, the form of the Doppler spectrum due to a gravity wave will be considered and it will be shown that the variance of the spectrum and that obtained from the probability density function are equivalent.

Let us assume that the radar being considered is capable of detecting the radial velocity of the atmosphere within the sampling volume without any turbulence present. That is, the Doppler spectrum due to turbulence is infinitely narrow. It is also assumed that no wind broadening or narrowing effects occur. If this is the case, the Doppler spectrum will be due to the gravity wave velocity alone.

Given a monochromatic gravity wave and no mean flow, the radial velocity will vary as

$$V = V_0 \sin(\omega_g t + \phi) \tag{A.1}$$

where V_0 is the maximum velocity, ω_g the gravity wave angular frequency and ϕ the phase at $t = 0$. Assuming that $\phi = 0$, the angular frequency shift seen by the radar due to the gravity wave as a function of time will then be

$$\omega = \frac{4\pi V_0}{\lambda} \sin(\omega_g t) \tag{A.2}$$

where λ is the radar wavelength. The received frequency will then be $\omega_0 + \omega$, where

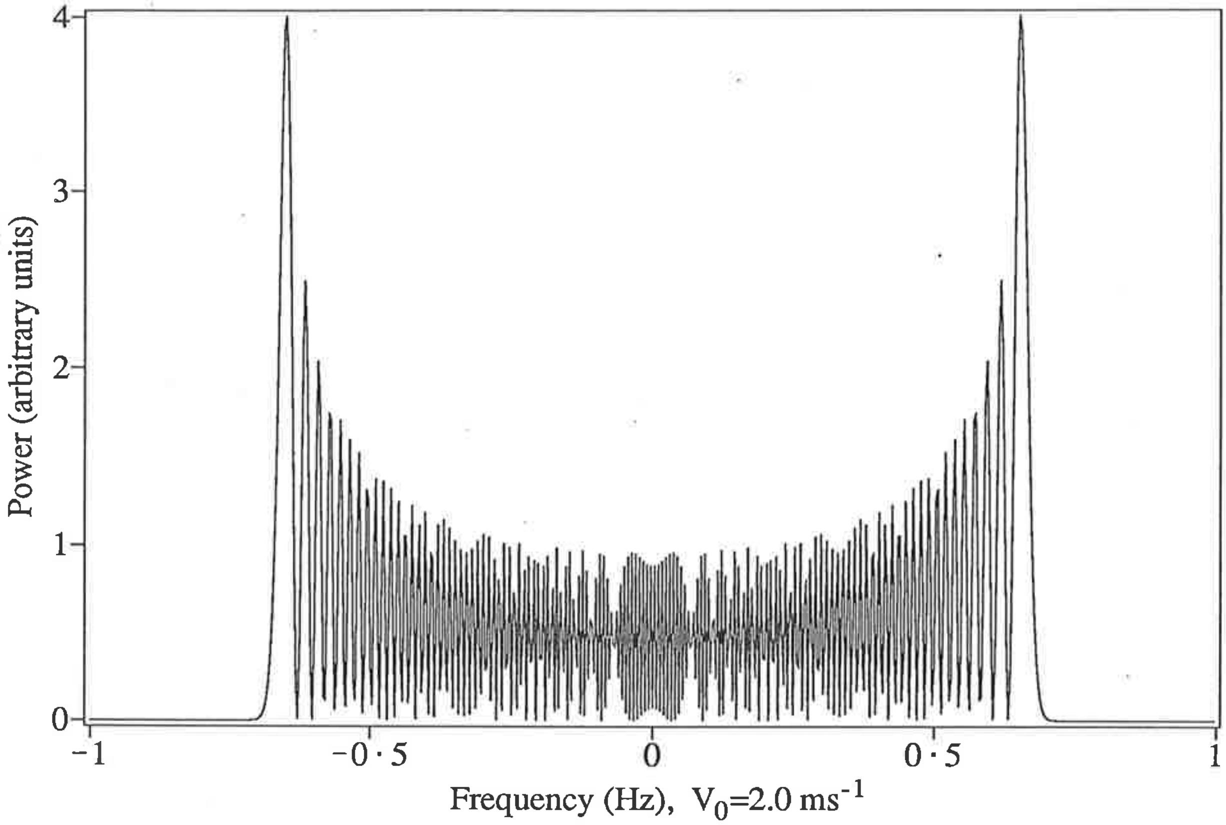

Figure A.1: The calculated Doppler power spectrum of the signal due to a monochromatic gravity wave.

ω_0 is the VHF carrier frequency. If this receiver detects a signal $E = E_0 e^{i\phi_T}$, then the frequency of the signal is $d\phi_T/dt$. Thus,

$$\frac{d\phi_T}{dt} = \omega_0 + \omega$$

or

$$\phi_T = \omega_0 t - \frac{4\pi V_0}{\lambda\omega_g}\cos(\omega_g t).$$

The Doppler spectrum can then be determined by calculating the Fourier transform of E. This has been done using an FFT (Singleton 1969) and the results are given in figure A.1. Note that in this case, ω_0 is set to zero and that a full cycle of the wave is sampled and transformed. If just part of a cycle had been sampled, only a segment of the above spectrum would result. Figure 3.5 results from half a wave being sampled.

The situation described above is actually that of frequency modulation where the modulation is sinusoidal. Treatments of this case give the amplitude of the components of the power spectrum as being proportional to Bessel functions of the first kind in the following way (see eg. Goldman 1948). Given that the frequency, ω is n steps of size

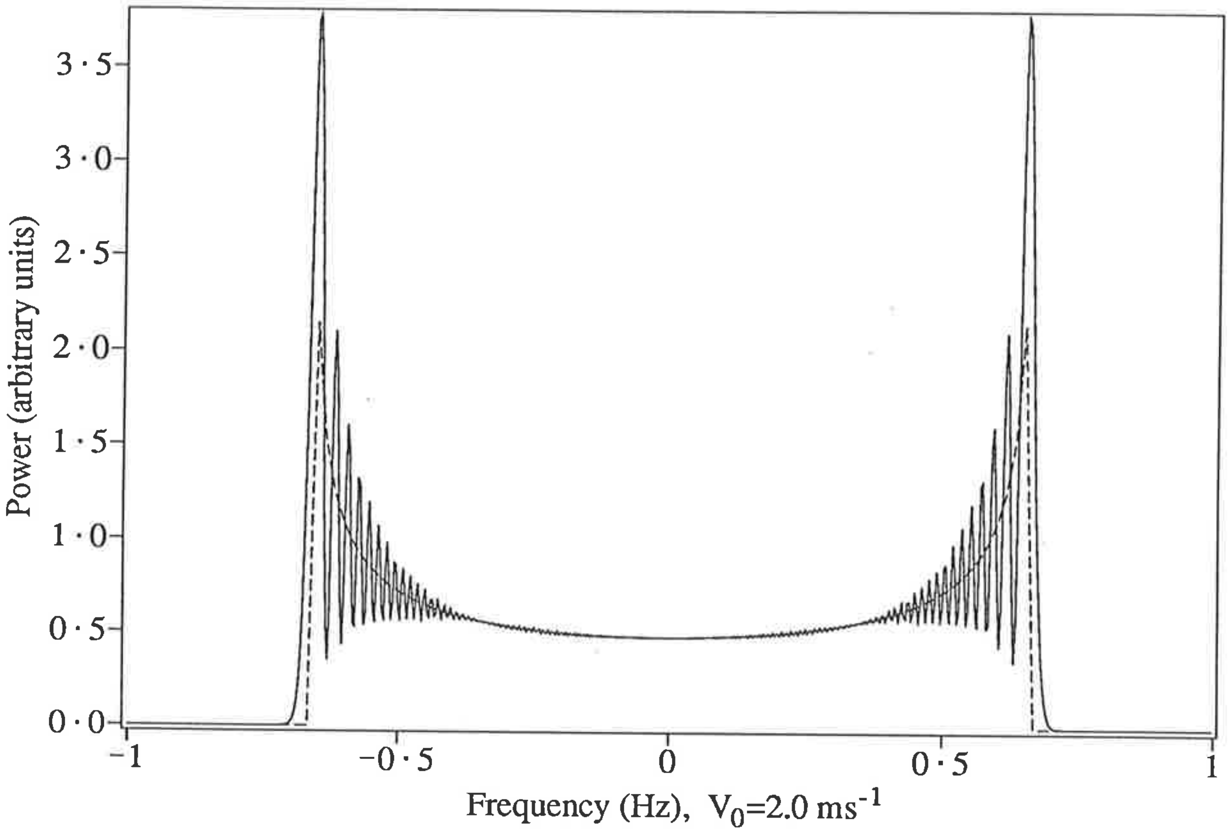

Figure A.2: The smoothed Doppler power spectrum (solid line) and the probability density function (dashed line).

ω_g from ω_0, i.e. $\omega = \omega_0 + n\omega_g$, then the power spectrum, $S(\omega)$, has the property that $S(\omega) = 0$ when n is non-integer and

$$S(\omega) \propto J_n^2(\frac{\Delta\omega}{\omega_g}) \tag{A.3}$$

where $\Delta\omega = 4\pi V_0/\lambda\omega_g$ is the maximum frequency excursion caused by the modulating wave and J_n is the nth order Bessel function of the first kind. In the cases of interest to us, $\Delta\omega/\omega_g$ is large and most of the energy in the spectrum is confined to the range $\omega_0 \pm \Delta\omega$. Properties of Bessel functions suggest that as $\Delta\omega/\omega_g$ becomes larger, the amplitude of the oscillations that can be seen in the power spectrum become smaller, tending toward a smooth curve (Goldman 1948).

Hocking (1989) showed that the probability of a gravity wave having a velocity between v and $v + dv$ is given by $P(v)$, where

$$P(v) = \frac{1}{\pi V_0\sqrt{1 - \frac{v^2}{V_0^2}}}. \tag{A.4}$$

This can be expressed in terms of frequency using $v = f\lambda/2 = \lambda\Delta\omega/4\pi$, where f is the ordinate used in the previous figures and $\Delta\omega$ is as defined previously.

Figure A.2 (solid line) shows the power spectrum of figure A.1 smoothed using a 5 point running mean (with weights 0.085, 0.25, 0.33, 0.25, 0.085). Also shown (dashed line) is the expected form of the probability density function. It can be seen that the smoothing of the power spectrum has resulted in a curve of similar form to the probability density function. The probability density function has been normalised so that the two lines coincide at zero frequency but this will not affect the variance values calculated from each distribution. In the case of a completely smooth power spectrum, they will be exactly the same. In practise, the oscillations in the power spectrum will mean its variance will differ slightly from the PDF value but not significantly or systematically.

Appendix B

The variance of the sum of n distributions

In Chapter 3, numerous spectra were added together. The mean and variance of the combined spectrum and its relationship to the individual spectra was of interest. An expression that was quoted in that chapter relating the above parameters will now be derived.

Given a distribution function $P(f)$, the mean of that distribution $\overline{P}$ is

$$\overline{P} = \frac{\int_{-\infty}^{\infty} f P(f)\, df}{\int_{-\infty}^{\infty} P(f)\, df} = \frac{\int_{-\infty}^{\infty} f P(f)\, df}{\mathcal{A}} \tag{B.1}$$

where $\mathcal{A} = \int_{-\infty}^{\infty} P(f)\, df$ is the area under $P(f)$. The variance of the distribution, σ_P^2 is

$$\begin{aligned}
\sigma_P^2 &= \frac{\int_{-\infty}^{\infty} (f - \overline{P})^2 P(f)\, df}{\int_{-\infty}^{\infty} P(f)\, df} \\
&= \frac{1}{\mathcal{A}} \int_{-\infty}^{\infty} f^2 P(f)\, df + \frac{\overline{P}^2}{\mathcal{A}} \int_{-\infty}^{\infty} P(f)\, df - 2\overline{P} \frac{\int_{-\infty}^{\infty} f P(f)\, df}{\mathcal{A}} \\
&= \frac{1}{\mathcal{A}} \int_{-\infty}^{\infty} f^2 P(f)\, df + \overline{P}^2 - 2\,\overline{P}\,\overline{P}
\end{aligned}$$

$$\sigma_P^2 = \frac{1}{\mathcal{A}} \int_{-\infty}^{\infty} f^2 P(f)\, df - \overline{P}^2. \tag{B.2}$$

We now consider n distributions $P_i(f)$ $i = 1 \ldots n$ each with a mean $\overline{P}_i$, variance σ_i^2 and with $\int_{-\infty}^{\infty} P_i(f)\, df = \mathcal{A}_i$. Let the distribution obtained by summing these n distributions be $P(f) = \sum_{i=1}^{n} P_i(f)$ and define $\int_{-\infty}^{\infty} P(f)\, df = 1$. The mean of $P(f)$, $\overline{P}$ will be

$$\overline{P} = \frac{\int_{-\infty}^{\infty} f P(f)\, df}{\int_{-\infty}^{\infty} P(f)\, df}$$

$$
\begin{aligned}
&= \int_{-\infty}^{\infty} f \sum_{i=1}^{n} P_i(f)\ df \\
&= \sum_{i=1}^{n} \int_{-\infty}^{\infty} f P_i(f)\ df
\end{aligned}
$$

$$
\overline{P} \;=\; \sum_{i=1}^{n} \overline{P}_i \mathcal{A}_i \quad \text{from B.1.} \tag{B.3}
$$

The variance of $P(f)$, σ_P^2 is then

$$
\begin{aligned}
\sigma_P^2 &= \frac{\int_{-\infty}^{\infty} (f-\overline{P})^2 P(f)\ df}{\int_{-\infty}^{\infty} P(f)\ df} \\
&= \int_{-\infty}^{\infty} f^2 P(f)\ df - \overline{P}^2 \quad \text{from equation B.2} \\
&= \int_{-\infty}^{\infty} f^2 \sum_{i=1}^{n} P_i(f)\ df - (\sum_{i=1}^{n} \overline{P}_i \mathcal{A}_i)^2 \text{ using B.1} \\
&= \sum_{i=1}^{n} \int_{-\infty}^{\infty} f^2 P_i(f)\ df - \sum_{i=1}^{n} \overline{P}_i^2 \mathcal{A}_i^2 - \sum_{i=1}^{n} \sum_{\substack{j=1 \\ j\neq i}}^{n} \overline{P}_i \overline{P}_j \mathcal{A}_i \mathcal{A}_j
\end{aligned}
$$

given $\sum_{j=1}^{n} \mathcal{A}_j = 1$ then $\mathcal{A}_i = 1 - \sum_{\substack{j=1 \\ j\neq i}}^{n} \mathcal{A}_j$ so

$$
\begin{aligned}
\sigma_P^2 &= \sum_{i=1}^{n} \left\{ \int_{-\infty}^{\infty} f^2 P_i(f)\ df - \overline{P}_i^2 \mathcal{A}_i (1 - \sum_{\substack{j=1 \\ j\neq i}}^{n} \mathcal{A}_j) \right\} - \sum_{i=1}^{n} \sum_{\substack{j=1 \\ j\neq i}}^{n} \overline{P}_i \mathcal{A}_i \overline{P}_j \mathcal{A}_j \\
&= \sum_{i=1}^{n} \left\{ \int_{-\infty}^{\infty} f^2 P_i(f)\ df - \overline{P}_i^2 \mathcal{A}_i \right\} + \sum_{i=1}^{n} \overline{P}_i^2 \mathcal{A}_i \sum_{\substack{j=1 \\ j\neq i}}^{n} \mathcal{A}_j - \sum_{i=1}^{n} \sum_{\substack{j=1 \\ j\neq i}}^{n} \overline{P}_i \mathcal{A}_i \overline{P}_j \mathcal{A}_j
\end{aligned}
$$

$$
= \sum_{i=1}^{n} \mathcal{A}_i \sigma_i^2 + \sum_{i=1}^{n} \overline{P}_i^2 \mathcal{A}_i \sum_{\substack{j=1 \\ j\neq i}}^{n} \mathcal{A}_j - \sum_{i=1}^{n} \sum_{\substack{j=1 \\ j\neq i}}^{n} \overline{P}_i \mathcal{A}_i \overline{P}_j \mathcal{A}_j. \tag{B.4}
$$

Now

$$
\begin{aligned}
\sum_{i=1}^{n} \sum_{j=i+1}^{n} \mathcal{A}_i \mathcal{A}_j (\overline{P}_i - \overline{P}_j)^2 &= \frac{1}{2} \sum_{i=1}^{n} \sum_{\substack{j=1 \\ j\neq i}}^{n} \mathcal{A}_i \mathcal{A}_j (\overline{P}_i - \overline{P}_j)^2 \\
&= \frac{1}{2} \sum_{i=1}^{n} \sum_{\substack{j=1 \\ j\neq i}}^{n} \mathcal{A}_i \mathcal{A}_j (\overline{P}_i^2 + \overline{P}_j^2 - 2\ \overline{P}_i \overline{P}_j) \\
&= \frac{1}{2} \left\{ \sum_{i=1}^{n} \sum_{\substack{j=1 \\ j\neq i}}^{n} \mathcal{A}_i \mathcal{A}_j \overline{P}_i^2 + \sum_{i=1}^{n} \sum_{\substack{j=1 \\ j\neq i}}^{n} \mathcal{A}_i \mathcal{A}_j \overline{P}_j^2 \right\} \\
&\quad - \sum_{i=1}^{n} \sum_{\substack{j=1 \\ j\neq i}}^{n} \mathcal{A}_i \mathcal{A}_j \overline{P}_i \overline{P}_j.
\end{aligned}
$$

The two terms in braces are the same, as swapping i and j will show, making this expression equal

$$\sum_{i=1}^{n} \overline{P}_i^2 \mathcal{A}_i \sum_{\substack{j=1 \\ j \neq i}}^{n} \mathcal{A}_j - \sum_{i=1}^{n} \sum_{\substack{j=1 \\ j \neq i}}^{n} \mathcal{A}_i \mathcal{A}_j \overline{P}_i \overline{P}_j.$$

These are the last two terms of equation B.4 so

$$\sigma_P^2 = \sum_{i=1}^{n} \mathcal{A}_i \sigma_i^2 + \sum_{i=1}^{n} \sum_{j=i+1}^{n} \mathcal{A}_i \mathcal{A}_j (\overline{P}_i - \overline{P}_j)^2. \tag{B.5}$$

Appendix C

Obtaining the effective pointing angle from the spatial correlation function

In the full correlation analysis (Briggs 1984), the spatial correlation function has the form

$$\rho(\xi,\eta) = \rho(A\xi^2 + B\eta^2 + 2H\xi\eta) \tag{C.1}$$

where ξ and η are perpendicular spatial coordinates; thus $\rho(\xi,\eta)$ =constant form ellipses. If the coordinate system used is aligned with the axes of these ellipses, and using the Gaussian form for ρ, $\rho(\xi,\eta)$ has the form

$$\rho(\xi,\eta) = \exp -[\frac{\xi^2}{\xi_1^2} + \frac{\eta^2}{\eta_1^2}] \tag{C.2}$$

where ξ_1 and η_1 are the e^{-1} widths of the spatial correlation function in the directions of the axes.

If ξ and η are expressed in units of wavelength, the angular power spectrum of downcoming energy can be calculated by taking the Fourier transform of $\rho(\xi,\eta)$ (see e.g. Ratcliffe 1956). If $W(S_1,S_2)$ is the energy coming from the direction $S_1 = \sin\theta_1$, $S_2 = \sin\theta_2$, where θ_1 and θ_2 are measured from the zenith in perpendicular directions along the two axes, then

$$W(S_1,S_2) \propto \int\int \exp -[\frac{\xi^2}{\xi_1^2}+\frac{\eta^2}{\eta_1^2}] \exp 2\pi i(S_1\xi+S_2\eta)\, d\xi\, d\eta \quad \text{(C.3)}$$

$$= W_0 \exp -[\pi^2\xi_1^2 S_1^2+\pi^2\eta_1^2 S_2^2]. \quad \text{(C.4)}$$

The form of $\rho(\xi,\eta)$ and $W(S_1,S_2)$ are shown in figure C.1 (reproduced from chapter 5).

If an antenna array is phased to produce a beam that points in a desired direction $S_1 = a_1$, $S_2 = a_2$, (as in figure C.1c) and the beam has a power polar diagram of the form

$$B(S_1,S_2) = B_0 \exp -[\frac{(S_1-a_1)^2+(S_2-a_2)^2}{S_0^2}],$$

(where S_0 is the beam e^{-1} width), the effective polar diagram will be the product of the polar diagram of the scattered or downcoming energy and the beam polar diagram (as illustrated in figure C.1d)i.e.

$$C(S_1,S_2) = W(S_1,S_2)\, B(S_1,S_2).$$

If $W(S_1,S_2)$ is a constant where $B(S_1,S_2)$ is non-zero, then the pointing direction (or direction of maximum gain) of the combined polar diagram will be the same as that of the beam itself. If $W(S_1,S_2)$ is not a constant, then the effective pointing direction of the combined polar diagram will differ from that due to the beam alone. The effective pointing direction for the case of the Gaussian scattering polar diagram presented above will now be considered.

The combined polar diagram is

$$C(S_1,S_2) \propto \exp -[\pi^2\xi_1^2 S_1^2+\pi^2\eta_1^2 S_2^2] \exp -[\frac{(S_1-a_1)^2+(S_2-a_2)^2}{S_0^2}] \quad \text{(C.5)}$$

$$\propto \exp -[\pi^2\xi_1^2 S_1^2 + \frac{(S_1-a_1)^2}{S_0^2} + \pi^2\eta_1^2 S_2^2 + \frac{(S_2-a_2)^2}{S_0^2}. \quad \text{(C.6)}$$

This will have a maximum where the partial differentials of $C(S_1,S_2)$ with respect to S_1 and S_2 are zero, i.e.

$$2\,\tfrac{S_1-a_1}{S_0^2} + 2\pi^2\xi_1^2 S_1 = 0, \quad 2\,\tfrac{S_2-a_2}{S_0^2} + 2\pi^2\eta_1^2 S_2 = 0. \quad \text{(C.7)}$$

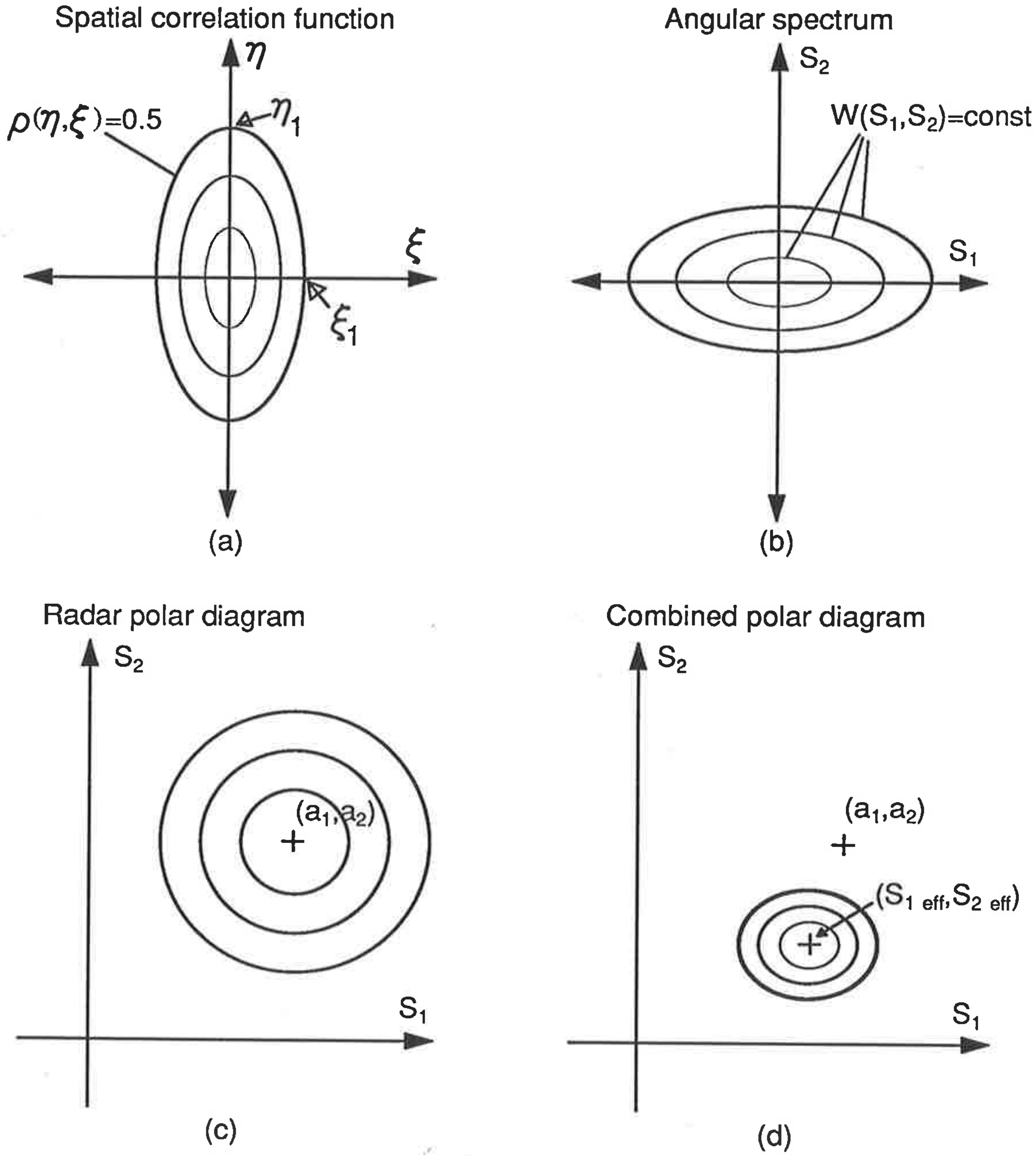

Figure C.1: The correlation ellipse (a), it's Fourier transform, the angular power spectrum (b), the radar polar diagram (c) and the effective polar diagram of the scatterers and radar combined (d).

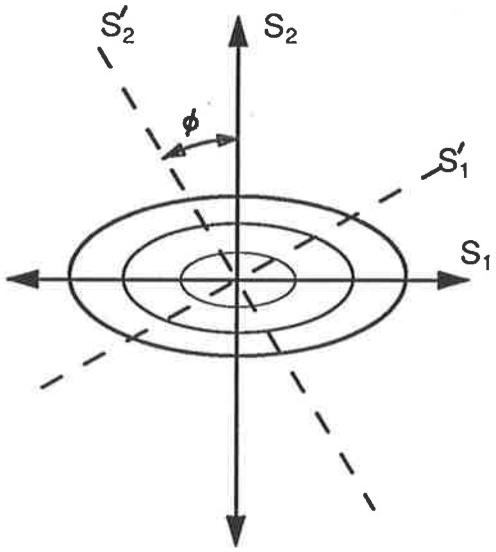

Figure C.2: The S_1, S_2 axes are rotated by an angle ϕ to S_1', S_2'. Contours of constant power in the angular spectrum are shown.

This gives

$$(S_1)_{eff} = \frac{a_1}{1+S_0^2\xi_1^2\pi^2}, \quad (S_2)_{eff} = \frac{a_2}{1+S_0^2\eta_1^2\pi^2}. \tag{C.8}$$

The work presented thus far is due to Briggs (private communication 1989). These results are now applied to the data collected using the Buckland Park MF array.

It should be noted that the semi-major axis of the correlation ellipse Fourier transforms into the semi-minor axis of the angular spectrum ellipse and it is the angular spectrum that is being considered in this derivation. Thus far, the axes S_1, S_2 have been aligned perpendicular to and parallel to the semi-minor axis of the angular spectrum ellipse respectively; this will not be the case in practise. The angle ϕ between North and the semi-major axis of the spatial correlation ellipse is calculated in the full correlation analysis. In order to apply the above results then, we must rotate the angular spectrum ellipse whose semi-minor axis is oriented at an angle ϕ from North so that this axis is not aligned with the S_2' axis in a new coordinate sytem S_1', S_2' where S_1' is eastward and S_2' is northward. This involves rotating the S_1, S_2 axes by an angle ϕ as shown in figure C.2. Then

$$S_1' = S_1 \cos\phi + S_2 \sin\phi \tag{C.9}$$

$$
\begin{aligned}
S_2' &= S_2 \cos\phi - S_1 \sin\phi && \text{(C.10)}\\
\text{So } (S_1')_{eff} &= (S_1)_{eff}\cos\phi + (S_2)_{eff}\sin\phi && \text{(C.11)}\\
&= \frac{a_1\cos\phi}{1+S_0^2\xi_1^2\pi^2} + \frac{a_2\sin\phi}{1+S_0^2\eta_1^2\pi^2} && \text{(C.12)}\\
(S_2')_{eff} &= (S_2)_{eff}\cos\phi + (S_1)_{eff}\sin\phi && \text{(C.13)}\\
&= \frac{a_2\cos\phi}{1+S_0^2\eta_1^2\pi^2} - \frac{a_1\sin\phi}{1+S_0^2\xi_1^2\pi^2}. && \text{(C.14)}
\end{aligned}
$$

The constants a_1 and a_2 in the above expressions are obtained from the directions in which the antenna array is phased to point. If a beam 11.6° off-zenith toward the East is used, then it can be seen (figure C.3a) that $\sin\phi = a_2/a_1'$, $\cos\phi = a_1/a_1'$ and $a_1' = \sin 11.6°$. This gives

$$
\begin{aligned}
(S_1')_{eff} &= \frac{\sin 11.6^\circ\ \cos^2\phi}{1+S_0^2\xi_1^2\pi^2} + \frac{\sin 11.6^\circ\ \sin^2\phi}{1+S_0^2\eta_1^2\pi^2} && \text{(C.15)}\\
(S_2')_{eff} &= \frac{\sin 11.6^\circ \sin\phi\cos\phi}{1+S_0^2\eta_1^2\pi^2} - \frac{\sin 11.6^\circ \sin\phi\cos\phi}{1+S_0^2\xi_1^2\pi^2}. && \text{(C.16)}
\end{aligned}
$$

In the regions of the atmosphere being considered in this thesis the wind motion is predominantly horizontal. Variations in zenith angle, which in this case are expressed by $(S_1')_{eff}$, have a significant effect on the radial velocity measured using the antenna beam and are important. The $(S_2')_{eff}$ term is far less significant. Although the beam is moved a few degrees North-South, this change in beam pointing angle has little effect on the radial velocity.

Similarly for a beam 11.6° off-zenith toward the North, $\sin\phi = -a_1/a_2'$, $\cos\phi = a_2/a_2'$ and $a_2' = \sin 11.6°$ (see figure C.3b) giving

$$
\begin{aligned}
(S_1')_{eff} &= \frac{\sin 11.6^\circ\ \sin\phi\cos\phi}{1+S_0^2\eta_1^2\pi^2} - \frac{\sin 11.6^\circ\ \sin\phi\cos\phi}{1+S_0^2\xi_1^2\pi^2} && \text{(C.17)}\\
(S_2')_{eff} &= \frac{\sin 11.6^\circ\ \cos^2\phi}{1+S_0^2\eta_1^2\pi^2} + \frac{\sin 11.6^\circ\ \sin^2\phi}{1+S_0^2\xi_1^2\pi^2}. && \text{(C.18)}
\end{aligned}
$$

Similar to the case above, the $(S_1')_{eff}$ term is not important for a Northward pointing beam.

The parameters S_0, ξ_1 and η_1 are e^{-1} widths of various Gaussian functions. These are related to the half-power half-widths by $(S_0)_{0.5} = \sqrt{\ln 2}S_0$, $(\xi_1)_{0.5} = \sqrt{\ln 2}\xi_1$ and $(\eta_1)_{0.5} = \sqrt{\ln 2}\eta_1$.

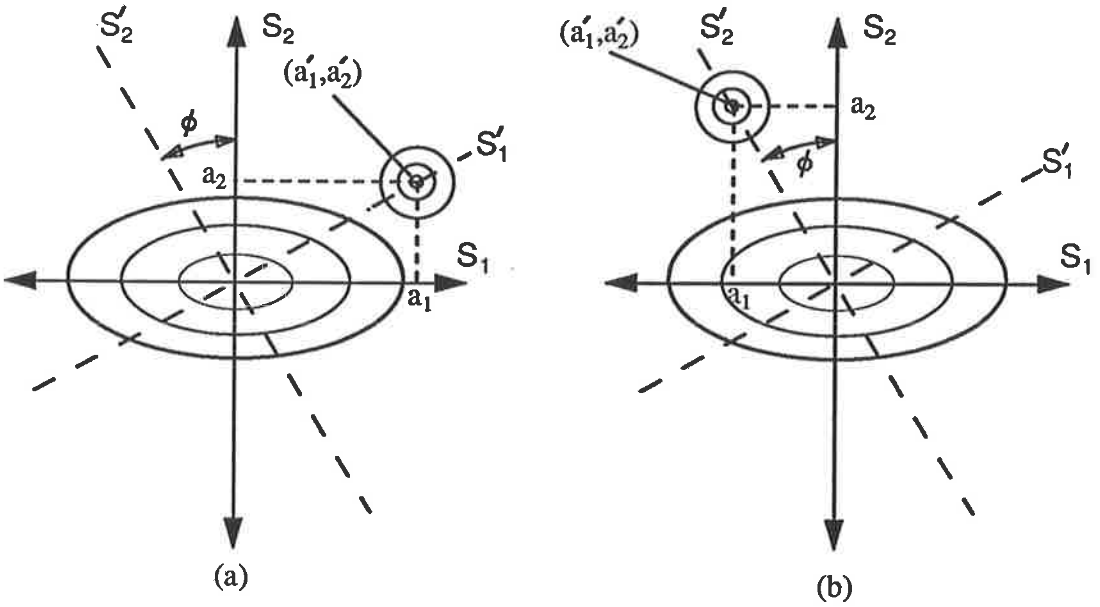

Figure C.3: The position of (a) an eastward pointing beam and (b) a northward pointing beam in primed coordinates.

Bibliography

D. G. Andrews, J. R. Holton, and C. B. Leovy. *Middle atmosphere dynamics.* Academic Press, 1987.

D. G. Andrews and M. E. McIntyre. Planetary waves in horizontal and vertical shear: the generalized Eliassen-Palm relation and the mean zonal acceleration. *Journal of the Atmospheric Sciences*, 33:2031–2048, 1976.

D. G. Andrews and M. E. McIntyre. Generalized Eliassen-Palm and Charney-Drazin theorems for waves on axisymmetric mean flows in compressible atmospheres. *Journal of the Atmospheric Sciences*, 35:175–185, 1978.

J. Apruzese, M. Schoeberl, and D. Strobel. Parameterisation of I. R. cooling in a middle atmosphere dynamics model. 1. Effects on the zonally averaged circulation. *Journal of Geophysical Research*, 87(11):8951–8966, 1982.

B. B. Balsley, W. L. Ecklund, D. A. Carter, and P. E. Johnston. The MST radar at Poker Flat, Alaska. *Radio Science*, 15(2):213–223, 1980.

B. B. Balsley, W. L. Ecklund, and D. C. Fritts. VHF echoes from the high latitude mesosphere and lower thermosphere: Observations and interpretations. *Journal of the Atmospheric Sciences*, 40:2451–2466, 1983.

P. M. Banks and G. Kockarts. *Aeronomy.* Academic Press, 1973.

J. J. Barnett and M. Corney. Middle atmosphere reference model derived from satellite data. *Handbook for MAP*, 16:47–85, 1985.

G. K. Batchelor. *Theory of homogeneous turbulence.* Cambridge University Press, 1953.

P. R. Bevington. *Data Reduction and Error Analysis for the Physical Sciences.* McGraw-Hill Book Company, 1969.

T. A. Blix. *In situ studies of turbulence in the middle atmosphere by means of electrostatic ion probes.* Technical Report NDRE/PUBL-88/1002, Norwegian Defence Research Establishment, P O Box 25 - N-2007 Kjeller, Norway, April 1988.

R. Bolgiano, Jr. Turbulent spectra in a stably stratified atmosphere. *Journal of Geophysical Research*, 64(12):2226–2229, 1959.

H. G. Booker. A theory of scattering by non-isotropic irregularities with application to radar reflections from the aurora. *Journal of Atmospheric and Terrestrial Physics*, 8:204–221, 1956.

S. A. Bowhill and S. Gnanalingam. Gravity waves in severe weather. *Handbook for MAP*, 20:128–135, 1986.

R. N. Bracewell. *The Fourier transform and its applications.* McGraw-Hill Kogakusha, 1978.

G. Brasseur and S. Solomon. *Aeronomy of the middle atmosphere.* D. Reidel Publishing Company, 1984.

B. H. Briggs. The analysis of spaced sensor records by correlation techniques. *Handbook for MAP*, 166–186, 1984.

B. H. Briggs, W. G. Elford, D. G. Felgate, M. G. Golley, D. E. Rossiter, and J. W. Smith. Buckland Park aerial array. *Nature*, 223:1321–1325, 1969.

K. A. Browning and R. Wexler. Velocity characteristics of some clear air dot angels. *Journal of the Atmospheric Sciences*, 23:592–604, 1966.

K. A. Browning and R. Wexler. The determination of kinematic properties of a wind field using Doppler radar. *Journal of Applied Meteorology*, 7:105–113, 1968.

S. J. Caughey, B. A. Crease, D. N. Asimakapoulos, and R. S. Cole. Quantitative bistatic acoustic sounding of the atmospheric boundary layer. *Quarterly Journal of the Royal Meteorological Society*, 104:147–161, 1980.

W. C. Chao and M. S. Schoeberl. On the linear approximation of gravity wave saturation in the mesosphere. *Journal of the Atmospheric Sciences*, 41(11):1893–1898, 1984.

S. Chapman and R. S. Lindzen. *Atmospheric tides.* Reidel, Dordrecht, Netherlands, 1970.

J. G. Charney and P. G. Drazin. Propagation of planetary-scale disturbances from the lower into the upper atmosphere. *Journal of Geophysical Research*, 66:83–109, 1961.

J. H. E. Clarke and L. T. Morone. Mesospheric heating due to convectively excited gravity waves - A case study. *Monthly Weather Review*, 109:990–1001, 1981.

D. Cunnold, F. Alyea, N. Phillips, and R. Prinn. A three dimensional dynamical-chemical model of atmospheric ozone. *Journal of the Atmospheric Sciences*, 32:170–194, 1975.

P. Czechowsky, I. M. Reid, and R. Rüster. VHF radar measurements of the aspect sensitivity of the summer polar mesospause echoes over Andenes (69° N,16° E), Norway. *Geophysical Research Letters*, 15(11):1259–1262, 1988.

P. Czechowsky, G. Schmidt, and R. Rüster. The mobile SOUSY Doppler radar: technical design and first results. *Radio Science*, 19(1):441–450, 1984.

R. J. Doviak and D. S. Znrić. *Doppler radar and weather observations.* Academic Press, 1984.

R. J. Doviak, D. S. Zrnić, and D. S. Sirmans. Doppler weather radar. *Proceedings of the IEEE*, 67:1522–1553, 1979.

T. J. Dunkerton. Inertia-gravity waves in the stratosphere. *Journal of the Atmospheric Sciences*, 41:3396–3404, 1984.

T. J. Dunkerton. Theory of internal gravity wave saturation. *PAGEOPH*, 130(2/3):373–397, 1989.

W. L. Eberhard, R. E. Cupp, and K. R. Healy. Doppler lidar measurement of profiles of turbulence and momentum flux. *Journal of Atmospheric and Oceanic Technology*, 6:809–819, 1989.

A. Eliassen and E. Palm. On the transfer of energy in stationary mountain waves. *Geofysiske Publikasjoner*, 22(3):1–23, 1961.

M. Ference, W. G. Stroud, J. R. Walsh, and A. G. Weisner. Measurements of temperatures at elevations of 30 to 80 kilometers by the rocket-grenade experiment. *Journal of the Atmospheric Sciences*, 13:5–12, 1956.

E. L. Fleming, S. Chandra, M. R. Schoeberl, and J. J. Barnett. *Monthly mean global climatology of temperature, wind, geopotential height, and pressure for 0–120km.* Technical Report 100697, National Aeronautics and Space Administration, NASA, Washington D.C., 20546, 1988.

A. S. Frisch and S. F. Clifford. A study of convection capped by a stable layer using Doppler radar and acoustic echo sounders. *Journal of the Atmospheric Sciences*, 31:1622–1628, 1974.

D. C. Fritts. Gravity wave saturation in the middle atmosphere: A review of theory and observations. *Reviews of geophysics and space physics*, 22:275–308, 1984.

D. C. Fritts. A review of gravity wave saturation processes, effects and variability in the middle atmosphere. *PAGEOPH*, 130(2/3):343–371, 1989.

D. C. Fritts and T. J. Dunkerton. Fluxes of heat and constituents due to convectively unstable gravity waves. *Journal of the Atmospheric Sciences*, 42(6):549–556, 1985.

D. C. Fritts and P. K. Rastogi. Convective and dynamical instabilities due to gravity wave motions in the lower and middle atmosphere: Theory and observations. *Radio Science*, 20:1247–1277, 1985.

D. C. Fritts, T. Tsuda, T. E. VanZandt, S. A. Smith, T. Sato, S. Fukao, and S. Kato. Studies of velocity fluctuations in the lower atmosphere using the MU radar. part II: Momentum fluxes and energy densities. *Journal of the Atmospheric Sciences*, 47(1):51–66, 1990.

D. C. Fritts and T. E. VanZandt. Effects of Doppler shifting on the frequency spectra of atmospheric gravity waves. *Journal of Geophysical Research*, 92(D8):9723–9732, 1987.

D. C. Fritts and R. A. Vincent. Mesospheric momentum flux studies at Adelaide, Australia: Observations and a gravity wave-tidal interaction model. *Journal of the Atmospheric Sciences*, 44(3):605–619, 1987.

D. C. Fritts and L. Yuan. Measurement of the momentum fluxes near the summer mesopause at Poker Flat, Alaska. *Journal of the Atmospheric Sciences*, 46:2569–2579, 1989.

N. M. Gavrilov and G. M. Shved. Study of internal gravity waves in the lower thermosphere from observations of the nocturnal sky airglow [O1] 5577 A in Ashkhabad. *Annales de Geophysique*, 38:789–803, 1982.

M. A. Geller. Dynamics of the middle atmosphere. *Space Science Reviews*, 34:359–375, 1983.

S. Goldman. *Frequency Analysis. Modulation and Noise.* McGraw-Hill Book Company, 1948.

E. E. Gossard and W. H. Hooke. *Waves in the atmosphere.* Elsevier scientific publishing company, 1975.

G. V. Groves. *Modeling of atmospheric structure, 70–130 km.* Technical Report AFGL-TR-87-0226, Air Force Geophysics, Hanscom Air Force Base, Massachusetts, U.S.A., 1987.

A. Haug and H. Pettersen. An interpretation of asymmetric cross-correlation functions in D- and lower E-region drift measurements. *Journal of Atmospheric and Terrestrial Physics*, 32:397–403, 1970.

B. Haurwitz. Frictional effects and the meridional circulation in the mesosphere. *Journal of Geophysical Research*, 66:2381–2391, 1961.

Y. Hayashi, D. G. Golder, J. D. Mahlman, and S. Miyahara. The effect of horizontal resolution on gravity waves simulated by the GFDL "SKYHI" general circulation model. *PAGEOPH*, 130(2/3):421–443, 1989.

P. H. Hildebrand and R. S. Sekhon. Objective determination of the noise level in Doppler spectra. *Journal of Applied Meteorology*, 13:808–811, 1974.

C. O. Hines. Internal atmospheric gravity waves at ionospheric heights. *Canadian Journal of Physics*, 38:1441–1481, 1960.

C. O. Hines. Eddy diffusion coefficients due to instabilities in internal gravity waves. *Journal of Geophysical Research*, 75:3937–3939, 1970.

C. O. Hines. Momentum deposition by atmospheric waves, and its effects on thermospheric circulation. *Space Research*, 12:1157–1161, 1972.

C. O. Hines. Early days of gravity waves revisited. *PAGEOPH*, 130:151–170, 1989.

W. K. Hocking. Angular and temporal characteristics of partial reflections from the D-region of the ionosphere. *Journal of Geophysical Research*, 84:845–851, 1979.

W. K. Hocking. On the extraction of atmospheric turbulence parameters from radar backscatter Doppler spectra-I. theory. *Journal of Atmospheric and Terrestrial Physics*, 45(2/3):89–102, 1983a.

W. K. Hocking. Mesospheric turbulence intensities measured with a HF radar at 35°S-II. *Journal of Atmospheric and Terrestrial Physics*, 45(2/3):103–114, 1983b.

W. K. Hocking. Measurement of turbulent energy dissipation rates in the middle atmosphere by radar techniques: a review. *Radio Science*, 20(6):1403–1422, 1985.

W. K. Hocking. Two years of continuous measurements of turbulence parameters in the upper mesosphere and lower thermosphere with a 2-MHz radar. *Journal of Geophysical Research*, 93:2475–2491, 1988.

W. K. Hocking. Target parameter estimation. *Handbook for MAP, in press*, 1989.

W. K. Hocking. Gravity wave oscillations as a cause of spectral broadening. *Handbook for MAP, in press*, 1989.

W. K. Hocking, P. May, and J Röttger. Interpretation, reliability and accuracies of parameters deduced by the spaced antenna method in middle atmosphere applications. *PAGEOPH*, 130(2/3):571–604, 1989.

W. K. Hocking, R. Rüster, and P. Czechowsky. Absolute reflectivities and aspect sensitivities of VHF radio wave scatterers measured with the SOUSY radar. *Journal of Atmospheric and Terrestrial Physics*, 48(2):131–144, 1986.

J. R. Holton. The role of gravity wave induced drag and diffusion in the momentum budget of the mesosphere. *Journal of the Atmospheric Sciences*, 39:791–799, 1982.

J. R. Holton. The influence of gravity wave breaking on the general circulation of the middle atmosphere. *Journal of the Atmospheric Sciences*, 40:2497–2507, 1983.

J. Holton and W. Wehrbein. A numerical model of the zonal mean circulation of the middle atmosphere. *PAGEOPH*, 118:284–306, 1980.

J. R. Holton and X. Zhu. A further study of gravity wave induced drag and diffusion in the mesosphere. *Journal of the Atmospheric Sciences*, 41(18):2653–2662, 1984.

R. R. Hodges Jr. Generation of turbulence in the upper atmosphere by internal gravity waves. *Journal of Geophysical Research*, 72:3455–3458, 1967.

R. R. Hodges Jr. Eddy diffusion coefficients due to instabilities in internal gravity waves. *Journal of Geophysical Research*, 74:4087–4090, 1969.

J. T. Houghton. The stratosphere and mesosphere. *Quarterly Journal of the Royal Meteorological Society*, 104:1–29, 1978.

J. T. Kiehl and S. Solomon. On the radiative balance of the stratosphere. *Journal of the Atmospheric Sciences*, 43(14):1525–1534, 1986.

J. Klostermeyer. Gravity waves and instabilities in the lower and middle atmosphere. In S. Fukao, editor, *International school on atmospheric radar - Lecture notes*, 1988.

C. G. Koop. A preliminary investigation of the interaction of internal gravity waves with a steady shearing motion. *Journal of Fluid Mechanics*, 113:347–386, 1981.

C. Leovy. Simple models of thermally driven mesospheric circulation. *Journal of the Atmospheric Sciences*, 21:327–341, 1964.

R. M. Lhermitte. Turbulent air motions as observed by Doppler radar. In *Proceedings of the 13th radar meteorolgy conference*, pages 489–503, 1968.

R. Lhermitte and H. Poor. Multi-beam Doppler sonar observations of tidal flow turbulence. *Geophysical Research Letters*, 10(8):717–720, 1983.

W. Liller and F. L. Whipple. High-altitude winds by meteor-train photography. In "Rocket Exploration of the Upper Atmosphere", special supplement to *Journal of Atmospheric and Terrestrial Physics*, 1, Pergamon, New York, 1954.

D. K. Lilly, D. E. Waco, and S. I. Adelfang. Stratospheric mixing estimated from high-altitude turbulence measurements. *Journal of Applied Meteorology*, 13:488–493, 1974.

B. C. Lindner. The nature of D-region scattering of vertical incidence radio waves. II-Experimental observations using spaced antenna reception. *Australian Journal of Physics*, 28:171–184, 1975.

R. S. Lindzen. Turbulence and stress owing to gravity wave and tidal breakdown. *Journal of Geophysical Research*, 86:9707–9714, 1981.

R. S. Lindzen. *Dynamics of the middle atmosphere*, pages 3–18. Terra Scientific, 1984.

J. London. Radiative energy sources and sinks in the stratosphere and mesosphere. In A. C. Aiken, editor, *Atmos. Ozone, Proc. NATO Adv. Study Inst.*, pages 703–721, 1980.

D. Lu, T. E. VanZandt, and W. L. Clark. VHF Doppler radar observations of buoyancy waves associated with thunderstorms. *Journal of the Atmospheric Sciences*, 41(2):272–282, 1984.

J. L. Lumley. The spectrum of nearly inertial turbulence in a stably stratified fluid. *Journal of the Atmospheric Sciences*, 21:99–102, 1964.

T. Matsuno. A quasi one-dimensional model of the middle atmosphere circulation interacting with internal gravity waves. *Journal of the Meteorological Society of Japan*, 60:215–226, 1982.

P. T. May. Statistical errors in the determination of wind velocities by the spaced antenna technique. *Journal of Atmospheric and Terrestrial Physics*, 50(1):21–32, 1988.

P. T. May, T. Sato, M. Yamamoto, S. Kato, T. Tsuda, and S. Fukao. Errors in the determination of wind speed by Doppler radar. *Journal of Atmospheric and Oceanic Technology*, 6(2):235–242, 1989.

J. R. McAfee, B. B. Balsley, and K. S. Gage. Momentum flux measurements over mountains: problems associated with the symmetrical two-beam radar technique. *Journal of Atmospheric and Oceanic Technology*, 6:500–508, 1989.

M. E. McIntyre. On the 'wave momentum' myth. *Journal of Fluid Mechanics*, 106:331–347, 1981.

C. E. Meek and A. H. Manson. Vertical motions in the upper middle atmosphere from the Saskatoon (52°N,107°W) M. F. radar. *Journal of the Atmospheric Sciences*, 46(6):849–858, 1989.

C. E. Meek and I. M. Reid. A simple model for testing the effects of gravity-wave-produced vertical oscillations of scattering irregularities on spaced-antenna, horizontal drift measurements. *Handbook for MAP*, 14:131–133, 1984.

C. E. Meek, I. M. Reid, and A. H. Manson. Observations of mesospheric wind velocities - 2. Cross sections of power spectral density for 48–8 hours, 8–1 hour and 1 hour to 10 min over 60–110 km for 1981. *Radio Science*, 20(6):1383–1402, 1985.

W. Meyer, R. Siebenmorgen, and H.-U. Widdel. Estimates of gravity wave momentum fluxes in the winter and summer high mesosphere over northern Scandinavia. *Journal of Atmospheric and Terrestrial Physics*, 51(4):311–319, 1989.

S. N. Mitra. A radio method of measuring winds in the ionosphere. *Proceedings of the Institute of electical engineers*, 96:441–446, 1949.

S. Miyahara and D. Wu. Effects of solar tides on the zonal mean circulation in the lower thermosphere: solstice condition. *Journal of Atmospheric and Terrestrial Physics*, 51(7/8):635–647, 1989.

P. Muller, G. Holloway, F. Heyney, and N. Pomphrey. Nonlinear interactions among internal gravity waves. *Reviews of Geophysics*, 24:493–536, 1986.

R. J. Murgatroyd. *The global circulation of the atmosphere*, pages 159–195. Royal meteorological society, 1969.

D. J. Murphy. *Vertical motions in the mesosphere.* Master's thesis, University of Adelaide, 1984.

R. S. Narcisi and A. D. Bailey. Mass spectrometric measurements of positive ions at altitudes from 64 to 112 kilometers. *Journal of Geophysical Research*, 70:3687–3700, 1965.

G. D. Nastrom, B. B. Balsley, and D. A. Carter. Mean meridional winds in the mid- and high-latitude summer mesosphere. *Geophysical Research Letters*, 9:139–142, 1982.

M. Nicolet and A. C. Aiken. The formation of the D region of the ionosphere. *Journal of Geophysical Research*, 65:1469–1483, 1960.

H. Ottersten. Radar backscattering from the turbulent clear atmosphere. *Radio Science*, 4(12):1251–1255, 1969.

W. H. Press, B. P. Flannery, S. A. Teukolsky, and W. T. Vetterling. *Numerical Recipes.* Cambridge University Press, 1986.

P. K. Rastogi and R. F. Woodman. Mesospheric studies using the Jicamarca incoherent-scatter radar. *Journal of Atmospheric and Terrestrial Physics*, 36:1217–1231, 1974.

J. A. Ratcliffe. Some aspects of diffraction theory and their application to the ionosphere. *Reports on Progress in Physics*, 19:188–267, 1956.

I. M. Reid. *Radar studies of atmospheric gravity waves.* PhD thesis, University of Adelaide, 1984.

I. M. Reid. Some aspects of Doppler radar measurements of the mean and fluctuating components of the wind field in the upper middle atmosphere. *Journal of Atmospheric and Terrestrial Physics*, 49(5):467–484, 1987.

I. M. Reid. MF Doppler and spaced antenna radar measurements of upper middle atmosphere winds. *Journal of Atmospheric and Terrestrial Physics*, 50(2):117–134, 1988.

I. M. Reid and R. A. Vincent. Measurements of mesospheric gravity wave momentum fluxes and mean flow accelerations at Adelaide, Australia. *Journal of Atmospheric and Terrestrial Physics*, 49(5):443–460, 1987.

F. Reif. *Statistical and thermal physics.* McGraw-Hill Kogakusha, 1965.

L. F. Richardson. *Weather prediction by numerical process.* Cambridge University Press, 1922.

D. Rind, R. Suozzo, N. K. Balachandran, A. Lacis, and G. Russell. The GISS global climate-middle atmosphere model. Part I: Model structure and climatology. *Journal of the Atmospheric Sciences*, 45(3):329–370, 1988a.

D. Rind, R. Suozzo, and N. K. Balachandran. The GISS global climate-middle atmosphere model. Part II: Model variability due to interactions between planetary waves, the mean circulation and gravity wave drag. *Journal of the Atmospheric Sciences*, 45(3):371–386, 1988b.

J. Röttger. Investigations of lower and middle atmosphere dynamics with spaced antenna drifts radars. *Journal of Atmospheric and Terrestrial Physics*, 43(4):277–292, 1981.

J. Röttger. The MST radar technique. *Handbook for MAP*, 13:187–232, 1984.

O. Røyrvik. Spaced antenna drift at Jicamarca, mesospheric measurements. *Radio Science*, 18(3):461–476, 1983.

O. Røyrvik and L. G. Smith. Comparison of mesospheric VHF radar echoes and rocket probe electron concentration measurements. *Journal of Geophysical Research*, 89(A10):9014–9022, 1984.

R. Rüster and I. M. Reid. VHF radar observations of the dynamics of the summer polar mesopause region. *Journal of Geophysical Research*, 95(D7):10005–10016, 1990.

G. Schmidt, R. Rüster, and P. Czechowsky. Complementary code and digital filtering for detection of weak VHF radar signals from the mesosphere. *IEEE Transactions: Geosciences and Electronics*, GE-17:154–161, 1979.

M. Schoeberl and D. Strobel. The zonally averaged circulation of the middle atmosphere. *Journal of the Atmospheric Sciences*, 35:577–591, 1978.

C. Sidi and F. Dalaudier. Temperature and heat flux spectra in the turbulent buoyancy subrange. *PAGEOPH*, 130(2/3):547–569, 1989.

R. C. Singleton. An algorithm for computing the mixed radix fast Fourier transform. *IEEE Transactions on Audio and Electroacoustics*, AU-17(2):93–103, 1969.

S. A. Smith and D. C. Fritts. Estimation of gravity wave motions, momentum fluxes and induced mean flow accelerations in the winter mesosphere over Poker Flat, Alaska. In *Proceedings of the 21st radar meteorolgy conference*, pages 104–110, 1983.

W. G. Stroud, W. Nordberg, W. R. Bandeen, F. L. Bartman, and P. Titus. Rocket-grenade measurements of temperatures and winds in the mesosphere over Churchill, Canada. *Journal of Geophysical Research*, 65:2307–2323, 1960.

V. I. Tatarski. *Wave propagation in a turbulent medium.* McGraw-Hill Book Company, 1961.

M. J. Taylor and M. A. Hapgood. Identification of a thunderstorm as a source of short period gravity waves in the upper atmospheric nightglow emissions. *Planetary and Space Science*, 36(10):975–985, 1988.

H. Tennekes and J. L. Lumley. *A first course in turbulence.* The MIT Press, 1972.

E. V. Thrane, Ø. Andreassen, T. Blix, B. Grandal, A. Brekke, C. R. Philbrick, F. J. Schmidlin, H. U. Widdel, U. von Zahn, and F. J. Lübken. Neutral air turbulence in the upper atmosphere observed during the energy budget campaign. *Journal of Atmospheric and Terrestrial Physics*, 47(1):243–264, 1985.

T. Tsuda, Y. Murayama, M. Yamamoto, S. Kato, and S. Fukao. Seasonal variation of the momentum flux in the mesosphere observed with the MU radar. *Geophysical Research Letters*, 17(6):725–728, 1990.

R. A. Vincent. Gravity-wave motions in the mesosphere. *Journal of Atmospheric and Terrestrial Physics*, 46(2):119–128, 1984.

R. A. Vincent and J. S. Belrose. The angular distribution of radio waves partially reflected from the lower ionosphere. *Journal of Atmospheric and Terrestrial Physics*, 40:35–47, 1978.

R. A. Vincent and I. M. Reid. HF Doppler measurements of mesospheric gravity wave momentum fluxes. *Journal of the Atmospheric Sciences*, 40:1321–1333, 1983.

R. A. Vincent, T. J. Stubbs, P. H. O. Pearson, K. H. Lloyd, and C. H. Low. A comparison of partial reflection drifts with winds determined by rocket techniques-1. *Journal of Atmospheric and Terrestrial Physics*, 39:813–821, 1977.

R. A. Vincent, T. Tsuda, and S. Kato. A comparative study of mesospheric solar tides observed at Adelaide and Kyoto. *Journal of Geophysical Research*, 93(D3):699–708, 1988.

R. A. Vincent, T. Tsuda, and S. Kato. Asymmetries in mesospheric tidal structure. *Journal of Atmospheric and Terrestrial Physics*, 51(7/8):609–616, 1989.

R. L. Walterscheid. Inertio-gravity wave induced accelerations of mean flow having an imposed periodic component: Implications for tidal observations in the meteor region. *Journal of Geophysical Research*, 86:9698–9706, 1981.

D. Y. Wang and D. C. Fritts. Mesospheric momentum fluxes observed by the MST radar at Poker Flat, Alaska. *Journal of the Atmospheric Sciences*, 47:1512–1521, 1990a.

D. Y. Wang and D. C. Fritts. Evidence of gravity wave-tidal interaction observed near the summer mesopause at Poker Flat, Alaska. *Journal of the Atmospheric Sciences, submitted*, 1990b.

B. J. Watkins, C. R. Philbrick, and B. B. Balsley. Turbulence energy dissipation rates and inner scale sizes from rocket and radar data. *Journal of Geophysical Research*, 93(D6):7009–7104, 1988.

W. Wehrbein and C. Leovy. An accurate radiative heating and cooling algorithm for use in a dynamical model of the middle atmosphere. *Journal of the Atmospheric Sciences*, 39:1532–1544, 1982.

J. Weinstock. On the theory of turbulence in the buoyancy subrange of stably stratified flows. *Journal of the Atmospheric Sciences*, 35:634–649, 1978a.

J. Weinstock. Vertical turbulent diffusion in a stably stratified fluid. *Journal of the Atmospheric Sciences*, 35:1022–1027, 1978b.

J. Weinstock. Energy dissipation rates of turbulence in the stable free atmosphere. *Journal of the Atmospheric Sciences*, 38:880–883, 1981.

J. D. Whitehead, W. R. From, K. L. Jones, and P. E. Monro. Measurement of movements in the ionosphere using radio reflections. *Journal of Atmospheric and Terrestrial Physics*, 45(5):345–351, 1983.

D. A. Wilson. Doppler radar studies of boundary layer wind profile and turbulence in snow conditions. In *Preprints of the 13th radar meteorolgy conference*, pages 191–196, 1970.

D. A. Wilson and L. J. Miller. *Atmospheric motion by Doppler radar*, chapter 13, pages 13–1 – 13–34. University of Colorado, Boulder, Colorado, 1972.

R. F. Woodman. Spectral moment estimation in MST radars. *Radio Science*, 20(6):1185–1195, 1985.

R. F. Woodman and A. Guillen. Radar observations of winds and turbulence in the stratosphere and mesosphere. *Journal of the Atmospheric Sciences*, 31:493–505, 1974.

R. F. Woodman and T. Hagfors. Methods of the measurement of vertical ionospheric motions near the magnetic equator by incoherent scattering. *Journal of Geophysical Research*, 75:1205–1212, 1969.

M. Yamamoto, T. Sato, P. T. May, T. Tsuda, S. Fukao, and S. Kato. Estimation error of spectral parameters of MST radar obtained by least squares fitting method and its lower bound. *Radio Science*, 23:1013–1021, 1988.

K. C. Yeh and C. H. Liu. The instability of atmospheric gravity waves through wave-wave interactions. *Journal of Geophysical Research*, 86:9722–9728, 1981.

D. S. Zrnić. Estimation of spectral moments for weather echoes. *IEEE Transactions: Geosciences and Electronics*, GE-17(4):113–128, 1979.